


Spring 1-1-2011

Dynamic Gas-Surface Interaction Modeling for Satellite Aerodynamic Computations

Marcin Dominik Pilinski

University of Colorado at Boulder, marcin.pilinski@colorado.edu

Follow this and additional works at: https://scholar.colorado.edu/asen_gradetds

 Part of the [Aerodynamics and Fluid Mechanics Commons](#), and the [Physical Chemistry Commons](#)

Recommended Citation

Pilinski, Marcin Dominik, "Dynamic Gas-Surface Interaction Modeling for Satellite Aerodynamic Computations" (2011). *Aerospace Engineering Sciences Graduate Theses & Dissertations*. 37.
https://scholar.colorado.edu/asen_gradetds/37

This Dissertation is brought to you for free and open access by Aerospace Engineering Sciences at CU Scholar. It has been accepted for inclusion in Aerospace Engineering Sciences Graduate Theses & Dissertations by an authorized administrator of CU Scholar. For more information, please contact cuscholaradmin@colorado.edu.

**Dynamic Gas-Surface Interaction Modeling for Satellite
Aerodynamic Computations**

by

M. D. Pilinski

B.S. in Aerospace Engineering, The University of Texas, 2005

B.S. in Physics, The University of Texas, 2006

M.S. in Aerospace Engineering Sciences, University of Colorado, 2008

A thesis submitted to the
Faculty of the Graduate School of the
University of Colorado in partial fulfillment
of the requirements for the degree of
Doctor of Philosophy
Department of Aerospace Engineering Sciences

2011

This thesis entitled:
Dynamic Gas-Surface Interaction Modeling for Satellite Aerodynamic Computations
written by M. D. Pilinski
has been approved for the Department of Aerospace Engineering Sciences

Prof. Brian Argrow

Prof. Scott Palo

Prof. Jeffrey Forbes

Prof. John Falconer

Dr. Kenneth Moe

Date _____

The final copy of this thesis has been examined by the signatories, and we find that both the content and the form meet acceptable presentation standards of scholarly work in the above mentioned discipline.

Pilinski, M. D. (Ph.D., Aerospace Engineering Sciences)

Dynamic Gas-Surface Interaction Modeling for Satellite Aerodynamic Computations

Thesis directed by Prof. Brian Argrow

Drag coefficients are a large source of uncertainty when predicting the aerodynamic forces on orbiting satellites. Accordingly, the focus of this research is to improve the fidelity of drag modeling by investigating the nature of gas-surface interactions in low earth orbit. The author has investigated to what extent oxygen adsorption can influence the parameters of drag coefficient models, most notably the energy accommodation coefficient. To accomplish this, several analysis techniques are applied. Fitted drag coefficients for 68 objects were provided by Air Force Space Command Drag Analysis Office and are analyzed using analytical and numerical aerodynamic models. Gas-surface parameters are estimated by comparing the model results to the observed coefficients. The results indicate that a successful and predictive relationship of the energy accommodation coefficient can be obtained with gas-surface models incorporating Langmuir adsorption. Good agreement with data has been obtained by using a cosine reflection model below 500 km. Furthermore, it is found that satellite accommodation coefficients can be explained by a model in which atomic oxygen binds to the surface with an energy of approximately 5.7 eV. Multi-axis accelerometer data from the CHAMP and GRACE satellites has also been analyzed to derive measurements of lift and drag which are compared to model predictions given different gas-surface assumptions. The results indicate that diffuse reflection is appropriate for CHAMP near 400 km and that the accommodation coefficient before 2008 ranges between 0.86 and 0.89. CHAMP accelerometer data is also combined with remote sensing estimates of density to arrive at values of drag coefficient which do not depend on empirical atmospheric models alone. This dataset confirms the predicted drop in accommodation with decreasing atomic oxygen pressure. The culmination of this work is an enhanced energy accommodation and drag coefficient model applicable between 100 km and 500 km altitudes for satellites in both circular and elliptical orbits.

Dedication

To Emily, my wife and best friend.

Acknowledgements

The author extends sincere gratitude to the many people who made this adventure and dream possible. First, to Tadeusz and Iwona Pilinski for their encouragement and high expectations. To Wanda and Janek Olszewski for encouraging my interest in science and technology. To my wife Emily, who was there through all the writing and research, thank you for your patience and support.

The author thanks Dr. Brian Argrow for advising and supporting this work as well as Dr. Scott Palo who encouraged me to pursue the doctoral thesis. Dr. Argrow and Dr. Palo have been wonderful and patient mentors and it has been a great benefit to the author to receive their tutelage. Dr. Jeff Forbes provided the critical encouragement to publish and has provided other gems of advice which the author will never forget. Mr. Chris Koehler took a chance to hire the author for the duration of his Masters work and made possible his coming to the University of Colorado at Boulder. Without that leap-of-faith, none of this would have been possible.

Drs. Kenneth and Mildred Moe have been an inspiration and constant source of scientific and non-scientific feedback which helped steer this work in a productive direction. The author would also like to thank them for a thorough introduction to the subject of satellite drag and gas-surface interactions.

Many thanks goes to Mr. Bruce Bowman for providing the fitted-ballistic coefficients, answering the author's questions with regards to the measurement technique, and for providing the motivation to study low-altitude satellite aerodynamics. The author also thanks Dr. Eric Sutton and Dr. Eelco Doornbos for the CHAMP and GRACE accelerometer datasets as well as for the thoughtful feedback and stimulating discussions. Thanks also to the Air Force Research Laboratory for funding the summer internship which led to the development of the SPARCS software used in this research.

Contents

Chapter	
1	Executive Summary 1
2	Introduction 3
2.1	Motivation 7
2.2	Scientific Questions 9
3	Review of Progress in Drag Coefficient Modeling and Gas-Surface Interactions for Rarefied Flow Applications 11
3.1	Gas-Surface Interactions and the Satellite Drag Coefficient 13
3.1.1	Laboratory Measurements of Gas-Surface Interactions 14
3.1.2	Gas-Surface Interactions in Earth Orbit 25
3.1.3	Scattering Kernels 35
3.1.4	Satellite Drag Coefficient Modeling 37
3.2	Drag Coefficients and the Development of Atmospheric Models 43
4	Aerodynamic Force Coefficient Computations 48
4.1	Integral Equations 54
4.2	Plate Models 55
4.3	Test-Particle Methods 56
4.3.1	Software Description 57
4.3.2	Preliminary Reference Frame Definitions 58

4.3.3	Cross-Sectional Area Computation	58
4.3.4	Aerodynamic Calculations	62
4.4	Direct Simulation Monte Carlo	67
4.5	Sensitivity to Inputs	68
4.6	Force Coefficient Lookup Tables	81
5	Satellite Observations	86
5.1	Measurements of Multiple Interactions With the Atmosphere	88
5.2	Fitted Ballistic Coefficients	93
5.2.1	Spheres	93
5.2.2	Rocket Bodies	96
5.3	Remote Sensing Observations of Atmospheric Density	99
5.4	Accelerometer Data: Multi-Axial Acceleration Measurements	104
6	Review of Analysis Methods	107
6.1	Using Fitted Ballistic Coefficients for Gas-Surface Interaction Evaluation	108
6.2	Multi-Instrument Analysis	118
6.3	Orthogonal Force Coefficient Analysis	119
6.4	From Drag Observations to Surface Parameters	125
7	Evidence of a Link Between Adsorption of Atomic Oxygen and Accommodation at High Thermospheric Pressures	128
7.1	Assumptions	128
7.2	Computational Method	128
7.3	Results	130
8	Dynamics of Adsorption Phenomena and the Satellite Drag Coefficient at High Thermospheric Pressures	138
8.1	Computational Method	138

8.2	Sensitivity Analysis to Model Assumptions	139
8.3	Initial Results	141
9	Evidence of Low Energy Accommodation Coefficients at Reduced Thermospheric Pressures	146
9.1	Multi-Instrument Results	148
10	Evaluating Gas-Surface Interactions Based on Orthogonal Force Coefficient Observations at Low Thermospheric Pressures	155
10.1	Small Angle Investigation	155
10.2	Yaw Maneuver Investigation	156
11	Semi-Empirical Model for Compact Shapes	170
11.1	Model Evaluation and Tuning	170
11.2	Extension to Satellites with Large Surfaces Parallel to the Free-Stream	183
11.3	Discussion	187
12	Conclusions and Recommendations	189
12.1	Discussion	189
12.1.1	Scattering Kernels	189
12.1.2	Energy Accommodation Measurements	190
12.1.3	Energy Accommodation Model	192
12.2	Recommendations	193
12.3	Conclusion	194
	Bibliography	196
	Appendix	
A	Drag Coefficient of a Cylinder	205

B Numerical Program Validation	208
---------------------------------------	-----

C SESAM Drag Coefficient Lookup Tables	212
---	-----

Tables

Table

4.1	CHAMP geometry models and their cross-sectional areas (in square meters) projected along different axes (Expressed in the CHAMP satellite body fixed or SBF coordinates). Highlighted in light-grey are the latest ESA model as well as well as the model developed for SPARCS. The often-used GFZ model is highlighted in dark-grey. The Δ columns indicate the difference in satellite projections in the positive and negative directions of any given axis i.e. $\Delta X = A_{+X} - A_{-X}$	64
4.2	Effect of omitting multiple reflections on C_D computations of the CHAMP satellite. Percentage values of multiply reflected molecules refer to the relative amount of potential secondary reflections which are allowed to remain inside the geometry.	73
5.1	Energy accommodation measurements believed to be applicable to Earth orbiting satellites. Information is included where available.	87
5.2	Laboratory and theoretical results for the surface-binding energies for atomic oxygen. The average binding energy for these materials is 4.3 eV.	88
5.3	Spherical tracking objects used to construct the accommodation coefficient model.	96
5.4	Spheres and rocket bodies used in the determination of SESAM parameters.	97
5.5	Description of relevant physical parameters measured by GUVI in the dayside limb.	101
6.1	Jacchia 70 density corrections as determined by Bowman and Moe [Bowman and Moe, 2005] and used to adjust the measured drag coefficients.	109

7.1	Solar maximum values of $n_O \cdot T_i$ and energy accommodation coefficient.	132
7.2	Solar minimum values of $n_O \cdot T_a$ and energy accommodation coefficient.	132
11.1	Optimal parameters for SESAM	170
11.2	Results of SESAM extended to satellites with long shapes	187
B.1	Convex geometry validation.	210
C.1	DSMC drag coefficient results for velocities of 7,500 m/s.	212
C.2	DSMC drag coefficient results for velocities of 10,300 m/s.	213

Figures

Figure

2.1	Vector variables of the drag equation.	5
2.2	CHAMP accelerometer-derived densities during 2003 using two different geometry models to compute $C_D A$. Above, ρ_A and ρ_B signify the average densities for 2003 when using the panel and ANGARA models respectively to solve for atmospheric density.	8
3.1	The Langmuir adsorption model assumes that the sticking probability is related only to the amount of adsorbate already occupying surface sites.	15
3.2	Example of Langmuir isotherms from Brunauer et al.[Brunauer et al., 1938].	16
3.3	Lattice based energy accommodation model described by Goodman [Goodman, 1974].	18
3.4	Accommodation coefficient measurements and models.	22
3.5	Energy accommodation measurements in the presence of adsorption as well measurements made in LEO.	24
3.6	The difference in rough and smooth ODERACS drag coefficients.	29
3.7	Independent measurements leading to estimates of the drag and accommodation coefficients.	31
3.8	Satellites which have been used to measure the energy accommodation coefficient.	33
3.9	Reflection distribution measured in LEO by Gregory and Peters and fit using a single-lobe Nocilla model [Gregory and Peters, 1987]. Also shown is the cosine distribution.	38
3.10	Reflection distribution measured in LEO by Gregory and Peters and fit using a single-lobe Nocilla model [Gregory and Peters, 1987]. Also shown is the cosine distribution.	39

4.1	The diffuse and quasi-specular reflection models.	50
4.2	Block diagram of SPARCS.	59
4.3	CHAMP local free-stream coordinate system with pitch and sideslip definitions.	60
4.4	The CHAMP body fixed frame (SBF).	61
4.5	Example of a satellite outline contour.	61
4.6	CHAMP cross-sectional area computed using the outline method.	62
4.7	Cross-sectional area computed using the test particle ('csa' mode) over a full range of pitch angels. Plate model area is shown in blue for comparison.	63
4.8	Flow generation boundaries showing initial and final states of generated molecules with an arbitrary satellite geometry.	66
4.9	3D display of ensemble results from the SPARCS program.	67
4.10	Drag coefficient sensitivity to (a) mean molecular mass, (b) free-stream speed, (c) wall tem- perature, and (d) atmospheric temperature at a range of accommodation coefficients.	69
4.11	The drag coefficient of a sphere and a flat plate during solar maximum and solar minimum.	71
4.12	Force coefficient sensitivity to geometry modeling. The GFZ panel model was originally used for density determination.	73
4.13	CHAMP cross-sectional area for different geometry models. Note that both the test particle and outline methods agree to better than 0.3%.	74
4.14	Descriptions of CHAMP geometry files constructed for use with SPARCS.	75
4.15	Solar maximum drag force coefficients computed using the SPARCS and plate GFZ plate models along the CHAMP satellite track at 414 km altitude.	77
4.16	Solar minimum drag force coefficients computed using the SPARCS and plate GFZ plate models along the CHAMP satellite track at 358 km altitude.	77
4.17	Comparison of densities computed using the GFZ plate ANGARA (courtesy of Dr. Doornbos) and SPARCS models.	78

4.18	CHAMP drag force coefficient ($C_D \times A$) and ratio of GFZ to SPARCS force coefficients along with NRLMSISE-00 and accelerometer density response at night during the October 2003 Halloween storms.	78
4.19	CHAMP drag force coefficient ($C_D \times A$) and ratio of GFZ to SPARCS force coefficients along with NRLMSISE-00 and accelerometer density response during daytime of the October 2003 Halloween storms.	79
4.20	Drag force coefficients ($C_D \times A$) for the forward and aft flying modes of CHAMP during February 2010.	79
4.21	Ratio of drag force coefficients computed using the GFZ plate model and the CHAMP1v1 model for the forward and aft flying modes. Note that the two models show greater disagreement in the aft flying mode.	80
4.22	Pitch and sideslip angles estimated for the CHAMP spacecraft.	81
4.23	CHAMP C_X lookup table interpolation with validation values.	83
4.24	CHAMP C_Y lookup table interpolation with validation values.	84
4.25	Extrapolating from the CHAMP lookup table in the accommodation parameter.	85
5.1	The analysis times of accommodation measurements overlaid on a plot of solar activity.	91
5.2	Estimated energy accommodation coefficients.	95
5.3	Silhouettes of rocket bodies in the fitted-ballistic dataset.	98
5.4	Sample size organized by latitude, altitude, and local solar time (LST) bins.	98
5.5	SL-6 (Molniya) observed C_D in the transition and free-molecular flow regimes.	100
5.6	The radiative transfer phenomena associated with FUV dayglow observation.	102
6.1	DSMC simulation of a sphere at 120 km perigee altitude undergoing transition flow.	112
6.2	Langmuir isotherm based C_D fits to observed data shown for the SL-6 rocket body 15955. Lookup table values (see Appendix C) on which the C_D fit is based are shown for reference. The accommodation coefficient associated with each look-up curve is indicated. V_p denotes the effective relative velocity at perigee.	115

6.3	Changes in the initial sticking coefficient as a function of the bonding energy and the Maxwellian energy distribution.	117
6.4	CHAMP satellite lift to drag ratio expressed in accelerometer measurement axes.	122
6.5	Winds modeled using HWM-07 at 450 km altitudes show a minimum wind near the exospheric temperature maxima and minima.	123
6.6	Examples in the variability of a_y/a_x slope measurements at small sideslip angles.	124
7.1	Flow diagram summarizing the computation procedure for accommodation coefficients.	130
7.2	Accommodation coefficients as a function of $n_O \cdot T_a$. The fit was based on data taken during solar minimum (blue diamonds) and solar maximum (red circles).	133
7.3	Estimated energy accommodation coefficients with the semi-empirical model.	135
8.1	Drag coefficients of randomly tumbling cylinders compared with the drag coefficient of a sphere.	140
8.2	Sensitivity of the ballistic coefficient of a rocket body. The gray area indicates the range of possible values based on minimum and maximum cross sectional areas.	142
8.3	Changes in the Langmuir parameter as a function of energy with resulting fit. All rocket bodies were given a constant 2% propellant margin.	144
8.4	Changes in the Langmuir parameter as a function of energy with resulting fit. Propellant margin was ascertained from comparisons with spherical satellite ballistic coefficients.	145
9.1	Coincidence data within 30 seconds and 150 km distance. The data was also restricted to exclude latitudes above 45°N and below 45°S latitudes.	149
9.2	GUVI and CHAMP density measurements averaged by 4 month bins. The error bars indicate the uncertainty in each measurement as reported in the CHAMP and GUVI files. Plotted in the lower panels are the solar f10.7 and geomagnetic A_P indices, measurement altitudes, latitudes, and local-solar times.	151

9.3	GUVI and CHAMP density differences as a function of altitude. The data was binned by altitude and the average is represented by the black line while the blue lines represent the standard deviation of each bin.	152
9.4	GUVI and CHAMP density differences as a function of atomic oxygen static pressure.	152
9.5	GUVI and CHAMP density difference histogram $200(\rho_{GUVI} - \rho_{CHAMP})/(\rho_{GUVI} + \rho_{CHAMP})$. The black dashed line indicates zero-mean and the blue dotted line shows the mean of the distribution.	153
9.6	Observed and modeled drag coefficients as a function of atomic oxygen static pressure.	153
9.7	Estimated accommodation coefficients with previously determined values from lower altitudes. The red line is a linear fit to the data.	154
10.1	Measurements and models of C_x/C_y slopes for the CHAMP satellite from data taken between 2001 and 2008.	157
10.2	Measurements of C_x/C_y slopes for the GRACE-A satellite from data taken between 2002 and 2008.	158
10.3	Measurements and models of C_x/C_y slopes for the GRACE-B satellite from data taken between 2002 and 2008.	159
10.4	Measurements of orthogonal (x and y) accelerations and their projection onto the lift and drag directions.	161
10.5	Comparison of test-particle and panel solutions for the drag and lift coefficients of CHAMP assuming fully diffuse reflection with an accommodation coefficient of 0.93.	162
10.6	Comparison of test-particle and panel solutions for the drag and lift coefficients of CHAMP assuming Schamberg reflection only with panel dependent accommodation based on the Goodman model.	163
10.7	Measurements and diffuse models of C_y/C_x made by CHAMP during a yaw maneuver on November 6th, 2002.	165

10.8 Measurements and diffuse models of C_L/C_D made by CHAMP during a yaw maneuver on November 6th, 2002.	165
10.9 Measurements and QS models of C_y/C_x made by CHAMP during a yaw maneuver on November 6th, 2002.	166
10.10 Measurements and QS models of C_L/C_D made by CHAMP during a yaw maneuver on November 6th, 2002.	166
10.11 RMS error v.s. GSI model parameters for cosine reflection (left) and a cosine/Schamberg model blend (right). The RMS values are computed by comparing both lift and drag as well as x and y direction accelerations. The minima indicate the most successful GSI parameters.	167
10.12 Mean ratios of measured to modeled density are computed for forward flying and sideways flying modes. The mean ratio from the sideways flying mode (R_s) is divided by that of the forward-flying mode (R_f) and the results ($ 1 - R_s/R_f $) are plotted above as a function of the GSI parameters. The two candidate values identified through lift/drag analysis are circled. Note that the cosine-reflection model with incomplete energy accommodation results in densities which are more consistent between the forward and sideways flying modes.	169
11.1 Implementation of SESAM.	171
11.2 Observed drag coefficients of spherical satellites compared to fixed accommodation and Goodman models as well as SESAM with $K_{L,o} = 1 \times 10^6 \text{ Torr}^{-1}$, $K_{L,o} = 5 \times 10^6 \text{ Torr}^{-1}$, and $K_{L,o} = 8 \times 10^6 \text{ Torr}^{-1}$. Average altitudes are shown in grey.	173
11.3 SESAM with $K_{L,o} = 5 \times 10^6 \text{ Torr}^{-1}$ compared with sphere data of different surface compositions	174
11.4 Ratios of observed and modeled ballistic coefficients for the entire dataset. The Cauchy distribution is plotted in gray for reference and the inset value is the RMS of the difference between the distribution and a zero-mean Cauchy distribution.	176

11.5	Distribution of rocket body fuel margins for three different ballistic coefficient models. Black lines indicate the maxima and minima of the distributions, the blue box extend from the bottom 25th percentile to the top 75th percentile, and the red line represents the median . . .	176
11.6	Ratios of observed and modeled BFACTORS for four models binned by altitude.	178
11.7	Ratios of observed and modeled densities resulting from drag analysis using SESAM as well as measurements made by the GUVI instrument.	179
11.8	Contours of constant α from the SESAM accommodation model as a function of satellite speed and atomic oxygen pressure. The circles represent atmosphere-independent measurements of accommodation.	181
11.9	Direct comparison of the SESAM accommodation coefficients at different values of $K_{L,f}$ with independent measurements.	182
11.10	Direct comparison of the SESAM accommodation coefficients at different values of m_s with independent measurements.	184
11.11	Comparison of the present accommodation model with fitted data and the preliminary model for circular orbits.	185
A.1	Cylinder of diameter d and length l flying at angle of attack β	205
B.1	The wedge used to validate against convex (integral) equations.	209
B.2	Test particle validation for a cube geometry (a) free stream normal to face, (b) free-stream at oblique angle	209
B.3	Concave (CHAMP) geometry validation.	211

Chapter 1

Executive Summary

This research focuses on the determination of appropriate gas-surface interaction models which are consistent with observations of satellite drag as well as with gas-surface physics applicable to the spacecraft environment. The thin upper atmosphere (thermosphere) in which many spacecraft orbit is composed primarily of atomic oxygen which adsorbs readily on spacecraft materials. A body of research accumulated since the beginning of the Space Age indicates that adsorption modifies the extent to which impinging molecules exchange energy with the surface. The parameter describing the extent of energy exchange is called the energy accommodation coefficient. A great deal of the work described herein is concerned with the prediction and measurement of accommodation coefficients at altitudes ranging from 100-500 km.

Fitted drag coefficients are computed by comparing observed drag accelerations and comparing them to models of atmospheric density. The results include the construction of an accommodation coefficient model based on fitted drag coefficient data. This model, called the Semi-Empirical Satellite Accommodation Model (SESAM), is verified for altitude ranges of 100-500 km. It was constructed under the assumption that the accommodation coefficient is a function of atomic oxygen concentration and satellite velocity. Furthermore, the model agrees with independent measurements of accommodation (not based on fitted drag coefficients) within experimental uncertainty. We have also performed a study on the feasibility of determining satellite coefficients through comparisons of satellite accelerometer measurements with remote sensing measurements of atmospheric density. The results of this study indicate that accommodation measurements made using this approach agree well with the aforementioned model indicating a decrease in accommodation coefficients at low atomic oxygen pressures.

A method for accommodation coefficient estimation based on the analysis of CHAMP and GRACE satellite lift to drag ratios is also applied. In addition to this, gas-surface parameters may be determined by looking at changes in the ratio of measured-to-modeled drag coefficients between various flight modes of the CHAMP satellite. This is especially true for yaw maneuvers wherein the geometry facing the free-stream changes significantly while atmospheric conditions do not. Until now, satellite gas-surface interactions have been treated mostly as static. In other words, the state-of-the-art aerodynamic methods for satellites assume a constant energy-accommodation coefficient and scattering-model for all times and atmospheric conditions [Sutton, 2008, 2009, Doornbos et al., 2009, Doornbos, 2011]. Results of the present work represent the first ever dynamic model of gas-surface interactions that is also capable of reproducing drag coefficients measured in orbit. Changes in gas-surface parameters which were previously captured only in sparse lookup-tables, can now be modeled as a function of free-stream parameters. This enables the realistic modeling of changes in the drag coefficient with changes in satellite altitude and solar-cycle conditions. Moreover, the new model allows for the computation of the dynamic and realistic response of the drag coefficient to environmental changes imposed by space weather effects.

This dissertation begins with an extended introduction to satellite drag and a brief motivation of the work to follow. Next, a review of theory and experiments including drag coefficient computation, generation of atmospheric models, and measurements of gas-surface interaction parameters on clean and adsorbate-covered surfaces is presented. Chapter 4 describes the analytical and numerical methods used in drag coefficient computation. A brief sensitivity study of the drag coefficient is presented to illustrate variability of C_D with atmospheric composition, temperature, and accommodation coefficient. The data sources used in the analysis are explained and summarized in chapter 5. This portion of the dissertation includes tabulated values of accommodation measurements in the laboratory and in orbit. The equations and analysis assumptions are then presented in chapter 6. Chapters 7 through 11 contain the results of the analysis including the SESAM implementation. The discussion and conclusions are contained in chapter 12.

Chapter 2

Introduction

Aerodynamic drag is often the most significant orbital perturbation in low Earth orbit and the modeling of this force and its variability is crucial to orbit determination and prediction as well as to the measurement of atmospheric density via satellite drag. The most uncertain parameter in determining aerodynamic forces (as well as in the determination of density from atmospheric drag) on satellites is the product of drag coefficient and cross-sectional area which is a function of satellite geometry, atmospheric properties, satellite velocity, and the nature of gas-surface interactions. The last category is often summarized by the energy accommodation coefficient, α , which is a measure of the energy transferred at the surface by incoming gas molecules and ranges from 0 (no energy transfer) to 1 (particles reflect with an energy distribution corresponding to the surface temperature). This is a very important variable and the satellite drag coefficient may change by as much as 30% depending on the accommodation coefficient [Pilinski et al., 2011a]. The primary relationship describing satellite drag (acceleration) as a function of density is described below (Equation 2.1).

$$\vec{a} = \frac{1}{2} \frac{C_d A}{m_{sc}} \rho V_r^2 \quad (2.1)$$

$$V_r = \left\| \vec{V}_{sc} - \vec{V}_w \right\| \quad (2.2)$$

It is also convenient to define the unit direction vector for the relative velocity, \vec{V}_r , between the atmosphere and satellite motion.

$$\hat{v}_r = \frac{\vec{V}_{sc} - \vec{V}_w}{V_r} \quad (2.3)$$

Above, \vec{a} is the drag acceleration vector (m s^{-2}), \vec{C}_a is the aerodynamic force coefficient vector, ρ is the mass density (kg m^{-3}), \vec{V}_w and \vec{V}_{sc} are the atmospheric wind and the spacecraft velocity vectors, respectively (m s^{-1}). The definition of \vec{C}_a is based on equation 2.1 such that

$$\vec{C}_a = \frac{2\vec{a}m_{sc}}{A\rho V_r^2} = \frac{2\vec{F}}{A\rho V_r^2} \quad (2.4)$$

The aerodynamic perturbation is largest in a direction anti parallel to \hat{v}_r while the lift forces (those orthogonal to \hat{v}_r) are relatively small in most cases [Doornbos, 2011]. Because of this, the aerodynamic acceleration \vec{a} is often approximated as the acceleration along the relative velocity direction $(\vec{a} \cdot \hat{v}_r)\hat{v}_r$ or \vec{a}_D . The three dimensional drag vector then simplifies to

$$C_D = \vec{C}_a \cdot \hat{v}_r \quad (2.5)$$

where C_D is the coefficient of drag. Equation 2.1 can therefore be rewritten as shown below.

$$\vec{a}_D = \frac{1}{2} \frac{C_D A}{m_{sc}} \rho V_r^2 (\hat{v}_r) \quad (2.6)$$

Note that the angle between \vec{C}_a and \hat{v}_r in the inertial frame is greater than 90° and the dot product in equation 2.5 is negative. Therefore equation 2.6 is often written with an explicit negative taking C_D to be a positive value. Furthermore, the product $C_D A/m_{sc}$ can be replaced by B , the inverse ballistic coefficient, sometimes referred to as the ‘‘B-FACTOR’’ ($\text{m}^2 \text{kg}^{-1}$). Equation 2.7 defines the inverse ballistic coefficient

$$B = b^{-1} = \frac{C_D A}{m_{sc}} \quad (2.7)$$

where b is the ballistic coefficient (kg m^{-2}) [Picone et al., 2002a]. The mass and cross-sectional area may be estimated a priori and assumed to be constant over the life of the orbit as long as the object does not break up, lose propellant, nor change orientation in an unknown way. However, the drag coefficient is a function of many parameters as mentioned above and cannot be assumed constant.

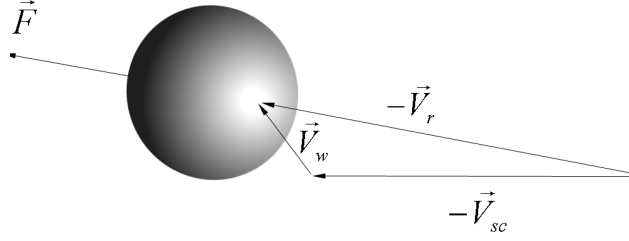


Figure 2.1: Vector variables of the drag equation.

These parameters include gas-surface interactions, satellite surface contamination, and atmospheric composition [Moe et al., 1998], and its estimation has proven to be a challenge for scientists and engineers studying the atmosphere. These parameters are functions of solar activity, altitude, season, satellite shape, and location among other things. One example of the consequence of drag coefficient mis-estimation is the introduction of density biases in atmospheric density models. Cook [1965] computed appropriate drag coefficients for satellites of compact shapes which could be applied for all altitudes and atmospheric conditions. At the time of his derivation, the parameters of gas-surface interaction in orbit could not be constrained due to lack of data and using a constant value was the best choice. We now have better understanding of how the drag coefficient varies with atmospheric properties [Moe and Wallace, 1993] and that the results of using constant C_D in the determination of atmospheric density are altitude dependent biases in the density models [Bowman and Moe, 2005].

Unless the satellite in question is spherical, uncertainties in cross sectional area can rival or exceed those in the drag coefficient. The proper computation of cross sectional area can be achieved with knowledge of the spacecraft attitude and accurate documentation and modeling of the spacecraft geometry. In the case of spacecraft for which attitude information is not available, as is the case for expended rocket stages, an average attitude and cross sectional area may be computed. Meanwhile, the accurate computation of drag and energy accommodation coefficients is impeded by a lack of data and understanding regarding the gas-surface interactions in low earth orbit (LEO) at 80-1000 km altitudes. The effect of the upper atmosphere, particularly of atomic oxygen, reactions with spacecraft materials has been studied extensively but the results cannot readily be applied to drag coefficient analysis [Banks et al., 2004, 2005]. This is because very little is

known regarding the nature of atomic oxygen-surface reactions in the context of how such reactions influence reflections of the free-stream from the satellite surface. Such information is needed to accurately compute the satellite drag coefficient. In the absence of direct measurements, the purpose of this work will be to estimate the nature of gas-surface interactions in LEO based on the observed aerodynamic forces.

Determining gas-surface parameters can be considered an inversion problem. Given measurements of the drag coefficient as well as a reasonable physical model of the aerodynamic interaction, gas-surface parameters may be estimated. Drag coefficient measurements can be made by solving the drag equation for C_D when the drag acceleration is measured and the atmospheric density is estimated using a density model. The drag coefficients obtained in this way are referred to as fitted drag coefficients. Inversions using fitted drag coefficients have been performed for spherical satellites in a study by Bowman and Moe [Bowman and Moe, 2005] and Pardini et al. [Pardini et al., 2010]. The difficulty with this approach is that it depends on the accuracy of the atmospheric model which itself may be influenced by assumptions about gas-surface interactions. As a consequence it is difficult to verify that the gas-surface parameters obtained from fitted drag coefficients are physically appropriate. At minimum however, these parameter values result in drag coefficients which are consistent with the atmospheric models used to obtain the measurements.

An alternative source of gas-surface parameters results from combining two or more independent measurements of satellite drag such as drag-force and drag-torque. The benefit of these measurements is that the resulting gas-surface parameters and their complimentary drag coefficients do not require any assumptions about atmospheric density. This method has been successfully applied in the past and constitutes a crucial but limited data set.

The subject of this work is the determination of gas-surface interaction (GSI) parameters applicable to satellites flying in LEO. Particular attention will be on the changes in these parameters with space-weather effects such as solar storms and the 11-year solar cycle and the resulting changes in the drag coefficient. The work will focus on the effective energy accommodation coefficient, that is the accommodation coefficient which may be applied equally to all satellite surfaces for the purpose of estimating drag. To accomplish this, the two above mentioned techniques are modified to extend inversion to non-spherical objects using numerical drag coefficient computation. The work also includes the comparison of measured drag with atmospheric densities

measured by remote-sensing techniques. In addition the project will look at multi-axial accelerometer data available from the CHAMP (CHallenging Minisatellite Payload [Reigber et al., 2002]) and GRACE (Gravity Recovery and Climate Experiment [Kang et al., 2003]) satellites to infer accommodation coefficients.

2.1 Motivation

Uncertainties in the satellite drag coefficient and area are the largest contributions to errors in determining atmospheric neutral density from satellite drag observations. It is not understood whether these errors cause density biases that are only functions of altitude and long-term conditions such as those estimated by Pardini et al. [Pardini et al., 2010] or if they cause continuously changing errors over time scales of spacecraft orbits as suggested by Reiter and Moe [Reiter and Moe, 1968]. Any short term variations would cause further difficulty in separating the product of drag coefficient and density ($C_D\rho$) with consequences to orbit predictions, orbit determination, and orbit lifetime analysis. Drag coefficients are sensitive to the nature of gas-surface interaction and atmospheric properties such as composition and temperature [Moe and Moe, 2005]. However, laboratory experiments which sought to characterize the gas-surface interaction have had difficulty in reproducing the conditions in low earth orbit, particularly the chemisorption of atomic oxygen on the surface [Moe and Moe, 2005, Thomas, 1967]. Chemisorption is also a difficult phenomenon to address with physical models. An example of this difficulty is that at the time of this writing, theoretical methods based on quantum mechanics have failed to solve even the long-standing problem of adsorption of water on a perfect lattice [Feibelman, 2010]. As a result, our focus will be on developing semi-empirical models of gas-surface interactions in LEO as opposed to modeling the microscopic quantum physics. At the present time, little quantitative information is available as to the fraction of contamination coverage present on spacecraft surfaces, how adsorption varies with atmospheric properties, and how the adsorption relates to drag coefficient parameters such as effective energy accommodation. Moreover references to inconsistent gas-surface interactions are scattered throughout aeronomic literature as pointed out by Vallado and Finkleman [2008].

Difficulties in drag coefficient modeling extend beyond gas-surface interactions. In order to evaluate the reflection properties of surfaces one must first take into account the correct geometry of the object and

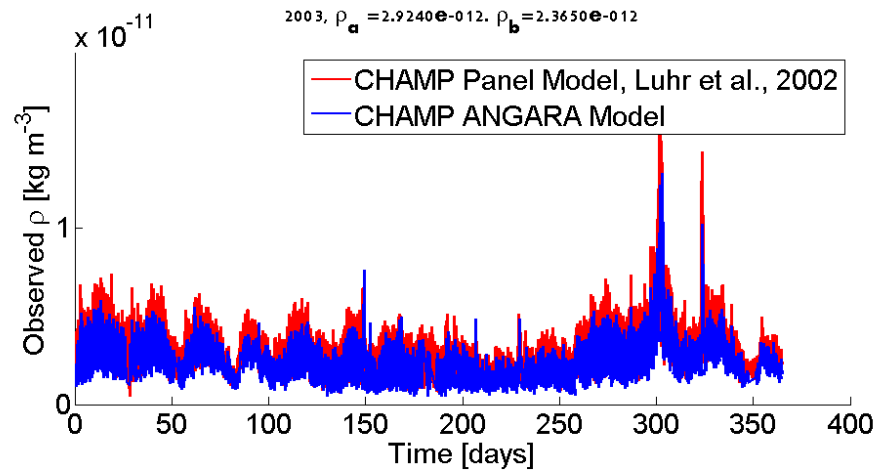


Figure 2.2: CHAMP accelerometer-derived densities during 2003 using two different geometry models to compute C_{DA} . Above, ρ_A and ρ_B signify the average densities for 2003 when using the panel and ANGARA models respectively to solve for atmospheric density.

how the airstream may be shadowed by features such as booms and solar panels. An example of model sensitivity can be seen in Figure 2.2 where two methods, one including shadowing (blue) and the other assuming no shadowing (red) are used to evaluate density based on drag measured by the CHAMP satellite. The two models also incorporate different assumptions about the size of satellite features. The density bias between the two models is 21% of the mean density value.

The desired accuracy of density measurements is 3%-5% of the total density value [Marcos et al., 2010]. In practice, density inversions are usually made under the assumption of constant ballistic and drag coefficients and/or constant gas-surface interactions. Such assumptions can introduce altitude dependent biases of as much as 25% in density. Furthermore, satellites flying below 200 km altitudes exhibit ballistic coefficients which can be 30-50% lower [Bowman and Hrcir 2007] than those computed using standard assumptions of fixed C_D or fixed GSI due to re-entry effects [Dogra et al. 1992]. Meanwhile, differences in satellite-geometry modeling have resulted in up to 40% errors in cross sectional area [Doornbos et al. 2009, Pilinski 2011]. Depending on the fidelity of GSI, re-entry, and geometry modeling, the resulting density errors can be as much as 25%, 200%, and 65% respectively. Therefore, in order to achieve 5% accuracy in density and drag estimates, an appropriate ballistic coefficient must be modeled for each satellite in the dataset.

2.2 Scientific Questions

The main science question of this research project can be expressed as follows.

What satellite gas-surface parameters result in physically realistic models of aerodynamic force behavior in LEO?

Past research indicates that adsorption and desorption do occur on spacecraft surfaces. Furthermore, it is understood that this phenomenon alters the nature of gas-surface energy exchange. Therefore, the hypothesis underlying this effort is that an appropriate model of adsorption can be the basis of a gas-surface model for satellite aerodynamic computations. To answer these question, observations of satellite forces will be compared to force models based on different sets of gas surface interactions. The observations will come from drag measurements (accelerometers or orbit decay) combined with atmospheric density model comparisons

or with remote-sensing estimates of density to yield drag coefficient data. Another source of observations is the existence of independent aerodynamic force measurements such as drag and lift on the CHAMP and GRACE satellites. The independent measurements can be combined to solve for density and gas-surface model parameters.

A number of secondary questions follow from the first query.

Can independent measurements of energy accommodation be obtained with available data sets?

Can a predictive energy accommodation model be developed to improve satellite drag calculations?

Which models of molecule reflection (scattering kernels) best reproduce the orbital measurements?

These questions deal with an evaluation of gas-surface interactions via the criterion of reproducing measurable orbital-drag results. An important consideration is whether the data available for constraining any given model are sufficient for that model to be extended for operational use. A salient factor in this consideration is the dearth of data and adequate predictive models for satellite gas-surface parameters, especially energy accommodation coefficients. Throughout the work, additional sources of accommodation coefficient estimates are obtained. For example, there are a large number of observations of rocket bodies which have, until now, not been leveraged to derive accommodation coefficients. The adsorption models will be based on adsorption behavior models adjusted to fit the observed data. A number of scattering kernels will be evaluated and the details of these will be explained in the following chapters.

Chapter 3

Review of Progress in Drag Coefficient Modeling and Gas-Surface Interactions for Rarefied Flow Applications

At the beginning of the Space Age, researchers such as King-Hele, Cook, Jacchia, and Champion [Jacchia, 1964, 1981, King-Hele, 1963a, 1965, 1992, Cook, 1970, Champion, 1975, 1983] used the observed decrease in satellite altitudes to derive atmospheric density values. The drag coefficient chosen in these experiments was usually taken to be 2.2. The use of this value in the drag and density records has been incorporated into the CIRA (COSPAR International Reference Atmosphere), Jacchia, and MSIS (Mass Spectrometer Incoherent Scatter) class atmosphere models. It is because of this that the variability of the satellite drag coefficient first came into question. In order for density to be derived from drag, a realistic drag coefficient had to be estimated. In the early 1960's Cook made a thorough effort to combine the knowledge of the day from the fields of gas-surface interaction and statistical mechanics to determine the most accurate value of drag coefficient possible [Cook, 1965]. He described the satellite drag coefficient (for a compact object) as an uncertain quantity which may change due to the nature of gas-surface physics, atmospheric composition and temperature, and the adsorption (or sticking) of atmospheric molecules to the surface. His assumption was that satellite surfaces will be heavily coated with atomic oxygen (AO) and that the incoming gas will collide not with the metallic satellite materials but rather with a complex landscape of adsorbed molecules and AO products. As a result of this contamination the ratio of incoming to surface mass will be increased and, according to hard spheres collision theory, the accommodation coefficient will be high. Cook computed the uncertainty in the drag coefficient to be 15% for compact shapes primarily due to lack of information regarding the accommodation coefficient. He also estimated the valid range of the "high" energy

accommodation assumption to be up to 400 km. While in 1965, the drag coefficient variability seemed to have been identified as a problem to be addressed, it was nevertheless a problem which was soon dismissed by many atmospheric scientists. The lack of significant progress beyond the early work of Cook and others is reflected by the following quotes from published literature. Note the difference in views of those who believe the C_D term is a bias from those who understand it to be a hinderance in improving drag predictions. The most recent quote reflects the status of the majority of atmospheric density models with the large errors being in part due to C_D uncertainty.

“The main source of uncertainty in the values of density obtained is probably due to the drag coefficient, which has an estimated standard deviation of 5-10 percent.” - D. G. King-Hele, 1965 [King-Hele, 1965]

“The systematic error in the densities from satellite drag is mostly attributable to the drag coefficient and is nearly immaterial in atmospheric modeling, as long as a plausible value for its constant part is assumed throughout.” -L. Jacchia 1981 [Jacchia, 1981]

“Density model errors on the order of 15%-20% one standard deviation have been recognized for all empirical models developed since the mid 1960s. These large density standard deviations correspond to maximum density errors of approximately 40-60% as observed in satellite drag data.” - B. Bowman, 2006 [Bowman et al., 2006]

“Drag coefficients determined under one set of hypotheses are often employed improperly in orbital assessments that use a different set of hypotheses.” - D. Vallado, 2006 [Bowman et al., 2006]

“A persisting deficiency in deriving these density values has been determination of the drag coefficient C_D . In empirical model development the value of $C_D = 2.2$ was customarily used. ... We further note also that orbital-drag based models inherently include average effects of winds and drag coefficients. However, since these can vary in an unknown manner, accurate density models require understanding variability of drag coefficients and neutral winds. ” - F. Marcos, 2006 [Bowman et al., 2006]

Since the study by Cook and others [Schamberg, 1959, Sentman, 1961] very little effort has been made by the aeronomic or rarefied gas communities to understand the nature of the satellite drag coefficient in the presence of adsorption and to incorporate the improved values into atmospheric density models. Other than the work done by Moe and Moe as well as Pardini [Moe et al., 1995, Pardini et al., 2010], the assumption of $C_D = 2.2$ has remained in the construction and interpretation of atmospheric models [Jacchia, 1964]. The continued use of 2.2 (or other constants) value by the Jacchia, most of the CIRA atmospheric models, and most recently the NRLMSISE-00 model has likely introduced altitude dependent biases in the total density

values [Moe and Bowman, 2005]. With the turn of the millennium, increasingly stringent objectives for satellite drag predictions have been motivated by improvements desired in the areas of satellite tracking, orbit determination and re-entry predictions [Marcos, 1985, Doornbos et al., 2009] to name a few. Many of these improvements require a drag prediction which is accurate to within 5% [Marcos, 1985, Marcos et al., 2010]. Unfortunately, such improvement is not possible regardless of the accuracy of atmospheric models due to the outstanding issues concerning drag coefficients. The correction of this problem will depend on progress made in the area of gas-surface interactions and their quantitative effect on satellite drag.

In spite of recent improvements and clarifications in modeling parameters [Moe and Moe, 2005, Gregory and Peters, 1987, Pardini et al., 2010, Pilinski et al., 2010], such progress is still lacking. The 2008 COSPAR International Reference report, for example, cites drag coefficients as the primary uncertainty in satellite drag-derived density (provided that the area of the satellite in question is known). The report further explains how drag coefficient variability can cause errors in density which are not just simple biases. [Moe and Moe, 2008]

3.1 Gas-Surface Interactions and the Satellite Drag Coefficient

Once a molecule interacts with a surface it can be trapped, stick to the surface, or scatter from the surface. In this section we will give a review of the theory of these interactions in a historical context. Maxwell theorized in the 1860's that a fraction of the particles incident upon a wall was absorbed and then re-emitted diffusely with a kinetic temperature equal to the wall temperature [Schamberg, 1959]. He made the assumption that the remaining particles are reflected in a perfectly specular manner, that is, the angle of reflection equals the angle of incidence and no kinetic energy is lost by the particle in the process. In 1875, it was found that flux through tubes at low pressures was higher than that predicted by fluid dynamics and attributed this to boundary slip [Trilling, 1967]. Boundary slip is the phenomenon of the velocity of fluid particles being non-zero with respect to the surface as would be the case in the boundary layer and continuum-flow assumption. This data was qualitatively explained by Maxwell's theory of gas-surface interaction wherein molecules reflecting from a wall retained some but not all of their initial momentum. In a similar way, temperature slip was described by Smoluchowski and the concept of the

thermal accommodation coefficient, α , was born to describe the exchange of heat at the boundary [Schaaf and Chambre, 1961]. Knudsen then generalized accommodation to describe energy and momentum exchange (energy accommodation coefficient and momentum accommodation coefficient). Attempts at describing the physics behind the accommodation coefficient have been made with several approaches. These methods fall into the categories of hard-sphere models, where a grid of spheres interacts elastically with an incoming particle, lattice models which describe the surface particles as an interconnected linear system, and quantum interaction models which take into account the diffraction effects resulting from wave interactions at the surface [Trilling, 1967]. Baule's 1914 classical model of accommodation was an early representation of the accommodation coefficient as a function of gas and surface mass ratio [Masel, 1996]. The model developed by Goodman [Goodman, 1967] was found to give improved results for clean surfaces. Goodman performed an intensive numerical analysis using a 2-D array of spheres and a variety of incidence angles and velocities. Because classical models are a function of the mass ratio, μ , of the incoming to the surface molecule mass, the presence of surface contaminant will change the ratio thus changing the accommodation for an atmospheric molecule impinging at or near an occupied adsorption site.

3.1.1 Laboratory Measurements of Gas-Surface Interactions

Prior to the 1920's, measurements of the accommodation coefficient were inconsistent and difficult to reconcile with theoretical models. At this time, Langmuir investigated surface conditions in relation to these measurements and found that foreign particles coating these surfaces considerably changed the way they interact with ambient gas [Moe et al., 1998, Moe and Moe, 2005]. Langmuir revolutionized the study of contaminated surfaces (almost all engineering surfaces are "contaminated") by introducing the concept of an adsorption isotherm pictured in Figure 3.2. The isotherm described adsorption kinetics as a function of pressure at a given temperature. Langmuir's work was based on the insight that the surface had a finite number of adsorption sites and that the rate of adsorption is reduced as more sites become occupied. This is schematically represented in Figure 3.1. He also standardized the use of the terms *adsorbate* for the incoming gas and *adsorbent* for the surface material to which the adsorbate sticks.

When all of the available adsorption sites are covered by molecules, the surface is said to be covered in

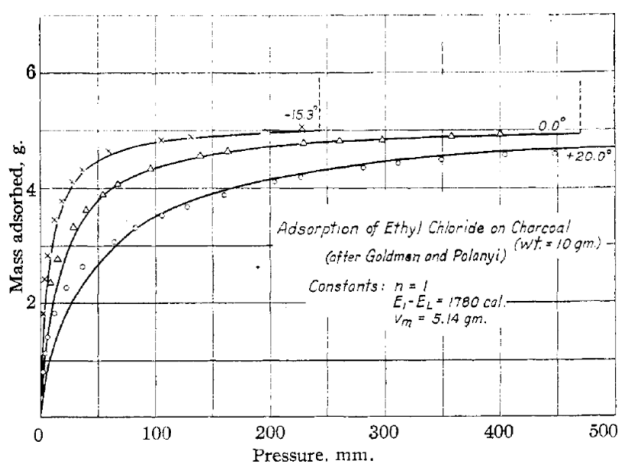


Figure 3.2: Example of Langmuir isotherms from Brunauer et al. [Brunauer et al., 1938].

one “monolayer” of adsorbate. Note that crystalline (single-crystal) surfaces contain an average of 1.1×10^{15} adsorption sites per square centimeter [Oura et al., 2003]. In other words, when adsorption measurements are recorded in monolayers, this usually refers to a unit equivalent to 1.1×10^{15} molecules. Langmuir’s theory of adsorption continues to be used to this day in a wide variety of applications. He received a Nobel prize for this work in 1932.

Brunauer classified adsorption into five types of behavior [Masel, 1996]. Type I isotherms represent adsorption that increases with pressure and eventually leveling off at some saturation value. The Langmuir isotherm is in the Type I class which is usually indicative of monolayer formation. Type II isotherms increase with pressure and level off initially before increasing again at higher pressures. These representations, such as the BET model, deal with multi-layer adsorption. A rarer form of adsorption is type III which begins with small amounts of adsorption then grows exponentially. This rapid increase in adsorption is caused by island formation or a “coagulation” of adsorbate on the surface. Strong adsorbate-adsorbate interactions speed up the sticking process once island formation begins. Type I through III models deal with flat surfaces while Type IV and V treat adsorption on porous materials. Type IV and V isotherms behave like type II or III isotherms at the onset until the pores of the material are saturated and adsorption levels off with pressure [Masel, 1996]. The first class includes mostly modifications of the Langmuir model to include heterogeneous adsorption and adsorption-adsorption reactions. Heterogeneous adsorption is the treatment

of different classes of adsorption sites. This can include surface contaminants on an otherwise perfect lattice or rough or stepped surfaces where the binding energies vary over the surface. Heterogeneous or multi site models have been shown in the 1960's to improve pressure gauge data in spaceborne experiments [Moe et al., 1972]. The empirical Freundlich isotherm has two parameters to Langmuir's one and can therefore better fit observed data but has no physical underpinning.

All isotherms discussed here are equilibrium processes which assume that adsorption is a reversible process and the adsorbate is in equilibrium with the adsorbing mass. Surface reactions of incoming gas with spacecraft materials have been shown on the Long Duration Exposure Facility (LDEF) [Banks et al., 2005, Reddy, 1995, Meshishnek et al., 1995, Whitaker et al., 1993] and in ground studies [Reddy, 1995, Tagawa et al., 1990]. Furthermore, some AO has been shown to recombine into molecular oxygen in both space and ground experiments [Kasprzak et al., 1968, Krankowsky et al., 1968]. This certainly begs the (yet unanswered) question as to the extent of adsorption reversibility in LEO. Furthermore, many of the isotherms described so far can be used to represent associative and dissociative adsorption. Associative desorption occurs when two molecules or atoms bind while adsorbed on the surface and desorb together. The opposite scenario is the dissociation of an adsorbate molecule before coming off the surface. The recombination of AO and dissociation of molecular oxygen on spacecraft surfaces is just one example of this.

Adsorption has historically been classified into physisorption and chemisorption depending on the binding energy with the surface (also referred to as the heat of adsorption). This somewhat arbitrary distinction is made at a binding energy of approximately 0.5 eV per molecule (11.53 kcal/molecule, 48.2 kJ/molecule) [Oura et al., 2003]. While physisorption refers to van der Waals forces (10-100 meV), chemisorption includes covalent and ionic bonds (1-10 eV) [Oura et al., 2003]. Since Earth orbiting spacecraft surface-temperatures can range between 250K and 350K [Paxson et al., 2008, Jenkins et al., 2002], the surface thermal energy ($k_B T_w = 20 - 30$ meV) precludes most physisorption processes from occurring.

One of the early laboratory measurements of accommodation [Doughty and Schaetzle, 1969] used a quartz torsional balance to directly measure the forces experienced by a surface subjected to a high flux neutral beam. The mean kinetic energy of the neutral beam was varied from 16 to 150 eV and the accommodation measured at a selected number of incidence angles. The gas used was Argon and Nitrogen and the

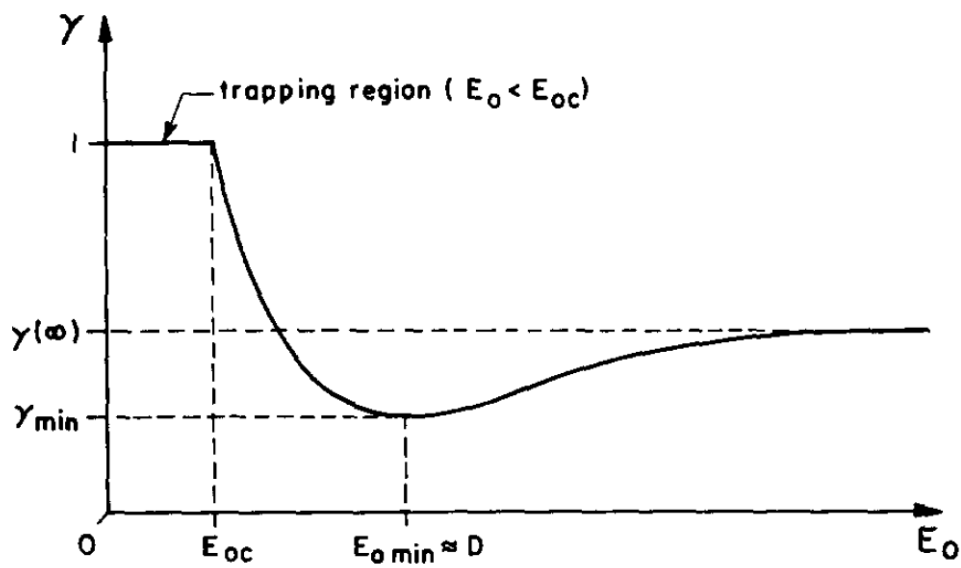


Figure 3.3: Lattice based energy accommodation model described by Goodman [Goodman, 1974].

surface samples of aluminum and varnish were mostly covered with adsorbed molecules. Contrary to Goodman's classical theory no asymptotic behavior was observed and instead the energy accommodation dropped with increasing energy by 18% over the kinetic energy range. The minimum which would theoretically occur when the incident energy is just slightly higher than the binding energy was not observed. It is possible that the reduction in accommodation is due to the fact that the trapping efficiency (or initial sticking coefficient) is lower at higher incident kinetic energies. In fact, Masel [1996] demonstrate a theoretical model of trapping efficiency which predicts a drop in adsorption efficiency at or below the adsorption energy. The model is based on classical approximations and agrees well with measurements of trapping efficiency. A reduced trapping efficiency would lead to a lower adsorption rate which would in turn expose more of the surface lattice. The collision of incoming molecules with the clean surface lattice is associated with a theoretically lower accommodation coefficient than the gas-adsorbate interaction. Kostoff et al. measured energy accommodation decrease on contaminated surfaces at energies ranging from 0.003 eV to 6 eV for helium and Argon impinging on mica and aluminum [Kostoff et al., 1967, Moe et al., 1998]. Kostoff's experiments indicated a 10-40% drop in energy accommodation with increasing energy. Sputtering can be considered as a candidate mechanism for removal of adsorbate and the corresponding reduction of accommodation coefficients. In 1974 Winters and Sigmund measured sputtering yields for several incident gases impinging on adsorbed nitrogen on a tungsten surface [Winters and Sigmund, 1974]. The sputtering yield (number of atoms sputtered from the surface per incident ion) increased almost linearly with the kinetic energy of incident Argon. The yield was 0.3 for kinetic energies of 150 eV and 0.0 below kinetic energies of 10 eV. Note that the 30% change in yield over 150 eV of incident kinetic energy matches suspiciously well with the reduction of accommodation observed by Doughty and Scheatzle. Though the agreement may be a coincidence it appears that sputtering plays at least a partial role at extremely high kinetic energies ($\gg 10$ eV). However, based on the sputtering measurements and the 15 eV energies for molecular nitrogen traveling at 10 km/s, we do not expect this to be a significant phenomenon at most spacecraft velocities.

Another phenomenon may be responsible for the desorption of atomic oxygen from satellite surfaces. Fukutani et al. [1993] describe the phenomenon of single-photon and multi-photon, Ultraviolet-induced, desorption of oxides from a metal surface when the photon energy is between 3.5eV and 6.4eV. Yokota et al.

[2004] also found that the desorption of oxygen products is increased when atomic oxygen, directed on a polymer surface, is illuminated with UV light with a wavelength of 172 nm. Such experiments demonstrate that molecules chemisorbed on metals and polymers can be induced to desorb in the presence of ultraviolet radiation. Such radiation is plentiful in the LEO environment ($3 \times 10^{-3} \text{ mW cm}^{-2}$ for radiation between 175.4 and 190.5 nm [Anderson and Smith, 2009]) and may be able to speed the rate at which equilibrium coverage of chemisorbed material changes.

The body of research regarding gas-surface interactions paints a picture of distinct behaviors for “contaminated” and “clean” surfaces [Moe and Moe, 2005]. While clean surfaces are generally associated with quasi-specular reflection and small values of accommodation, surfaces covered with adsorbate reflect diffusely and with much more complete energy accommodation. Energy accommodation is an important parameter which determines momentum exchange with the surface and significantly modifies the value of the drag coefficient.

Let us now explore what the observed values of accommodation coefficients are under the various conditions. Thomas [1967] presented a thorough review of accommodation measurements performed in the laboratory between 1911 and 1963. He immediately distinguishes two classes of experiments: work which was “done with an attempt to control the solid surface coverage” and work performed “without such an attempt”. In cases where the surface condition were not controlled, the accommodation measurements were widely inconsistent varying almost over half the full range of 0 to 1 for any surface-gas pair. The work without controlled surfaces includes some of the experiments performed by Knudsen and can be used to deduce qualitative features of accommodation behavior. For example, light molecules tend to have lower α values, the α is reduced with temperature of the surface and can reach unity at very low temperatures. The trends are not consistent between measurements however and there is much confusion in the literature where the surface conditions have not been controlled. With the meticulous cleaning of surfaces and the elimination of adsorption, Thomas [1967] reported accommodation values which were much lower for the noble gases and which show less dependence on temperature. The values for helium, neon, argon, krypton, and xenon impinging on tungsten at room temperature were approximately 0.01 0.04 0.3 0.5 0.8 respectively. These measurements agree roughly with the accommodation coefficients computed using Baule’s formula

and Goodman's simplified classical "correlation" formula [Goodman, 1967]. Thomas found better agreement with the Baule formula but only after he adjusted the surface mass to compensate for gas molecules interacting with more than one surface atom. Figure 3.4 shows the relationship between classical theory and measurements on clean surfaces. The average of the data is shown in a black solid line and agrees well with the average Goodman model. The only notable outliers are Neon and stainless steel. The stainless steel value found by Ramesh and Marsden [1974] was not included in the averages.

For surfaces covered by adsorbate, the accommodation coefficient information can be categorized into data inferred from spacecraft observations and laboratory experiments seeking to emulate the LEO environment. The laboratory results will be summarized in this section while the orbital results are summarized in the next section. In the early 1990's, the first energy accommodation study was performed using an AO source in the laboratory by Krech et al. [1993]. They synthesized a neutral AO beam with kinetic energies centered around 5 eV which closely matches the conditions in orbit. Since the pressures in their chamber were approximately 10^{-5} - 10^{-6} Torr (not UHV) adsorption was probably occurring in the chamber. The surfaces exposed to the AO beam were glass, nickel and gold. All had energy accommodation coefficients of around 0.60 though the experimental uncertainty was relatively high at ± 0.3 . Collins and Knox [1994] used measurements of momentum accommodation coefficients to deduce parameters of the corresponding Nocilla model. The measurements included 10eV N_2^+ on Aluminum as well as 2-15 eV N_2 and Ar on gold, aluminum and copper. Correlation relationships based on these measurements are used to arrive at reflection parameters for the Nocilla model (to be discussed in more detail later). The energy accommodation coefficient they arrived at was between 1.00 and 0.80 depending on incidence angle (value averaged over unit sphere). The reflection angle falls between the specular and normal directions. Minton et al. [2004] measured the energy accommodation of neutral Argon and CO_2 at spacecraft velocities to provide better drag predictions for spacecraft orbiting Mars. They measured accommodation coefficients on composite panel, white paint, and glass in the presence of adsorption. The measured accommodation coefficient values were between 0.90 and 0.97 with almost no dependence on the ratio of gas molecule to surface molecule masses. Viecelli et al. [2004] computed values of accommodation of water vapor on condensed water. This is a salient experiment as the reflecting surface is composed entirely of condensed phase of the incoming gas which is analogous to

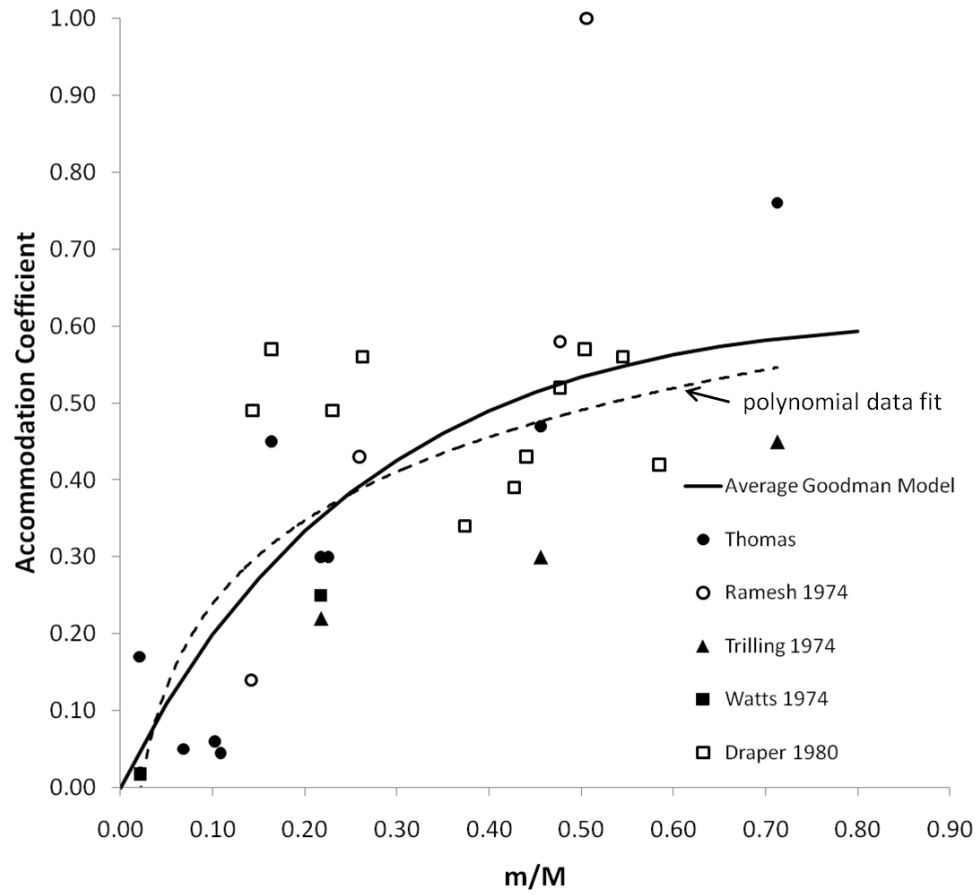


Figure 3.4: Accommodation coefficient measurements and models.

AO approaching a spacecraft surface fully covered with adsorbate. The resulting accommodation coefficient was 0.99 and provides evidence that the Goodman model can underestimate accommodation by nearly 40% when the incident and surface molecules are the same. Figure 3.5 summarizes the results of accommodation measurements on contaminated surfaces.

The context of surface chemistry is important for evaluating the parameters of surface reflection models which are probably modified by adsorption. The following brief review deals with the subject of surface chemistry particularly as it relates to the interaction of AO with various materials. When a molecule adsorbs to the surface, it can either stay bonded, return to the gas phase, move along the surface, or react with other molecules on the surface. We will focus mainly on the phenomena of surface reactions. AO is known to be highly reactive and to “attack” certain materials especially polymers [White et al., 2005]. In this process the oxygen atom bonds with some part of the surface molecule and removes it or causes another portion of the molecule to be removed. Atomic oxygen can also react with the incoming gas molecules while adsorbed to the surface. This phenomenon primarily occurs by one of two mechanisms. The Langmuir-Hinshelwood [Masel, 1996] mechanism describes a process wherein both reactants adsorb to the surface then react to form an adsorbed complex which eventually desorbs into the gas-phase. The Eley-Rideal mechanism [Masel, 1996] occurs when one reactant is already chemisorbed on a surface while the second reactant collides with it while still in the gas phase. The two reactants react during the collision and the result is an adsorbed complex which can eventually return to the gas phase. In the 1970's Wood studied the adsorption kinetics and surface reactions of AO impinging on silver and gold surfaces [Wood, 1971]. His experiments led to the conclusion that silver forms an oxide layer and continues to adsorb oxygen well beyond the monolayer level. Approximately 3% of the incoming atoms recombine on the surface by means of the Langmuir-Hinshelwood process and 7% are lost by adsorption resulting in a total loss coefficient of 10%. For gold, Wood measured a loss coefficient of 30% and found that adsorption does not continue beyond monolayer coverage. While the loss coefficient is higher for gold, the Langmuir-Hinshelwood rate is a factor of 10 lower. This indicates that on gold, AO recombines by the Eley-Rideal mechanism with 20% of the molecules lost to this process. Wood also measured the initial rates of adsorption and desorption to be 3.3×10^{14} atoms per square centimeter per minute and 1.01×10^{14} atoms per square centimeter per minute

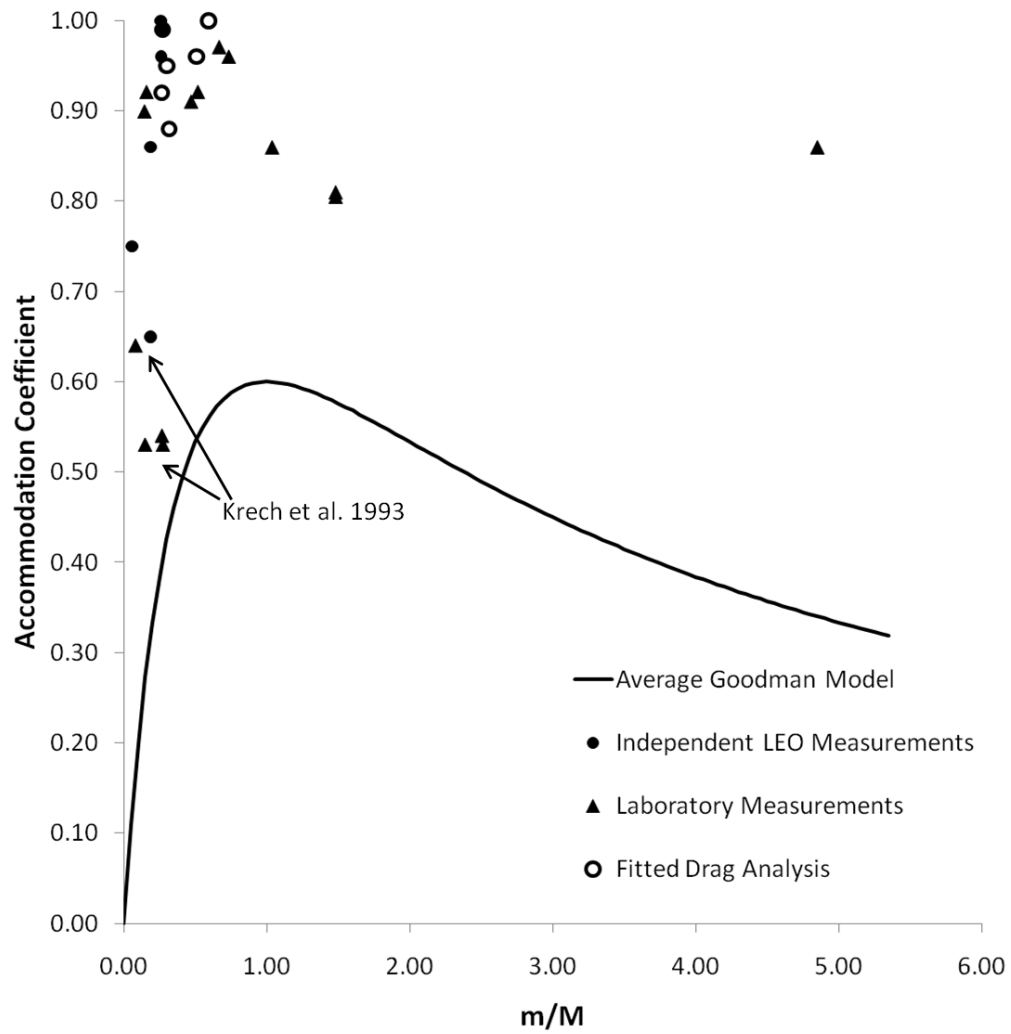


Figure 3.5: Energy accommodation measurements in the presence of adsorption as well measurements made in LEO.

respectively on silver. At a pressure of 1.4×10^{-7} Torr, this translated to approximately 70 minutes to reach surface saturation and 20 minutes to completely desorb from the surface. For gold the adsorption and desorption rates were about 1.7×10^{14} atoms per centimeter squared per minute and 1.5×10^{14} atoms per centimeter squared per minute respectively. From zero coverage, gold reaches saturation in eight minutes and from monolayer coverage undergoes complete desorption in approximately 1 hour when the chamber pressure was 1.4×10^{-7} Torr. Chambers et al. [1996] used the resistivity of thin films to measure the erosion rates of polyethylene (plastic), PTFE (Teflon), silica (SiO_2), and carbon under an exposure of AO equivalent to LEO levels. The erosion rates of silica and carbon were negligible (below measurement sensitivity) indicating that oxygen atoms did not react significantly with glass-like materials. Taken in the context of earlier experiments performed by Riley and Giese [1970] these results indicate that AO adsorbs on glass but does not recombine on or react with the glass surface significantly. These results are consistent with a series of experiments performed by Balat-Pichelin et al. [2003] who measured the AO recombination coefficient on SiO_2 to be 0.3% at a surface temperature of 770K and 1% at 1400K with an almost log-linear trend in between. The high surface temperatures were meant to emulate the re-entry environment. Extrapolating the findings to average surface temperatures of 300K results in AO recombination coefficients less than 0.01% on glass.

3.1.2 Gas-Surface Interactions in Earth Orbit

At this time there is no direct observations of adsorption occurring on spacecraft surfaces. It is therefore impossible to ascertain whether there are cases when multi-layer adsorption is appropriate for drag coefficient computations in LEO. Moe and Moe [1967, 1969] and Moe et al. [1972] have documented the effects of adsorption on the inside surfaces of pressure gauges (made from Pyrex material) flying on spacecraft during 1963 and 1968. They found that introducing an adsorption model based on Langmuir's isotherm explained the observed pressure profiles inside the gauge. The level of coverage estimated in their study was approximately 0.002 monolayers. The low values of surface coverage suggest that the Langmuir isotherm may be more appropriate for satellite surface adsorption than the BET model. If the pressure gauge coverage values from the Spades and Explorer 17 missions are also representative of adsorption on satellite surfaces, then a small fraction of a monolayer can significantly change the accommodation coefficient and

reflection properties of the surface. Van der Waals forces and the poisoning of neighboring adsorption sites in some adsorbate/adsorbent pairs can explain such behavior. By extending the range of forces exerted by the adsorbate molecule on incoming molecules to nearest-neighbor sites, the amount of adsorbate needed to change the properties of the entire surface is drastically reduced [Rudzinski and Everett, 1992].

In 1968, Kasprzak et al. [1968] reported on an interesting discrepancy between measurements of AO using different types of mass spectrometers aboard sounding rockets. The experimenters flew both open source and closed source instruments on the same rockets. While open source mass spectrometers allow gas access to the analyzer with a minimum of gas-surface collisions, the atoms and molecules entering closed source instruments must pass through an accommodation chamber and experience many conditions. By comparing the differences between the two AO measurements Kasprzak et al. arrive at a loss coefficient of about 12%-16% on instrument surfaces and attributed this mainly to surface reactions that form N_2O and CO_2 . The loss of AO on surfaces has been studied in the laboratory as well. [Riley and Giese, 1970] reported that much of the AO reflected at vacuum pressures between $10^{-5} - 10^{-7}$ Torr was adsorbed to a Pyrex surface at room temperature. In fact 57% of the incident atoms were not re-emitted from the glass and the reflected angular distribution was closely approximated by the cosine law. Riley and Giese also investigated the fate of the lost atoms and stated that the majority of them did not undergo recombination nor reacted with surface impurities to form CO_2 or N_2O . Their experiment helped explain qualitatively some of the early findings by Kasprzak et al.. This work also suggested that AO adsorption may hide the properties of the underlying surface as the loss coefficients measured from stainless steel (SS304), teflon, gold and titanium were within a range of 40% to 55%. Lake and Nier [1973] attempted to reconcile large (as much as factor of five) discrepancies in the measurement of AO in space. A vacuum experiment was designed in which the AO reflected from a surface could be isolated from that reaching the analyzer directly without collisions. By comparing the ratio of the two results with Monte Carlo analysis a loss coefficient of 40% to 50% was estimated for various surfaces. Lake and Nier concluded that although the CO_2 generation occurs on the surface and is initially proportional to the flux of incident AO, the ratio drops slowly as the source of carbon contamination is presumably depleted (or occluded by adsorbate). Furthermore, no evidence was found for significant recombination of oxygen on the surface although adsorption and storage of AO was

cited as a plausible possibility. A similar experiment also found that CO_2 production on the surface tends to diminish with time and almost disappear completely with the formation of a single monolayer of surface adsorption [Lake and Mauersberger, 1974]. The experiment was performed over long time spans (days) and revealed that recombination of AO reaches an asymptote after the adsorption of one monolayer. Furthermore Lake and Nier [1973] found that it took more than 36 hours for the effects of adsorption to abate after the AO beam was deactivated. Gold, aluminum, and nichrome were investigated and it was found that all surfaces reach monolayer adsorption at about the same time although the AO loss to reactions was reduced on aluminum (20% loss coefficient versus 35%). The distinction between this and the previous experiments is probably due to the differences in time scales (fluences) involved. The lower loss coefficient described by Lake and Nier [1973] may be indicative of the adsorbate not reaching maximum coverage. Contemporary to this research was a flight of cryocooled mass spectrometers which showed significantly higher number densities of AO than were observed with non-cooled instruments [Offermann and Trinks, 1971, Offermann, 1972]. The cooled instruments reduced the mobility of gas that has interacted with the surfaces by increasing the sticking probabilities. As a result, a much higher ratio of incoming AO could be observed directly. While these experiments confirm the presence of adsorption (indeed the cooled instrument depends on it) on spacecraft surfaces, they contradict somewhat the findings by Lake, Nier, Riley and Giese [Lake and Nier, 1973, Riley and Giese, 1970] that large proportions of AO are not associated or converted to CO_2 .

The evaluation of gas-surface effects in Earth orbit was not solely reserved to mass spectrometers. Moe and Moe [1967] re-analyzed pressure gauge data from the Explorer 17 satellite and found clear evidence of surface adsorption. Explorer 17 was spin stabilized and the pressure gauge aperture faced alternatively into (ram direction) and out of (wake direction) the incoming flow. The gauge walls were constructed from glass. Measured wake pressures were consistently higher than could be explained by standard pressure gauge equations [Moe and Moe, 1967]. The researchers were able to reconcile observations with theory by adjusting the pressure equations with a Langmuir model [Moe and Moe, 1967, 1969] of adsorption. Several years later, pressure gauge data from the Spades satellite was similarly analyzed with the addition of heterogeneous adsorption sites into the pressure model [Moe et al., 1972]. The computations, performed for AO and two types of adsorption site, enhanced the accuracy of data analysis by as much as 60%. Based on the Explorer

IV calculations, the maximum level of adsorption on the glass walls was 0.002 of a monolayer. It is unclear if this low level of adsorbate coverage was due to the short time spent in the exposed flow or if it is the saturation value for that adsorbate/adsorbent pair. The gauge on Explorer XVII faced away from the flow for half of each rotation so that, depending on the rate of desorption on glass, coverage may not have accumulated significantly. The effect of AO adsorption on the satellite drag coefficient was first seen in the simultaneous flights of Cannonball and Musket Ball satellites. Cannon Ball was covered with solar cells (which are often covered with protective glass) while Musket Ball had an entirely brass surface [Champion, 1975]. Both satellites had a perigee of 140 km altitude and the drag acceleration measured on both was within 1-2%. Because the satellites flew through almost identical average atmospheric densities the results obtained indicated that their drag coefficients were also within 1-2%. The six Orbital Drag Environment RADar Calibration Spheres (ODERACS) flew in 1994 at an initial altitude of 350 km. They included spheres of different compositions and surface roughness but of identical area-to-mass ratios [Moe and Bowman, 2005]. The measured drag acceleration of the rough spheres was higher by as much as 3% than smooth spheres indicating a drag coefficient of rough surfaces that is likewise increased. The difference between rough and smooth spheres was reduced to below 1% with a decrease in altitude as seen in Figure 3.6. Such a reduction is consistent with the higher concentrations of AO at lower altitudes. The variability between the various materials (chrome, paint, and iridite) was less than 1.5% [Moe and Bowman, 2005]. Using a hard-spheres model Moe and Bowman [2005] predicted that the variability, had the surface been uncontaminated by adsorbate, would have been in excess of 5%. Both the ODERACS and earlier Cannon/Musket Ball experiments suggest that AO adsorption masks the surface properties of spacecraft from the incoming flow and homogenizes the gas-surface interactions across various surface materials.

Satellite orbits have a variety of eccentricities which significantly modulate the magnitude of their velocities. At perigee, or closest approach, the free-stream velocity can range from 7.5 km/s for a near circular orbit to 10 km/s for an orbit with an eccentricity of 0.75. This varies the kinetic energy of AO impinging on satellite surfaces from 4.8 eV to 8.7 eV. Accordingly, a subject of interest related to satellite drag coefficients has been the dependence of gas-surface interaction on the kinetic energy of the free stream. Goodman gives a review of the theoretical research in the area of gas surface interactions including classical and

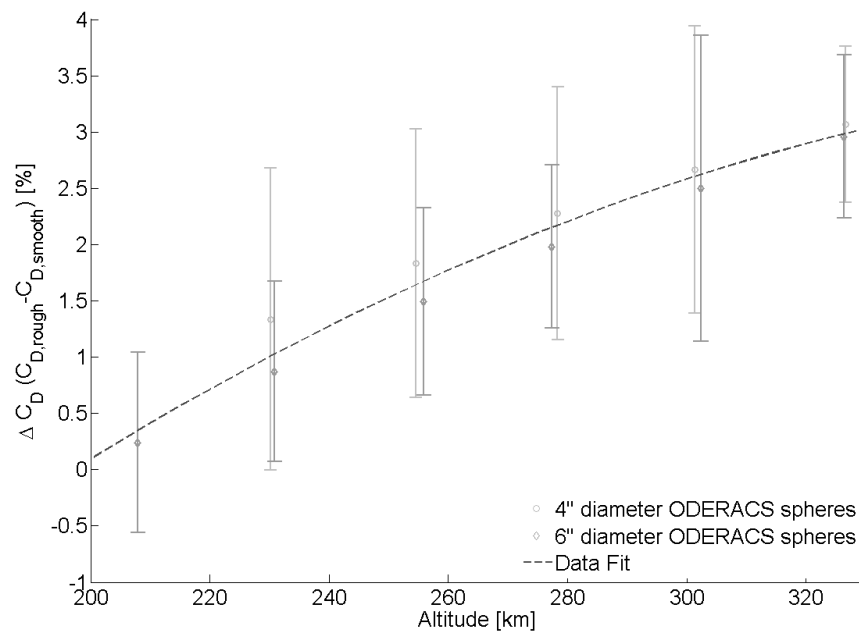


Figure 3.6: The difference in rough and smooth ODERACS drag coefficients.

quantum mechanical methods spanning the 1960s and 1970s. He describes a classical lattice model adopted by Cook [Goodman, 1974] which predicts that at energies above the binding energy, the energy accommodation will asymptotically approach a value between 0 and 1. As energy is lowered the accommodation coefficient goes through a minimum before rising to unity at an incidence energy equal to that of binding.

There is a class of spacecraft measurements referred to as paddlewheel (or windmill satellites). The paddlewheel satellite spins like a propeller (the blades are usually solar panels) while traveling in an elliptical orbit. At perigee, the propeller spin is attenuated (or accelerated depending on the pitch of the blades and spin direction) and the velocity of the spacecraft is reduced lowering the apogee altitude. Both measurements (apogee decay and spin decay) contained information about the product of drag coefficient and density. Providing two independent measurements of the interaction with the airstream enables the determination of both air density and drag coefficient. Then by using a realistic model of the gas-surface interaction, the energy accommodation coefficient could be determined. Note that because diffuse, highly accommodated reflections seem to be the norm in LEO, the assumption of a cosine distribution (Maxwellian with no specular component) is valid. The discussion will return to the subject of reflection distributions later. What is required when analyzing the paddlewheel data however is a single parameter model such as a Maxwellian with variable energy accommodation.

The concept of a paddlewheel satellite as a propeller-shaped object sensing aerodynamic torques is one example of a more general idea. After all, using a measure of aerodynamic torques to solve for atmospheric density is completely analogous to measuring density via observations of drag forces acting on satellites. What makes these combined measurements unique is the measurement of two independent effects of the satellite-atmosphere interaction. This can be drag-torque and drag-force, drag-force and lift-force, or two measurements of drag made by satellites of distinct shapes (drag coefficients) flying very close together. Schematics of these techniques are illustrated in Figure 3.7 along with references for each type of measurement. The labeled vectors indicate free-stream velocity (\vec{V}_∞), spin axis ($\vec{\omega}$), drag-torque (\vec{L}_D), drag-force (\vec{F}_D), and lift-force (\vec{F}_L).

Only four such independent measurements have been analyzed to date. The first paddlewheel analysis was performed in 1966 by Moe on data retrieved from the Explorer VI satellite [Moe, 1966]. Explorer VI flew

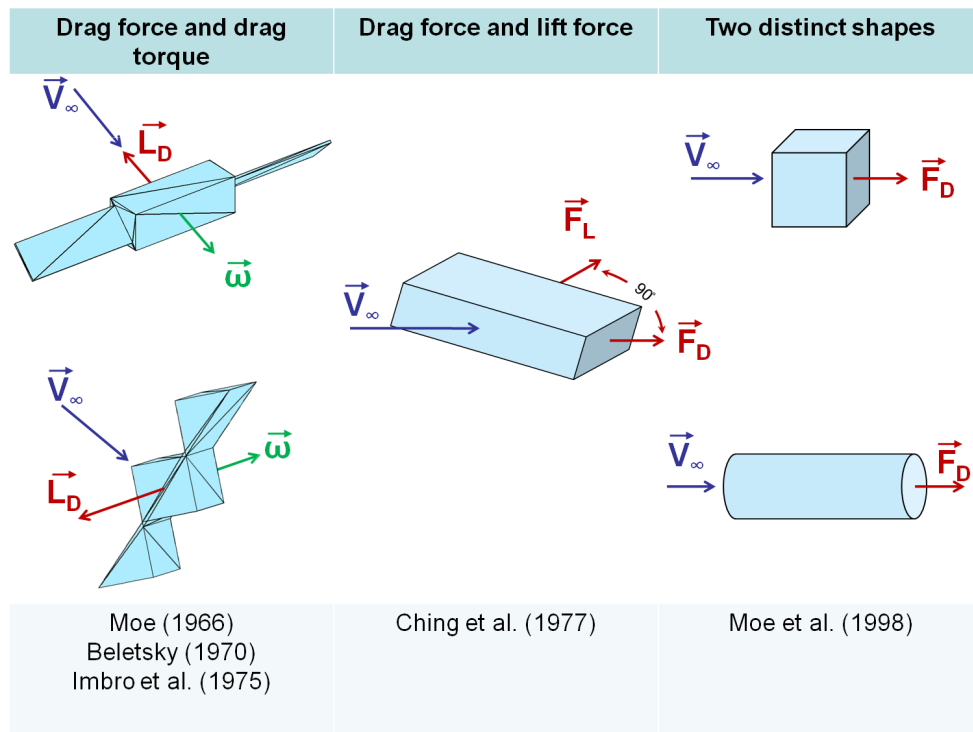


Figure 3.7: Independent measurements leading to estimates of the drag and accommodation coefficients.

in a highly eccentric orbit ($e = 0.76$) with a perigee altitude of approximately 260 km. Soon after, the orbit and spin decays of Ariel II ($e = 0.07$) at an altitude of 290 km was analyzed by Moe [1968] and re-analyzed over longer time spans by Imbro et al. [1975]. Following these American and British satellites, Beletsky analyzed the Russian Proton II satellite ($e = 0.03$) at a perigee altitude of 168 km [Beletsky, 1970]. Due to variation in the direction of Proton's spin axis, the analysis was perhaps the most complicated of all three of these paddlewheels. The S3-1 satellite semi-major axis decay and inclination change were analyzed by Ching et al. [1977] to extract lift and drag information necessary for computing the accommodation coefficient ($e = 0.22$) at 159 km altitude. None of the satellites mentioned above were specifically designed to make accommodation measurements. The data produced was coincidentally, thought not always conveniently, suitable for specification of accommodation coefficients.

Another independent set of drag measurements is derived from the observations of orbital decay of compact and long satellites which fly with their long dimension aligned with the velocity vector. Moe et al. [Moe et al., 1998] performed a gas-surface analysis on the satellites used by Marcos (S3-4, SETA-1, SETA-2, AE-C, AE-D, AE-E) [Marcos, 1985]. The gas-surface analysis was based on the marked difference in drag between the compact and long satellites under similar atmospheric conditions. By adjusting the energy accommodation coefficient the two data sets could be reconciled. This was achieved at a value of α equal to 0.99 for an average altitude of 200 km. Another simultaneous analysis by Harrison and Swinerd of satellite drag was performed on satellites at altitudes between 800 and 1000 km where the primary constituent is helium instead of AO [Harrison and Swinerd, 1996]. Variations in the shape and attitudes of the analyzed satellites (one spherical and one a box with extended solar panels) enabled Harrison and Swinerd to deduce some gas surface interaction parameters. The results of this analysis indicated that the average re-emission velocity was consistent with an energy accommodation value of 0.75 (average over incident energies reported by Harrison and Swinerd). Unlike the low-altitude satellites (200-600 km), this analysis involved a reflection distribution which was not cosine in nature but instead fell between the normal and specular directions [Harrison and Swinerd, 1996]. Direct measurements of accommodation below 200 km altitude and in a near circular orbit were performed by Blanchard and Buck [1985]. Blanchard et al. used multi-axial accelerometer measurements on the shuttle orbiter [Blanchard et al., 1992] to deduce the lift-to-

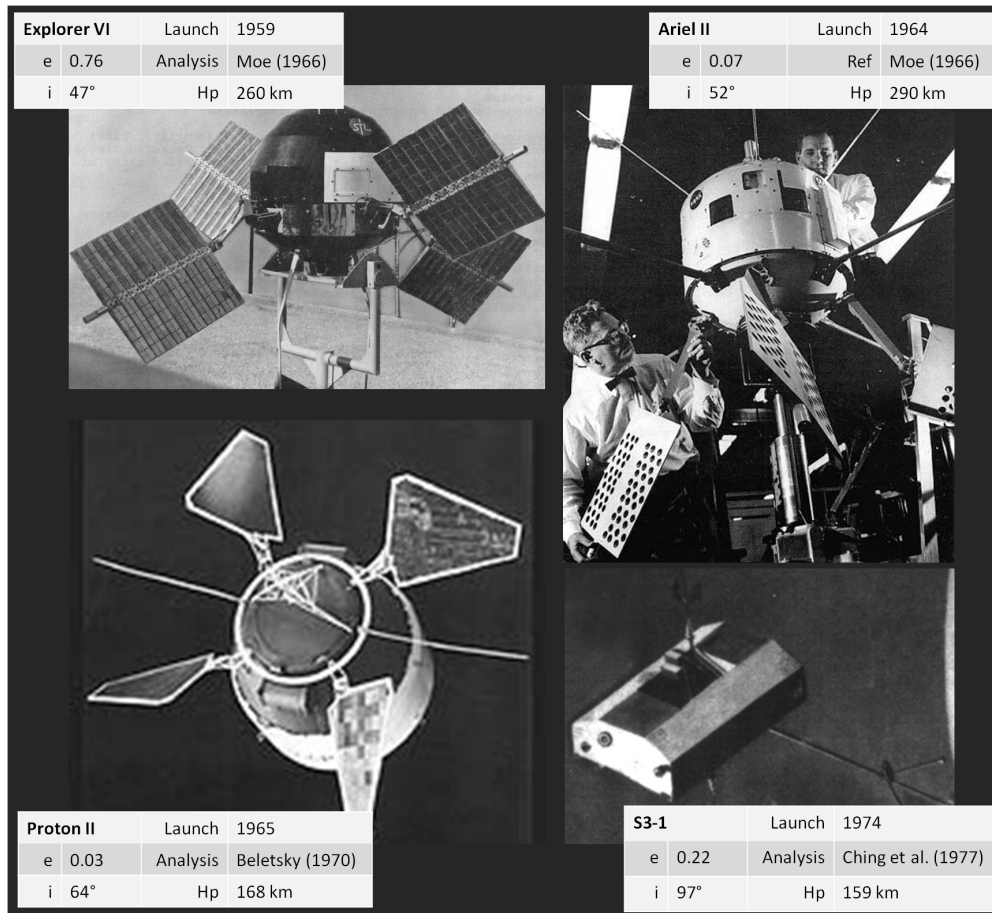


Figure 3.8: Satellites which have been used to measure the energy accommodation coefficient.

drag ratios during re-entry. From analysis of the lift-to-drag ratio, they arrived at a Maxwellian coefficient of 0.91 (91% diffuse and 9% specular) at 160 km. This is equivalent to a diffuse accommodation coefficient of 0.93 [Moe et al., 1998]. It is important to note that the shuttle was observed to enter transition flow at around 165 km and that this would have an effect on the measurements as molecule-molecule interactions become more important. In fact, the authors themselves comment that another shuttle re-entry indicates completely diffuse reflection with full accommodation.

A prevalent class of orbital energy accommodation measurements results from the fitting of spacecraft drag observations (these could be semi-major axis decay observations or accelerometer measurements) to empirical models of atmospheric density in order to solve for ballistic coefficients of these objects. If the masses and areas of the spacecraft are known, then the drag coefficient may be obtained. This drag coefficient along with a sufficient reflection model (usually cosine reflection distribution) is used to estimate the energy accommodation coefficients. The results are sensitive to the accuracy of the density model used and corrections for known altitude dependent model-biases must be applied prior to solving for the accommodation coefficient [Pardini et al., 2010, Pilinski et al., 2010]. The gas-surface parameters estimated using this approach will be referred to as fitted coefficients. Moe and Bowman analyzed the data of spherical objects to arrive at atmospheric model bias values and published the accommodation coefficients used for solar maximum and solar minimum conditions as a function of altitude [Moe and Bowman, 2005]. Pardini et al. similarly analyzed fitted drag coefficients of both spherical and non-spherical satellites during solar maximum conditions. Both Moe and Bowman and Pardini et al. published energy accommodation values which decreased with altitude as well as lower levels of solar activity. In other words, a reduction in atmospheric density is generally associated with a reduction in the energy accommodation coefficient and a corresponding increase in the drag coefficient. Another study by Moore and Sowter [Moore and Sowter, 1991] estimated tangential and normal momentum accommodation coefficients for the satellite ANS-1 during solar minimum at an altitude of 260 km. Moore and Sowter relied on both semi-major axis and inclination measurements but because their gas-surface model (Schamberg) was constrained by two free parameters, atmospheric density models had to be used to arrive at a solution. The resulting tangential momentum accommodation was 0.93 which resulted in a C_D for a sphere of 2.05. Unfortunately, this value cannot be

achieved using the cosine reflection model but the closest possible drag coefficient result gives an energy accommodation coefficient of unity. Furthermore, the analysis of Ariel II [Imbro et al., 1975] which resolved the accommodation coefficient at similar ranges of solar activity, altitude and eccentricity, yielded a spherical C_D of 2.25 and an accommodation coefficient of 0.86. It is possible that the results of Moore and Sowter were influenced by an altitude dependent bias in the J77 and MSISE79 density models. If we assume the Ariel II measurement to be accurate (because it is independent of any density model) then the atmospheric model bias at that altitude is approximately 9% and compares well with the 9-10% published J70 bias estimates of Pardini et al. [Pardini et al., 2010].

3.1.3 Scattering Kernels

Scattering kinetics are crucial to the computation of forces imposed by rarefied gas flows and a brief overview of development in this area will follow. Already a picture is emerging of AO adsorption at spacecraft altitudes. Riley and Giese measured a nearly diffuse reflection distribution as a result of that in a laboratory experiment [Riley and Giese, 1970]. On the other hand, many clean surface experiments result in quasi specular reflection [Trilling, 1967, Thomas, 1967, Moe and Moe, 2005]. The diffuse component of the Maxwellian model is based on the cosine distribution which is perhaps the most commonly used reflection distribution for spacecraft drag applications. This simple distribution states that the probability of reflection is proportional to the cosine of the angle between the surface normal and the direction of reflected velocity. In other words, there is a maximum possibility of molecules being reflected along the surface normal and a zero probability that a molecule is reflected exactly parallel to the surface regardless of the direction of incoming molecules. The Schamberg quasi-specular model allows all molecules to be reflected within a lobe of specified width and concentrated at an arbitrary angle from the surface. The width of the lobe and relationship between incident and reflection angles are adjustable parameters in the model. Schamberg defines the angular probability distribution of reflections within the lobe to be a scaled cosine distribution within the defined beam-width [Schamberg, 1967]. The input parameters like lobe width and direction can be arbitrarily chosen. Moe et al. [Moe and Moe, 2005] recommend the use of Goodman's correlation formulas [Goodman, 1967] to constrain the inputs to Schamberg's model. Goodman's formulas constrain

the accommodation coefficient as a function of mass ratio but also as a function of incident direction. Additionally Goodman specified a formula which relates the incidence angle to the reflection angle (angle from the surface-normal vector to the center of the reflected lobe) which is generally between the incidence angle and the surface normal. This angular dependence is based on numerical and laboratory measurements of reflections from clean surfaces [Goodman, 1967].

In 1963 Nocilla introduced a reflection model based on the concept of a drifting Maxwellian distribution [Nocilla, 1963]. The drifting Maxwellian is a classic Maxwellian velocity distribution function which is centered about some vector representing the bulk velocity of a gas. Such a formulation is commonly used to describe the gas impinging on a surface. In order to define the model one must specify the speed ratio (kinetic to thermal velocity ratio), magnitude of the reflected bulk velocity, and the angle between the bulk velocity and the surface. Later, Hurlbut and Sherman developed the application of the Nocilla model for calculations of drag and lift coefficients in free-molecular flow [Hurlbut and Sherman, 1968]. In this representation of the Nocilla model, the reflection is constrained by an accommodation coefficient which is a function of incidence angle as well as the bulk reflection angle and reflected speed ratio. Just as the accommodation coefficient is an empirical quantity, the other two parameters may be defined by Goodman's correlation formulas for reflected molecules. The Nocilla model is quite versatile and can reproduce specular, quasi-specular, and fully diffuse reflections provided that suitable relationships for the three input parameters are defined.

Another prominent model is the Cercignani-Lampis (CL) scattering kernel which includes some of the concepts introduced by Nocilla but expresses them in a more mathematically rigorous manner [Cercignani and Lampis, 1997]. In the CL model the Maxwellian reflection distribution is not only "drifting" as it was in the Nocilla model but is also shifted by a normal energy accommodation coefficient and tangential momentum accommodation coefficient. As with the Nocilla model, the extremes of completely diffuse and specular reflections may be reproduced.

In the 1980's, Gregory and Peters performed an experiment on the space shuttle to measure the angular distribution of molecules reflected from a surface in LEO. The resulting reflection distribution from a carbon surface was highly diffuse with only 2% of the oxygen reflecting in what appeared to be a specular lobe. The authors note that the appearance of the lobe could have been the effect of sensor inhomogeneity and the

fact that the observed lobe was supra-specular (closer to the surface than the specular angle) contradicts the finding of Goodman and others [Goodman, 1967, Hurlbut and Sherman, 1968]. Figures 3.9 and 3.10 show the data with reflection distribution fits for a single and double lobe case. While the analysis of the space shuttle data was performed using the Nocilla model, the cosine distribution approximates the data reasonably (blue dotted lines). Since only one such experiment has been performed, it is unclear how θ_{out} changes with θ_{in} for the diffuse lobe. It is partially because of this uncertainty that the simpler cosine reflection model is often selected for computations.

Moe et al. make the assertion that more quasi-specular reflection is possible at higher altitudes and suggest that a blending of quasi-specular (Schamberg) and diffuse (partially accommodated Sentman model) reflections may be necessary at altitudes above 500 km [Moe et al., 1998]. Unfortunately, insufficient data exists at the time of this writing to constrain the relative ratios of such a blended model and how it may change under varying input conditions.

The energy loss at the surface and the direction of reflection have been treated separately in this review. This is because one may often mix various models of energy accommodation and reflection distribution (scattering direction). For example, the Maxwell [Niven, 1965, Bird, 1994] model uses a cosine reflection distribution with a unity energy accommodation coefficient then blends this reflection type with a specular reflection model having a unity energy accommodation coefficient. The Sentman model [Sentman, 1961] is entirely based on cosine reflected direction distribution with energy accommodation ranging from zero to unity. Meanwhile, Moe et al. [Moe and Moe, 2005] suggest blending a Sentman model with a quasi-specular one proposed by Schamberg [Schamberg, 1959]. In this implementation, the suggested accommodation coefficients are empirical values for the former and based on the Goodman hard-spheres model for the latter.

3.1.4 Satellite Drag Coefficient Modeling

The topic of drag coefficients in rarefied gases in the context of high altitude flight was first broached in the 1950's by Schamberg [Schamberg, 1959]. Schamberg made the assumption that the vehicle velocity far exceeds the thermal velocity of atmospheric molecules (hypersonic flow) and calculated coefficients of drag for several basic shapes. In Schamberg's model, reflected particles leave the surface in a lobe distribution

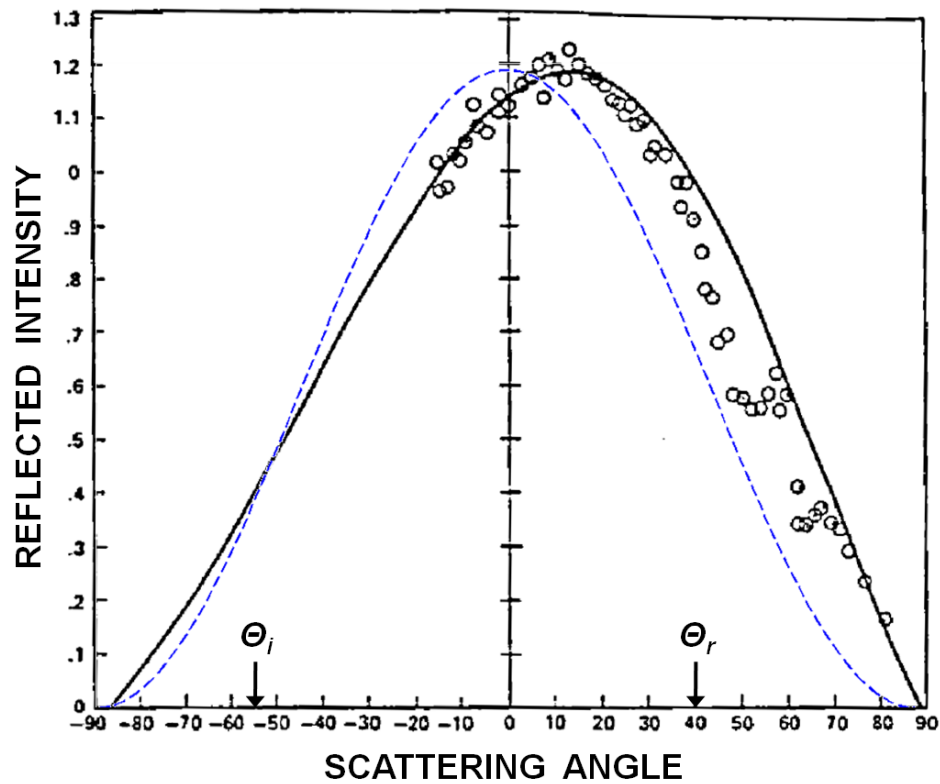


Figure 3.9: Reflection distribution measured in LEO by Gregory and Peters and fit using a single-lobe Nocilla model [Gregory and Peters, 1987]. Also shown is the cosine distribution.

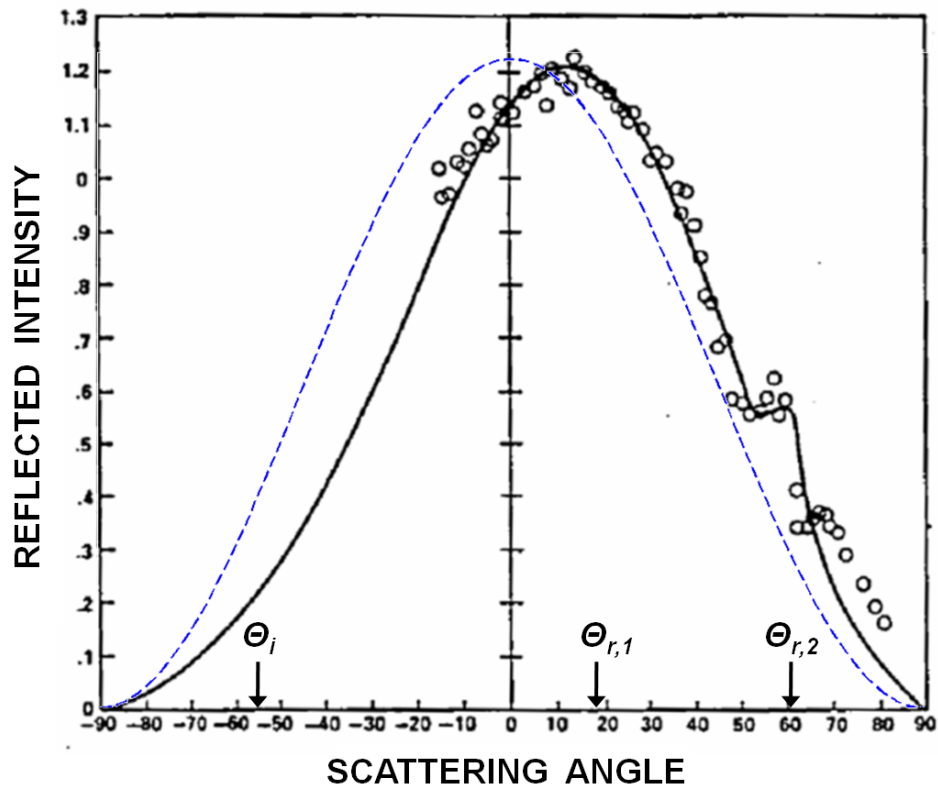


Figure 3.10: Reflection distribution measured in LEO by Gregory and Peters and fit using a single-lobe Nocilla model [Gregory and Peters, 1987]. Also shown is the cosine distribution.

centered around a vector related to the incoming velocity. This was expanded further by Cook [Cook, 1965] who, as described earlier, recommended the drag coefficient of 2.2 for compact shapes. Cook's work produced a good estimate at a time when very little was known about accommodation coefficients in orbit. His value was adopted in constructing many of the empirical models based on satellite drag. In 1961, Sentman constructed a physics-based analytical drag coefficient model which did not require the assumption of hyperthermal flow. Sentman's formulas for drag coefficients allowed a variable accommodation coefficient (reflection temperature) making the work very adaptable and, in fact, his equations are still widely used today [Sutton, 2008, Doornbos et al., 2009, 2010, Marcos et al., 2010].

The work of Moe and Moe has been instrumental in developing the theory which will be applied to this research as it is focused on the construction of realistic drag coefficients which can be confirmed by years of drag data. The method prescribed by Moe et al. [Moe et al., 1998] is the adaptation of the drag coefficient models of Sentman (diffuse) and Schamberg (quasi-specular) with the use of empirical accommodation coefficients profiles for the former and Goodman's model for the latter. This work has led to the realization that drag coefficients vary significantly with altitude and solar activity which has a profound effect on bias entered into the empirical models which were constructed using Cook's value of C_D for compact shapes or which assumed other fixed values. Moe et al. also estimated the uncertainties of various satellite shapes and found that long satellites which fly like an arrow have higher uncertainties in C_D than compact satellites [Moe et al., 1998].

It was recognized early during the Space Age that adsorption of AO will impact the mean accommodation coefficient on a satellite surface thus changing C_D [Cook, 1965, Reiter and Moe, 1968, Moe, 1973]. In 1969 Reiter discussed the possibility of short term changes in the accommodation coefficient due to net adsorption/desorption with changing atmospheric conditions [Reiter and Moe, 1968]. At the time of this writing there is still no data or theoretical estimates as to the time constants of such changes (it could be hours or months). Nor is there much information as to the magnitude of C_D change possible as a result of surface phenomena. A notable effort was undertaken in the 1970's and applied to the construction of the 1976 U.S. Standard Atmosphere. During this time, Moe and Nier were working to resolve the discrepancy in atmospheric composition measured by UV spectrography and spaceborne mass spectrometers. They

selected a third method of composition estimation based on temperature and scale height estimated from drag measurements [Moe, 1973]. However, drag coefficients which correctly represent gas-surface changes with altitude are required for the determination of scale heights. To accomplish this, Moe used the available paddlewheel measurements of accommodation to adjust the composition based on scale height [Moe, 1973]. This AO information was later used to interpolate and extrapolate between the accommodation coefficients of paddlewheel satellites and arrive at altitude dependent drag coefficients published in 1995 for simple shapes [Moe et al., 1995].

Several researchers have demonstrated improvements in the interpretation of accelerometer data with a rigorous computation of satellite drag coefficients. In the work of Sutton and Doornbos et al. [Sutton, 2009, Doornbos et al., 2009] accelerometer data from the CHAMP and GRACE missions has been interpreted using incomplete accommodation and diffuse reflection parameters (Sentman model) to arrive at high-resolution atmospheric density data sets. CHAMP and GRACE data spans 10 years of solar activity from solar maximum to solar minimum and altitudes ranging from 500 km to 250 km altitudes. The accommodation coefficient for these satellites was fixed at a value of 0.93 in the analysis of aerodynamic drag. This results in a C_D for CHAMP which is nearly halfway between the C_D values computed for accommodation coefficients of 0.65 and 1.00, the full range expected for paddlewheel satellites. It is unclear whether choosing the median value was the motivation behind this choice or whether the accommodation was based on tabulations compiled by previous researchers [Pardini et al., 2010, Moe and Bowman, 2005].

Based on the review of literature pertaining to gas-surface interactions and satellite drag coefficient the following conclusions may be drawn.

- There is a marked difference in reflection properties depending on whether the surface is covered with adsorbate or not. Reflections from clean surfaces tend to exhibit low values of energy accommodation and quasi-specular reflection lobes while reflections from contaminated surfaces have higher values of accommodation and diffuse reflection distributions.
- The high degrees of accommodation and diffuse reflection observed in LEO can be attributed to the chemisorption of AO to spacecraft surfaces.

- Many of the studies by Moe et al. [Moe and Wallace, 1993, Moe et al., 1996, 1998, Moe and Moe, 2005, 2008] take a value near unity for the energy accommodation coefficient at 200 km circular orbits as an established fact. In light of the evidence from the shuttle gas-surface reflection experiment, paddlewheel satellites, and laboratory experiments on contaminated surfaces, this is a justified choice.
- Atomic oxygen does not recombine significantly on silicate and forms only a fraction of a monolayer on silicate surfaces. Silicate is used in the form of quartz to cover solar cells and constitutes a large fraction of many LEO spacecraft surface areas.
- Transition metals such as iron, gold and silver have been shown to accept large fractions of AO monolayer coverage. Atomic oxygen also seems to recombine more readily into molecular oxygen on these surfaces with recombination coefficients in excess of 20%.
- Adsorption theory suggests a decrease in adsorption with a drop of adsorbate pressure in the gas phase. If accommodation is linked to the level of adsorption as suggested, this would mean that accommodation will drop to levels predicted by Goodman's model at higher altitudes and lower solar activities. This is consistent with tabulated values of accommodation coefficients for spacecraft.
- There is both theoretical and experimental evidence to suggest that trapping probability and adsorption efficiency decrease as the energy of incident molecules increases.
- Desorption is probably not caused by sputtering but UV absorption is a potential mechanism for desorption.
- The adsorption/desorption process on a satellite surface has timescales which are significantly larger than the rate of collisions. Therefore momentum change associated with adsorption and desorption may be neglected in the force computations for satellite aerodynamics. Instead, the adsorbed molecules play an indirect role in that they change the average energy exchange of incoming molecules with the surface.

These assumptions are based in previous experiments and theory and will form the theoretical backbone of the present research.

3.2 Drag Coefficients and the Development of Atmospheric Models

Use of constant C_D in constructing empirical atmospheric density models introduced 5-15% altitude dependant errors [Bowman and Moe, 2005, Moe et al., 2010]. The cause of this is that the drag coefficient responds to changes in temperature and composition both of which change drastically with altitude. Furthermore, there is evidence that the accommodation coefficient changes with altitude and that this is an important driver behind changes in C_D . In the 1960 and 1970s, when the first observations of orbital decay were being analyzed to solve for thermospheric density [King-Hele, 1965], there was considerable disagreement between density derived from satellite drag and that measured by mass spectrometers and pressure gauges. A great part of this disagreement was due to the adsorption and recombination of AO, the primary constituents at many of the measurement altitudes, on the surfaces of mass spectrometers and pressure gauges. Another cause for disagreement between the techniques was the choice of accommodation coefficient used to compute C_D . In the early days of the Space Age, Cook realized this limitation but for the lack of any data on the subject chose $\alpha = 1$ for all objects at all altitudes and solar conditions [Cook, 1965]. This simplification, necessary at the time, was the origin of the commonly used value of 2.2 for the drag coefficients of compact spacecraft. In constructing the 1976 COESA model (Committee on Extension of the Standard Atmosphere), Moe used an accommodation coefficient which varied with altitude to reconcile the measurements of flux measuring instruments (pressure gauges and mass spectrometers) with drag measurements (solutions of the drag equation) [Moe, 1973]. This approach was later complemented by paddlewheel measurements of the energy accommodation coefficient which confirmed the drop in accommodation with altitude predicted by Moe et al. The present state of understanding is that laboratory experiments on clean surfaces [Thomas, 1967] and the associated gas-surface models do not adequately represent the spacecraft environment below 700 km altitude. Clean surface reflections have been shown to be primarily quasi-specular and sometimes exhibit a backscatter lobe [Moe and Moe, 2005]. On the contrary, contaminated surfaces exhibit diffuse reflection with complete fractional energy loss. The investigation of spaceborne pressure gauges and mass spectrometers [Moe and Moe, 1967, Riley and Giese, 1970] has shown that AO adsorbs to the surface. This discovery along with the high fractional energy loss measured on spacecraft surfaces [Reiter

and Moe, 1968, Beletsky, 1970, Imbro et al., 1975, Ching et al., 1977, Gregory and Peters, 1987, Bowman and Moe, 2005, Pardini et al., 2010] paint a picture of diffuse reflections from surfaces which are contaminated with AO. Furthermore, the surface contamination causes gas-surface interactions to be almost independent of the surface material [Kostoff et al., 1967, Hurlbut and Sherman, 1968]. Consequently the application of clean-surface parameters to spacecraft drag coefficients has led to unphysical results [Moe and Moe, 2008].

Modeling of gas-surface interactions has consequences for operational models of satellite drag. The Air Force's high accuracy satellite drag model (HASDM) has recently led to unprecedented improvements in the prediction of satellite drag [Bowman and Storz, 2003, Marcos et al., 2010]. HASDM relies on adjusting an empirical model based on orbital decay observations of 75 calibration objects. These satellites are generally in eccentric orbits and cover a variety of altitudes, latitudes, and local times. The atmospheric model is adjusted by changing 13 global correction parameters in the Jacchia 70 (J70) atmospheric model to match the observed orbital decay in a least squares differential correction. More precisely, a least squares batch algorithm minimizes the difference between a "true" and "modeled" inverse ballistic coefficient ("B true" and "B modeled") for each reference object by converging on a spherical harmonic temperature field solution. An inverse ballistic coefficient (hereafter referred to as the ballistic coefficient), B , is the product $C_D A/m$ where m is the spacecraft mass. The reference objects have been suitably chosen such that the A/m term variability is small. The "modeled" ballistic coefficient is the orbital determination solution based on assuming a density modeled by the adjusted J70. Meanwhile the "true" coefficient is the 31-year average of the "modeled" value and will be referred to as \bar{B} from now on. Recall from equation 2.1 however that drag measurements only provide information about the product of C_D and density. Therefore, any physical variability in C_D , due to a change in the nature of gas-surface interaction, will couple into the density solution. There is some evidence [Bowman, 2002] which indicates that HASDM compensates for basic physical changes in C_D due to the variability in reflection kinematics with changing atmospheric composition. Remaining unmodeled changes in C_D will be interpreted by HASDM as density variation. Furthermore, it is unclear if errors in the drag coefficient variability of the 75 objects cancel out on average or introduce biases depending on atmospheric conditions. This is a concern if the physics underlying the C_D variation are consistent for each object used in HASDM. The main assumption underlying HASDM is the existence of a static \bar{B} which is

the same as the 31 year average of the modeled ballistic coefficient. In reality this value will vary based on the 31 year period chosen and may very well change as a function of solar activity time-scales which are much shorter. For example, a change of 2.5% in “B true” has been observed due to the choice of averaging period alone [Bowman, 2002]. While it is true that HASDM has been very successful in improving orbital drag predictions, further improvements are possible via the introduction of more advanced C_D modeling. To uncouple drag coefficient and density variability in HASDM, it would be necessary to replace \bar{B} by a physically accurate model of $C_D A/m$ including adequate representation of gas-surface physics.

Another class of global atmospheric models called global circulation models apply first principles physics and solve continuity and mass transport equations for the whole atmosphere. Such is the case with the National Center for Atmospheric Research Thermosphere Ionosphere Electrodynamics Global Circulation Model (TIE-GCM) [Fuller-Rowell et al., 2007] which simulates the coupled interaction between the thermosphere ionosphere and electrodynamics up to 600 km altitude. It has been found by Qian et al. [Qian et al., 2009] that adjusting the eddy diffusivity at the lower boundary of this model can reproduce the observed drag variability observed by satellites in LEO. These adjustments represent seasonal differences in gravity wave breaking around 100 km altitude which in turn change thermospheric composition and density by altering the rate at which AO is removed at that altitude range. In the study by Qian et al. [Qian et al., 2009] the eddy diffusivity was solved for as a function of time using Fourier decomposition and atmospheric data available from satellite drag. The analysis period spanned solar minimum to solar maximum. During this time, there could have been a change in the accommodation coefficient as a function of time and the corresponding change in drag coefficient would have been entered into the eddy-diffusivity results. This is yet another example where correct drag coefficient magnitudes based on physically appropriate models are needed to accurately define atmospheric parameters. Furthermore, since the predicted changes in eddy diffusivity change the amount of AO available at any given altitude, the surface chemistry in LEO will also be effected and may introduce an annual/semi-annual variation in C_D which will alias back into the annual/semi-annual corrections of TIE-GCM.

The effect of AO on the energy accommodation coefficient and the subsequent influence this has on drag coefficients of satellites has been studied by Moe et al. as well as Pilinski et al. [Moe et al.,

1998, Moe and Moe, 2005, Pilinski et al., 2010] As will be shown later, this phenomenon can influence recent findings regarding the earth's atmosphere. One such discovery is the compelling evidence that the thermosphere is contracting due to cooling brought on by an increase in atmospheric carbon dioxide. Emmert et al. [Emmert et al., 2004b] and Solomon et al. [Solomon et al., 2010] have indicated a decreasing secular trend in satellite drag records spanning over 30 years. Since this decrease in atmospheric density will most likely be accompanied by a decrease in AO flux to satellite surfaces, there may be a long-term secular trend in the drag coefficients of satellites used to study the atmosphere. Based on preliminary work performed as a part of this thesis, there is evidence that the shrinking of the atmosphere may be greater than that computed using constant drag coefficients.

Yet another interesting occurrence is the most recent solar minimum which was deeper than any other recorded since the beginning of the Space Age [Solomon et al., 2010]. Standard drag analysis, which uses the assumption that drag coefficients are computed using constant gas-surface interaction parameters, will tend to underestimate the depth of the recent minimum.

The precise satellite accelerometers flown on the CHAMP and GRACE satellites have afforded a detailed, high-resolution study of satellite drag during the past 10 years. The datasets have been used [S. Bruinsma et al., 2006, Forbes et al., 2006, Sutton, 2007, Doornbos et al., 2009, 2010] to shed light on atmospheric dynamics important to making better predictions of satellite drag. This high-cadence record spans the maxima and minima of solar and atmospheric activity and altitude ranges of 500 km to 250 km (as of the end of August 2010). Therefore, it is reasonable to expect that the gas-surface interactions for CHAMP and GRACE will change with the changing atmospheric conditions. At the time of this writing, the density data sets based on CHAMP and GRACE data are computed under the assumption of constant gas-surface interactions and may impose unwanted biases in the thermospheric density record. Furthermore, one of the obstructions in deriving the winds from CHAMP accelerometers has been the difficulty in computing accurate lift coefficient for this satellite. This is a result of significant flow shadowing not represented in commonly used analytical techniques.

Improved satellite drag values can result in better orbital and re-entry predictions. This is especially true as the scientific and operational communities strive to improve beyond 15% levels in atmospheric density

representation and drag predictions. Due to the dynamic nature of both atmospheric density and satellite drag coefficient it is important to describe the dynamics of each separately and accurately to achieve forecast capability.

Chapter 4

Aerodynamic Force Coefficient Computations

Equations 2.1 and 2.3 in Chapter 2 describe the aerodynamic drag force experienced by a spacecraft in free molecular flow (FMF). As previously stated, the atmospheric drag force on satellites is a direct function of the $C_D\rho$ product and errors in C_D contribute directly to the fidelity of density measurements and orbital drag predictions. The same is true of the cross-sectional area and spacecraft mass as seen in Equations 2.1 and 2.3. Cross-sectional area computation, though not as involved as drag coefficient estimation, is not a trivial process if the satellite attitude is changing in unknown ways or if the exact spacecraft geometry is unknown. The computation of cross sectional area will be treated in section 4.3.3. To decouple the product of drag coefficient and density, a physically appropriate estimate of the coefficient must be made and must take into account the effects of gas-surface energy accommodation, usually written as a coefficient that is a measure of the relative amount of kinetic energy molecules transfer during reflection from the satellite surface. In general, aerodynamic computations for a satellite surface can be divided into the specification of the incoming velocity distribution, the outgoing velocity distribution, and the summation of the resulting force vectors. The incident velocity function can be modeled using the Maxwellian distribution as shown below.

$$f(V_{in,j}) = \frac{m^{3/2}}{(2\pi k_B T_a)^{3/2}} \exp \left[\left(-\frac{m}{2k_B T_a} \right) (V_{in,j} - V_{r,j})^2 \right] \quad (4.1)$$

Here, $V_{in,j}$, is one of the components of the molecules' incoming velocity while $V_{r,j}$, is the j 'th component of bulk, or mean velocity. There are several choices of the outgoing velocity distribution as discussed in Chapter 3 but all of them require the specification of a physically appropriate energy accommodation value.

The accommodation coefficient, α , is treated as an empirical parameter effective over the entire satellite surface. Momentum and its time rate of change (force) are particularly sensitive to accommodation and it has been postulated [Moe and Moe, 2005] that in low earth orbit α is strongly related to atomic oxygen adsorption on the satellite surface. Thus, the altitude dependence of the drag coefficient is driven by changes in the quantity of atomic oxygen surface-adsorption which indicates that changes in atmospheric density can also lead to changes in a satellite's drag coefficient. The accommodation coefficient is formally defined as [Schaaf and Chambre, 1961]

$$\alpha = \frac{T_{k,in} - T_{k,out}}{T_{k,in} - T_w} \quad (4.2)$$

where $T_{k,in}$ is the bulk kinetic temperature of incoming molecules, $T_{k,out}$ is the distribution temperature of the reflected molecules, and T_w is the temperature the reflected distribution would have if molecules were re-emitted at the temperature of the surface [Bird, 1994]. Kinetic temperature can be written as [Bird, 1994]

$$T_{k,in} = \frac{mV_r^2}{3k_b} \quad (4.3)$$

where V_r is the magnitude of incident velocity (determined by the relative motion of the spacecraft and the atmosphere) and k_b is the Boltzmann constant. The reflected kinetic temperature at the surface is defined as

$$T_{k,out} = \frac{m}{3k_b} V_r^2 (1 - \alpha) + \alpha T_w \quad (4.4)$$

Written in terms of the most probable reflection velocity, Equation 4.4 becomes Equation 4.5.

$$V_{out} = V_r \left[\frac{2}{3} \left(1 + \alpha \left(\frac{3k_B T_w}{mV_r^2} - 1 \right) \right) \right]^{1/2} \quad (4.5)$$

Strictly speaking Equation 4.3 only applies to monatomic molecules but the error in drag coefficient introduced by treating molecular nitrogen using Equations 4.3 and 4.4 is estimated to be less than 1%.

Two types of reflection are usually ascribed to gas-surface interactions in low-earth orbit [Gregory and Peters, 1987, Moe et al., 1995, Moe and Moe, 2005]. The majority of interactions below 500 km [Moe

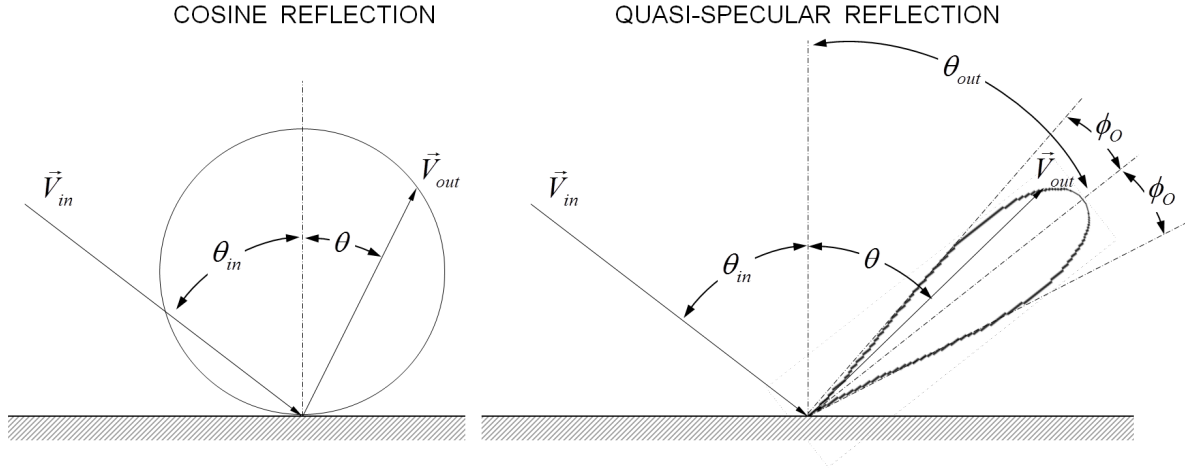


Figure 4.1: The diffuse and quasi-specular reflection models.

and Moe, 2005] are diffuse in character with a scattering kernel which approximates the cosine. This type of scattering was described by Maxwell [Niven, 1965] where the velocities of reflected molecules are centered around the surface normal vector in a cosine distribution. The second type is quasi-specular reflection where the molecules are reflected in a narrow lobe which is centered around the specular direction. When computing the drag coefficient, a successful technique [Moe et al., 1998] is the adaptation of the drag coefficient models of Sentman (diffuse) [Sentman, 1961] and Schamberg (quasi-specular) [Schamberg, 1959] with the use of empirical accommodation coefficient profiles for the former and Goodman's model of accommodation [Goodman, 1967] for the latter. These models were first introduced in the previous chapter. Sentman's model adapts the diffuse (or Maxwellian) energy distribution with a variable accommodation coefficient (this is also referred to as diffuse reflection with incomplete accommodation). The quasi-specular version of Schamberg's model reflects the majority of molecules around a direction such that the angle of reflection (θ_{out}) is smaller or equal to the incident angle (θ_{in}). These reflection models are visually presented in Fig. 4.1. The cosine distribution is described in Equation 4.6 and is sometimes referred to as a raised cosine distribution.

$$f(\theta) = \frac{1}{\pi} (1 + \cos(2\theta)) \quad (4.6)$$

Equations 4.5 and 4.6 form the basis for Sentman's diffuse reflection model with incomplete accommodation. Integrating the incoming and outgoing momentum flux for a planar surface element Sentman derived the following normal and tangential force coefficients.

$$C_{n,diff} = \left(\cos^2 \theta_{in} + \frac{1}{2s^2} \right) (1 + \text{erf}(s \cos \theta_{in})) + \frac{\cos \theta_{in}}{s\sqrt{\pi}} e^{-s^2 \cos^2 \theta_{in}} + \sqrt{\frac{T_{k,out}}{T_a}} \left[\frac{\sqrt{\pi}}{2s} \cos \theta_{in} \left(1 + \text{erf}(s \cos \theta_{in}) + \frac{1}{2s^2} e^{-s^2 \cos^2 \theta_{in}} \right) \right] \quad (4.7)$$

$$C_{t,diff} = \sin \theta_{in} \cos \theta_{in} (1 + \text{erf}(s \cos \theta_{in})) + \frac{\sin \theta_{in}}{s\sqrt{\pi}} e^{-s^2 \cos^2 \theta_{in}} \quad (4.8)$$

In the equations above, erf() denotes the error function defined as

$$\text{erf}(x) = \frac{2}{\sqrt{\pi}} \int_0^x \exp(-t^2) dt \quad (4.9)$$

while the speed ratio s is defined as

$$s = \left| \vec{V}_r \right| \beta \quad (4.10)$$

and $\beta = \sqrt{m/(2k_B T_a)}$ and can be thought of as the reciprocal of the most probable thermal speed. The Schamberg quasi-specular reflection model is described by Equation 4.11 where ϕ_o is the lobe half-width and θ_{out} is the center of the lobe measured from the surface normal direction. Equation 4.12 provides an accommodation coefficient model as a function of incidence angle. This accommodation function is used together with Schamberg's quasi-specular model and is based on Goodman's correlation function.

$$f(\theta) = \begin{cases} 1 + \cos\left(\frac{\pi}{\phi_o}(\theta - \theta_{out})\right) & \text{if } -\phi_o \leq \theta - \theta_{out} \leq \phi_o \\ 0 & \text{else} \end{cases} \quad (4.11)$$

$$\alpha(\theta_{in}) = 3.6\mu \frac{\sin(\theta_{in})}{(1 + \mu)^2} \quad (4.12)$$

Note that Schamberg [Schamberg, 1959] defines the incidence angle from surface normal and uses a cosine instead of the sine in Equation 4.12. The μ in the equation above is the ratio of the incident particle mass

to the mass of the surface atoms. Goodman also developed a formula for the average reflection angle as a function of incidence angle which is reproduced in Equation 4.13

$$\sin\theta_{out} = (\sin\theta_{in})^\nu \quad (4.13)$$

where $\nu \geq 1$, θ_{out} is the average reflection angle and θ_{in} the incidence angle defined from the surface normal. In the case of fully diffuse (cosine) reflection ν is infinite and θ_{out} always takes on the value of 0 while for specular reflection ν is equal to 1.00 and θ_{out} is equal to θ_{in} . Equation 4.13 can be used to compute θ_{out} for Equation 4.11. In order for Equation 4.13 to reproduce the reflection data of Gregory and Peters [Gregory and Peters, 1987] who measured a reflection angle of 40° when the incidence angle was 55° , ν must take on the value of 2.215. The reflection velocity appropriate for Schamberg reflection [Schamberg, 1959, Doornbos et al., 2009] is written in equation 4.14.

$$V_{out} = V_r \sqrt{1 + \alpha(\theta_{in}) \left(\frac{T_w}{T_{k,in}} - 1 \right)} \quad (4.14)$$

When $T_w \ll T_{k,in}$, which is the case for orbital velocities, the reflection speed can be approximated by $V_r \sqrt{1 - \alpha}$. The reflected velocity direction can then be written as [Moore, 1985]

$$\hat{v}_r = \frac{\sin\theta_r}{\sin\theta_i} v_{in} + \left(\frac{\sin\theta_{out}}{\sin\theta_{in}} \cos\theta_{in} + \cos\theta_{out} \right) \hat{n} \quad 0 \leq \theta_{out}, \theta_{in} \leq \pi/2 \quad (4.15)$$

Normal and tangential force coefficients have been derived for the Schamberg model by Moore and Sowter [Moore and Sowter, 1991]. Again, the normal coefficient (C_n) acts in a direction normal to a flat surface element. Meanwhile, the tangential coefficient (C_t) acts along a vector parallel to the surface element which also lies in a plane defined by the incident velocity and surface normal. The coefficients for Schamberg's quasi-specular (QS) reflection can be written as

$$C_{n,qs} = 2\cos^2\theta_{in} \left[1 + \Phi(\phi_o) \frac{V_{out}}{V_r} \frac{\cos\theta_{out}}{\cos\theta_{in}} \right] \quad (4.16)$$

and

$$C_{t,qs} = 2\cos\theta_{in}\sin\theta_{in} \left[1 - \Phi(\phi_o) \frac{V_{out}}{V_r} \frac{\sin\theta_{out}}{\sin\theta_{in}} \right] \quad (4.17)$$

where

$$\Phi(\phi_o) = \frac{1 - (2\phi_o/\pi)^2}{1 - 4(2\phi_o/\pi)^2} \frac{\frac{1}{2}\cos 2\phi_o - (2\phi_o/\pi)}{\cos\phi_o - (2\phi_o/\pi)} \quad (4.18)$$

accounts for the scatter of molecules around the reflected direction (\hat{v}_{out}) Moore and Sowter [1991]. For ϕ_o equal to 0 , 10 , 25 , 45 , 60 , and 90 degrees, the values of $\Phi(\phi_o)$ are approximately 1.00, 0.99, 0.97, 0.90, 0.84 and 2/3 respectively [Imbro et al., 1975]. Both C_n and C_t in equations 4.14 and 4.17 are computed under the assumptions of hyperthermal flow. This means that the ratio of bulk velocity to thermal velocity is very large and the speed ratio (s) can be assumed infinite. Furthermore, the direction of incoming molecules is not diffuse but instead lies along a single vector corresponding to the bulk velocity.

An important assumption underlying almost all the analysis techniques applicable to satellites in LEO is that the flow is in the free molecular regime characterized by a relatively high Knudsen number, $K_N > 10$. The Knudsen number, $K_N = \lambda/L$, is the ratio of mean-free path, λ , to a characteristic length, L , and is an indicator of the importance of intermolecular collisions relative to molecule-surface collisions. The information presented here is used to compute the Knudsen number using the mean free path between incident and reflected molecules. Note that this is different from the free-stream Knudsen number which is the mean free path between incident molecules only. The derivation of the incident-reflected Knudsen number for a satellite is provided by Sentman [Sentman, 1961] and the result is shown here.

$$K_N \approx \frac{\sqrt{\pi}}{2n_{in}s\pi d^2} \sqrt{\frac{T_{k,out}}{T_a}} \quad (4.19)$$

where s is the speed ratio, n_{in} is the number density of the incident molecules, T_a is the temperature of the atmosphere, $T_{k,out}$ is the kinetic temperature of the outgoing molecules, and d is the average molecular radius of the two interacting species. Applying this equation to a spherical satellite 1-m in diameter flying through the lower atmosphere at $7,500 \text{ m s}^{-1}$ leads to $K_N > 10$ above 220 km altitude at solar maximum conditions ($A_p=5$ and $F10.7=225 \text{ sfu}$).

4.1 Integral Equations

Once a set of incident and reflected velocity distributions is chosen, it may be used to compute the force on a surface element due to incident and outgoing molecules. For shapes such as spheres, flat-plates, cones, and cylinders, the incoming and outgoing forces may be integrated over the surface analytically. Such integral equations for basic shapes have been presented by Schamberg, Sentman, Bird, as well as others [Schamberg, 1959, Sentman, 1961, Karr, 1969, Bird, 1994, Storch, 2002].

The following equations [Bird, 1994] govern free-molecular flow force coefficients on a sphere and on a flat plate with one side exposed to the flow under the assumptions of diffuse reflection (Sentman's model)

$$C_{D,sphere,diff} = \frac{2s^2+1}{\sqrt{\pi}s^3} \exp(-s^2) + \frac{4s^4+4s^2-1}{2s^4} \operatorname{erf}(s) + \frac{2\sqrt{\pi}}{3s} \sqrt{T_{k,out}/T_a} \quad (4.20a)$$

$$C_{D,plate} = \frac{2}{s\sqrt{\pi}} \exp(-s^2 \sin^2(\theta_{in})) + \frac{\sin(\theta_{in})}{s^2} (1 + 2s^2) \operatorname{erf}(s \sin(\theta_{in})) + \frac{\sqrt{\pi}}{s} \sin^2(\theta_{in}) \sqrt{T_{k,out}/T_a} \quad (4.20b)$$

where θ_{in} is the angle between the surface-normal and incident velocity vectors. While the lift coefficient of a sphere is zero, for a plate it can be written as

$$C_{L,plate,diff} = \frac{\cos\theta_{in}}{s^2} \operatorname{erf}(s \cos\theta_{in}) + \frac{1}{s} \sqrt{\pi} \cos\theta_{in} \sin\theta_{in} \sqrt{\frac{T_{k,out}}{T_a}} \quad (4.21)$$

Equation 4.21 defines the lift for a plate in the direction perpendicular to the free-stream velocity and in the plane defined by the free-stream velocity and surface normal. In general however, spacecraft experience lift in both the orbit normal (side forces) and orbit-radial directions (aerodynamic lift) due to interaction with the atmosphere and care must be taken to define the lift vector consistently. The equations above are based on Sentman's model of diffuse reflection with partial accommodation and are also referred to as integral equations in literature. The temperature T_a refers to the thermal temperature of the ambient gas irrespective of its bulk motion (not to be confused with the incident kinetic temperature in Equation 4.3). Equation 4.4 was used to compute the reflection temperatures based on a range of accommodation coefficients expected in LEO. The physical interpretation of β is a reciprocal of most probable thermal speed. Temperature T_a

in the definition of β and in Eq. (4.20a) refers to the thermal temperature of the ambient gas irrespective of its bulk motion and is not to be confused with the incident kinetic temperature in Equation (4.3). The integral equation for a cylinder is included in Appendix A.

Schamberg's model also leads to integral equations for some simple shapes. For a flat plate with one side facing the stream, the drag coefficient can be derived from equations 4.16 and 4.17.

$$C_{D,plate,qs} = C_{t,qs}\sin\theta_{in} + C_{n,qs}\cos\theta_{in} \quad (4.22)$$

Recall that θ_{in} is the incidence angle measured from the surface normal vector. For a sphere, Schamberg [Schamberg, 1959] derives

$$C_{D,sphere,qs} = 2 \left[1 + 2\Phi(\phi_o) \frac{V_{out}}{V_r} \left(I_1(\nu) - \frac{1}{\nu+3} \right) \right] \quad (4.23)$$

where $I_1(\nu)$ is the definite integral

$$I_1(\nu) = \int_0^1 x \sqrt{(1-x^{2\nu})(1-x^2)} dx . \quad (4.24)$$

and the limiting values are $I_1(1) = 1/4$ for the specular case and $I_1(\infty) = 1/3$ for the diffuse case.

4.2 Plate Models

One method for obtaining the force coefficient of an arbitrary shape is to compute the force coefficients of each surface element (equations 4.20b and 4.22) in a finite element surface-mesh and combine it to form the drag coefficient of the entire object. The analytical solutions are carried out for N_s species considered in the computation and combined as a weighted mean. Equation 4.25 demonstrates this concept for the k 'th panel in the geometry.

$$C_{D,k} = \frac{\sum_{j=1}^{N_s} C_{D,j} n_j m_j}{\sum_{j=1}^N n_j m_j} \quad (4.25)$$

The results from each of the N_p panels can then be combined to compute a force coefficient for the entire shape. First the total cross sectional area is computed for the panel model.

$$A_{ref} = \sum_{k=1}^{N_p} A_{proj,k} \quad (4.26)$$

In equation 4.26, A_{ref} is the cross sectional area projected in the direction of the free-stream velocity

$$A_{ref,k} = \begin{cases} A_{plan,k} |\hat{n}_k \cdot \hat{V}_i| & \text{if } \hat{n}_k \cdot \hat{V}_i < 0, \text{ panel facing incoming flow} \\ 0 & \text{if } \hat{n}_k \cdot \hat{V}_i \geq 0, \text{ panel facing away from flow} \end{cases} \quad (4.27)$$

where $A_{plan,k}$ is the geometric area (planform area) of the k'th panel. Next the panel results are weighted by panel area to produce the total force coefficient as shown in equation 4.28.

$$C_D = \frac{\sum_{k=1}^{N_p} C_{D,k} A_{plan,k}}{A_{ref}} \quad (4.28)$$

This analytic approach does not account for secondary reflections nor shadowing inside concave geometries such as the Starshine satellite surfaces. However, plate models are used as points of reference for quantifying the improvement in drag coefficients afforded by the numerical techniques and for computing force coefficients of convex geometries.

4.3 Test-Particle Methods

A configurable software package was developed to aid in the evaluation of gas-surface interactions in a free-molecular flow. The following set of requirements was defined for the numerical computation of drag coefficients.

- Compute satellite force (and torque) coefficients numerically due to satellite atmosphere interactions
- Consider altitudes in Earth orbit of around 200 km and up
- Take into account concave geometry (multiple collisions)
- Configurable gas-surface interactions (angular distribution, energy accommodation coefficient)
- Configurable free-stream properties (temperature, composition, velocity magnitude and direction)
- Satellite geometry defined by standard CAD output file

- Source code must be available
- Cross sectional area calculation

The resulting software is called Statistical Program for Aerodynamic and Radiation pressure Coefficient Simulation (SPARCS). SPARCS is an alternative to other force coefficient computation programs such as plate models, direct simulation Monte Carlo (DSMC) schemes, and other test-particle codes. The plate model is the method currently employed by many drag analyses for force coefficient analysis. This method is fast but does not take into account shadowing and multiple reflections which can be significant for complex geometries such as the CHAMP satellite. One of the goals of this project is to provide a method for assessing when the plate model is adequate for a desired level of precision. Bird's DSMC code, called DS3V for Direct Simulation 3D Visual program [Bird, 2007], is capable of computing shadowing and secondary reflections as well as molecule-molecule interactions for transition (re-entry) flow computations. However, this program does not allow for the inclusion of complex gas-surface interactions, cannot model radiation pressure, nor can it be used to compute cross-sectional areas of complex objects. ANGARA is a code developed by the European Space Agency and Hypersonic Technology Göttingen (HTG) to model shadowing for aerodynamic and radiation pressure force computations as well as cross-sectional area estimates. However, due to the requirements of source code availability and interchangeable gas-surface interactions, SPARCS is the only selection which fulfills all of the requirements.

The software is implemented in MATLAB [Hanselman and Littlefield, 2001] due to the large amount of software subroutines already available and the limited development time frame. In order to increase portability and speed however, the software was validated and rewritten into C at the lowest levels. SPARCS has three modes specified by the user which cover the three user cases (aerodynamics, radiation pressure, cross-sectional area).

4.3.1 Software Description

Figure 4.2 is a block diagram of the aerodynamic mode. The code is written primarily in MATLAB with the exception of the FLOW GENERATION and time-critical parts of FIND SURFACE IMPACTS

blocks which were written in C.

4.3.2 Preliminary Reference Frame Definitions

One of the inputs to the test-particle model is the pitch and sideslip angle of the free-stream. These angles (ϕ and β respectively) are defined in Figure 4.3. Note that free-stream angles ($\phi = 0, \beta = 0$) correspond to free-stream velocity in the positive X direction (molecules moving from left to right along X).

The CAD fixed reference frame (shown in blue) will be the same as the local frame in the CAD program used to generate the model. The CHAMP satellite body fixed frame (SBF) will also be referenced in this work. This is the official body fixed frame of CHAMP data products. The CHAMP SBF is illustrated in Figure 4.4. Nominally the SBF X axis would be aligned with the flight direction, the Z axis would be aligned with nadir, and the Y axis completes a right handed system.

4.3.3 Cross-Sectional Area Computation

The SPARCS software developed for this research includes two methods of cross sectional area computations. The first is referred to as the outline method. In this code the contour corresponding to the outline of the satellite projection is iteratively refined. Figure 4.5 shows an outline computation for the CHAMP satellite model. An example of cross-sectional area map generated for CHAMP is shown in Figure 4.6.

In addition, a test particle Monte Carlo method is included for cross-sectional computations. A hyperthermal ($s > 100$) beam is generated at the flow boundaries in the direction of interest. Next, the number of molecules found to impact the surface is compared to the total number of molecules generated at the boundaries. The equation below shows how cross sectional area is computed from this information.

$$A_{\text{ref}} = \frac{N_{\text{impacts}}}{N_{\text{generated}}} \sum_{k=1}^6 (\hat{n}_{b,k} \cdot \hat{r}_O) A_k \quad (4.29)$$

Here, $\hat{n}_{b,k}$ is the unit normal of flow boundary k (there are six flow boundaries), \hat{r}_O is the line-of-sight direction, and A_k is the planform area of the flow boundaries when the flow boundary is facing into the line-of-sight direction and 0 when the flow boundary is facing away. Figure 4.6 shows an example of cross sectional area variation computed for the CHAMP model. Note that the area varies by 20% in the nominal

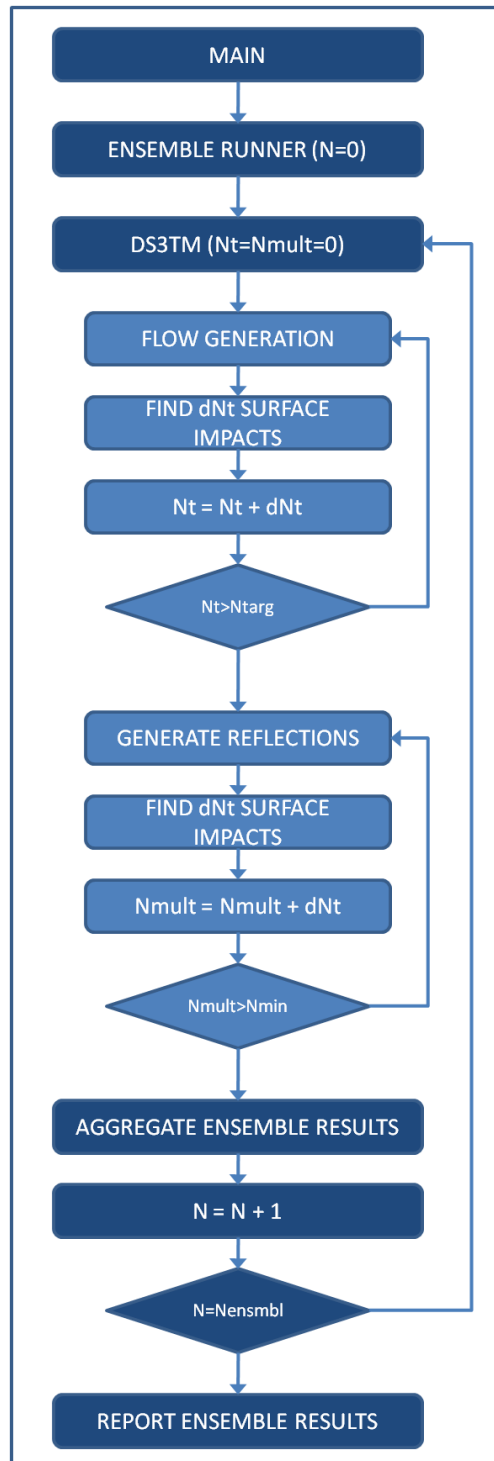


Figure 4.2: Block diagram of SPARCS.

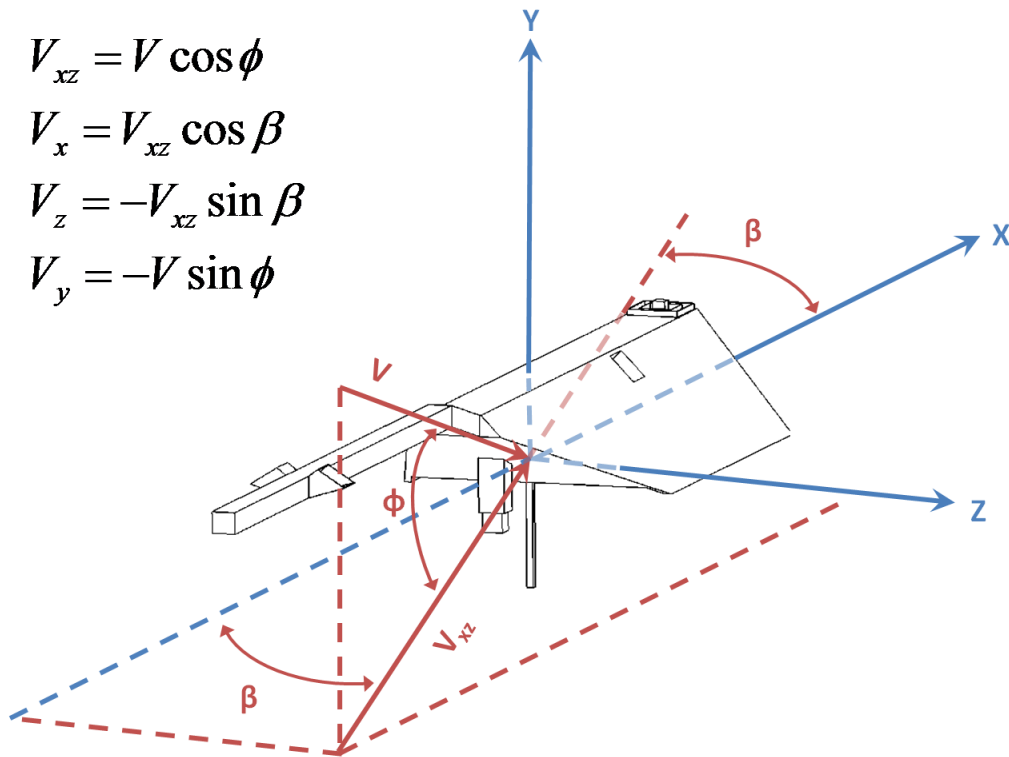


Figure 4.3: CHAMP local free-stream coordinate system with pitch and sideslip definitions.

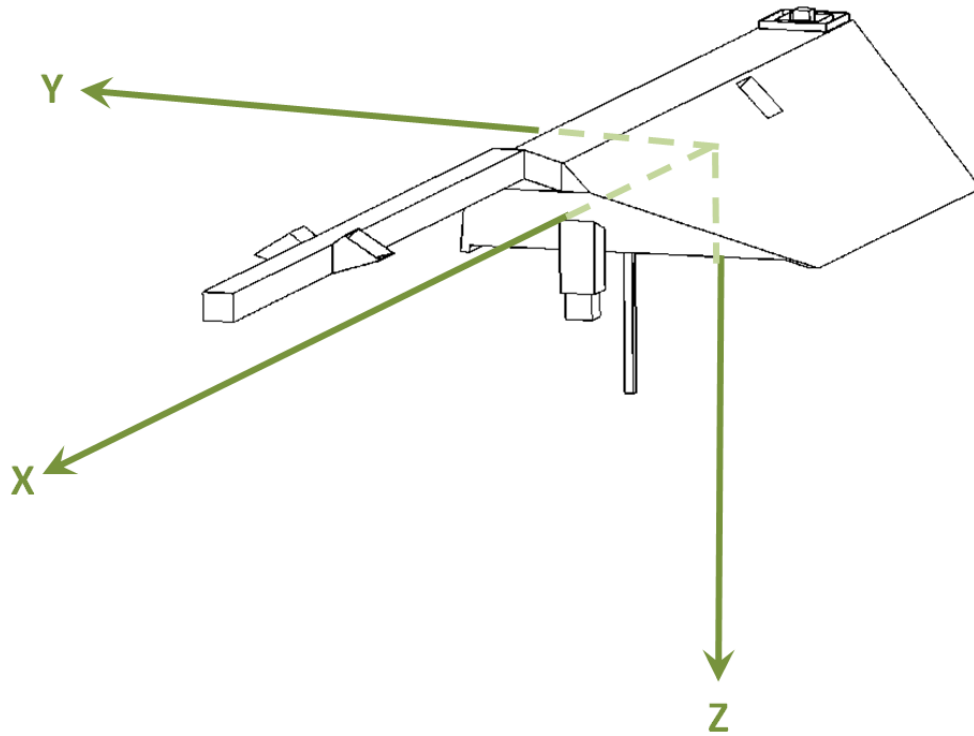


Figure 4.4: The CHAMP body fixed frame (SBF).

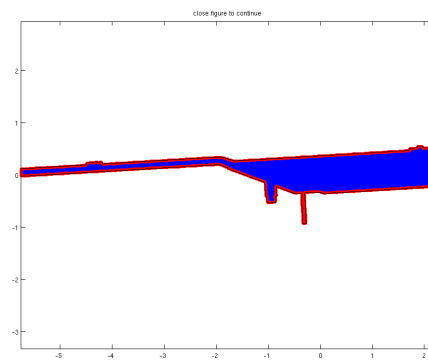


Figure 4.5: Example of a satellite outline contour.

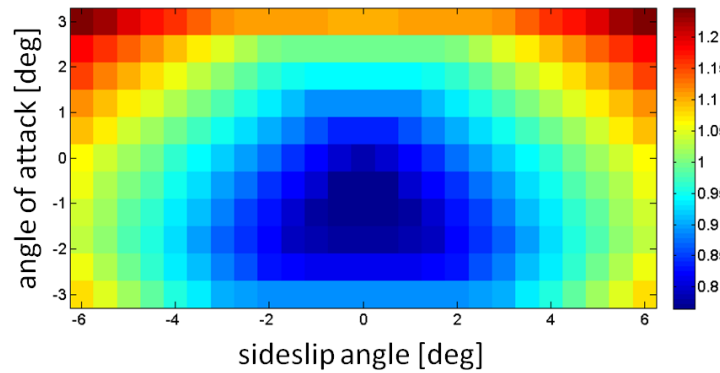


Figure 4.6: CHAMP cross-sectional area computed using the outline method.

range of free-stream orientations for the CHAMP satellite. Figure 4.7 demonstrates the variability over the full range of CHAMP satellite pitch and sideslip angles.

Since the computation of force coefficients involves multiplying drag coefficients by projected area, the overall satellite drag is directly impacted by the cross sectional area computation. Table 4.1 lists cross sectional areas projected on the various sbf axes of CHAMP for each model appearing in literature as well as our new model, CHAMPv1.lv11. Note the great variation among the different models. Highlighted in green are the most recent models used by ESA as well as the most recent model developed for this project. One model previously used for CHAMP and GRACE analysis, the GFZ panel model, is highlighted in red. Notice that the GFZ panel geometry is an outlier in terms of cross sectional area in the most critical axis (+X). CHAMPv1.lv11 agrees with the state of the art ANGARA HTG within about 1.6% in X, 2.1% in Z, and 9.9% in Y. The agreement between positive and negative projections is also shown in the table and is a measure of computational method consistency. We have computed cross sectional area using both test-particle and outline methods. The two methods agree within 1%.

4.3.4 Aerodynamic Calculations

The model begins by initializing the velocities of molecules at the flow boundaries. Molecule positions are randomly selected on each boundary and the flux through each boundary is scaled to the theoretical effusion (\dot{N}) across a boundary as given by the equations below.

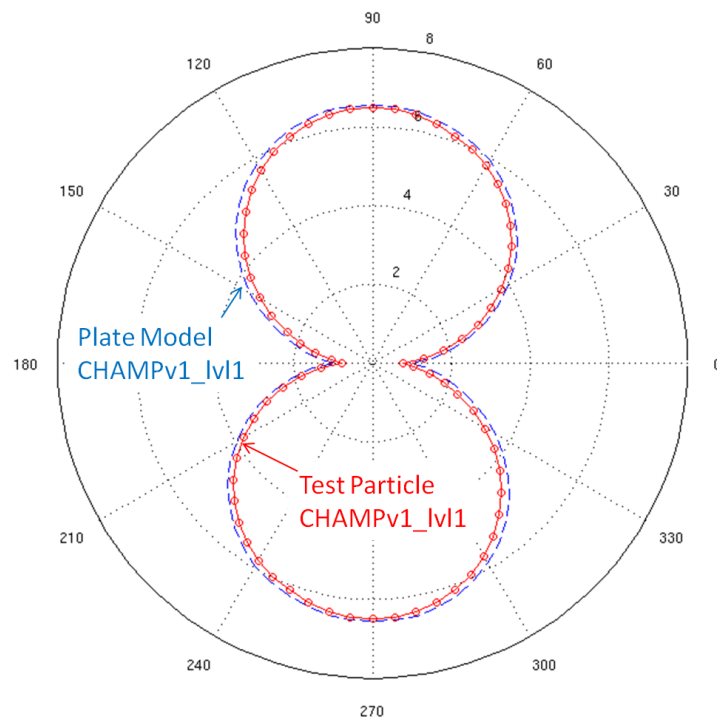


Figure 4.7: Cross-sectional area computed using the test particle ('csa' mode) over a full range of pitch angles. Plate model area is shown in blue for comparison.

Table 4.1: CHAMP geometry models and their cross-sectional areas (in square meters) projected along different axes (Expressed in the CHAMP satellite body fixed or SBF coordinates). Highlighted in light-grey are the latest ESA model as well as the model developed for SPARCS. The often-used GFZ model is highlighted in dark-grey. The Δ columns indicate the difference in satellite projections in the positive and negative directions of any given axis i.e. $\Delta X = A_{+X} - A_{-X}$.

	Front (+X)	Back (-X)	Left (+Y)	Right (-Y)	Bottom (+Z)	Top (-Z)	ΔX	ΔY	ΔZ
CH-IT-DID-0001	0.743	0.743	3.120	3.120	6.444	6.444	0.000	0.000	0.000
ANGARA (DEOS, old)	0.576	0.642	2.992	2.994	6.511	6.438	-0.066	-0.002	0.073
ANGARA (HTG)	0.794	0.784	3.245	3.240	6.621	6.586	0.011	0.005	0.035
Panels (GFZ)	0.470	0.461	3.378	3.378	6.690	6.295	0.010	0.000	0.395
Panels (Bruinsma)	0.637	0.461	3.378	3.378	6.690	6.295	0.176	0.000	0.395
Panels (DEOS)	0.743	0.752	3.122	3.122	6.456	6.464	-0.009	0.000	-0.008
CHAMPv1_lv1 Outline	0.781	0.782	2.938	2.939	6.487	6.487	-0.002	0.000	0.000
CHAMPv1_lv1 Test Particle	0.782	0.779	2.937	2.933	6.477	6.496	0.003	0.003	-0.019
CHAMPv1_lv1 - ANGARA (HTG):	-1.6%	-0.4%	-9.9%	-9.8%	-2.1%	-1.4%			
CHAMPv1_lv1 - Panels (GFZ):	39.8%	41.0%	-15.0%	-15.0%	-3.2%	3.0%			

$$\dot{N} = \frac{\exp(-s^2 f^2) + \sqrt{\pi} s f (1 + \operatorname{erf}(s f))}{2\beta\sqrt{\pi}} \quad (4.30)$$

$$f = \hat{v}_r \cdot \hat{n} \quad (4.31)$$

Next the incoming velocities are selected by sampling from a drifting Maxwellian distribution at temperature T_a and bulk velocity \vec{V}_r . Ray tracing is then performed to the surface elements and a reflection velocity is selected based on the desired gas-surface model. In the case of the diffuse distribution, the reflection temperature is chosen based on an accommodation coefficient as shown in Equation 4.4. The incoming (\vec{V}_{in}) and outgoing (\vec{V}_{out}) velocities as well as the molecular mass (m) are used to compute the momentum change. In order to convert the total momentum change summed over all collisions into a force, a physical time step must be estimated. To do this we compare the computed number of molecules passing through a flow boundary to the theoretical flux at that boundary.

$$dt = \left| \frac{N_{\text{computed}}}{\dot{N}A} \right|_{\text{boundary}} \quad (4.32)$$

$$\vec{F} = \frac{\sum_{k=1}^{N_{\text{computed}}} (\vec{V}_{out,k} - \vec{V}_{in,k}) m}{dt} \quad (4.33)$$

Finally, the individual aerodynamic force coefficients are computed.

$$\vec{C}_a = \frac{2\vec{F}}{nmA_{\text{ref}}V_r^2} \quad (4.34)$$

The SPARCS model is designed to accumulate an ensemble average force coefficient and moment coefficient vector. This approach allows the $1-\sigma$ uncertainty estimate for each coefficient to be computed.

A salient questions at this point is: how many ensemble runs and/or molecule-surface impacts should one choose? The answer depends on several factors including geometry complexity, extent of concavity, flow molecular mass and temperature, as well as the accommodation coefficient. It is important that before embarking on a large array of simulation runs, the necessary number of ensemble runs to achieve the desired $1-\sigma$ uncertainty in the coefficient of interest be investigated. For the most complete CHAMP geometry file,

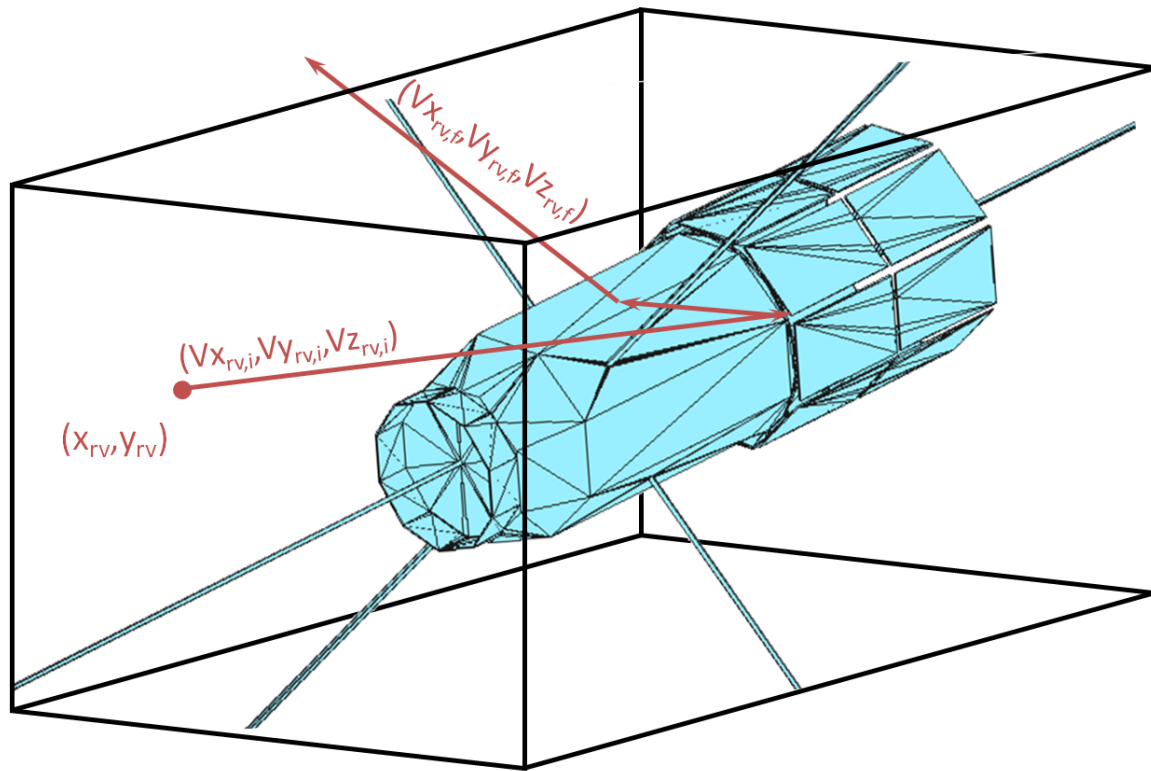


Figure 4.8: Flow generation boundaries showing initial and final states of generated molecules with an arbitrary satellite geometry.

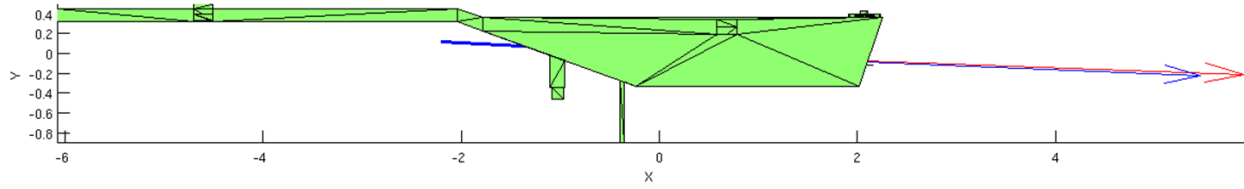


Figure 4.9: 3D display of ensemble results from the SPARCS program.

which is composed of 280 elements, 200 ensemble runs each including an average of 6000 impacts are sufficient per set of input parameters to achieve an uncertainty of 0.2% or less. Approximately 50 ensemble runs can achieve an uncertainty of under 1%. Another parameter of interest is the number of impacts per-ensemble per-surface-element. It is desirable for the average value of this parameter to fall between at least 30 and 100 for the aerodynamic results to be statistically significant.

Figure 4.9 is an example of SPARCS output with the light blue vector representing the plate model \vec{C}_a solution and the red vector representing the test particle solution while the bold blue line represents the free-stream direction. Example of model runs and validation are provided in Appendix B.

4.4 Direct Simulation Monte Carlo

In this section the Direct Simulation Monte Carlo (DSMC) method is briefly reviewed. We focus on the freely available Direct Simulation 3-D Visual (DS3V) program developed by Bird [Bird, 2009]. DS3V, like all DSMC codes employs a volumetric mesh which spans the flow volume. This mesh is a rectangular grid with cells in the mesh being labeled as either in the flow, inside the object volume, or at the flow-object boundary. Much like the test-particle technique the DSMC procedure first samples from an incoming velocity distribution (represented as a drifting Maxwellian) to initialize the velocities of N simulated molecules per cell. In DSMC each simulated molecule represents F_N real molecules. The time counter is set to zero and the motion of the molecules is propagated for time step Δt_{DSMC} .

$$\Delta t_{DSMC} \approx \frac{2V_C}{N\bar{N}F_N \cdot (\sigma c_r)_{max}} \quad (4.35)$$

The \bar{N} in equation 4.35 is the ensemble time-average of N , σ is the collision cross section, c_r is the relative

molecular speed of a collision pair, and V_C is the cell volume. In this scheme, there are $1/2N\bar{N}F_N \cdot (\sigma_{c_r})_{max} \Delta t_{DSMC}/V_C$ molecule pairs selected for collisions per time step and the scheme is referred to as the no time counter (NTC) [Bird, 1992]. The collision probability for the selected molecules is $\sigma_{c_r}/(\sigma_{c_r})_{max}$. The program also detects molecule collisions in the boundary cells and performs the gas-surface and molecule-molecule reflection computations. After the new velocities have been computed (post-collision) the molecule positions are propagated in time by Δt . After the molecules are moved, the time step is recomputed and another round of collision selections begins. Thus, the essence of DSMC is that molecular motion and intermolecular collisions can be treated separately over very short time intervals [Bird, 1992]. The DS3V program can be used to study the effects of accommodation coefficient in transition flows. Transition flows are flows where molecule-molecule interactions can no longer be neglected but which cannot be solved using Navier-Stokes equations due to a breakdown in the continuity assumptions. Transition flows are usually associated with altitudes of 160 km and below for large objects such as the space shuttle and 120 km for smaller objects such as 1-m microsattellites (though this could be higher at solar maximum and for very large rocket bodies).

4.5 Sensitivity to Inputs

We will now explore the functional dependence of satellite drag on several parameters to identify the primary drivers of drag coefficients and to gain perspective on the later numerical analysis. Unless stated otherwise, the sensitivity study is performed for atmospheric temperature of 900 K, a mean molecular mass of 16 amu (atomic oxygen), $V_r = 7,800 \text{ m s}^{-1}$, and $T_w = 300\text{K}$. Figure 4.10 demonstrates that the drag coefficient has a strong dependence on α via its relationship with $T_{k,out}$. As already mentioned, α has been found to be a function of altitude and the functional dependence has been explored by several researchers, most recently by Pardini et al. [Pardini et al., 2010] and Pilinski et al. [Pilinski et al., 2010].

The drag coefficient is also sensitive to the mean molecular mass, \bar{m} (see Figure 4.10 (a)). To investigate how this parameter might change in the spacecraft environment, a circular orbit of varying altitude was propagated through a simulated atmosphere. The atmospheric model is the Naval Research Laboratory Mass Spectrometer and Incoherent Scatter Radar extending to the Exosphere or NRLMSISE-00 [Picone

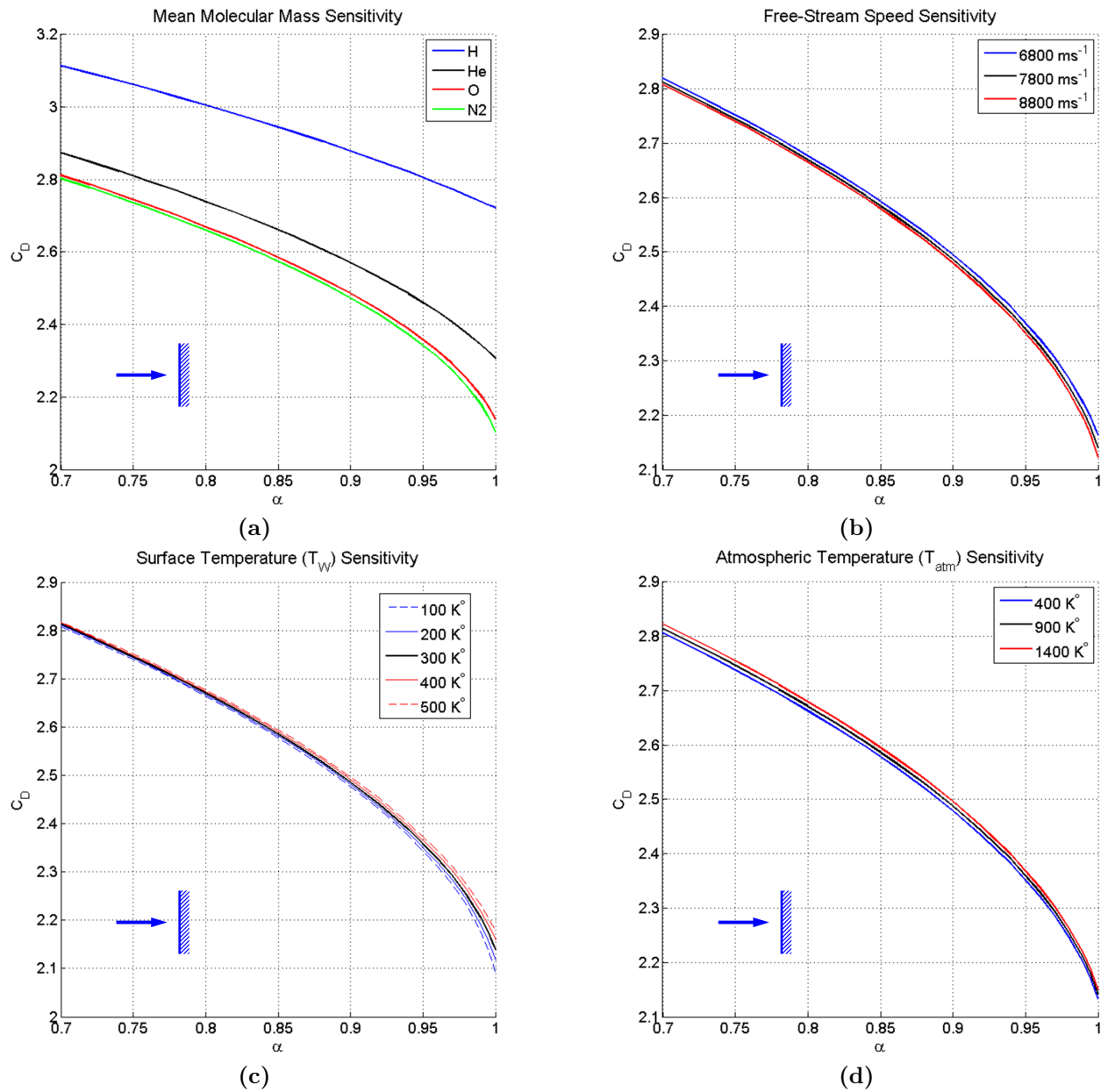


Figure 4.10: Drag coefficient sensitivity to (a) mean molecular mass, (b) free-stream speed, (c) wall temperature, and (d) atmospheric temperature at a range of accommodation coefficients.

et al., 2002b]. In the numerical implementation, mean molecular mass is replaced by the actual mass of the most abundant species whose contributions are modeled separately then combined via equation 4.25. We limit our numerical analysis to molecular nitrogen and atomic oxygen because these are likely to be the dominant species in the atmosphere during solar maximum at and below 500 km altitude. At solar minimum and at higher altitudes it is important to include the contributions of helium and hydrogen. The effect of these lighter atmospheric elements is to increase C_D as can be seen in Figure 4.10 (a).

The total velocity magnitude, V_T , is seen to change the drag coefficient by only $\pm 0.9\%$ over a velocity range of $\pm 1000 \text{ ms}^{-1}$. Note however that the accommodation coefficient itself may be a function of V_T so any comparative analysis should be restricted to objects flying at approximately the same speed. Furthermore, a variation of $\pm 100\text{K}$ in the surface temperature of the spacecraft, T_w , results in a change in drag coefficient of approximately $\pm 1.0\%$ at full accommodation. This variability is reduced significantly at lower accommodation coefficient values. The sensitivity to atmospheric temperature is seen in Figure 4.10 (d). A conservative atmospheric temperature error of $\pm 500\text{K}$ results in just $\pm 0.3\%$ uncertainty in the drag coefficient of the flat plate (although the effect on slender objects with the long axis in the direction of flight is more significant [Doornbos et al., 2009]). It is important to remember that these sensitivities relate to the coefficient of drag, C_D , and not to the drag force. For example, a deviation of $\pm 500\text{K}$ in atmospheric temperature is likely to be associated with a significant change in local atmospheric mass density which would alter the overall drag. From these sensitivity considerations, the overall root-mean square expected uncertainty in modeled C_D is around $\pm 2\%$. Note that for elongated shapes, a sensitivity study is available in a report commissioned by the European Space Agency [Doornbos et al., 2009] as well as a paper by Sutton [Sutton, 2009].

Given the orbit-averaged atmospheric properties along with Equations 4.20a and 4.20b, we can now investigate some representative drag coefficient values at various altitudes. Figure 4.11 illustrates the amount of change in drag coefficient due to changes in altitude, shape, and solar activity. The altitude and solar activity response is primarily a result of accommodation coefficient and mean molecular mass variability.

The drag coefficient of concave shapes is sensitive to the computation method as well. Appendix B includes the comparisons of test-particle results with plate model solutions for the CHAMP satellite (Figure B.3). The plate model underestimates drag coefficient of CHAMP by approximately 7.5%. This is because

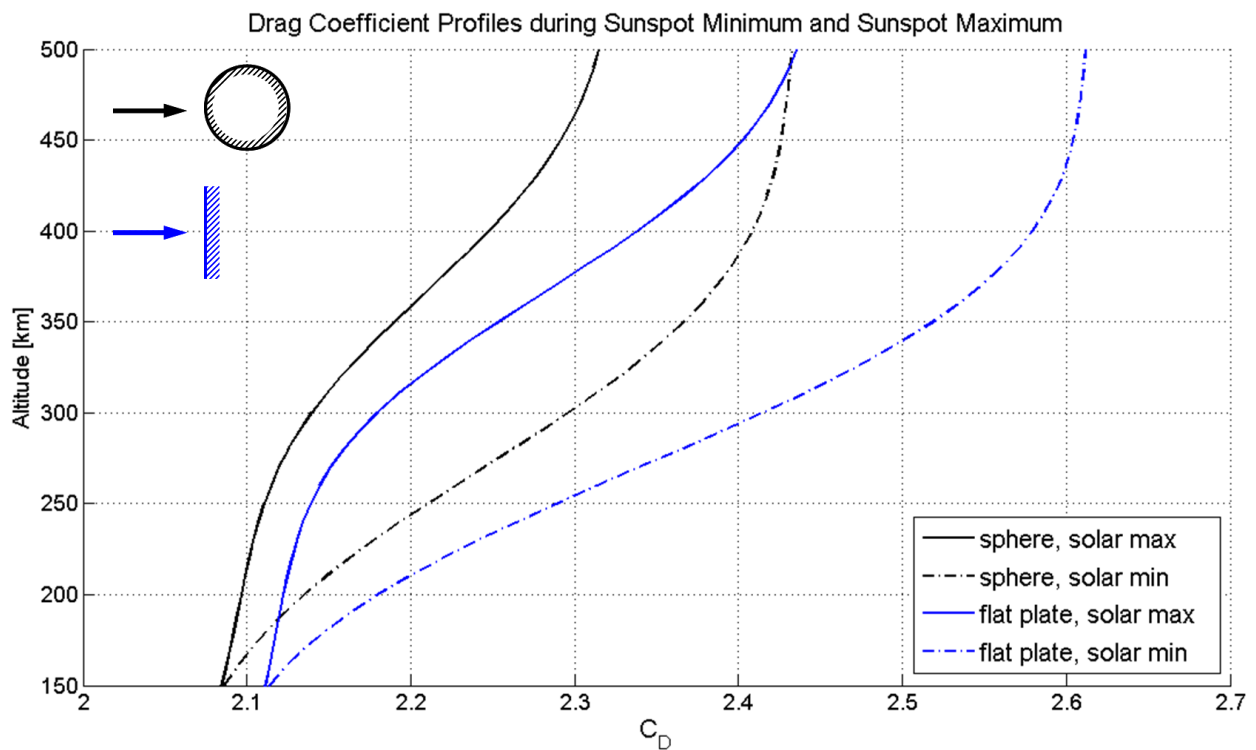


Figure 4.11: The drag coefficient of a sphere and a flat plate during solar maximum and solar minimum.

the plate model cannot account for flow shadowing and generally overestimates A_{ref} in equation 4.34. While convex shapes can be handled adequately by integral equations and plate models, significant errors may result from computing aerodynamic coefficients of concave objects like the CHAMP satellite.

We will now look at how input parameters change the force coefficient including geometry model, orientation, multiple reflection modeling, space weather and flight mode for the CHAMP satellite. Figure 4.12 illustrates force coefficients for three values of energy accommodation and a selection of geometry models described in Table 4.1. It is clear that the GFZ plate model is an outlier. This model underestimates the force coefficient due to its significantly lower cross sectional area projected in the X direction. The consequence of this is an overestimation of neutral thermospheric density. The newest ESA model (ANGARA HTG) agrees well with the model presented in this report. Changes in cross section (which lead to changes in force coefficients) are a function of angle of attack and satellite geometry. Figure 4.13 is the cross sectional area variation with angle of attack. The three different models are the full-geometry model, a simplified CHAMP geometry which includes the front boom but no star cameras, GPS antenna, communications antenna, nor ion drift meter, and a simplified model without a boom. These models are illustrated in Figure 4.14. The three models diverge significantly especially at positive angles of attack. The difference in A_{ref} around 0 degree pitch is 12%. The computations were performed using both test particle and outline methods and the results across the two methods agree within 0.3%.

It is of interest to examine to what extent multiple reflections can change the drag coefficient compared with shadowing alone. Table 4.2 is the summary of a number of SPARCS test particle runs performed with multiple reflections, with a partial number of multiple reflections, and with no multiple reflections. The partial numbers of multiple reflections are defined by the percentage of molecules to undergo more than one reflection on the surface. After this percentage of molecules has left the flow-boundaries, the ensemble is complete. The effect of such truncation is at most 1% for the CHAMP model when all multiple reflections have been neglected. The effect of neglecting 5% of the reflections is a change in C_D between 0.1% and 0.2%. It is therefore possible to truncate multiple reflections with minimal loss of precision at least for the CHAMP satellite.

The variability of the drag coefficient under a range of realistic input parameters occurring along the

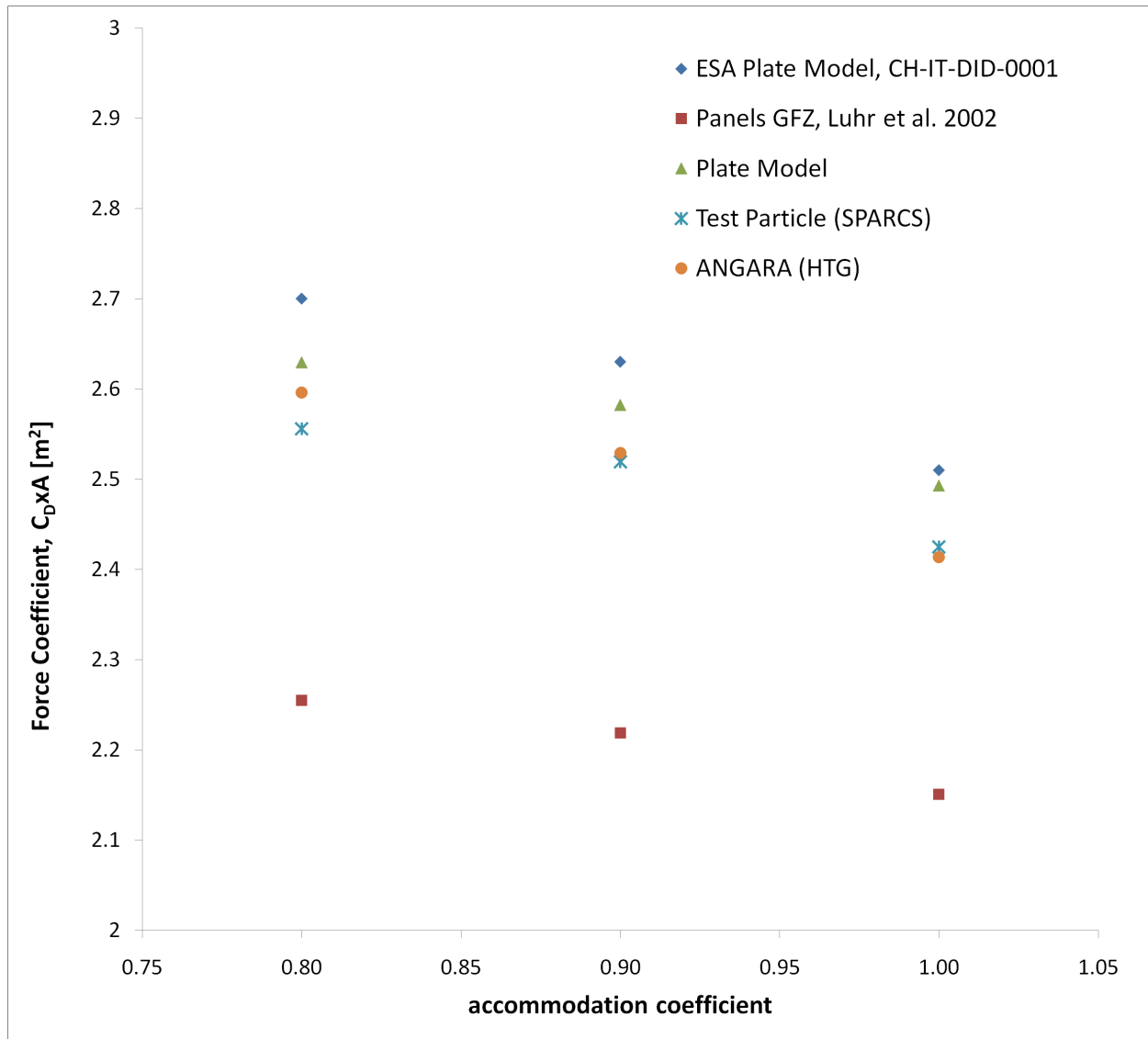


Figure 4.12: Force coefficient sensitivity to geometry modeling. The GFZ panel model was originally used for density determination.

Table 4.2: Effect of omitting multiple reflections on C_D computations of the CHAMP satellite. Percentage values of multiply reflected molecules refer to the relative amount of potential secondary reflections which are allowed to remain inside the geometry.

Percent Multiply Reflected:	100%	95%	0%	Plate Model
$\alpha = 1.00$	3.685	3.692	3.721	3.359
change from 100%	-	0.2%	1.0%	-8.8%
$\alpha = 0.60$	3.369	3.371	3.380	2.972
change from 100%	-	0.1%	0.3%	-11.8%

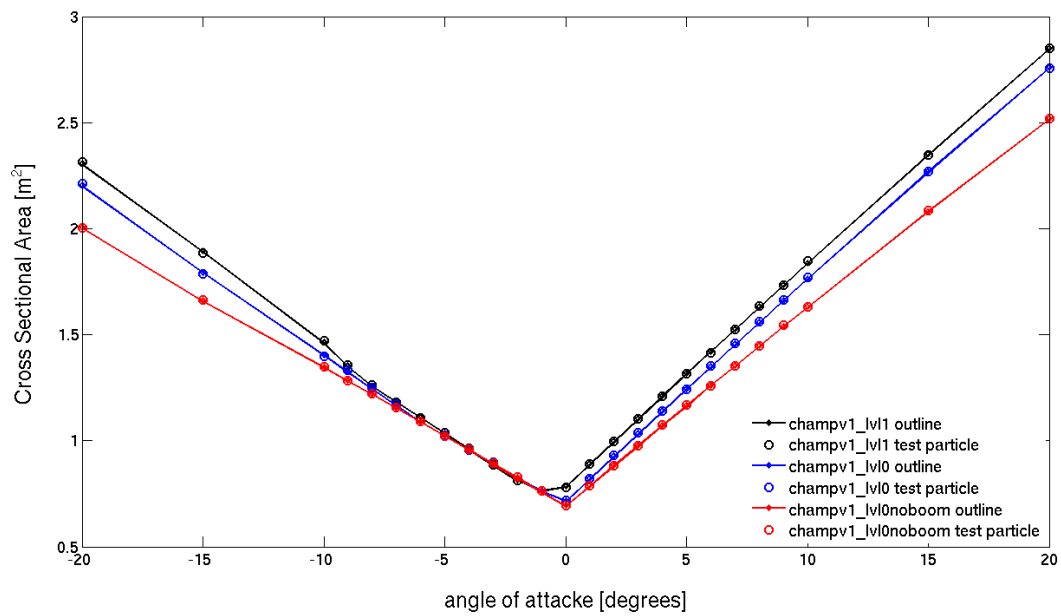


Figure 4.13: CHAMP cross-sectional area for different geometry models. Note that both the test particle and outline methods agree to better than 0.3%.

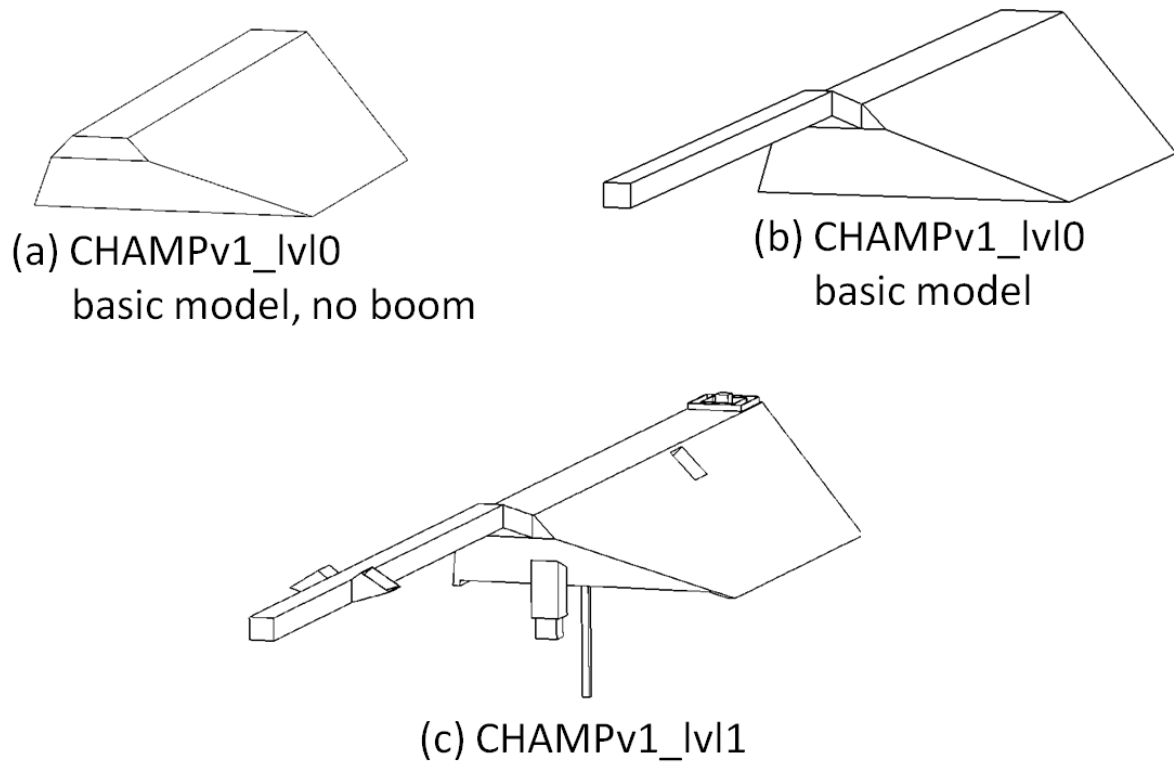


Figure 4.14: Descriptions of CHAMP geometry files constructed for use with SPARCS.

track of the CHAMP satellite is also addressed. The input parameters have been modeled using satellite attitude measurements and NRLMSISE-00. Figure 4.15 and Figure 4.16 show the force coefficients using the GFZ panel model as well as the full CHAMP model (level 1 model) developed for this work. Note the significant difference between the force coefficient computation methods. The present model C_{DA} is larger than the GFZ model during both 2002 and 2007 conditions. The force coefficient drops from 2002 to 2007 by about 8-10%. This is primarily due to a drop in atmospheric temperature at lower altitudes and lower solar activity. To demonstrate the effect which different geometry models and computation methods have on the measured density, the accelerometer-based density measurements were recomputed using the SPARCS drag coefficients and the results plotted in Figure 4.17. Note that the newly computed density is lower and shows less agreement with NRLMSISE-00. This may be due to an additional error source in the density analysis (accelerometer calibration for example), a bias in NRLMSISE-00 or some combination of the two. The newly computed density also compares well with analysis performed using the newest ANGARA model [Doornbos et al., 2009, 2010].

The drag coefficient is also sensitive to changes in the space environment. Figure 4.18 and Figure 4.19 show the drag force variability during the Halloween storm of 2003 during nighttime and daytime passes respectively. There is a much clearer relationship between the storm occurrence and force coefficient at night time. The ratio of GFZ plate model to SPARCS coefficients is also plotted and shows a strong relationship with storm activity. The relationship is caused by a change in shadowing as the composition and temperature change in the atmosphere. This example shows that both the drag coefficient and drag coefficient model errors are functions of space weather.

Next, the forward and aft flying modes are compared. CHAMP switched to aft-flying (boom pointing back) mode in February of 2010. The distribution of drag force coefficients for the two modes during February 2010 is shown in Figure 4.20. There is approximately an 8% difference in force coefficients between the two modes. The ratio of GFZ plate model to SPARCS computations is compared in Figure 4.21. The average model ratio changes from approximately 0.85 to 0.81. The greater disagreement with the plate model is caused by an increase in shadowing for the aft flying mode (the CHAMP boom is now in the satellite wake).

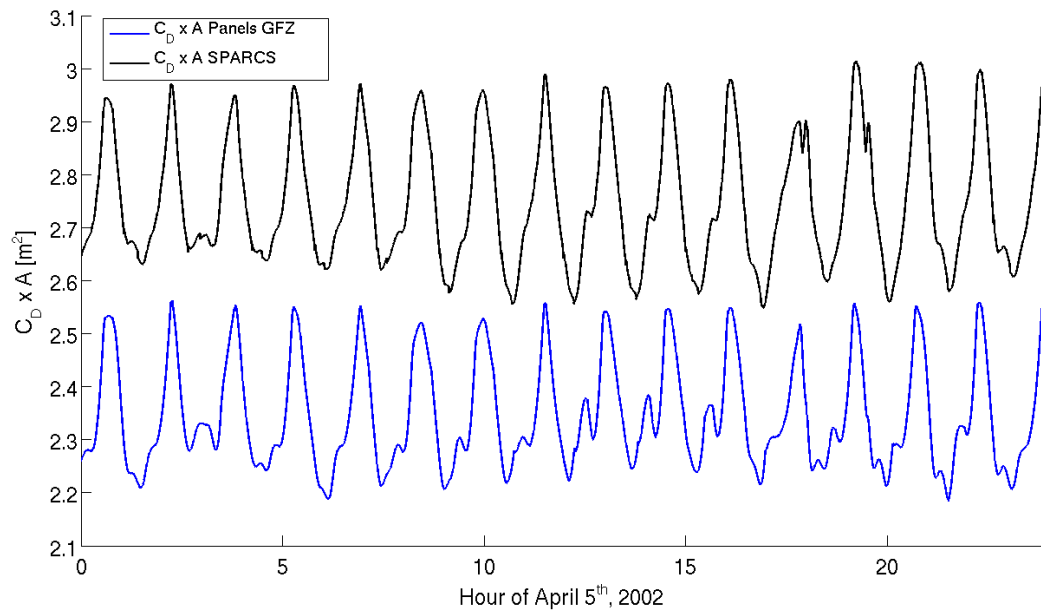


Figure 4.15: Solar maximum drag force coefficients computed using the SPARCS and plate GFZ plate models along the CHAMP satellite track at 414 km altitude.

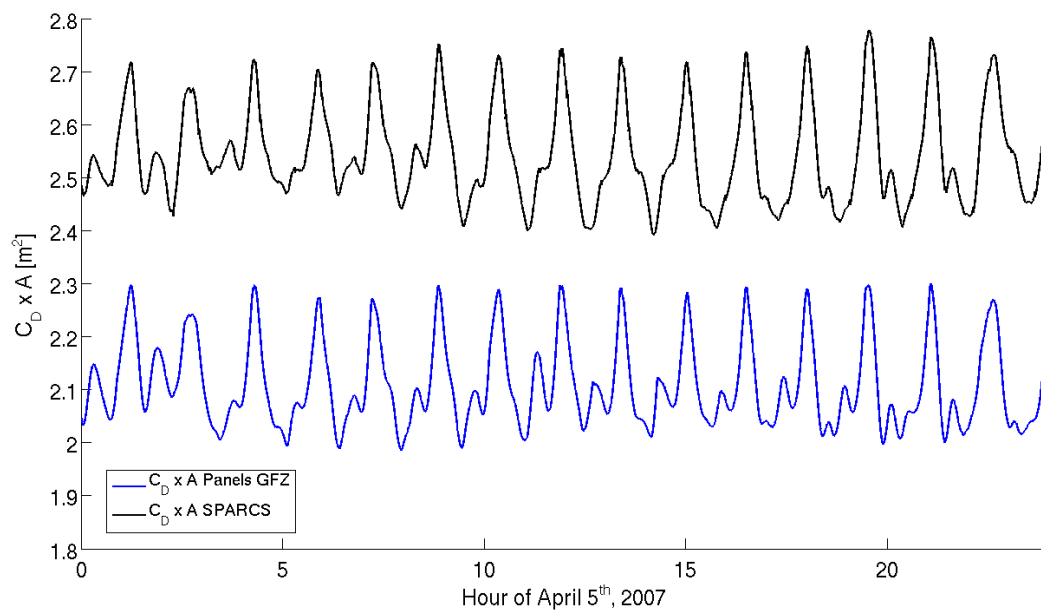


Figure 4.16: Solar minimum drag force coefficients computed using the SPARCS and plate GFZ plate models along the CHAMP satellite track at 358 km altitude.

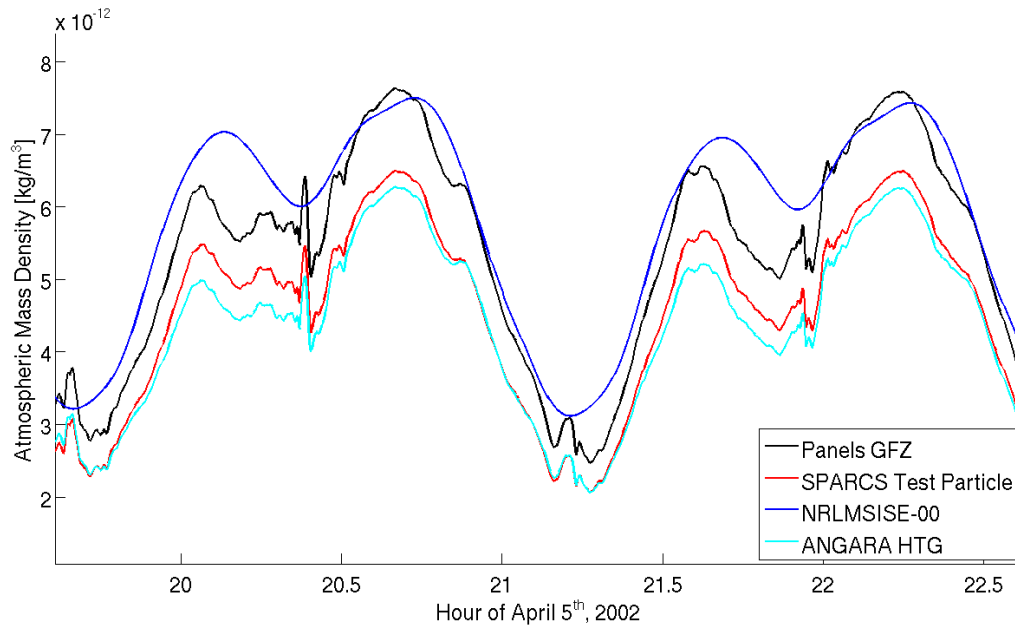


Figure 4.17: Comparison of densities computed using the GFZ plate ANGARA (courtesy of Dr. Doornbos) and SPARCS models.

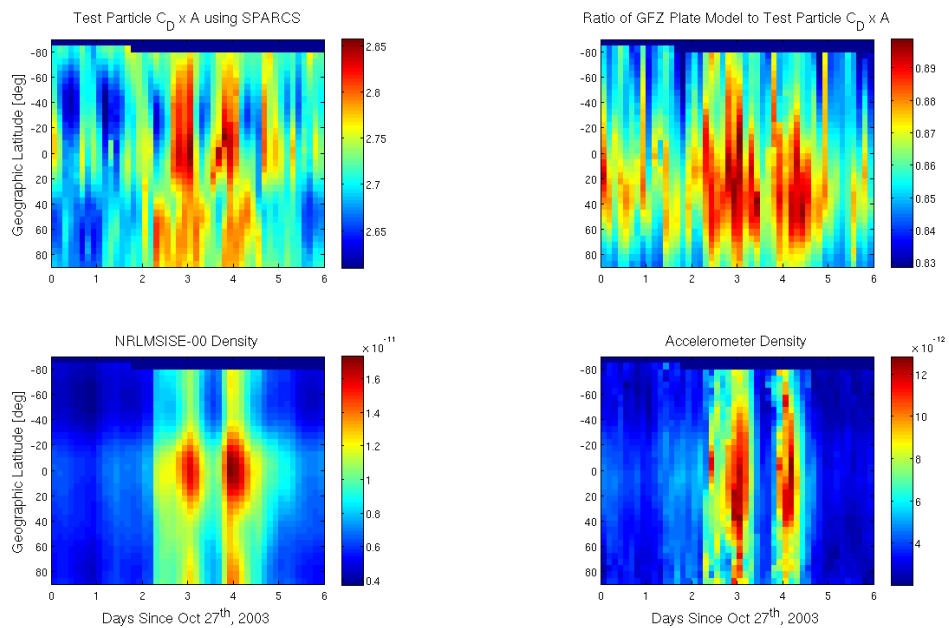


Figure 4.18: CHAMP drag force coefficient ($C_D \times A$) and ratio of GFZ to SPARCS force coefficients along with NRLMSISE-00 and accelerometer density response at night during the October 2003 Halloween storms.

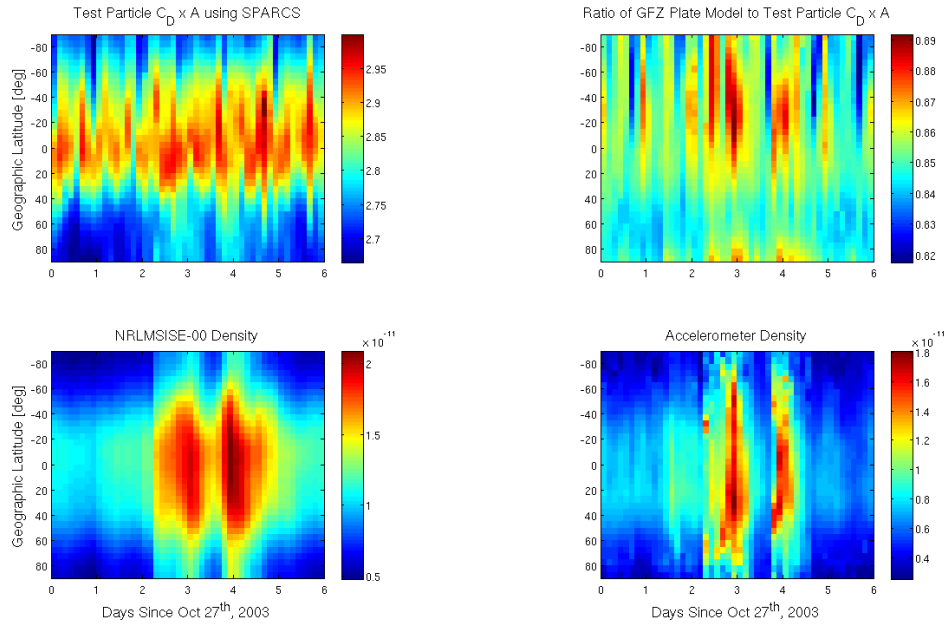


Figure 4.19: CHAMP drag force coefficient ($C_D \times A$) and ratio of GFZ to SPARCS force coefficients along with NRLMSISE-00 and accelerometer density response during daytime of the October 2003 Halloween storms.

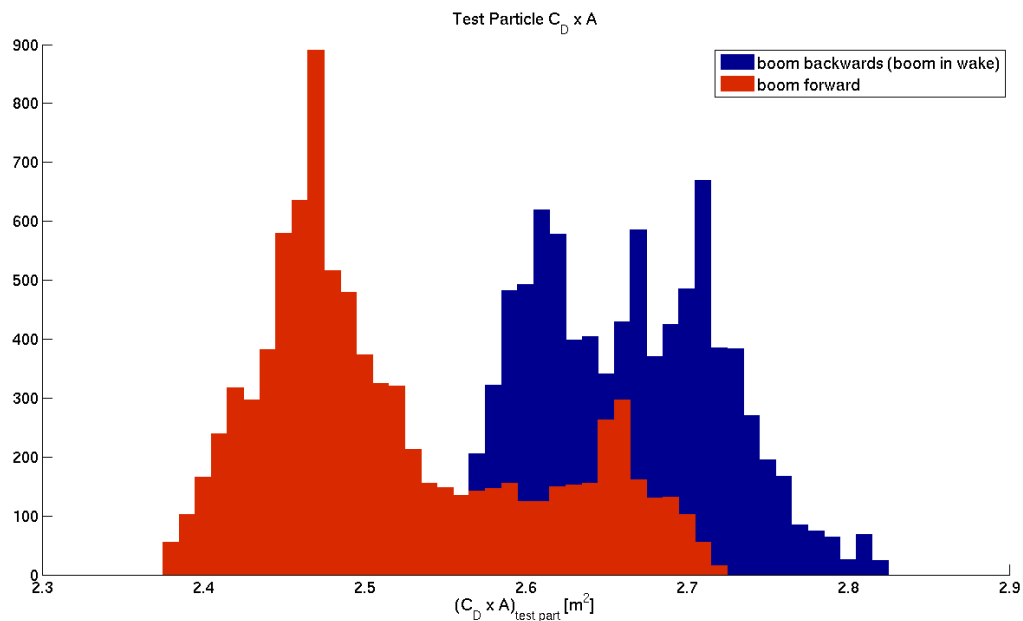


Figure 4.20: Drag force coefficients ($C_D \times A$) for the forward and aft flying modes of CHAMP during February 2010.

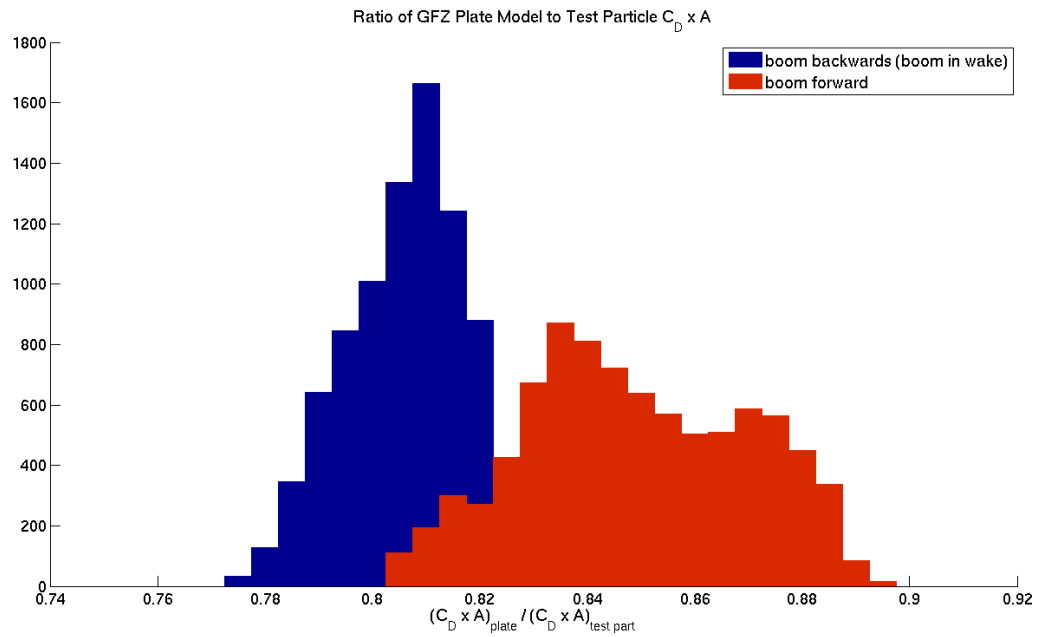


Figure 4.21: Ratio of drag force coefficients computed using the GFZ plate model and the CHAMP1v1 model for the forward and aft flying modes. Note that the two models show greater disagreement in the aft flying mode.

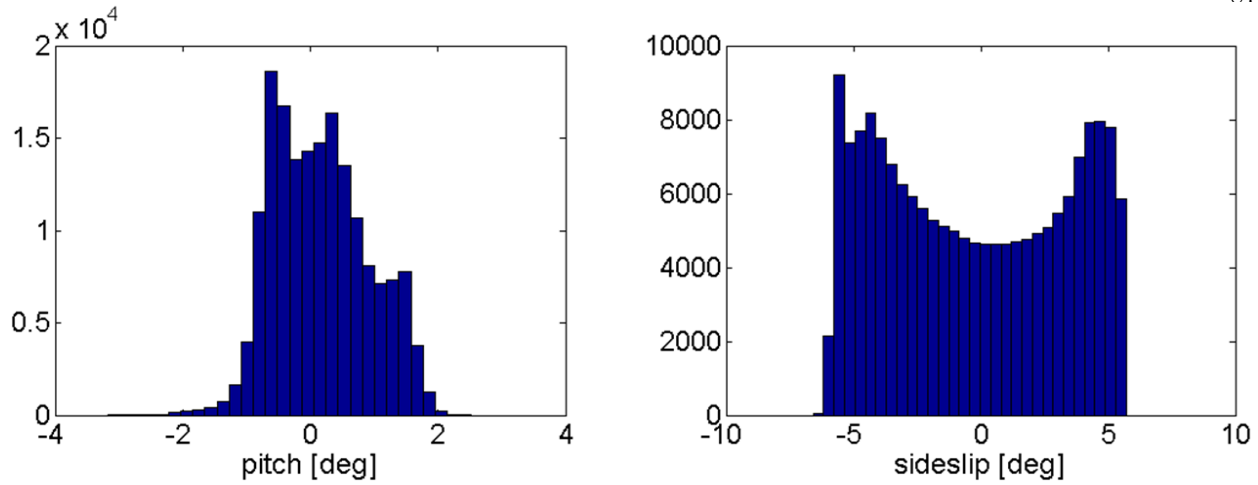


Figure 4.22: Pitch and sideslip angles estimated for the CHAMP spacecraft.

4.6 Force Coefficient Lookup Tables

In order to achieve sufficient (better than 0.5%) ensemble $1-\sigma$ uncertainty, the CHAMP satellite drag model must run for approximately 4-8 minutes on a dual processor 2-GHz workstation. The use of SPARCS in the analysis of accelerometer data or inside an orbit propagation routine would be quite time consuming as each day of data contains 8640 accelerometer measurements requiring 24-48 days of computation to process a single day of accelerometer data. A look-up table is constructed and interpolated based on a series of SPARCS analyses to achieve the increased accuracy of SPARCS while keeping computation time to below 0.1 seconds per force coefficient. Figure 4.22 shows the pitch and sideslip angles in the standard forward flying mode for the CHAMP satellite. These distributions will serve to bound the input parameters of our look-up table.

Values of $C_D \times A$ are compiled for six sideslip angles between -6 degrees and 0 degrees (force coefficients are symmetric about zero in the sideslip direction for the CHAMP geometries considered here) and eight angles between -3 degrees and +2 degrees pitch. More angles are selected near zero as the rate of change of force coefficient is higher near zero for the CHAMP satellite. The 48 point (6 by 8) data structure is a force coefficient map and is constructed for C_x , C_y and C_z in the CHAMP free-stream reference frame (see Figure 4.3). This map is made for eight values of $V_r \sqrt{m} / \sqrt{2k_B}$ as illustrated in Figure 4.23 and Figure 4.24. The

eight values are used to compute the coefficients of a 6th order polynomial as a function of $V\sqrt{(m)}/\sqrt{2k_B}$ for each sideslip and pitch angle in the map. The procedure is repeated for atmospheric temperatures of 100 K, 500 K, 1000 K, and 1750 K. The atmospheric temperature axis is interpolated using a cubic spline fit. The look-up table is validated by scanning the input parameter space simultaneously in temperature, orientation, and velocity for several masses. Tables were constructed for the the plate model as well as the test particle results to estimate errors due to interpolation alone (free of statistical scatter inherent in test particle computations). The result is that the interpolation errors are around 0.1% (in C_D as a percentage of the total C_D value) based on validation against the plate model. Extrapolation is also performed as there are a small number of CHAMP orientations just outside the look-up table boundaries. Extrapolation is performed by scaling the nearest test particle value to the plate model, then using the plate model and scaling factor to estimate the test particle value outside the map. The extrapolation of values more than 2 degrees outside the map will cause errors of more than 2% and will not be allowed. The extrapolation procedure is also performed in the accommodation coefficient parameter. All test particle values in the look-up tables were computed using the energy accommodation value of 0.93. Preliminary results indicate that the force coefficient may be reasonably estimated at any value of accommodation by scaling to the plate model. These results are shown in Figure 4.25 and indicate errors of less than 2% for accommodation extrapolation in a range of 0.60 and 1.00.

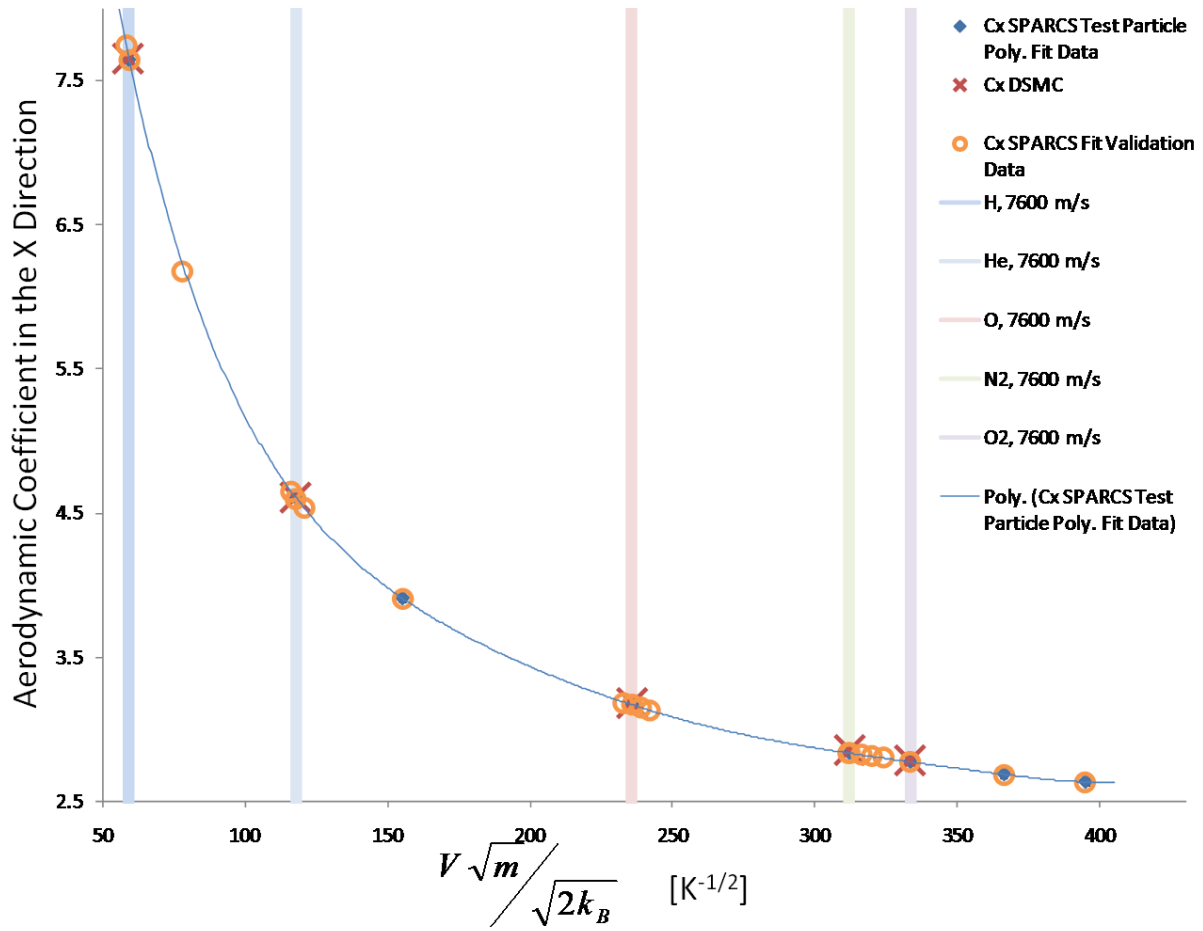


Figure 4.23: CHAMP C_X lookup table interpolation with validation values.

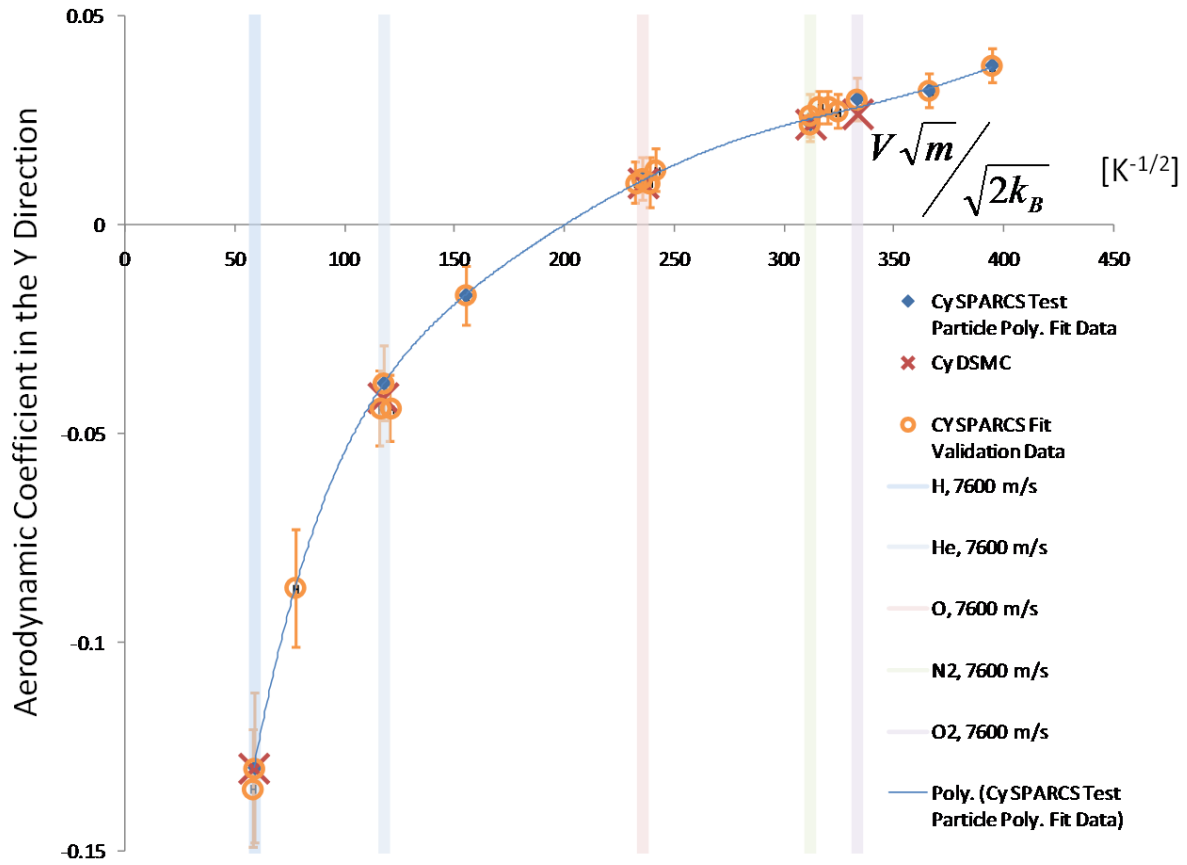


Figure 4.24: CHAMP C_Y lookup table interpolation with validation values.

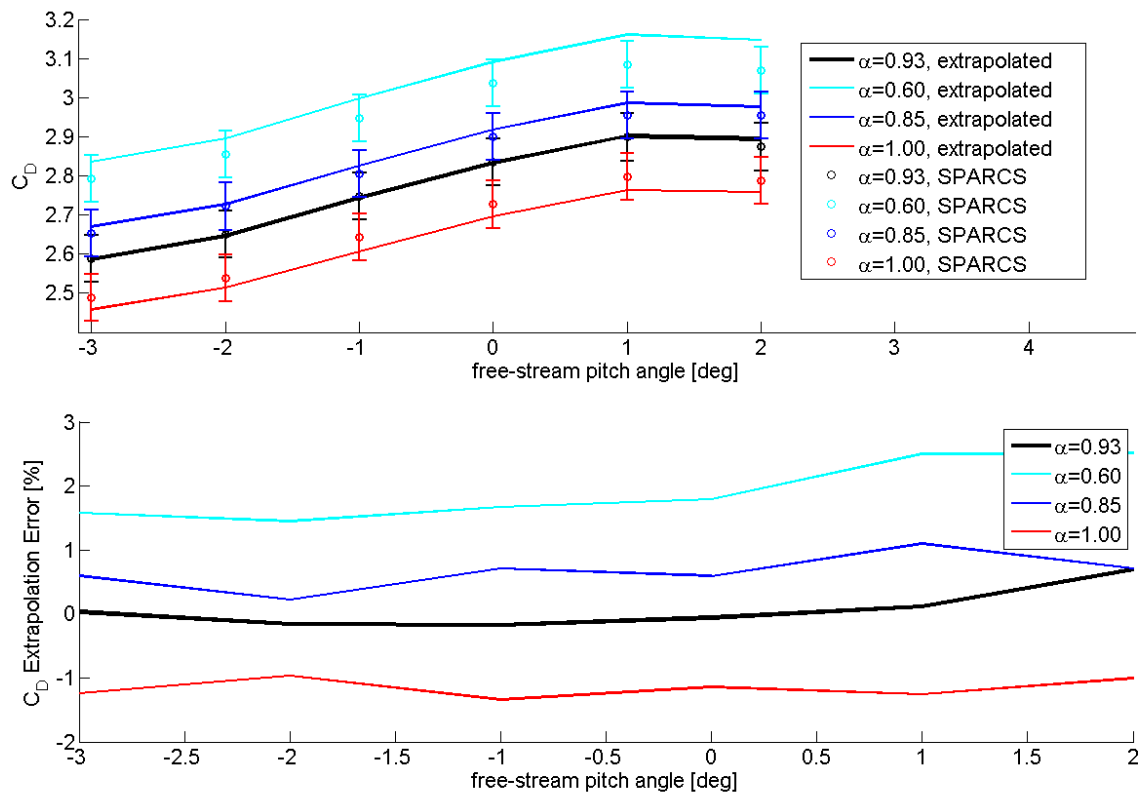


Figure 4.25: Extrapolating from the CHAMP lookup table in the accommodation parameter.

Chapter 5

Satellite Observations

A number of previous studies and experiments have been performed to identify the energy accommodation coefficient for satellites. These studies are summarized in Table 5.1. Note that density-independent (paddlewheel, lift/drag) and fitted drag coefficient analyses are included. The conditions under which the measurements or estimates were made vary widely and include free-molecular and transition flow as well as solar minimum and solar maximum conditions. Another variable is the orbital eccentricity which determines the free-stream kinetic energies. This research constitutes the first attempt made at combining all available measurements into a model of accommodation coefficients for satellite drag computation. This effort is also complimented by augmenting the amount of data available.

Since the proposed research includes the evaluation of scattering kernels, it will be necessary to base the evaluation on measurements of scattering made in LEO. Unfortunately, few studies exist which provide information as to the angular distribution of reflected molecules. They include Gregory and Peters shuttle experiment [Gregory and Peters, 1987] which constitutes the only direct measurement, Harrison and Swinerd's simultaneous evaluation of Starlette and Stella [Harrison and Swinerd, 1996], and Blanchard and Buck's study of lift-to-drag ratio of the space shuttle [Blanchard and Buck, 1985]. The three distributions found by these researchers to agree with observed data are a fully accommodated Nocilla model (350 km) approaching the cosine distribution, a partially accommodated Nocilla model (800-1000 km), and a classical Maxwellian with a small specular fraction (160 km) respectively.

Accommodation measurements will also be evaluated in the context of incident kinetic energy. Therefore, it becomes useful to know the experimental range of oxygen bond strengths with surfaces. Table 5.2 lists

Table 5.1: Energy accommodation measurements believed to be applicable to Earth orbiting satellites. Information is included where available.

Alt.*	e	α	Source Notes	Reference
200 km		0.99 ± 0.01	Long and compact satellite comparison	Moe et al. [1998]
290 km	0.76	0.65 ± 0.10	Explorer 6 paddlewheel	Moe [1966]
307 km	0.07	0.86 ± 0.04	Ariel 2 paddlewheel	Imbro et al. [1975]
300 km	0.06	0.97 ± 0.03	ANS1 lift/drag (average of two measurements)	Moore and Sowter [1991], Sehnal [1983]
169 km	0.22	0.99 ± 0.01	S3-1 lift/drag	Ching et al. [1977]
182 km	0.03	1.00 ± 0.00	Proton 2 paddlewheel	Beletsky [1970]
150 km	0.00	1.00 ± 0.00	Moe tabulated sphere meas. (solar min)	Moe and Bowman [2005]
200 km	0.00	0.99 ± 0.01	Moe tabulated sphere meas. (solar min)	Moe and Bowman [2005]
250 km	0.00	0.97 ± 0.03	Moe tabulated sphere meas. (solar min)	Moe and Bowman [2005]
300 km	0.00	0.93 ± 0.03	Moe tabulated sphere meas. (solar min)	Moe and Bowman [2005]
350 km	0.00	0.89 ± 0.03	Moe tabulated sphere meas. (solar min)	Moe and Bowman [2005]
150 km	0.00	1.00 ± 0.00	Moe tabulated sphere meas. (solar max)	Moe and Bowman [2005]
200 km	0.00	1.00 ± 0.00	Moe tabulated sphere meas. (solar max)	Moe and Bowman [2005]
250 km	0.00	0.99 ± 0.01	Moe tabulated sphere meas. (solar max)	Moe and Bowman [2005]
300 km	0.00	0.98 ± 0.02	Moe tabulated sphere meas. (solar max)	Moe and Bowman [2005]
350 km	0.00	0.97 ± 0.03	Moe tabulated sphere meas. (solar max)	Moe and Bowman [2005]
400 km	0.00	0.95 ± 0.03	Moe tabulated sphere meas. (solar max)	Moe and Bowman [2005]
450 km	0.00	0.93 ± 0.03	Moe tabulated sphere meas. (solar max)	Moe and Bowman [2005]
500 km	0.00	0.90 ± 0.03	Moe tabulated sphere meas. (solar max)	Moe and Bowman [2005]
200 km	0.01	1.00 ± 0.00	Fitted C_D , Cosmos (solar max)	Pardini et al. [2010]
275 km	0.07	0.99 ± 0.01	Fitted C_D , Cosmos (solar max)	Pardini et al. [2010]
300 km	0.00	0.99 ± 0.01	Fitted C_D , Calsphere/Cosmos (solar max)	Pardini et al. [2010]
400 km	0.00	0.96 ± 0.03	Fitted C_D , Calsphere/Cosmos (solar max)	Pardini et al. [2010]
480 km	0.00	0.95 ± 0.03	Fitted C_D , SNOE (solar max)	Pardini et al. [2010]
500 km	0.00	0.92 ± 0.03	Fitted C_D , Calsphere (solar max)	Pardini et al. [2010]
630 km	0.00	0.88 ± 0.03	Fitted C_D , Clementine (solar max)	Pardini et al. [2010]
160 km	0.00	1.00 ± 0.00	HIRAP Shuttle Reentry Data (STS-7 ^b)	Blanchard and Buck [1985]
800-1000 km	0.02	0.90 ± 0.10	Fitted C_D 's of Starlette/Stella (Nocilla reflection ^c),	Harrison and Swinerd [1996]

* Half scale height added for elliptical orbits (from King Hele [King-Hele, 1963a]).

^a measurements near 200 km altitude covering solar minimum to solar maximum

^b STS-6 lift/drag results deviate from a fully diffuse, fully accommodated model but Blanchard and Buck report that this was likely caused by an increase in atmospheric density which caused STS-6 to experience transition flow at a higher altitude than STS-7

^c Energy accommodation in table recomputed based on cosine reflection model

Table 5.2: Laboratory and theoretical results for the surface-binding energies for atomic oxygen. The average binding energy for these materials is 4.3 eV.

Surface	E_B [eV]	Reference
Si 100	3.4	Engstrom et al. [1991]
Al 111	7.6	Trost et al. [1998]
Kapton	1.5	Chen and Lee [2006]
Fe 110/100	1.5-3.4	Błoński et al. [2005, 2007]
Graphite	11.2	Lee and Chen [2000]
Au 111	2.2-3.7	Baker et al. [2009]

measurements of the heat of adsorption of atomic oxygen on various surfaces. The surfaces most applicable to spacecraft are Kapton, silicon (due to its presence in both glass and solar cells), aluminum, and iron. The average surface binding-energy for the materials in the table is around 4.3 eV. Note that this is close to the 4.8-5.2 eV value for average free-stream energy in a circular LEO orbit. For reference, the strength of the O₂ bond is approximately 5.2 eV.

5.1 Measurements of Multiple Interactions With the Atmosphere

The concept of a paddlewheel satellite as a propeller-shaped object sensing aerodynamic torques is one example of a more general idea. After all, using a measure of aerodynamic torques to solve for atmospheric density is completely analogous to measuring density via observations of drag forces acting on satellites. What makes absolute measurements unique is the measurement of two independent effects of the satellite-atmosphere interaction. This can be drag-torque and drag-force, drag-force and lift-force, or two measurements of drag made by satellites of distinct shapes (drag coefficients) flying very close together. Schematics of these techniques are illustrated in Figure 3.7 along with references for each type of measurement.

In the classic paddlewheel concept as described by Reiter and Moe [Reiter and Moe, 1968] the satellite is a major-axis spinner with the spin axis roughly aligned with the satellite velocity at perigee. This allows for a straightforward determination of drag torques because the drag-torque vector, due to the propeller geometry, is also aligned with the spin axis. Satellite drag is measured simultaneously through the observations of semi-major axis decay or satellite accelerometers.[King-Hele, 1963b, Doornbos et al., 2009] This example

is shown in the upper left corner of Figure 3.7. An alternative paddlewheel design is also shown in the lower portion of the left panel. In this configuration the torque and spin axes are aligned with the orbit normal. This means that the satellite “rolls along” its orbit and a torque is generated which is parallel to the spin axis due to the difference in force experienced by the front and back sides of the paddles. The orbit-normal orientation of the satellite spin axis enables the use of a rotating accelerometer system such as the one on the Drag and Atmospheric Neutral Density Explorer (DANDE) [Pilinski, 2009]. The accelerometers on DANDE are designed to achieve 30 ng precision which is equivalent to a 1%-2% precision in acceleration measurements at 350 km during average solar maximum conditions. This is sufficient for the purposes of the paddlewheel experiment though would require averaging multiple orbital periods during solar minimum.

There are two standard methods of determining atmospheric density from satellite drag. One technique involves the measurement of satellite forces through the use of sensitive accelerometers such as those found on the CHAMP and GRACE satellites.[Doornbos et al., 2009, Sutton, 2008] In this method the density is solved for from equation 2.1. Another other method is to determine density through observations of orbit perturbations measured via satellite tracking. Recent advances in this field include the Energy Dissipation Rate method which uses special perturbation orbit propagation to compute atmospheric drag [Storz, 1999, Bowman and Storz, 2003]. Emmert et al. [Emmert et al., 2004a] and Picone et al. [Picone et al., 2002a] also developed a method for accurately processing two-line element (TLE) data by numerically integrating the equation relating change in average mean-orbital motion and atmospheric density. This method has been used to study long term atmospheric density variations going back to the 1960s (for examples see Emmert et al.[Emmert et al., 2004a, Emmert, 2009]). An earlier more rudimentary way of density estimation is the observation of the rate of change of semi-major axis or, equivalently, the orbital period [King-Hele, 1963b] which analytically relates density to the observed orbit change. The Energy Dissipation Rate (special perturbations) and TLE methods result in more accurate drag predictions by including orbit perturbing effects such as Earth’s gravitational harmonics and atmospheric winds and because they do not require assumptions about the atmospheric scale height to be made.

The variability of the accommodation coefficients as measured by paddlewheel satellites with altitude, solar activity, and eccentricity is visible in Table 5.1. All values presented in Table 5.1 were arrived at under

the assumption of completely diffuse (cosine) reflection. The available paddlewheel measurements also span a range of solar activity as shown in Figure 5.1. In spite of the wide variation of conditions under which the measurements were made, several useful conclusions may be drawn. The first is that accommodation is nearly complete at very low altitudes (around 200 km and below). The second is that accommodation seems to decrease with increasing altitude and eccentricity. In addition to the paddlewheel measurements, Marcos computed the ratio of atmospheric densities observed by satellites to those of atmospheric models at an average altitude of 200 km [Marcos, 1985]. The data included compact shapes as well as long cylindrical satellites with a 9% difference in density ratios between the two sets. Moe et al. leveraged this information to show that the use of correct accommodation coefficients can reconcile the densities computed from both long and compact satellites [Moe et al., 1998]. The result was a value of the accommodation coefficient of 0.99.

The observation that the accommodation coefficient is close to unity at 200 km was used in constructing the base density for the US Standard Atmosphere (1976) [Moe, 1973, Minzner, 1977]. This work has served as the basis for other atmospheric models and the resulting drag coefficients have been used to analyze satellite drag in the 200 km region. Furthermore, the paddlewheel data presented in Table 5.1 combined with the discovery of atomic oxygen adsorption in pressure gauges led to the theory that atomic oxygen adsorbs to satellite surfaces and increases the accommodation coefficient [Moe and Moe, 1967]. This theory has been corroborated by Moe and Bowman [Moe and Bowman, 2005] through their analysis of drag on spherical satellites of various surface composition and surface treatments. The results show that composition and surface treatment do not result in significant drag coefficient differences indicating that the gas-surface interaction is instead dominated by the presence of adsorbate. This theory, along with the paddlewheel data, suggest that accommodation coefficients will decrease at higher altitudes and low solar activities due to a decrease in the level of atomic oxygen. Consequently, the accommodation coefficients presented in the analysis of spheres by Bowman and Moe have been arrived at by extrapolating the accommodation values at 200 km to higher altitudes at solar minimum and solar maximum [Bowman and Moe, 2005]. In their analysis, the ratio of atomic oxygen to molecular nitrogen was used as the extrapolation variable. It is important to note that this ratio is derived from measurements of scale height which are relatively insensitive to drag

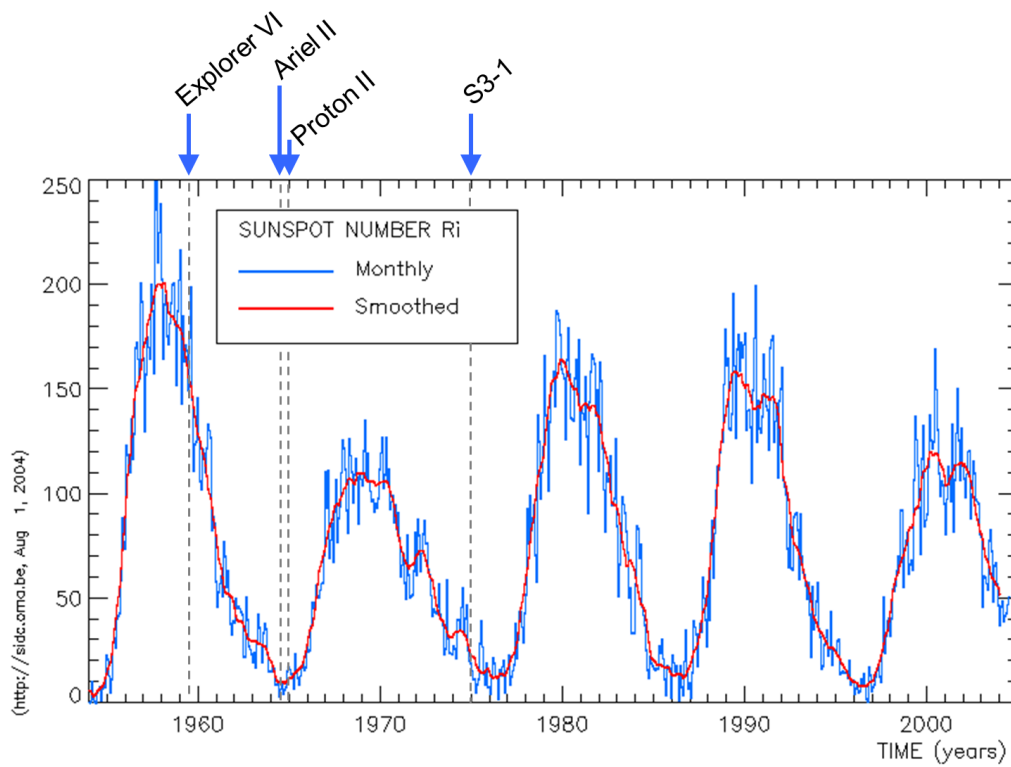


Figure 5.1: The analysis times of accommodation measurements overlaid on a plot of solar activity.

coefficient assumptions. Recently, Pilinski et al. [2010] have shown that the accommodation coefficient can be modeled using the static pressure of atomic oxygen as the input variable and an extrapolation based on Langmuir's adsorption isotherm.

Analysis of atmospheric model biases can be based (in part) on a comparison of fitted drag coefficients with physical drag coefficients computed using accommodation values based on paddlewheel data extrapolation.[Bowman and Moe, 2005, Pardini et al., 2010] In this way, the original paddlewheel measurements are critically linked to our knowledge of absolute densities above 200 km. This relationship has consequences for our understanding of upper atmospheric processes. One example of this is the study of the long-term secular decrease in thermospheric density caused by increased levels of carbon dioxide in the atmosphere. [Emmert, 2009]

The significant decrease of accommodation reported in the analysis of Explorer VI is attributed to the high eccentricity of its orbit and the associated increase in speed at perigee. At higher incident kinetic energies adsorption may be reduced because a significant fraction of impinging molecules impact the surface above the adsorption energy (the adsorption energy could be anywhere from 2 eV to 10 eV). This would lead to a lower accommodation coefficient. Such a reduction has been confirmed in laboratory measurements of accommodation coefficients on surfaces covered by adsorbate.[Doughty and Schaetzle, 1969, Masel, 1996] Currently, the paddlewheel dataset provides the only indication of this effect in Earth orbit. Accommodation dependence on kinetic energy has applications to aerobraking and drag analysis of satellites orbiting in highly eccentric orbits.

Even though the independent measurements of paddlewheel satellites afford great insight into gas-surface interactions in the spacecraft environment as well as atmospheric densities, their relative scarcity hinders significant further progress in these areas. For example, there are insufficient accommodation measurements at a range of both atomic oxygen concentrations and incident kinetic energies to build a general model of satellite accommodation coefficients. This gap in accommodation data has been filled by comparing drag coefficients fitted to calibrated atmospheric models with physical drag coefficient models such as equations 4.20a and 4.20b. However, as such fitted measurements are used at higher altitudes and during extreme minima or maxima in solar activity, they are in need of confirmation from an independent mea-

surement such as a paddlewheel satellite. Such a validation effort would improve the quality of atmospheric density models and enhance our understanding of gas-surface interactions in LEO. There already exists much evidence to suggest that the accommodation and drag coefficients respond to the concentration of atomic oxygen. However, there is no information available as to the temporal and spatial quality of this response, especially the characteristic time scale of adsorption and accommodation changes. Although theory suggests that the night-time and day-time accommodation coefficient of a satellite should be different at the same altitude due to a change in atomic oxygen pressure, no paddlewheel data exists to confirm this phenomenon. This situation is applicable to many satellites flying in circular orbits including CHAMP and GRACE which have been used extensively to study the spatial structure of the upper atmosphere via analysis of their accelerometer data. [S. Bruinsma et al., 2006, Sutton, 2008]

5.2 Fitted Ballistic Coefficients

Bruce Bowman (Air Force Space Command, Space Analysis Office) kindly provided the fitted drag coefficient based on HASDM analysis described in chapter 2 [Bowman and Storz, 2003]. Fitted drag coefficient values have been provided for 68 satellites as a function of altitude and time for objects in both circular and elliptical orbits. The fitted drag coefficients correspond to spherical satellites as well as tumbling-cylinders (rocket bodies). Altitudes range from 105 to 520 km and the data spans solar minimum and maximum conditions. The eccentricity range is approximately 0.0 to 0.8. The fitted drag coefficients are corrected by atmospheric bias values published by Bowman and Moe [Bowman and Moe, 2005].

5.2.1 Spheres

Accommodation coefficients for solar minimum and maximum are shown in Fig. 5.2 [Bowman and Moe, 2005, Pardini et al., 2010, Moe et al., 1995, Ching et al., 1977, Imbro et al., 1975, Beletsky, 1970]. The empirical values indicated by unbarred data points (Pardini et al. 2009, Moe and Bowman 2005, Moe et al. 1995) have been computed by comparing satellite drag measurements with adjusted atmospheric models to deduce observed drag coefficient values. The observed drag coefficients at several altitudes were then modeled physically to invert the appropriate accommodation coefficients reproduced in Fig. 5.2 [Pardini

et al., 2010]. Values obtained in this way will be referred to as fitted accommodation coefficients. It is important to understand that the fitted coefficients used in this analysis depend directly on the atmospheric model and indirectly on a priori assumptions about accommodation as a function of altitude. The reason for this dependence is that the biases in the density model are themselves estimated based on satellite drag observations [Bowman and Moe, 2005]. Model bias is estimated by comparing fitted drag coefficients with theoretical values that are based on existing knowledge of accommodation coefficients. Therefore, the resulting energy accommodation values are not absolute and independent but are instead relative to the atmospheric model and the a priori assumptions of accommodation altitude profiles. Other methods of accommodation measurement include paddlewheel satellites (black circles) which measured spin-decay and drag or drag and lift simultaneously. The horizontal bars in Fig. 5.2 indicate the reported uncertainty in the paddlewheel measurements. The uncertainty in the fitted accommodation results are estimated at approximately $\pm 3\%$. Two data points, one fitted and one measured via paddlewheel, are indicated in Fig. 5.2. These points are outliers which are located away from the concentration of data. The fitted outlier corresponds to the European Clementine satellite (not the interplanetary mission) which had a complicated shape with deployable solar panels [Pardini et al., 2010]. The paddlewheel outlier is the Ariel 2 satellite. The Ariel 2 measurement is 7% lower than the fitted drag coefficients at a similar altitude. The discrepancy could be due to measurement uncertainties or because Ariel 2 flew at the least active time during the solar cycle. It is also possible that the nature of gas-surface interactions changes as a function of incident molecule speed (kinetic energy). In this case fitted accommodation coefficients of objects in near circular orbits would be expected to differ from the Ariel 2 observation which corresponds to a 400 m/s increase in incident speed.

The drag study by Bowman and Moe [Bowman and Moe, 2005] analyzed a number of spherical objects during the 1989-1995 time frame covering both solar minimum and maximum. These spherical objects (listed in Table 5.3) were used by Bowman and Moe along with the High Accuracy Satellite Drag Model (HASDM) [Bowman and Storz, 2003] to infer the accommodation coefficients at several altitudes during both solar minimum and solar maximum. Their results are shown in Table 5.1. The satellites flying before 1990 correspond to solar maximum while those flying after 1990 correspond to solar minimum of solar cycle 22. Based on orbit altitude and the binary parameter of solar activity (sunspot maximum or minimum), the

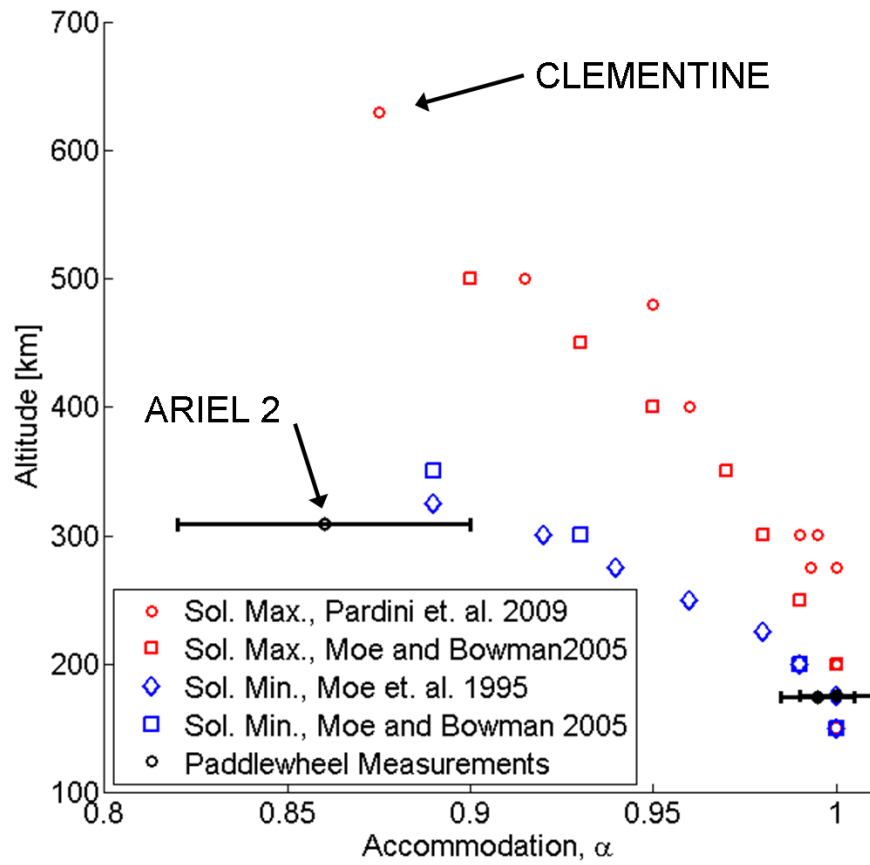


Figure 5.2: Estimated energy accommodation coefficients.

Table 5.3: Spherical tracking objects used to construct the accommodation coefficient model.

Type	Ref. No.	Obs. Yr.	Alt. Range	Inc.
Taifun-Yug	11796	1989	206-277 km	82.9
Taifun-Yug	13750	1989	232-377 km	65.8
Taifun-Yug	15446	1990	232-355 km	65.8
Calsphere	04958	1989	355-501 km	88.3
Taifun-Yug	21190	1995	205-302 km	65.8
ODERACS	22990	1994	230-327 km	56.9
ODERACS	22994	1994-95	208-326 km	56.9

accommodation coefficients for these objects can be determined from Table 5.1. These tabulated values are used in the work described here to test the preliminary dependence of accommodation on modeled atomic oxygen density.

5.2.2 Rocket Bodies

Fitted ballistic coefficients of additional objects were used to enhance the energy accommodation model and to test the theory that increased kinetic energies lead to a decrease in adsorption efficiency. Table 5.4 lists the rocket bodies (RB) and spheres (S) used for this work. Note that some of the objects in Table 5.4 are the same as those used for the initial test study (Table 5.3). The data spans several solar cycles from 1969 to early 2004.

Rocket body cross sectional areas have been computed by averaging the projected area of an exact geometry model over many orientations generated from a distribution which corresponds to random tumbling. The geometry model silhouettes can be seen in Figure 5.3 with a one meter marker shown for reference.

Figure 5.4 shows the distribution of perigee sampling for all objects in the dataset. Note that the data covers altitudes from 105 km to approximately 520 km. Latitude sampling is concentrated around the equator as well as 60° S due to the critical inclination of Molnia-class rocket bodies (SL-6 in Table 5.4). There is significant data at almost all local solar times with slightly more samples in the afternoon sector.

Figure 5.5 illustrates an example of fitted ballistic coefficients along with two models. The data is from observations of two SL-8 rocket bodies. Most of the periodicity is due to errors in the atmospheric

Table 5.4: Spheres and rocket bodies used in the determination of SESAM parameters.

Names	Type	NORAD Tracking Numbers	Dry Mass / Prop. Mass	Area	Surface
SL-3 (Vostok block-E 3rd-stage)	RB	04120,05143,05328,07418,07969,09854,10135,11056,11156,11269	820/2344 kg	7.83 m ²	Al, Paint
SL-8 (Kosmos 3M 2nd-stage)	RB	19332,20042	1435/18700 kg	10.8 m ²	Al, Paint
SL-6 (Molnia block-L 4th Stage)	RB	11556,12519,16125,19544,20258,20446,03223,14319,15955,15983,16686,16939	1160/5500 kg	8.33 m ²	Al Thermal-blanket
Ariane H10	RB	19332,20042	1500/10800 kg	23.8 m ²	Al
Ariane H10+	RB	23332	1630/11140 kg	24.2 m ²	Al
Ariane H10-III	RB	23782,23817,24847,25069,25154,25313,25895,26057,26625	1770/11863 kg	24.3 m ²	Al
PAM-D (Payload Assist Module)	RB	13136,17708,20304,20363,21932,22016,22659,24878,25032,26409	209.7/4431 kg	2.23 m ²	Ti
Taifun-Yug	S	11796,13750,15446,21190	750/na kg	3.14 m ²	Al
Calsphere	S	04957,04958,04963	0.73/na kg	0.0507 m ²	2 Al, 1 Au
4-in ODERACS	S	22990,22991,23472	1.482/na kg	0.0081 m ²	1 CrO ₃ , 1 Al, 1 Paint
6-in ODERACS	S	22994,22995,23471	5.0/na kg	0.0182 m ²	1 CrO ₃ , 1 Al, 1 CrO ₂
Starshine I	S	25769	39.46/na kg	0.193 m ²	Al, SiO ₂
Starshine II	S	26996	38.56/na kg	0.193 m ²	Al, SiO ₂
Starshine III	S	26929	90.04/na kg	0.701 m ²	CrO ₂ , SiO ₂
Sputnik 40	S	24958	2.270/na kg	0.0305 m ²	Al
Sputnik 41	S	25533	2.330/na kg	0.0305 m ²	Al
Sputnik 99	S	25685	4.830/na kg	0.0305 m ²	Al

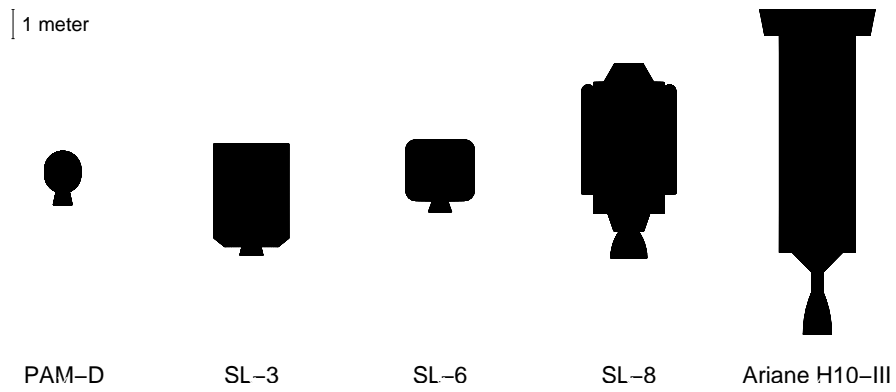


Figure 5.3: Silhouettes of rocket bodies in the fitted-ballistic dataset.

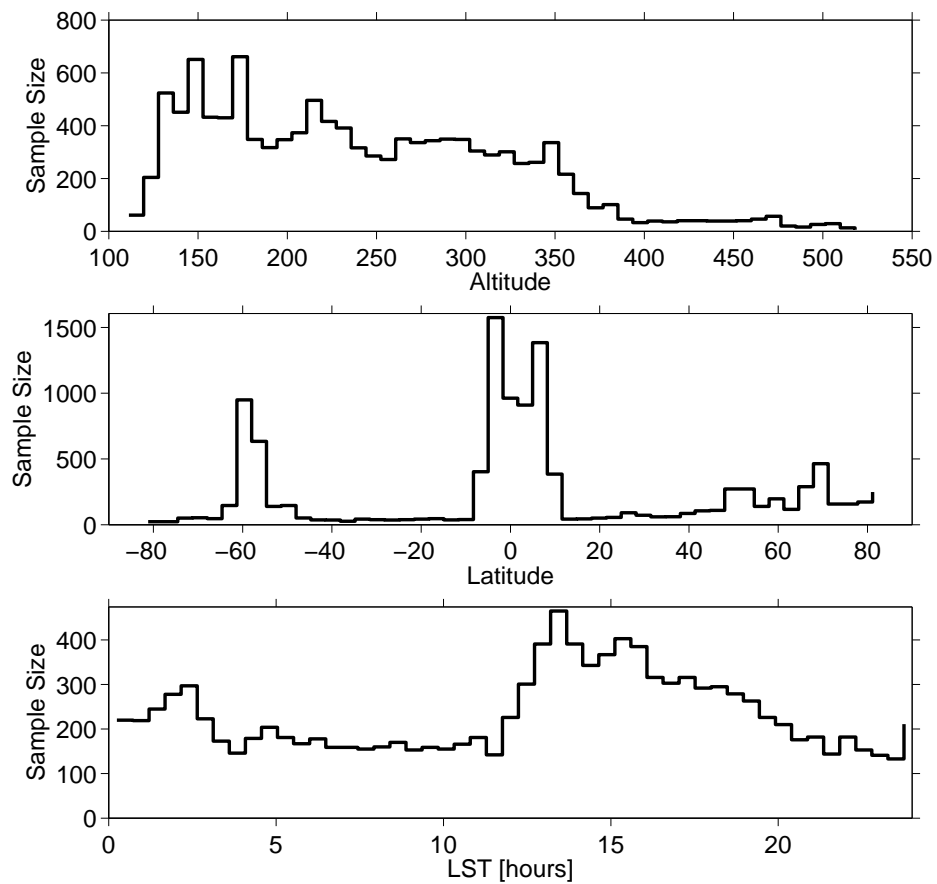


Figure 5.4: Sample size organized by latitude, altitude, and local solar time (LST) bins.

model used to generate the fitted ballistic coefficients. Two sources of atmospheric model error include the misrepresentation of the semiannual variation as a function of solar activity and the modeling of thermospheric heating from solar ultraviolet radiation [Bowman and Tobiska, 2006]. Because the semi-annual variation is a temporal phenomenon and the altitude of the satellites is decreasing with time, the periodic component appears to be a function of altitude. Two ballistic coefficient models are also shown in Figure 5.5. The first is SESAM which is described later in the dissertation. The second is a ballistic coefficient model which assumes that the average of the fitted ballistic coefficient at the onset of the dataset is the “true” ballistic coefficient [Bowman, 2002]. This averaging is a standard method of determining reference ballistic coefficients for density computations [Bowman, 2002, Picone et al., 2002a]. Notice that both the data and SESAM models deviate from the “true” value. As we will see later, this deviation in ballistic coefficient is a result of a decrease in drag coefficient caused partly by an increase in accommodation and partly by the shielding effect of reflected molecules in the transition regime.

5.3 Remote Sensing Observations of Atmospheric Density

The GUVI instrument is part of the TIMED mission and was launched into a 74.1° inclination, 625 km circular orbit in December of 2001. The objectives of the TIMED mission are to characterize the density, temperature, and winds between 60 and 180 km. A technical description of the instrument design was given by Paxton et al [Paxton, 2004]. GUVI was built by John Hopkins University Applied Physics Lab and the Aerospace Corporation. The instrument is designed to take spectra of the far ultraviolet dayglow which, while limb scanning, provides signatures of major thermospheric species O, N₂, and O₂. Table 5.5 describes the environmental parameters and spectral bands measured by GUVI in the dayside limb which are of interest to this study. The LBHS and LBHL regions refer to two regions of the Lyman-Birge-Hopfield band of molecular nitrogen. These bands are excited by photoelectron ionization or ionization via precipitating solar particles. Photoelectrons are formed in the upper atmosphere when atmospheric gases are ionized by solar radiation with wavelengths less than 40 nm. While emission in the oxygen doublet and LBH bands corresponds to concentrations of the emitters, O and N₂, molecular oxygen is inferred through the molecular absorption of this radiation as described by Beer’s law. Beer’s law states that the FUV radiation will be

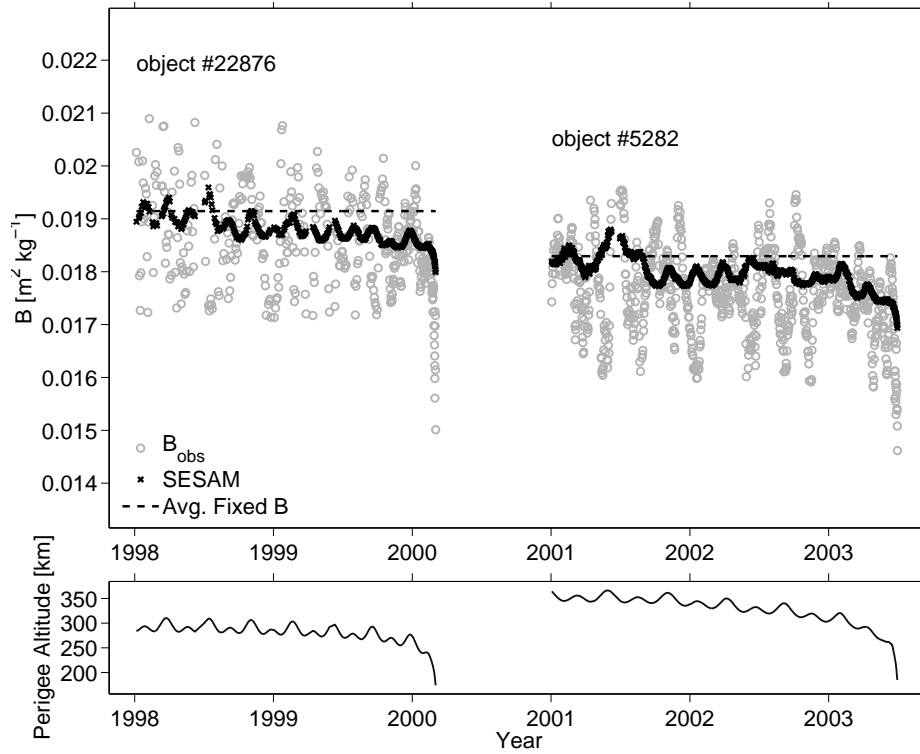


Figure 5.5: SL-6 (Molniya) observed C_D in the transition and free-molecular flow regimes.

Table 5.5: Description of relevant physical parameters measured by GUVI in the dayside limb.

Spectral Band	Passband	Parameter
LBHS	141.0-152.8 nm	Amount of O_2 as seen in absorption
LBHL	167.2-181.2 nm	N_2 concentration, Temperature
OI(135.6)	134.3-137.7 nm	O altitude profile
OI(130.4)	128.3-131.8 nm	O_2 absorption

attenuated as $\exp(-\beta_a x)$ where β_a is dependent on the integrated column density of O_2 between the source and the GUVI instrument and x is the distance to the source. Figure 5.6 provides a schematic overview of FUV dayglow phenomena.

The GUVI instrument uses a rotating mirror to scan in the cross-track direction (perpendicular to spacecraft motion) producing a 100 km by 100 km footprint with every step of the mirror. This 100 km is distributed across 14 spatial pixels at each of the 191 steps. Of these 191 cross-track locations, 32 are reserved for the limb over approximately 13° of the scan. At the limb, the combined data product is 32 cross track locations with 14 along-track pixels each, each with 160 spectral bins. Due to downlink limitations these spectral bins are compressed to just five “colors”, four of which are described in Table 5.5. The tangent altitudes of the 32 limb scans range from 110 to 520 km. The spectra are produced simultaneously for each of the 14 along-track pixels using a Rowland circle spectrograph (grating type) and a microchannel plate is placed before the detector as a means of signal amplification. The instrument is calibrated on orbit by scanning the mirror to observe the full (160 spectral bins) spectra of certain references stars.

The raw data is processed on the ground by first converting radiance observations into Rayleighs (level 1). The level 2 data include geolocated products such as densities and temperatures as well as their uncertainties collocated to the geographic location and available online (<http://guvi.jhuapl.edu/levels/level2b/limb2/>). The instrument produces approximately 390 limb scans per orbit covering a full range of latitudes and providing ample opportunity for coincidences with the CHAMP spacecraft as well as overlap with low perigee rocket-body observations.

The inversion used to determine the concentrations of O, N_2 , and O_2 from dayglow is of the maximum likelihood type using NRLMSIS-00 as the forward model for concentration. The first step is the prediction of

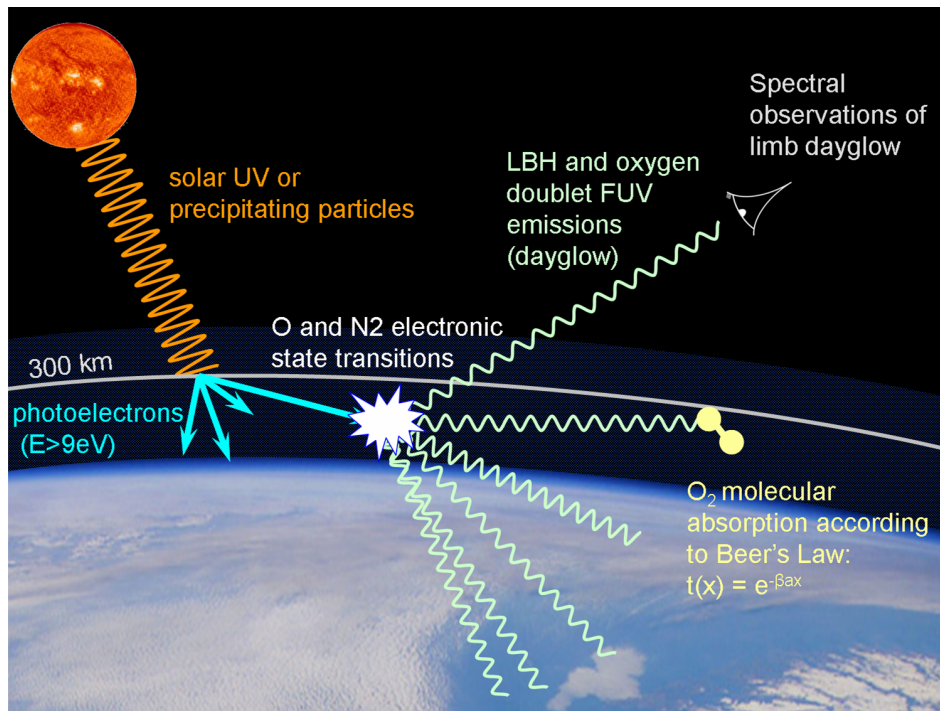


Figure 5.6: The radiative transfer phenomena associated with FUV dayglow observation.

intensities of certain FUV bands using the forward model. These are then compared to measured intensities. Model parameters are then adjusted in order to bring the modeled and observed intensities into agreement while producing the solution for concentration values. Because of the use of NRLMSISE profiles, the process also results in the inversion of the atmospheric temperature. The LBH and OI (atomic oxygen doublet) bands are excited by photoelectrons in the atmosphere and exhibit dayglow emissions. These bands were chosen because they have different sensitivities to N_2 and O concentrations while being simultaneously affected by O_2 molecular absorption. Furthermore, these emissions are simple processes except at high solar zenith angles where multiple scattering and self absorption of the dayglow photoelectrons may become significant. Accordingly, the GUVI limb inversions are limited to a solar zenith angle of less than 80° which causes periodic temporal gaps in the density data. A g-factor which describes the excitation rate (per second per molecule) is also simulated in the forward model as an altitude profile calculated based on the integrated column concentration of O, N_2 , and O_2 between the inversion location and the sun. This and other details about the inversion process are described by Meier Meier and Picone [1994]. The g-factor is multiplied by the modeled molecular concentration and integrated along the line of sight to the instrument to predict the total emission. Tangent altitudes above 300 km are not used in the inversion because the g-factor model (chosen for efficiency) does not apply above this altitude. However, due to the use of the NRLMSISE-00 model in the density forward model, densities are extrapolated to higher altitudes. The NRLMSISE model is scaled using four linear parameters. Parameter f_{N_2} , f_{O_2} , and f_O independently scale the number densities inside NRLMSISE while f_{10} scales the 10.7 cm wavelength flux input. The resulting number density for species x based on GUVI observations is computed as shown in equation 5.1.

$$n_x^{GUVI} = f_x \times n_x^{MSIS} (f_{10} \times F_{10.7P}, f_{10} \times F_{10.7A}) \quad (5.1)$$

F10.7P and F10.7A indicate the measured values of the 10.7 cm solar radio flux on the previous day and the 81-day average respectively. A distinct feature of this method is that the solutions for concentrations do not depend on absolute instrument calibration because the important information is contained in the shape of the altitude profile of emission rates. At CHAMP altitudes the inversion is estimated to be accurate within approximately $\pm 5\%$ depending on errors in the forward model but irrespective of the solar conditions. The

inversion 1- σ precision can vary from $\pm 5\%$ during solar maximum to $\pm 20\%$ during solar minimum.

Errors in density profile measurements include assumptions about spherical geometry, neutral density profiles, and collision cross sections assumed in the retrieval. The assumption that each snapshot of the limb can be ascribed to a single altitude can also be a source of error. In reality, each along-track pixel views a portion of the curved limb at slightly different altitudes. Validation of the GUVI instrument inversions and the closely related Special Sensor Ultraviolet Scanning Imager (SSUSI) have not been performed due to the lack of direct composition measurements [Paxton, 2002]. However, because O, N₂, and O₂ comprise the majority of the atmosphere below 400 km, it is possible to sum their mass contribution and compare the product with total mass density derived from satellite drag. Emmert et al. [2006] compared GUVI with global densities derived from a large set of orbiting bodies with perigees at altitudes ranging from 200 km to 600 km. The same study also compared GUVI densities with the NRLMSISE model. The comparison of GUVI and NRLMSISE densities found a bias in the GUVI values of around -5% in the region of interest (350-450 km) and a standard deviation of $\pm 10 - 17\%$. Altitude dependence of the bias in the drag result was stronger than that in the GUVI measurements.

The limb scan concentrations are converted to mass density by multiplying the number density of each measured constituent by its mass. However, since GUVI concentrations do not include minor species such as N, He and H, the mass density of these was modeled using NRLMSISE and the GUVI measurements augmented by that amount. The process is described in Equations 5.2 and 5.3. The mass density of the modeled minor constituents did not exceed 5% of the total mass density over the course of the analysis.

$$\Delta\rho^{minor} = \frac{n_{He}^{MSIS}m_{He} + n_H^{MSIS}m_H + n_N^{MSIS}m_N}{\rho_{total}^{MSIS}} \quad (5.2)$$

$$\rho^{GUVI} = (n_O^{GUVI}m_O + n_{N_2}^{GUVI}m_{N_2} + n_{O_2}^{GUVI}m_{O_2}) \times (1 + \Delta\rho^{minor}) \quad (5.3)$$

5.4 Accelerometer Data: Multi-Axial Acceleration Measurements

Accelerometer data available from three satellites. The CHAMP satellite has covered altitudes of 250 km to 500 km from July 2000 until its re-entry in September of 2010. The two GRACE satellites (referred to as GRACE-A and GRACE-B) have been aloft from March 2002 until the present and cover

altitudes of 530 to 450 km. The two GRACE satellites fly within approximately 200 km of each other. In this analysis, accelerometer data processed by Sutton [2008] will be used. Sutton performed a significant amount of analysis including attitude data processing and the removal of radiation pressure accelerations from the accelerometer data. One modification of Sutton's data set is the replacement of the force coefficients computed using the Luhr et al. model with the new SPARCS geometry model for CHAMP which takes into account geometry shadowing (see Table 4.2). To aid in the re-processing of density and force data, the CHAMP lookup tables will be used as discussed in Chapter 4. Additional lookup tables must be generated for accommodation coefficients other than 0.93 so that the 2% C_D extrapolation error can be reduced. The accelerometer data sets include coordinate rotation matrices which allow for the transformation of satellite and atmospheric velocity in the earth-fixed reference frames into the local body frame.

$$V_{r,SBF} = V_{r,TRS} [A_{TRS}^{CRS}]' [A_{SBF}^{CRS}] \quad (5.4)$$

Equation 5.4 is the coordinate transformation where $V_{r,SBF}$ is V_r expressed in the satellite body fixed frame (SBF), $V_{r,TRS}$ is the velocity in the terrestrial reference system (TRS), $[A_{TRS}^{CRS}]'$ is the transpose of the transformation matrix from TRS to the celestial reference system (CRS), and $[A_{SBF}^{CRS}]$ is the transformation from CRS to SBF. In the dataset developed by Sutton [Sutton, 2008], V_{TRS} , $[A_{TRS}^{CRS}]$ and $[A_{SBF}^{CRS}]$ are provided at 10 second intervals along with accelerometer measurements. Once the relative velocity V_r is transformed into the local frame (SBF), pitch and sideslip angles can be computed as shown in Figure 4.3 after an additional transformation from the SBF to the free-stream (CAD) frame. The dataset also provides access to tabulated values of solar and albedo radiation pressures as well as accelerometer scale factor and bias values.

The CHAMP satellite was launched into an 87.3° inclination 440 km, near-circular orbit in 2000. CHAMP carries precise accelerometers which have been used ([Sutton, 2007, Doornbos et al., 2009]) to determine thermospheric mass densities and winds with unprecedented temporal and geographic coverage. The accelerometer operates by adjusting electrostatic forces to balance a proof-mass inside of a containment cage. Because the satellite is exposed to body forces (such as drag) and the proof mass is not, their orbits diverge necessitating constant adjustments. The resulting acceleration precision is around $3 \times 10^{-9} \text{ms}^{-2}$ at 1

Hz [Sutton, 2008, Doornbos, 2011]. The CHAMP satellite accelerometer data is down-sampled to once every 10 seconds in order to reduce peaks caused by spacecraft maneuvers. Accelerometer bias and scale factors are calibrated periodically by precise orbit-determination using GPS measurements of acceleration [Helleputte et al., 2009].

In order to determine atmospheric density and winds from drag, accelerometer scale factor and bias are estimated to obtain calibrated acceleration values in the in-track and cross-track directions. Non-aerodynamic forces are then modeled and subtracted. Solar radiation pressure is the major non-aerodynamic force considered. Next, spacecraft attitude data is combined with precise orbit positioning to estimate the velocity of the atmosphere with respect to the spacecraft. The two sources of relative velocity considered are spacecraft motion and the corotation of the atmosphere. The relative velocity information is used to determine the projected cross-sectional area and drag coefficient. Estimates of atmospheric composition and temperature necessary for the drag coefficient computation are produced using NRLMSISE model with measured inputs of solar 10.7 cm radiation and the geomagnetic A_p index. Details of the drag coefficient computation will be discussed later. Acceleration, cross sectional area, and drag coefficient information are entered in equation 2.1 which is solved for density. CHAMP density data derived by Sutton et al. [Sutton, 2007] is available online at (<http://sisko.colorado.edu/sutton/data.html>).

Chapter 6

Review of Analysis Methods

So far, we have discussed the accommodation coefficient as a single quantity to be applied to the entire satellite geometry. This is the assumption inherent in Equations (4.4) and (4.20a) which develop the drag coefficient of a sphere as a function of α . It is likely that due to variations in flow shadowing and angle of attack, the value of α changes over the surface of a satellite. For example, consider a flat plate facing into the free-stream velocity together with one which is oriented parallel to the free-stream flying in the upper atmosphere. The flux onto the two surfaces will depend on the temperature of the atmosphere, the angle of attack, and the magnitude of the velocity. Under an expected range of satellite conditions ($7,000 \text{ m/s} < V_r < 10,000 \text{ m/s}$ and $500 \text{ K} < T_a < 1,500 \text{ K}$), the surface facing into the flow will experience a higher flux of atomic oxygen as well as a higher rate of adsorption, and would therefore have a higher accommodation coefficient according to the assumptions stated thus far. The surface oriented parallel to the flow would have a lower flux of atomic oxygen and lower energy accommodation than that facing into the flow. However, because the drag coefficient of a plate at low angle of attack is lower than that of a plate flying normal to the flow, the averaged or effective drag coefficient would be closer to that of the surface elements facing into the flow. The result is that the effective accommodation coefficient is dominated by the accommodation coefficients of the surface elements with the highest contributions to drag. This weighted averaging is also applied over the various species of the atmosphere and incident kinetic energies. Orbital measurements of α are therefore a result of a weighted average of the accommodation coefficients for each species and energy in the atmosphere. Equation (6.1) formally expresses the idea of this effective parameter as the integration of surface-element drag coefficients over the surface of a satellite geometry.

$$\frac{\int C_D(\alpha, \vec{r}) dA}{A} = \frac{\sum_{j=1}^N (\int \int C_D(\alpha_{s,j}(\vec{r}, E), E, \vec{r}) dA dE) n_j m_j}{A \sum_{j=1}^N n_j m_j \int dE} \quad (6.1)$$

Here, \vec{r} refers to the position of each surface element with respect to the flow, and n_j and m_j are the atmospheric species number densities and masses respectively. The inner integral on the right side is performed over the surface of the satellite and the outer integral over the applicable range of energies for species j . Furthermore, different surface materials display different adsorption kinetics. For example silver can take up atomic oxygen beyond monolayer coverage while glass seems to adsorb only a small fraction of a monolayer and the various surface materials have different rates of adsorption [Wood, 1971, Riley and Giese, 1970]. While the effective parameter α is a global constant for any particular geometry, $\alpha_{s,j}$ is a surface, energy, and species dependent property and would coincide closely with laboratory measurements if they could reproduce the adsorption environment in Earth's thermosphere. The effective parameter α corresponds to a constant value measured in orbit for a particular satellite and for specific flow conditions. From here we will refer to the effective accommodation as simply accommodation or α and will take this to signify a parameter which is constant over the surface of the satellite.

6.1 Using Fitted Ballistic Coefficients for Gas-Surface Interaction Evaluation

Fitted drag coefficients are produced when drag observations are combined with modeled atmospheric density to solve for a satellite's ballistic coefficient. In order to use empirical atmospheric models such as Jacchia 70 or NRLMSISE-00 [Jacchia, 1981, Picone et al., 2002b] the altitude biases must first be removed. Bowman and Moe as well as Pardini et al. [Bowman and Moe, 2005, Pardini et al., 2010] tabulated values of known altitude biases and these values are reproduced in Table 6.1. These biases ($c(h)$) indicate how much the model is overestimating the density or the percentage by which the fitted drag coefficient is underestimated. Another adjustment involves a correction to any periodic errors in the fitted drag coefficient time series by applying a low-pass filter. Such periodic errors are the result of density model deficiencies in local-solar time dependence of the atmosphere (true for Jacchia models) and representation of the semi-annual variation. Once the fitted C_D is corrected it may be compared to the physical equations for drag. The corrected C_D values will be referred to as observed drag coefficients $C_{D,obs}$.

Table 6.1: Jacchia 70 density corrections as determined by Bowman and Moe [Bowman and Moe, 2005] and used to adjust the measured drag coefficients.

Altitude [km]	200	250	300-350	400-500
Correction [%]	7	9	11	12

$$C_{D,fit} = \frac{2a_{obs}m_{sc}}{\rho_{mod}AV_r^2} \quad (6.2a)$$

$$C_{D,obs} = C_{D,fit}c(h) \quad (6.2b)$$

Next, a model of C_D is constructed as a function of accommodation coefficient and the observed C_D values are inverted with the use of this model to yield accommodation coefficient estimates. The accommodation coefficient was defined in Equation 4.2 and related to the drag coefficient in Equations 4.3 through 4.4 and 4.20a through 4.20b.

In order to obtain accommodation coefficients from fitted ballistic coefficients the data must first be multiplied by the assumed mass and divided by the cross sectional area estimate (see Table 5.4) to produce observed drag coefficients $C_{D,obs}$. For spheres, a priori information regarding area and mass is available. For rocket bodies, a consistent procedure must be implemented to determine the mass. Liquid-fuel rocket boosters are highly optimized structures which can contain upwards of 80% propellant by mass [Isakowitz et al., 1999]. A fuel margin (left over propellant at burnout) of 10% in this case would mean a 29% increase in post burnout mass from the published dry mass. In order to estimate the true object mass, we will compare the estimated GSI parameters for a rocket body with those of a sphere flying through similar conditions (atomic oxygen concentration and incident kinetic energy). We will return to the determination of mass later.

Before analyzing the fitted ballistic coefficient data, a number of auxiliary data products corresponding to each B_{obs} data-point must be generated. We begin by propagating each orbit using the general perturbations orbit model SGP4 [Vallado et al., 2006]. The orbit propagation was based on evolving orbital elements of each rocket body and sphere in Table 5.4 which were downloaded from CelesTrak

(<http://www.celestrak.com/>) in the NORAD two-line element format. Next, the NRLMSISE-00 model is evaluated along the reference orbit to estimate parameters such as total atmospheric density and temperature. Effective properties corresponding to perigee measurements of B_{obs} are now obtained by computing the weighted average of property Y at measurement epoch t_i and observation time span of Δt . The computation of effective properties is described in equation 6.3 where the observation time span, Δt , is generally taken to be 1.5 days for consistency with the generation of fitted ballistic coefficients [Storz et al., 2005].

$$\langle Y(t_i) \rangle_{\Delta t} = \frac{\int_{t_i - \Delta t}^{t_i} Y(t) \rho_M(t) C_{D,est}(t) V_{sc}(t)^3 F(t) dt}{\int_{t_i - \Delta t}^{t_i} \rho_M(t) C_{D,est}(t) V_{sc}(t)^3 F(t) dt} \quad (6.3)$$

Note that in the equation above, $\langle Y(t_i) \rangle_{\Delta t}$ is the effective property associated with measurement i , ρ_M is the total mass density computed by NRLMSISE-00, V_{sc} is the spacecraft velocity magnitude computed by SGP4, $C_{D,est}$ is the drag coefficient from equation 4.20a assuming $\alpha = 1.00$, and F is the wind factor [Picone et al., 2002a] defined as

$$F = \frac{\|\vec{V}_{sc} - \vec{V}_w\|^2}{V_{sc}^3} [\hat{v}_r \cdot \vec{V}_{sc}] \quad (6.4)$$

which accounts for the fact that a deviation in the relative wind direction from the spacecraft direction of flight causes a reduction in drag. The wind vector, \vec{V}_w , is computed based on a co-rotating atmosphere model in the following way

$$\vec{V}_w = \omega_e \hat{k} \times \vec{R}_{eq} \quad (6.5a)$$

$$\vec{R}_{eq} = R_x \hat{i} + R_y \hat{j} \quad (6.5b)$$

where \hat{i} , \hat{j} , \hat{k} , are unit vectors corresponding to the three basis vectors of the earth-centered earth-fixed coordinate frame, R_x and R_y are the x and y components of satellite position (computed with SGP4), and ω_e is the average rotation rate of the earth ($\omega_e = 7.2921151467064 \times 10^{-5}$ rad/s) [Tapley et al., 2004]. Note that the weighting factor inside the integrals of equation 6.3 can be thought of as the work done by aerodynamic drag along the satellite orbit. This is because the integral of $\rho_M(t) C_{D,est}(t) V_{sc}(t)^3 F(t) dt$ is

equivalent to the integral of $\rho_M(t)C_{D,est}(t)V_{sc}(t)^2F(t)dl$ where $dl = V_{sc}(t)dt$ is a differential arc length along the orbit. This formulation is equivalent to that used by Picone et al. [Picone et al., 2002a] to deduce effective atmospheric densities from NORAD two-line elements except that here we do not remove the drag coefficient from inside the integral. The drag coefficient remains in equation 6.3 due to the high apogee altitudes experienced by some of the reference objects in our dataset. Accordingly, some satellites move regularly between an oxygen rich atmosphere and one which is dominated by lighter species such as helium and hydrogen within a single orbit causing the drag coefficient to change drastically.

There are three effective properties which lie at the heart of parameterizing the accommodation model. The first is the estimated atomic oxygen pressure or (P_O in equation 6.7) which is computed along the orbit based on outputs of the NRLMSISE-00 atmospheric model.

The parameter describing atomic oxygen pressure is computed by multiplying the partial acceleration equation (equation 2.6) by spacecraft mass and dividing by cross-sectional area. The resulting force-per-area equation is

$$P_O = F_O/A = \frac{1}{2}\rho_O C_{Din,O} V_r^2 \quad (6.6)$$

where ρ_O is the mass density of atomic oxygen and $C_{Din,O}$ is the drag coefficient for incoming molecules only. The equation for $C_{Din,O}$ is taken to be the equation for the drag coefficient of a sphere with the reflection temperature set to zero. In other words, the term $\frac{2\sqrt{\pi}}{3s} \sqrt{T_{k,out}/T_a}$ in equation 4.20a is set to zero and the result is substituted into equation 6.6 and results in equation 6.7.

$$P_o = \frac{1}{2}\rho_O V_r^2 \left(\frac{2s^2 + 1}{\sqrt{\pi}s^3} \exp(-s^2) + \frac{4s^4 + 4s^2 + 1}{2s^4} \text{erf}(s) \right) \quad (6.7)$$

In the equation above, ρ_O is taken to be the number density n_O as reported by NRLMSISE-00 multiplied by m_O which is equal to 2.656×10^{-26} kg. Note that at high values of the speed ratio, $s \gg 1$, the result scales as the dynamic pressure $P_o \approx \rho_O V_r^2$. Alternatively, when neglecting velocity variability while keeping the speed ratio moderately high, the second term in the parentheses of equation 6.7 captures most of the variability. In this case this variability in the pressure parameter scales as $P_O \approx \text{constant} + 2/s^2$ or applying

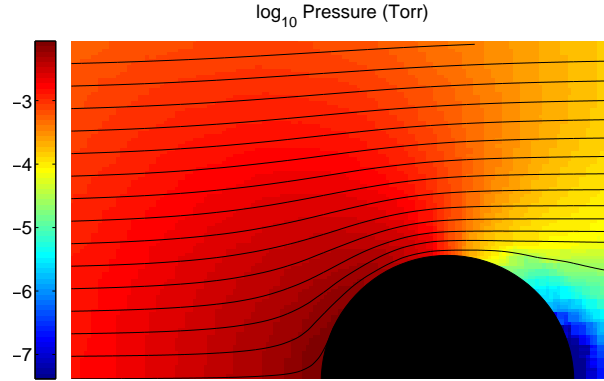


Figure 6.1: DSMC simulation of a sphere at 120 km perigee altitude undergoing transition flow.

the definition of the speed ratio $P_o \approx \text{constant} + n_O T_a k_B / \text{constant}$ which is equivalent to static pressure. Note that throughout this work, the atomic oxygen pressure or pressure-proxy refers to the dynamic and static pressures of atomic oxygen combined unless otherwise stated. The second effective parameter is the relative velocity V_r (equation 2.2) which is used to compute the incident kinetic energy of atomic oxygen ($E_r = 1/2 m_O V_r^2$). Finally, the mean molecular mass, \bar{m} , is computed along the reference orbit based on NRLMSISE-00 composition values.

$$\bar{m} = \frac{n_H m_H + n_{He} m_{He} + \dots + n_{O_2} m_{O_2}}{n_H + n_{He} + \dots + n_{O_2}} \quad (6.8)$$

All three parameters are mapped to a fitted ballistic observation through equation 6.3.

In order to evaluate energy accommodation from fitted drag coefficients it is necessary to first generate a mapping from C_D to α . This is done via lookup tables generated by DSMC runs at various values of accommodation coefficient. DSMC computations of a sphere are made between 120 km and 300 km altitudes. As discussed above, this allows for the treatment of data from the transition regime. Figure 6.1 shows an example of a DSMC simulated flow field at 120 km. For altitudes below 120 km, the model is linearly extrapolated while above 300 km equation 4.20a is used. The lookup values are shown in Figure 6.2. After $C_{D,obs}$ profiles are computed for all objects in Table 5.4, they are inverted to form solutions of effective energy accommodation parameters. To do this, a modeled drag coefficient is computed and compared with the observations. The modeled drag coefficient is based on a Langmuir isotherm generated by adjusting the

Langmuir parameter (K_L) for each type of object at several kinetic energy bins. The isotherm constitutes the “forward-model” in our inversion which will later become the basis of the semi-empirical accommodation model for satellites. Therefore our objective is to determine the functional relationship of K_L which best fits the available drag coefficient data. In previous work by Pilinski et al. [Pilinski et al., 2010] a possible relationship between Langmuir isotherms and accommodation is introduced which we will now exploit with a few modifications. This relationship begins by expressing the effective fractional coverage of atomic oxygen, θ' , as a function of the atomic oxygen pressure.

$$\theta' = \frac{K_L(E)P_O}{1 + K_L(E)P_O} \quad (6.9)$$

Note that we assume the Langmuir parameter, $K_L(E)$, is a function of kinetic energy only. Next, the coverage parameter is converted to accommodation by assuming the accommodation on adsorbed surface sites, α_a , is unity and rewriting equation 6.1 in the following way.

$$\alpha = (1 - \theta')\alpha_s + \theta' \quad (6.10)$$

In equation 6.10 α_s is computed by averaging Goodman’s empirical equation [Goodman, 1967] over a half sphere. The result is shown in equation 6.11 where μ is the ratio of incoming average molecular mass (\bar{m}) to surface (m_s) molecule mass (equation 6.12). We use an average surface mass value of 65 amu for all objects in the dataset in order to simplify the computations.

$$\alpha_s = \frac{2.4\mu}{(1 + \mu)^2} \quad (6.11)$$

$$\mu = \frac{\bar{m}}{m_s} \quad (6.12)$$

The accommodation coefficient, α , is then used as a lookup parameter in the DSMC C_D tables (illustrated in Figure 6.2) or in the computation of $T_{k,out}$ in the integral equation for a drag coefficient of a sphere (equation 4.20a). Recall that the integral equation is only applied when the data altitude exceeds the

maximum tabulated altitude. The resulting drag coefficient will be referred to as $C_{D,mod}$ and can now be compared with $C_{D,obs}$ in the following way.

$$CF = \sum_{k=1}^{N_{obs}} (C_{D,obs,k} - C_{D,mod,k})^2 \quad (6.13)$$

The cost function, CF , described by equation 6.13 is computed for the number of available data points N_{obs} for a particular satellite and a range of incident kinetic energies. The value of $K_L(E)$ in equation 6.9 is chosen as to minimize the cost function. The result of the inversion procedure is also shown in Figure 6.2.

Processing all observed data in the manner described above results in a series of Langmuir parameters ($K_L(E)$) binned by kinetic energy values. The functional relationship of $K_L(E)$ is assumed to have the following form.

$$K_L(E) = s_o(E, E_b, T_a)K_{L,o} + K_{L,f} \quad (6.14)$$

Equation 6.14 describes a transition from an initial Langmuir parameter associated with velocities in circular orbits, $K_{L,o}$, to a final value, $K_{L,f}$, associated with highly eccentric orbits. This transition is driven by an adsorption parameter called the initial sticking coefficient or s_o [Oura et al., 2003]. A simple model for s_o is that any molecule with an incident kinetic energy exceeding the adsorption binding energy will not adsorb to the surface. In order to assess this quantity we first write the Maxwellian velocity distribution of incident molecules as the following equation [Bird, 1994]

$$f(\vec{v}) = \frac{n_O}{(\pi a^2)^{3/2}} \exp\left(-\frac{(\vec{v} - \vec{V}_r) \cdot (\vec{v} - \vec{V}_r)}{a^2}\right) \quad (6.15)$$

where $a = \beta^{-1}$ and n_O is the number density of atomic oxygen. In order to simplify the estimation of molecular kinetic energy we will assume that the in-track (defined as the x direction) components of v and V_T are significantly larger than the thermal and off-track components ($v_x \gg v_y$, $v_x \gg v_z$, and $V_r \approx V_{r,x}$).

Writing a explicitly in the exponential function, equation 6.15 now becomes

$$f(v_x) = \frac{n_O}{(\pi a^2)^{3/2}} \exp\left(-\frac{m_O (v_x - V_r)^2}{2k_B T_a}\right) \quad (6.16)$$

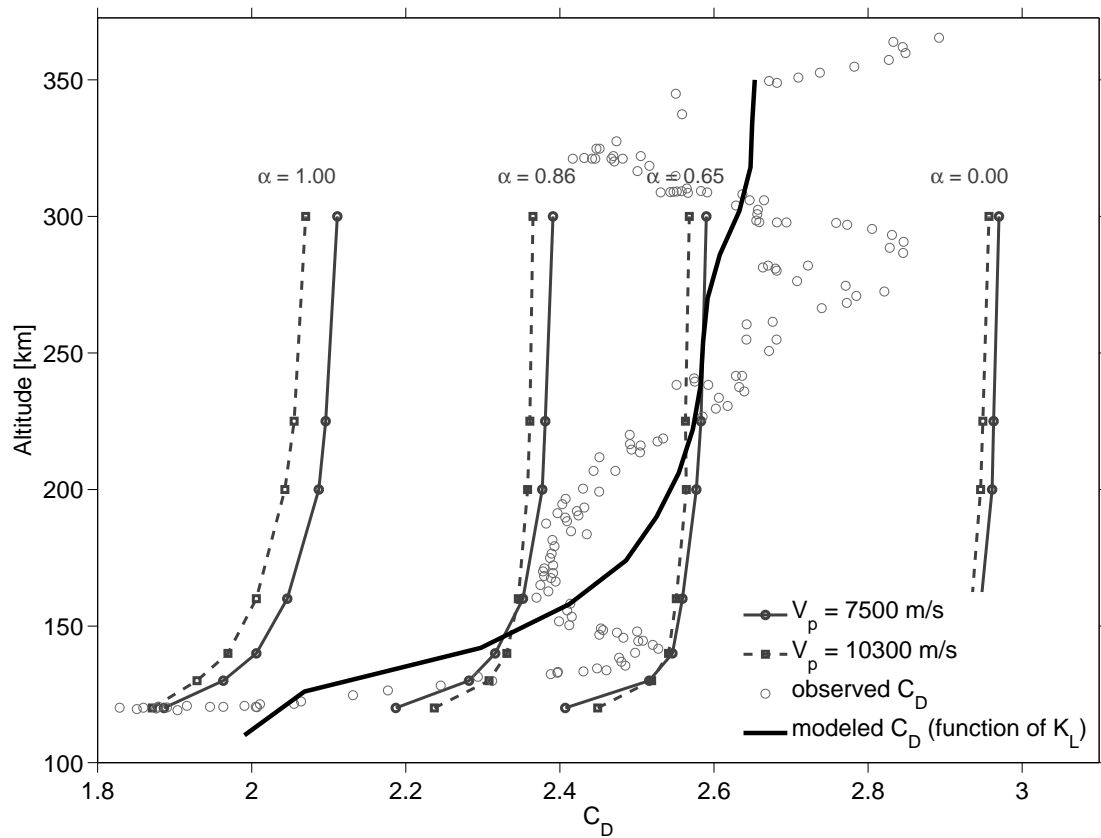


Figure 6.2: Langmuir isotherm based C_D fits to observed data shown for the SL-6 rocket body 15955. Lookup table values (see Appendix C) on which the C_D fit is based are shown for reference. The accommodation coefficient associated with each look-up curve is indicated. V_p denotes the effective relative velocity at perigee.

Note that in equation 6.16 the mass of atomic oxygen is used as it is the primary adsorbate in this model. Now, the $(-1/2)m(v_x - V_r)^2$ is expanded into $(1/2)m(-V_r^2 + 2V_r v_x - v_x^2)$ and rewritten into the form $-(1/2)mV_r^2 + 2\sqrt{m/2}V_r\sqrt{m/2}v_x - (1/2)m(-v_x^2)$. Using the definition of kinetic energy ($E = (1/2)mv^2$) equation 6.16 is rewritten as equation 6.17.

$$f(E) = \frac{n_O}{(\pi a^2)^{3/2}} \exp\left(\frac{-E_r + 2\sqrt{E_r E_x} - E_x}{k_B T_a}\right) \quad (6.17)$$

It is now time to implement the assumption that an impinging atomic oxygen atom is only adsorbed if its ram direction kinetic energy (E_r) does not exceed the adsorption or binding energy (E_b). Accordingly, the initial sticking coefficient s_o can be defined as the normalized fraction of the energy distribution which falls below the adsorption energy (equation 6.18a).

$$s_o = \frac{\int_0^{E_b} D(E)f(E)dE}{\int_0^{\infty} D(E)f(E)dE} \quad (6.18a)$$

In equation 6.18a, $D(E)$ is a measure of the efficiency of adsorption at any given energy and is associated with phenomena such as tunneling or other intrinsic changes in GSI [Goodman, 1974, Kay and Coltrin, 1988, Błoński et al., 2005]. Assuming $D(E) = 1$ then performing the integration results in equation 6.18b.

$$s_o = \left(\sqrt{\pi k_B T_a E_r} \left[\operatorname{erf}\left(\frac{\sqrt{E_b - \sqrt{E_r}}}{\sqrt{k_B T_a}}\right) + \operatorname{erf}\left(\sqrt{\frac{E_r}{k_B T_a}}\right) \right] + k_B T_a \exp\left(-\frac{E_b + E_r}{k_B T_a}\right) \left[\exp\left(\frac{E_b}{k_B T_a}\right) - \exp\left(\frac{2\sqrt{E_b E_r}}{k_B T_a}\right) \right] \right) \left(\sqrt{\pi k_B T_a E_r} \left[\operatorname{erf}\left(\sqrt{\frac{E_r}{k_B T_a}}\right) + 1 \right] + k_B T_a \operatorname{erf}\left(-\frac{E_r}{k_B T_a}\right) \right)^{-1} \quad (6.18b)$$

The concept described in equation 6.18b is visually demonstrated in Figure 6.3. Note that the sticking coefficient goes to unity far below the bonding energy and to zero when the average kinetic energy significantly exceeds E_b .

Now the functional relationship between Langmuir parameters and kinetic energy can be leveraged to fit the binned $K_L(E)$ data. We employ a nonlinear least squares fit which results in estimates of $K_{L,o}$, $K_{L,f}$, E_b , and T_a . For rocket bodies the fit parameters are a function of the assumed mass and several iterations of data-fits are performed each with a different assumption for the mass of the spacecraft. Spacecraft mass is adjusted by modifying the propellant margin as shown in equation 6.19

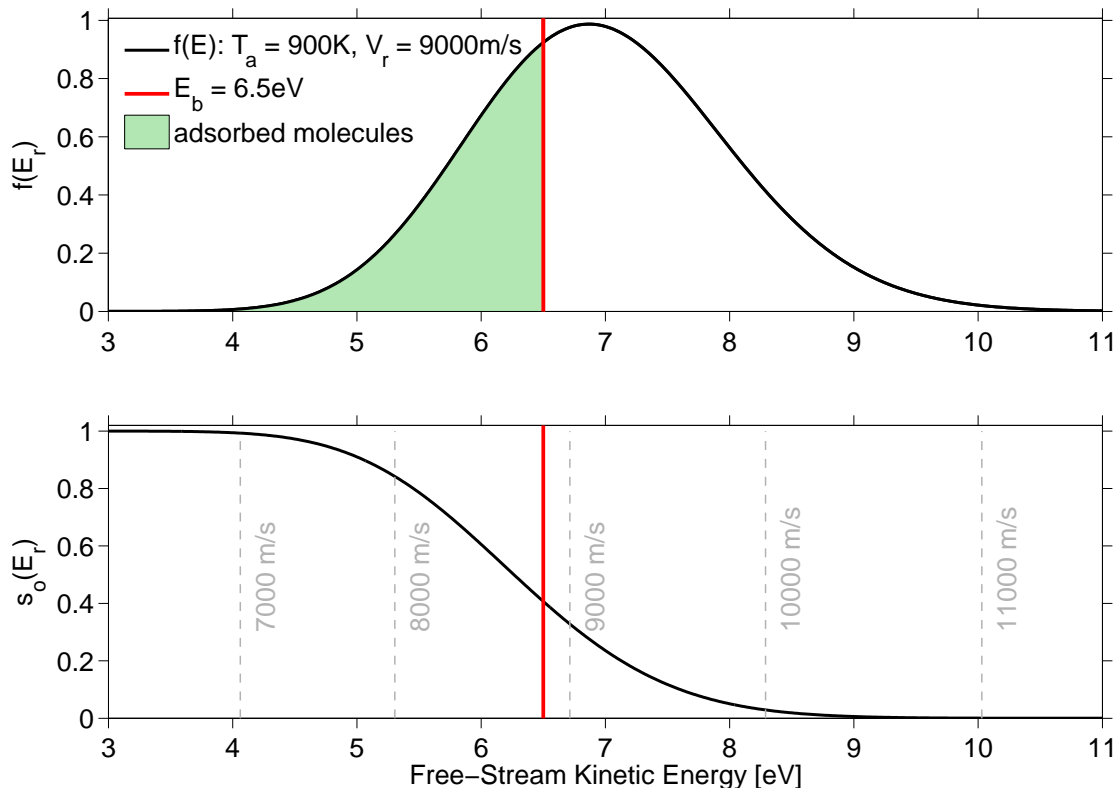


Figure 6.3: Changes in the initial sticking coefficient as a function of the bonding energy and the Maxwellian energy distribution.

$$m_{sc} = m_{dry} + \eta_{prop} m_{prop} \quad (6.19)$$

where m_{dry} and m_{prop} are the masses of the rocket body without propellant and the mass of the propellant (see Table 5.4) respectively while η_{prop} is the propellant margin remaining after the final engine burn. For each rocket body, a value of η_{prop} is chosen such that the $K_{L,o}$ resulting from the nonlinear fit is equal to the average $K_{L,o}$ value for all spherical rocket bodies (5×10^6). Thus we avoid the need to assume an arbitrary value of accommodation coefficient at a certain altitude, atomic oxygen pressure, or velocity in order to fix rocket body masses. Note that the propellant margin should be a positive near-zero fraction (for an optimized launch). In practice, the estimated η_{prop} may contain errors in the estimated cross sectional area causing it to be slightly negative. Nevertheless, a benefit of this method is that it allows for a quality check of the resulting model parameter fits.

6.2 Multi-Instrument Analysis

When measurements of drag and density are co-located in space and time they may be used in a similar way to modeled density comparisons described in section 6.1 to estimate energy accommodation. One useful example of this is remote sensing observations of atmospheric density. When such observations are combined with measurements of atmospheric drag acceleration on a satellite they can be used to solve for the drag coefficient. In Equation 6.20 accelerations measured by method 1, $a_{obs,1}$, are combined with an independent measurement of density made by method 2, $\rho_{obs,2}$. The best estimate of the relative velocity of the atmosphere with respect to the acceleration measuring spacecraft is V_r , m_{sc} is the mass of the spacecraft and A is its cross sectional area. All these parameters are functions of time for the CHAMP and GRACE spacecraft.

$$C_{D,mult} = \frac{2a_{obs,1}m_{sc}}{\rho_{obs,2}AV_r^2} \quad (6.20)$$

An example of such multi-instrument analysis could be measurements collected by accelerometers on a satellite combined with remote sensing observations of ultraviolet airglow which may be inverted to

constrain the density. Once $C_{D,mult}$ is obtained along a satellite orbit it can be used with a model of the gas-surface interaction to back out the accommodation coefficient.

6.3 Orthogonal Force Coefficient Analysis

The CHAMP and GRACE satellites measure accelerations in both the in-track (along the orbit) and cross-track (perpendicular to orbit) directions. This allows for the measurement of two independent interactions with the free-stream and leads to the solution of at least one gas-surface parameter. Cross-track measurements have been used by Sutton and Forbes as well as Doornbos to determine the zonal winds from CHAMP [Sutton, 2007, Doornbos et al., 2010]. The primary uncertainties in the analyses are the precision of the cross-track measurements as well as drag and lift coefficient and cross-sectional area models. With the generation of precise look-up tables for the drag coefficient of CHAMP (see Section 4.6) the problem of cross-track accelerometer analysis may be addressed. This is because the lookup tables were computed while taking into account shadowing, multiple-reflections, and a more complete representation of CHAMP satellite geometry. In the nominal flight mode for CHAMP and GRACE, the cross-track signal magnitude is approximately 5-7% of the in-track magnitude but has most of the same errors. The errors include thermospheric winds, solar radiation pressure modeling errors, as well as errors in accelerometer scale factor and bias. The relatively low signal-to-noise ratio in the cross-track direction can be addressed by averaging the many measurements made over the lifetime of the satellite. For the majority of the CHAMP satellite mission, the sideslip angle ranges from $\pm 6^\circ$ (for example, see Figure 4.22). Therefore, the ratio of side (y direction) to front (x direction) force coefficients may be used instead of lift and drag because there is no singularity in the range of relatively small angles involved. Consider the separate components of the \vec{C}_a equation (equation 2.4) in Chapter 2 as

$$a_x = \frac{C_x A}{m_{sc}} \rho V_r^2 \quad (6.21)$$

$$a_y = \frac{C_y A}{m_{sc}} \rho V_r^2 \quad (6.22)$$

where C_x and C_y are the force coefficients in the x and y directions respectively. Dividing equation 6.22 by equation 6.21 results in the following relationship.

$$\frac{a_y}{a_x} = \frac{C_y}{C_x} \quad (6.23)$$

Note that the ratio in equation 6.23 is independent of both atmospheric density and relative velocity. In fact, C_y/C_x can be approximated as a function of spacecraft orientation which is measured, free-stream temperature and velocity which is modeled using NRLMSISE-00 and HWM-07, as well as the GSI parameters which are unknown. Once the test-particle force-coefficient model is applied to the CHAMP satellite and a suitable averaging window is chosen, one can create a time series of the C_y/C_x ratio at various sideslip angles and GSI assumptions. In other words, for any sideslip angle β , the C_y/C_x ratio will be a function of the gas-surface model and level of accommodation of the impinging molecules. Comparing the measured ratio (a_y/a_x) to the model under various assumptions of GSI and accommodation can give insight into which GSI parameters are appropriate under the relevant flight conditions. However, the sideslip angle is itself a function of the cross-track wind which is not known precisely. It is because of this that the average cross track wind must be estimated before accelerometer data can be used to study gas-surface interactions. There are two ways to model cross-track winds for the estimation of the sideslip angle. One is to apply a simple model based solely on the corotation of the atmosphere (equation 6.5a) and the other is to use an empirical model such as the Horizontal Wind Model HWM-07 [Drob, 2008] added to atmospheric corotation. In this analysis, both methods will be used to provide an estimate of the sensitivity of the gas-surface measurement to cross-track winds for the small range of sideslip angles (from -6° to $+6^\circ$ with negative and positive angles being equivalent due to satellite symmetry).

We must also assume that the accommodation coefficient does not change drastically during the course of a single orbit. This assumption allows for a reduction in some of the uncertainty due to cross-track wind modeling. Wind errors can be reduced therefore by avoiding high latitudes (where winds can be high and rapidly changing) and restricting the analysis to low levels of geomagnetic activity. Figure 6.4 illustrates the magnitudes of the C_y to C_x ratio as a function of sideslip angle for a variety of accommodation coefficients. Note that the estimation of accommodation coefficients via this technique would be most sensitive at values

of α close to unity. Since the assumed value of CHAMP α is 0.93 the method should at least indicate whether or not this value is appropriate at all points during the CHAMP mission lifetime.

Furthermore, computing long-term average values of a_y/a_x will take advantage of the climatology of thermospheric winds thereby making the empirical HWM model more applicable to the estimation of winds. This is because empirical models are usually better suited at predicting climatological or long-term values.

The maximum sideslip angle due to corotation happens near the equator and for the CHAMP satellite results in a sideslip angle of around 6 degrees corresponding to a corotating wind magnitude of around 800 m/s. The zonal wind magnitudes superimposed on the corotation can range from 100-200 m/s at the equator to 500-700 m/s in the polar regions (during quiet conditions) [Doornbos et al., 2010] with the most variability observed at higher latitudes. Isolating certain local solar times can also be beneficial for reducing wind-induced error. For example, winds near the equator can be very small around the daytime temperature maximum which is centered at approximately 15:30 local solar time (Figure 6.5). Figure 6.5 also indicates that winds are minimal at the night-time temperature minimum. However, because of the higher signal to noise ratio afforded by greater day-time densities, the analysis will be restricted to solar local times between 13 and 18 hours.

The instantaneous sideslip angle is indicative of the wind direction in the spacecraft body frame and therefore the measured C_y/C_x can be related to wind angle β . As can be seen in figure 6.4 however, such a measurement of wind direction is only possible if one can specify which C_y/C_x curve the measurements exist on, i.e. what the correct gas surface interaction is. In our example, the difference between an α of 0.90 and 1.00 can cause an error in the cross-track wind of 100 m/s at the equator. By improving the knowledge of the gas-surface interactions for satellites like CHAMP, errors in cross-track wind measurements could be improved.

For the CHAMP satellite, yaw-maneuvers extend the range of sideslip angles to between -12° to $+180^\circ$. For example on November 6th 2002, the CHAMP satellite flew at a sideslip angle near 90° for approximately 7 orbits. The transition from β angles near 0° to ones near 90° provides an opportunity to compare a wide range of a_y/a_x measurements to C_y/C_x values using various assumptions of gas surface interaction. Note that at a sideslip angle of 90° , a_x is nearly zero and the quantities in equation 6.23 become undefined. To

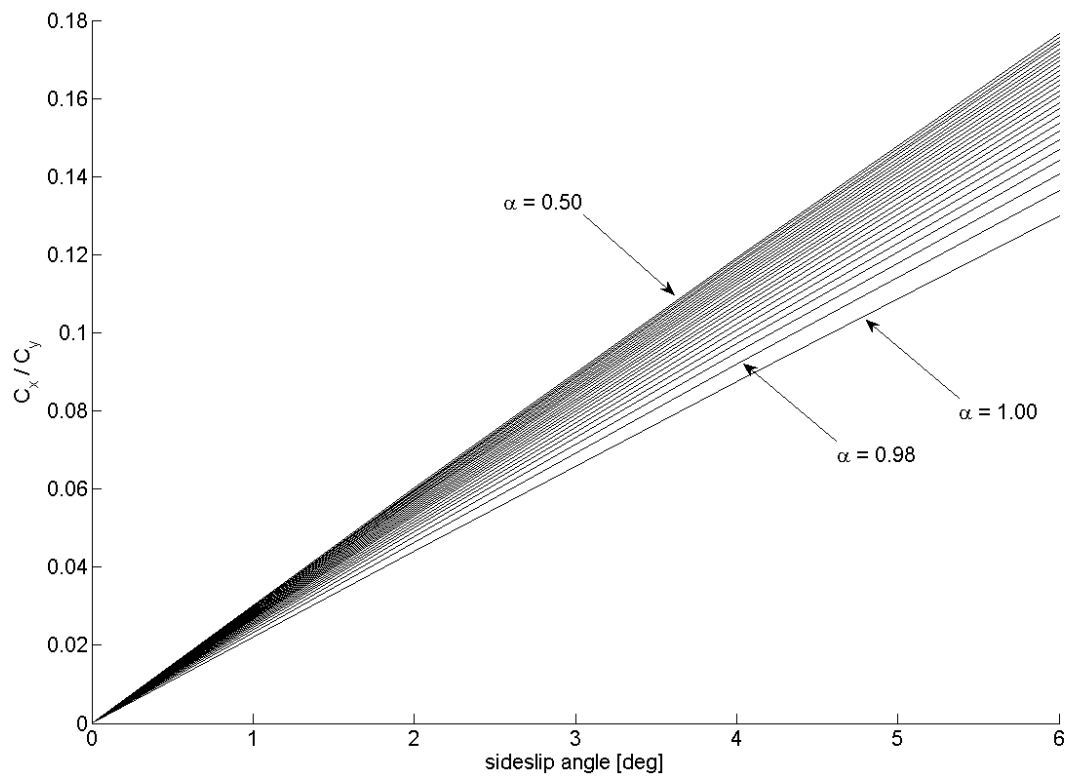


Figure 6.4: CHAMP satellite lift to drag ratio expressed in accelerometer measurement axes.

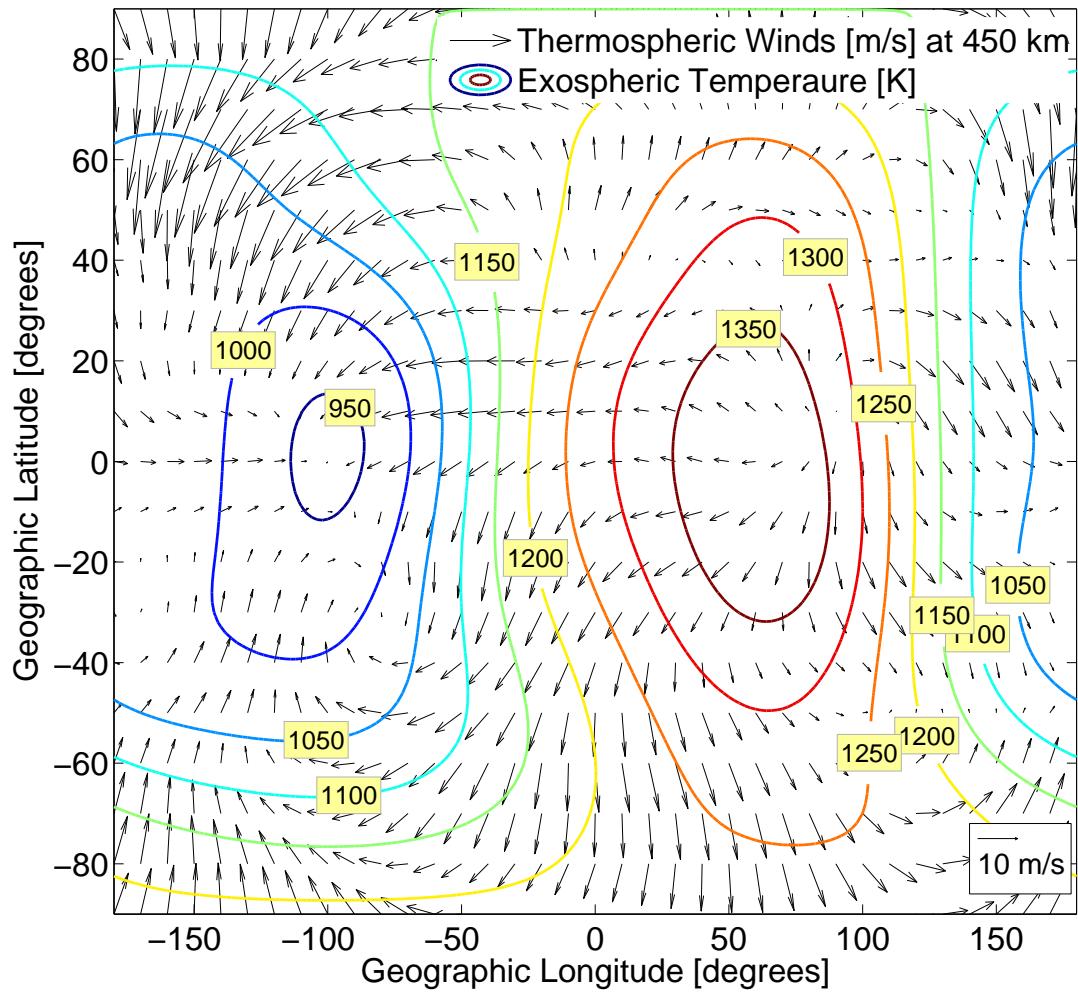


Figure 6.5: Winds modeled using HWM-07 at 450 km altitudes show a minimum wind near the exospheric temperature maxima and minima.

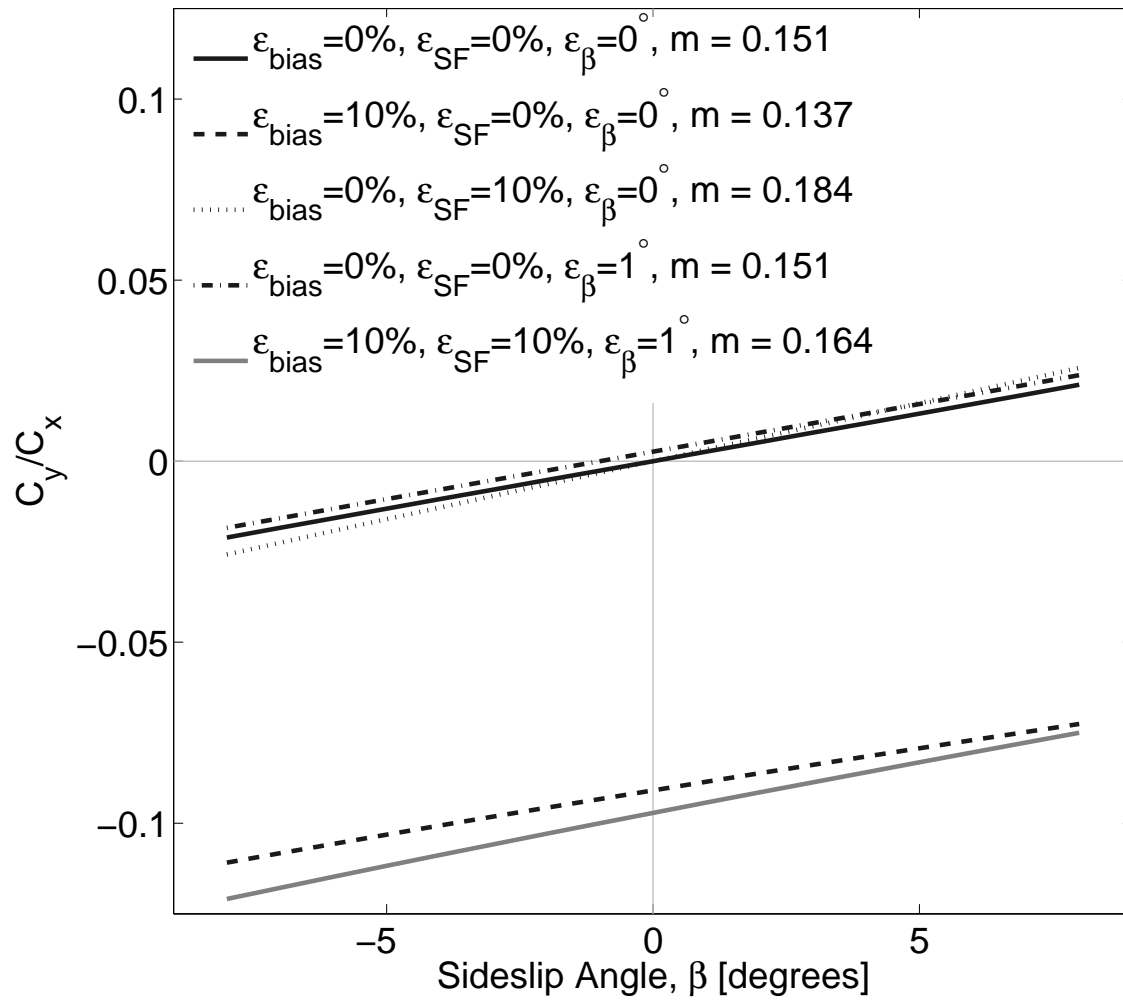


Figure 6.6: Examples in the variability of a_y/a_x slope measurements at small sideslip angles.

address this problem, a comparison of lift and drag coefficients may be carried out. Recall from Chapter 2 that the drag coefficient C_D is defined as $\vec{C}_a \cdot \hat{v}_r$ in equation 2.5. Similarly the lift coefficient may be written as

$$C_L = \vec{C}_a \cdot \hat{l} \quad (6.24)$$

where \hat{l} is a unit vector in the horizontal lift direction defined as

$$\hat{l} = \hat{z} \times \hat{v}_r \quad (6.25)$$

and \hat{z} is the basis vector in the z direction (see Figure 4.4). For the CHAMP satellite, \vec{C}_a will be computed using numerical techniques described in Section 4.3 and a precise 280 element CHAMP model. The measured accelerations can also be expressed as drag and lift components

$$a_D = \vec{a} \cdot \hat{v}_r \quad (6.26)$$

$$a_L = \vec{a} \cdot \hat{l} \quad (6.27)$$

and in following the same process as in equations 6.21 through 6.23, one can arrive at the expression

$$\frac{a_L}{a_D} = \frac{C_L}{C_D} \quad (6.28)$$

which is defined over all sideslip angles.

6.4 From Drag Observations to Surface Parameters

Much of the experimental component of this work depends on the interpretation of observed satellite drag through comparisons of measurements with physical models. Thus far the model of choice has been that of Sentman's diffuse reflection [Sentman, 1961] with a variable accommodation coefficient. This is because of the simplicity and wide range of applicability of this model by others [Sutton, 2009, Moe and Moe, 2005, Doornbos et al., 2009, Bowman and Moe, 2005]. Furthermore, the fully diffuse Sentman model

provides a straightforward mapping between C_D and the average accommodation coefficient. The average energy accommodation coefficients can be estimated using other models as well although these generally require assumptions as to the additional parameters involved (see Chapter 3). Another model which will be evaluated is that proposed by Moe et al. and is a hybrid model of Sentman's fully diffuse and Schamberg's quasi-specular model [Moe and Moe, 2005]. Quasi-specular reflection will be constrained using Goodman's formulas for accommodation and reflection angle.

The relationship between accommodation coefficients estimated in orbit and atomic oxygen pressure may help shed light on the gas-surface phenomena occurring in LEO. The NRLMISISE-00 model will be used to provide the number density estimates of atomic oxygen at any given time during a satellite's orbit. For satellites which fly in circular orbits, the variations in dynamic pressure are not significant from satellite to satellite as V_r remains constant within a few percent. The primary parameters which affect the flux of oxygen to the surface of a satellite will be the number density and temperature of the gas. The temperature will particularly affect the flux of molecules impinging the sides of a satellite. Therefore, one useful parametrization or proxy of atomic oxygen flux is the product $n_O \cdot T_a$ where both number density and the atmospheric temperature are taken from the NRLMSIS-00 model [Picone et al., 2002b]. The parameter $n_O \cdot T_a$ is the static pressure divided by the Boltzmann constant. A more general form of the incoming pressure was described in equation 6.7.

Based on the history of space-based observations and laboratory measurements, the proposed model of satellite accommodation coefficient is based on both adsorbed and clean surface interactions. The effective accommodation coefficient will be described as

$$\alpha = (1 - \theta') \alpha_s + \theta \alpha_a \quad (6.29)$$

where θ' is the effective surface coverage of adsorbate, α_s is the accommodation coefficient of the gas impinging on the uncovered surface, and α_a is the accommodation coefficient of the gas impinging on sites occupied or affected by adsorbed molecules. This hybrid expression has been introduced by Goodman [Goodman, 1974] and applied in the analysis of laboratory experiments of Onsager heat of transport for water molecules [Biggs and Phillips, 2008] with coverage modeled using the BET isotherm. This is the

first time this model is used to compute satellite gas-surface interaction parameters.

The concept of effective coverage (θ') is introduced here to distinguish between surface saturation and surface coverage (θ). Surface coverage is taken to mean the fraction of adsorption sites occupied by adsorbate and is the quantity measured in most ground based surface science experiments. Meanwhile, effective coverage, or θ' , is the fraction of the surface affected by adsorbate where effects extend to changes in the sticking coefficient and are taken to be equivalent to changes in accommodation. This definition leads to the following expression for θ' .

$$\theta' = b\theta \quad (6.30)$$

Equation 6.30 is a formal distinction between the effective coverage which can be measured using changes in the accommodation coefficient and the real coverage. It is arbitrarily based on a linear relationship between the two with a constant of proportionality b .

$$\theta' = \begin{cases} 0 & \text{when there is no adsorbate on the surface } (\theta = 0) \\ 1 & \text{all of the surface area is affected by adsorbate } (0 < \theta \leq 1) \end{cases} \quad (6.31)$$

Equation 6.31 introduces the assumption that to an incoming molecule a fully saturated surface behaves like one in which all the surface sites are covered with adsorbate. In other words, the same phenomenon which prevents the adsorption of additional molecules onto vacant sites also causes those sites to have an accommodation coefficient equivalent to α_a . An integral part of this research is the examination of these assumptions in LEO conditions.

Chapter 7

Evidence of a Link Between Adsorption of Atomic Oxygen and Accommodation at High Thermospheric Pressures

7.1 Assumptions

The first assumption underlying this work is that the energy accommodation coefficient in Earth's lower orbits (below 500 km altitude) is driven primarily by the amount of atomic oxygen adsorbed on the spacecraft surface. Therefore, adsorbed molecules shield the incoming flow from surface properties such as treatment and composition [Moe and Bowman, 2005]. Another important assumption is that molecules are reflected from the surface in a diffuse, or cosine, distribution with a kinetic temperature $T_{k,out}$ determined by equation 4.4. According to previous work on satellite drag coefficients, this assumption is valid for satellites flying below 500 km altitude [Moe and Moe, 2005].

7.2 Computational Method

To account for the temporal variations in solar activity, a functional relationship between time-specific atmospheric conditions and the accommodation coefficient is desired. This will allow the computation of accommodation coefficients to any arbitrary time. Since the physical explanation for accommodation is based on atomic oxygen adsorption, a modeled parameter based on atomic oxygen pressure would be ideal. The product of the density of atomic oxygen and atmospheric temperature ($n_O \cdot T_a$) was chosen as the input parameter. Both atomic oxygen number density, n_O , and atmospheric temperature, T_a , are modeled using NRLMSISE-00 [Picone et al., 2002b] with solar activity inputs (A_p and F10.7) taken from measurement

archives. The measurement and modeling of atomic oxygen number densities has presented many challenges such as recombination of atomic oxygen inside of mass spectrometers and uncertainties in the ionization cross-section. Since NRLMSISE-00 depends on mass spectrometer data for this information, our model cannot be fixed to an absolute input scale. Instead we will rely on a relative estimation of the atomic oxygen assuming that the relative errors are smaller than the absolute accuracy within the atmospheric model.

First, the orbits of seven spherical satellites used by Bowman and Moe [Bowman and Moe, 2005] were propagated at various altitudes and times during 1989-1995 to find the average atmospheric conditions along their trajectories. The spherical tracking objects used are listed in Table 5.3. The accommodation coefficients which were ascribed to those spheres (via interpolation in Table 5.1) were then matched with average values of $n_O \cdot T_a$ as computed by the NRLMSISE-00 model in our orbital simulations. This was done for each satellite at three to seven different altitudes resulting in 38 data points spanning a range of altitudes and solar conditions. Finally, a least-squares fit was used to match an analytical model to the resulting data set. The chosen analytical model is the Langmuir isotherm which describes the fraction of monolayer surface adsorption by a particular species as a function of the static pressure of that species [Adamson, 1990] at a certain constant surface temperature. This model was selected because of its simplicity and because it has been successfully used to reconcile space borne pressure gauge observations of atomic oxygen [Moe and Moe, 1967]. Equation (7.1) is the definition of the Langmuir isotherm in terms of a scaled static pressure component (static pressure divided by Boltzmann's constant), P , and a single constant, K_L , which is also used as the fitting parameter. The value of P was set equal to $n_O \cdot T_a$. We have assumed a linear relationship between surface coverage of atomic oxygen and energy accommodation. In other words, the model describes a macroscopic accommodation coefficient which is an average of unaccommodated collisions between incoming molecules and the spacecraft material and completely accommodated collisions between the incoming molecules and the adsorbate layer. This assumption allows us to write accommodation directly in the form of the Langmuir formula (equation 7.1). Note that this formula is a simplification of equation 6.9 wherein θ' is set equal to α .

$$\alpha = \frac{K_L \cdot P}{1 + K_L \cdot P} \quad (7.1)$$

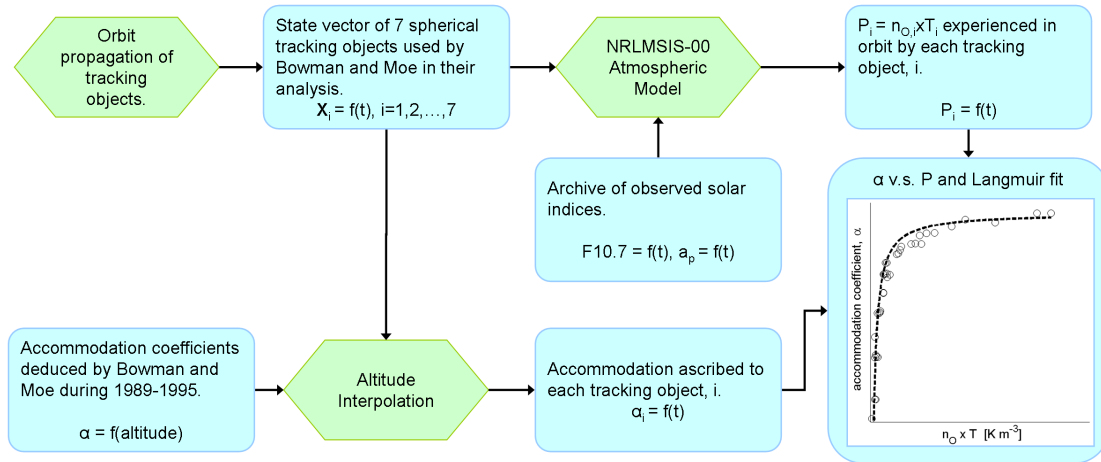


Figure 7.1: Flow diagram summarizing the computation procedure for accommodation coefficients.

The computational method is summarized in Figure 7.1. In essence, we have presented the available accommodation measurements as a function of simulated atomic oxygen static pressure (scaled by k_b) then fitted an adsorption-derived function to the data resulting in a semi-empirical model of energy accommodation.

7.3 Results

The semi-empirical model along with data from spherical satellites during both solar maximum and minimum are shown in Figure 7.2 and Tables 7.1 and 7.2. The tabulated data include specific spherical-object reference numbers (NORAD references), the times of simulation, the average altitude during that time, as well as the value of $n_O \cdot T_a$ and the accommodation coefficient. The black solid curve in Figure 7.2 represents an analytical fit of the results to the Langmuir isotherm. The average error between the accommodation coefficient determined through the analysis of smooth spheres and the Langmuir isotherm fit with $K_L = 4.98 \times 10^{-17} \text{ m}^3 \text{ K}^{-1}$ is -0.9% with a standard deviation of $\pm 1.7\%$. This agreement gives a physical underpinning to the extrapolation scheme and validates the assumption of a straightforward relationship between energy accommodation and the fraction of atomic oxygen adsorbed at the surface. Note the deviations of the accommodation curve from the Langmuir isotherm, especially at the knee of

the curve where the model is systematically higher than the data. This may be indicative of secondary adsorption effects such as multilayer formation (islands) [Thomas, 1967, Adamson, 1990] or recombination of atomic oxygen. Other explanations include relative errors in the modeled number density of atomic oxygen in NRLMSISE-00 and uncertainties in the original tabulation of accommodation coefficients. It is also possible that the least-squares fit results in an overdependence on the low and high pressure regions leaving the mid-pressure transition with more errors. Note that the fitting parameter, K_L , depends on the method of n_O and T_a estimation. The value of $4.98 \times 10^{-17} \text{ m}^3 \text{ K}^{-1}$ obtained for K_L in this chapter is a result of using the NRLMSISE-00 neutral density model and the application of this value should only be performed with NRLMSISE-00. The use of a different atmospheric model for the estimation of n_O and T_a would require a recomputation of K_L .

In order to compare the model with tabulated data, we compute accommodation coefficients along circular orbits of 30° inclination at a range of altitudes for both solar minimum ($A_p = 5$ and F10.7 = 75 sfu) and solar maximum ($A_p = 5$ and F10.7 = 225 sfu). Figure 7.3 demonstrates the agreement with accommodation measurements (discrete points). The model successfully predicts the gradual decrease in accommodation as the altitude changes from 150 km to 200 km and the more rapid drop which occurs above 300-400 km altitude. Relative differences between solar minimum and maximum are also reproduced. Most measurements are within 50 km of the model curve and the best agreement occurs below 500 km altitude. A notable outlier is the solar maximum measurement at 630 km corresponding to the Clementine satellite [Pardini et al., 2010]. One explanation for this is that the adsorption model ceases to accurately represent the physics of gas-surface interactions above 500 km. It is possible for example, that when a significant fraction of the surface is exposed to the free stream at higher altitudes, the accommodation coefficient will be determined to a larger extent by the particular material of the satellite surface. This material, or substrate, accommodation coefficient can take on values ranging from 0.0 to 0.9 depending on the ratio of molecular masses of incoming and surface molecules and the incident angle [Moe and Moe, 2005]. In contrast, the present model implicitly assumes a substrate accommodation coefficient of 0.0 for all cases. The likely consequence of this is that our model underestimates the accommodation coefficient at higher altitudes such as those of the Clementine satellite. Also, Clementine had a complex shape which tends to introduce

Table 7.1: Solar maximum values of $n_O \cdot T_i$ and energy accommodation coefficient.

Obj.	Yr	doy_o	doy_f	Alt [km]	$n_O \cdot T_a$ [K m ⁻³]	α
11796	89	22	24	272	1.86×10^{15}	0.99
11796	89	68	78	225	5.70×10^{15}	1.00
11796	89	165	171	198	7.60×10^{15}	1.00
13750	89	68	77	372	6.02×10^{14}	0.96
13750	89	151	155	347	5.93×10^{14}	0.97
13750	89	199	203	322	6.86×10^{14}	0.98
13750	89	232	236	296	1.27×10^{15}	0.98
13750	89	253	255	272	2.32×10^{15}	0.99
13750	89	263	266	234	3.71×10^{15}	0.99
13750	89	270	273	192	8.24×10^{15}	1.00
15446	89-90	354	3	347	6.67×10^{14}	0.97
15446	90	31	35	322	7.52×10^{14}	0.99
15446	90	58	63	298	1.19×10^{15}	0.98
15446	90	81	84	271	2.06×10^{15}	0.99
15446	90	91	93	249	2.55×10^{15}	0.99
15446	90	99	102	218	4.32×10^{15}	1.00
4958	89	174	176	498	6.69×10^{13}	0.90
4958	89	227	229	448	1.96×10^{14}	0.93
4958	89	240	242	423	1.95×10^{14}	0.94
4958	89	248	250	395	4.07×10^{14}	0.95
4958	89	253	254	372	5.88×10^{14}	0.96
4958	89	257	258	346	7.56×10^{14}	0.97

Table 7.2: Solar minimum values of $n_O \cdot T_a$ and energy accommodation coefficient.

Obj.	Yr	doy_o	doy_f	Alt [km]	$n_O \cdot T_a$ [K m ⁻³]	α
21190	94	339	342	298	2.89×10^{14}	0.93
21190	95	39	41	273	4.61×10^{14}	0.95
21190	95	69	71	249	8.84×10^{14}	0.97
21190	95	80	82	226	1.41×10^{15}	0.98
21190	95	88	89	198	2.92×10^{15}	0.99
22990	94	70	73	323	2.02×10^{14}	0.91
22990	94	145	148	298	2.35×10^{14}	0.93
22990	94	222	225	274	3.17×10^{14}	0.95
22990	94	245	248	249	6.12×10^{14}	0.97
22990	94	262	265	221	1.42×10^{15}	0.98
22994	94	106	108	323	2.41×10^{14}	0.91
22994	94	288	291	299	3.44×10^{14}	0.93
22994	94	352	355	273	4.39×10^{14}	0.95
22994	95	33	36	251	7.69×10^{14}	0.97
22994	95	48	50	225	1.36×10^{15}	0.98
22994	95	56	57	202	2.24×10^{15}	0.99

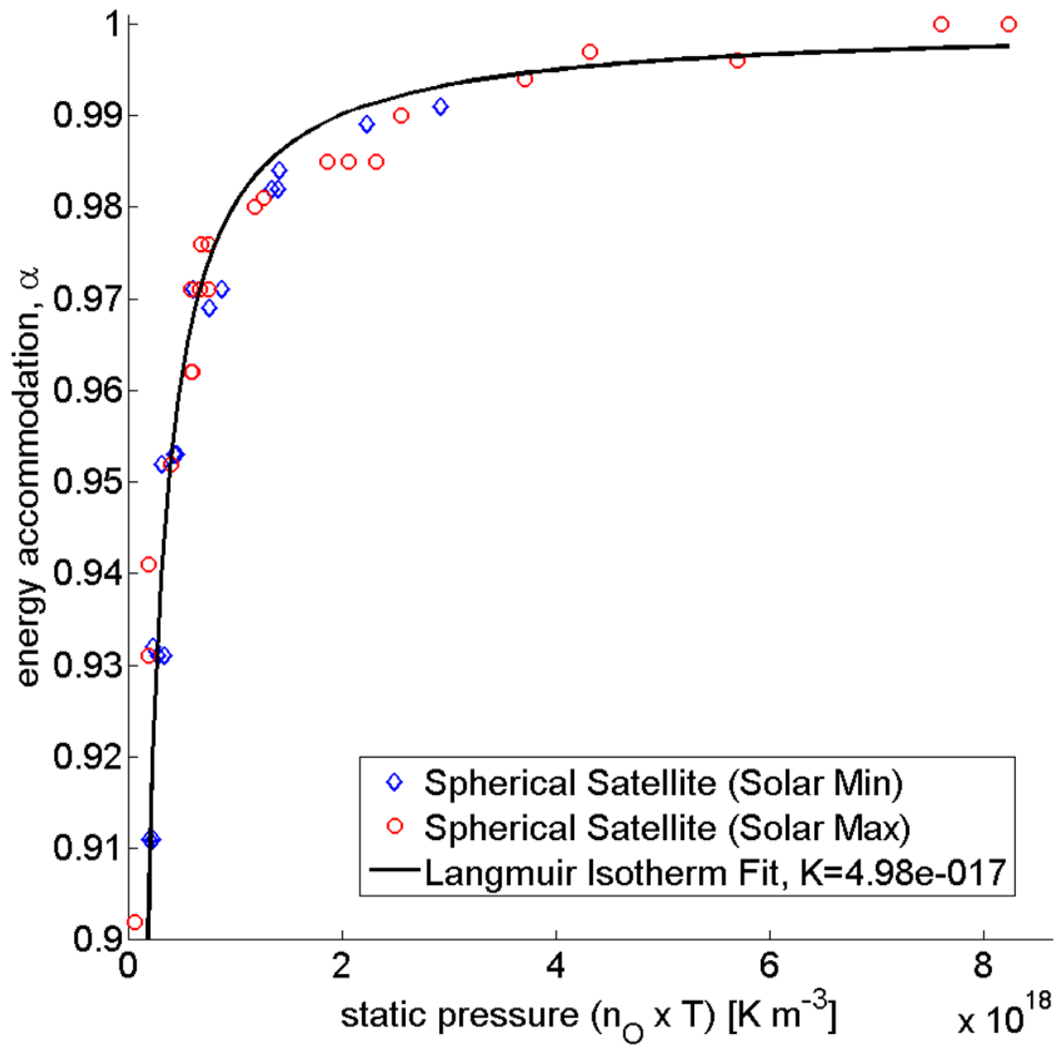


Figure 7.2: Accommodation coefficients as a function of $n_O \cdot T_a$. The fit was based on data taken during solar minimum (blue diamonds) and solar maximum (red circles).

uncertainty into drag coefficient computations. While this may account for some of the discrepancy, it is important to keep in mind that because of the non-commutative nature of equation (6.1), values derived using spherical satellites may not match exactly the values measured using other shapes. Furthermore, the modeled curves in Figure 7.3 correspond to average atmospheric conditions and may not adequately represent the orbital environment for specific observation objects such as Clementine. As mentioned earlier, the Ariel 2 paddlewheel accommodation measurement at 308 km altitude is lower than both the general trend of the solar-minimum data set and the model prediction. One possibility for this could be an error in the reported atmospheric model bias at the Ariel 2 altitude. Furthermore, the orbiting objects used to construct our model had near zero eccentricities with differences in perigee and apogee heights of no more than 50 km. Meanwhile Ariel 2 was inserted into an orbit with an eccentricity of approximately 0.07 and a difference between perigee and apogee heights of roughly 1,000 km. The eccentric orbit accounts for approximately a 400 m/s increase in incident speed at perigee which could change the adsorption kinetics and lower the overall accommodation coefficient. Finally, the paddlewheel analysis of Ariel 2 included 17 days [Imbro et al., 1975] of data while the analysis of the spherical tracking objects via fitted ballistic coefficients usually includes several months of data. This shorter time span coupled with the atmospheric sampling experienced in a more eccentric orbit (where perigee and apogee altitude differ by more than several scale heights), could have resulted in differences in the averaged atmospheric conditions of the Ariel 2 measurement relative to the fitted ballistic coefficient analyses used in the present model. The accommodation coefficient of Ariel 2 may therefore be different from the accommodation coefficients of other objects at similar altitudes due to differences in average temperature and atomic oxygen pressure in orbit.

Equation (7.2) describes the implementation of the accommodation model. Both n_O and T_a are retrieved from NRLMSISE-00 for a particular set of locations, times, and solar conditions.

$$\alpha = \frac{4.98 \times 10^{-17} \cdot n_O \cdot T_a}{1.00 + 4.98 \times 10^{-17} \cdot n_O \cdot T_a} \quad (7.2)$$

Physically, this equation holds for all values of $n_O \cdot T_a$ and for satellite surface temperatures of approximately 300 K. Since a variation of $\pm 100\text{K}$ in the surface temperature results in a change in drag coefficient of approximately $\pm 1.0\%$, the uncertainty due to surface temperature in the drag coefficient equation is small.

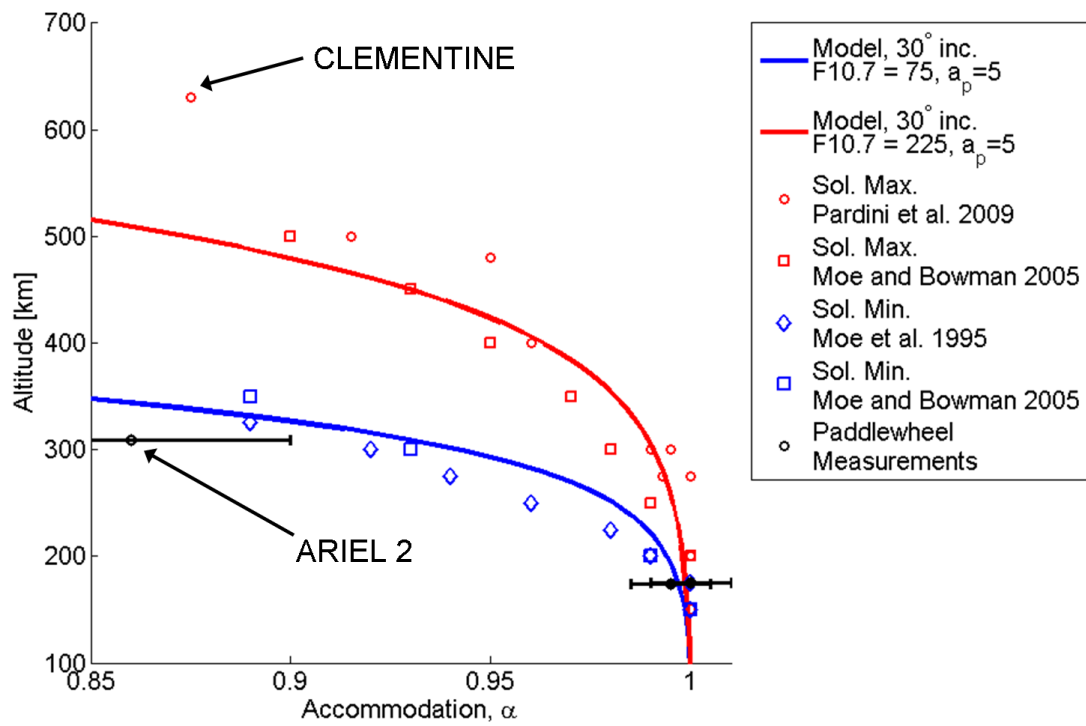


Figure 7.3: Estimated energy accommodation coefficients with the semi-empirical model.

It is more difficult to assert how the isotherm might change due to an increase or decrease in the surface temperature. It is likely that due to the chemical nature of the atomic oxygen surface bond, the bond energy will exceed the thermal energy in the surface lattice thereby making adsorption insensitive to the changes in satellite temperatures over the free-molecular regime. At the present time however, insufficient data on the variation of satellite accommodation coefficients with surface temperature exist to adequately answer this question.

In terms of data validation, there are no orbital accommodation data that exist for orbits of low eccentricity at values of α lower than 0.85. An estimate for the verified range of this model is therefore between 0.85 and 1.00 in accommodation and 150 to 500 km in altitude. Another restriction is the eccentricity of the satellite orbit. The measured accommodation coefficient of Explorer 6 (eccentricity of 0.76) was 0.65 [Moe and Moe, 2005]. In contrast, the accommodation of Ariel 2 (eccentricity of 0.07) with a comparable perigee altitude to that of Explorer 6, was measured to be 0.86. One possibility for this difference is that atomic oxygen impinging at high kinetic energies does not adsorb as readily as atomic oxygen approaching the surface near or below the energy of adsorption. Another reason may be that at high eccentricities the time spent within the Earth's lower atmosphere is insufficient for significant adsorption to occur. However, the value measured for satellite S3-1 [Ching et al., 1977], with an eccentricity of 0.22, was consistent with another measurement at similar altitude and lower eccentricity indicating that time spent in the lower atmosphere is less important than the energy with which molecules strike the surface and the static atomic oxygen pressure. Because of the Explorer 6 discrepancy, the application of equation (7.2) should be restricted to orbits with eccentricities less than or equal to 0.07. Analysis of data in Figure 7.2 indicates that the model tends to overestimate the accommodation coefficient for most values of $n_O \cdot T_a$ with a maximum deviation between data and model of -0.04 and +0.07. An estimate of the maximum model error is therefore -0.04 and +0.07 around the values resulting from equation (7.2) with the accommodation coefficient restricted to values between 0.00 and 1.00. The mean error between data and model is -0.01 with a standard deviation of ± 0.02 .

Unlike the fitted accommodation coefficients, paddlewheel measurements (black circles in Figure 7.3) are independent of atmospheric models which makes them ideal for confirming the accuracy of the accommo-

dation model. Unfortunately only a handful of independent measurements of accommodation are available. Furthermore, the incident kinetic energies corresponding to these measurements vary along with the static pressures of atomic oxygen. While accommodation coefficients may depend on both of these variables, the present model presents accommodation coefficients as a function of static pressure at a constant kinetic energy. This lack of control in the kinetic energy in the paddlewheel data set probably prevents direct comparison of the preliminary model and paddlewheel measurements. It is encouraging however, that paddlewheel observations below 200 km match the model prediction within one percent. Due to the accommodation coefficient assumptions underlying the determination of atmospheric model bias, the fitted accommodation coefficients reflect only relative variations in accommodation. Therefore, our model represents only relative variation in accommodation coefficient above 200 km.

When using the accommodation model to compute physical drag coefficients (for example by using equation (4.20a)) and applying the results to predict satellite drag forces, one must also correct the atmospheric model being used for altitude-dependent density biases. Density biases for the J70 and JB2006 models are presented by Pardini et al. [2010] as well as Bowman and Moe [2005]. Some biases in the NRLMSIS-00 model are presented by Picone et al. [2002b].

Chapter 8

Dynamics of Adsorption Phenomena and the Satellite Drag Coefficient at High Thermospheric Pressures

8.1 Computational Method

This chapter is focused on the drag coefficients of spherical and randomly tumbling rocket bodies. As an approximation for the drag coefficient, the integral equation for a cylinder is used and is included in Appendix A. In a free-molecular flow, a drag coefficient can be computed by evaluating equation 4.20a separately for each of the primary constituents in the free-stream. The results are then superimposed linearly via a weighted mean of partial mass densities [Pilinski et al., 2011a, Sutton, 2009]. When the satellite altitude is low enough such that molecule-molecule interactions cannot be neglected, Direct Simulation Monte Carlo (DSMC) methods are applied [Dogra et al., 1992]. DSMC simulates molecule-molecule as well as molecule-surface collisions on arbitrary shapes by representing the flow of a statistical sample of molecules and choosing appropriate collision frequencies within that sample. The DSMC code used in this research is DS3V [Bird, 2007]. A complete description of the method for energy accommodation analysis is given in Chapter 6, section 6.1 for objects flying in free-molecular flow. However, DS3V does not provide a method for directly modeling incomplete energy accommodation. The surface temperature in the DS3V model is modified instead to match the average $T_{k,out}$ computed for the molecules in the free-stream (equation 8.1).

$$T_{w,DS3V} = \frac{\bar{m}}{3k_B} V_r^2 (1 - \alpha) + \alpha T_w \quad (8.1)$$

8.2 Sensitivity Analysis to Model Assumptions

In order to simplify the modeling process as well as the inverse procedure of determining model parameters from observations, we will use a sphere to approximate the drag coefficient of a randomly tumbling object. The error associated with this assumption does not exceed 2% as can be seen in Figure 8.1 where the average C_D of a tumbling cylinder is compared with that of a sphere. The results in Figure 8.1 were computed using integral equations in the free molecular regime where the atmospheric temperature was 1100 K, the spacecraft wall temperature is 350 K, the composition is 82% atomic oxygen and 18% molecular nitrogen, and the spacecraft velocity is 10 km s^{-1} . The natural question which follows is whether or not the average is a good representation of central behavior of the drag coefficient for a tumbling object. To answer this question, consider that the typical observed tumbling period of rocket bodies ranges from 1 to 15 seconds (60 RPM to 4 RPM respectively)[Boahnhardt et al., 1989, Pontieu, 1997, Reynolds et al., 2001]. Furthermore, the duration of a perigee pass (defined by the time spent within a single scale height of perigee) in low Earth orbit can range from from 2 minutes to 90 minutes. Since the number of perigee passes during a 1.5 day orbit fit-span [Storz et al., 2005] may vary from 3 to 24 (depending on orbit type) it follows that total perigee pass times are approximately 6 minutes to 2160 minutes (highly elliptical to near-circular orbits). In other words, the rocket bodies execute from 24 to 8,640 tumble periods (highly elliptical to near-circular orbits) during a single observation for the slowest tumbling objects and 360 to 129,600 for the most rapidly tumbling objects. The large number of expected revolutions which take place during a single drag measurement substantiate the use of average ballistic coefficient properties.

The cross sectional area estimate can have a significant effect on the computation of a ballistic coefficient and on the computation of observed C_D from fitted ballistic coefficients. Figure 8.2 demonstrates the relative size of cross-sectional area uncertainty (gray region) compared with the modeled drag coefficient variability (dark black) and uncertainty in atmospheric density (dotted lines). The plotted example is based on the Ariane rocket upper stage which has the highest relative difference between minimum and maximum areas of all the objects in the dataset. While the ballistic coefficient variability due to cross sectional area is much larger than that due to drag coefficient effects we nevertheless assume a constant average area and drag

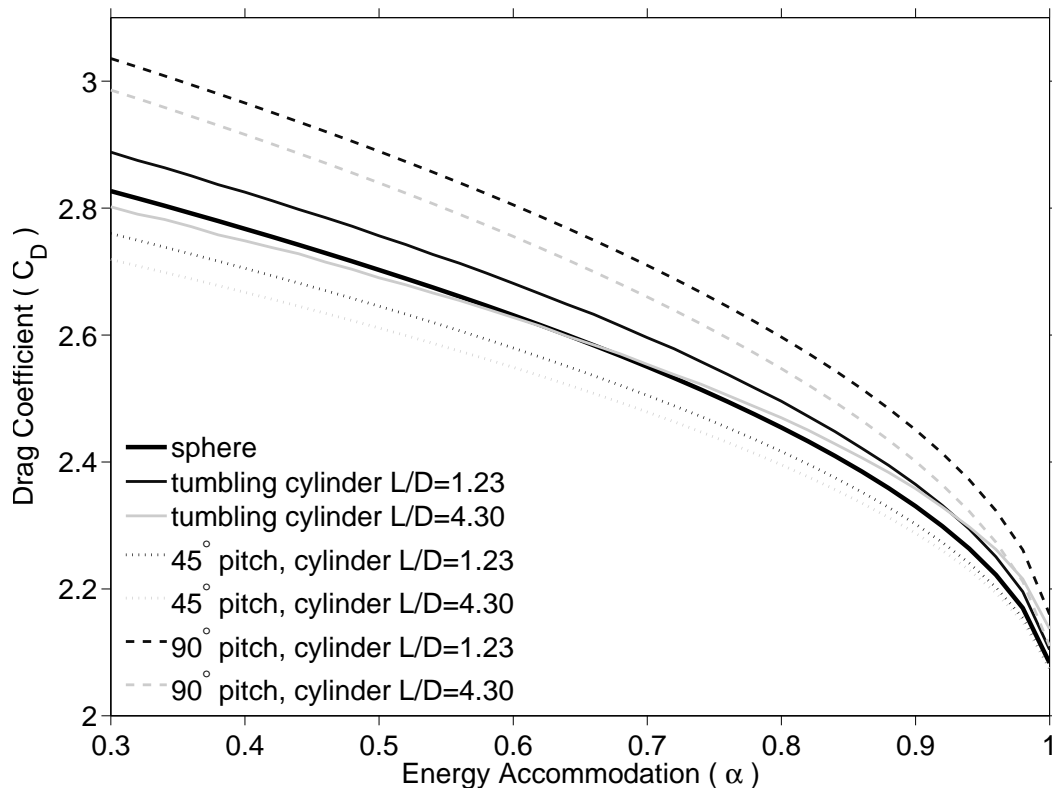


Figure 8.1: Drag coefficients of randomly tumbling cylinders compared with the drag coefficient of a sphere.

coefficient approximately equal to that of a sphere. This is because of the tumbling-rate argument presented above and because the $\pm 15\%$ (average) variability is observed to have a similar time-series for objects at approximately equal altitudes and orbital inclinations [Bowman and Storz, 2003]. The latter observation indicates that most of the short term variability in fitted ballistic coefficients is due to errors in atmospheric density and not to large changes in cross sectional area.

8.3 Initial Results

In order to adequately constrain the least-squares fit of Langmuir parameters, it was necessary to assume the high-energy value of the parameter ($K_{L,f}$). This value was initially fixed at $7 \times 10^3 \text{ Torr}^{-1}$ according to the data beyond 9000 m/s velocities. Figure 8.3 shows the results of binned Langmuir parameter fits under the assumption of a constant 2% propellant mass margin for all rocket bodies. The bottom of the plot indicates the number of samples (fitted ballistic coefficients) in each kinetic energy bin. Note how the Langmuir parameter is reduced with incident kinetic energy indicating that adsorption is less efficient at higher velocities. The data and fit are shown in Figure 8.4 and were analyzed with rocket body masses adjusted using the technique described in the above section. The sample size in each bin has changed because outlier rejection is applied before fitting the data and the exact distribution of K_L values differs based on the assumed mass of the rocket bodies. This second fit is also indicative of a reduction in adsorption efficiency at higher velocities. Furthermore, the standard deviation (indicated by error bars) is reduced significantly by applying the mass determination method. The fit parameters vary from 5.5 eV to 5.7 eV for E_b , 89 K to 93 K for T_a , and $1.2 \times 10^6 \text{ Torr}^{-1}$ to $2.0 \times 10^6 \text{ Torr}^{-1}$ for $K_{L,o}$. The adsorption, or binding, energy resulting from the orbit data fit is within a range of theoretical and laboratory results on various surfaces as seen in Table 5.2. However, the temperature which has to be assumed for incident Maxwellian distribution is clearly unphysical as the perigee altitudes vary from 110 km to 500 km where temperatures range from 200 K to 1400 K. A low temperature in the fit accounts for the steep initial drop in K_L as a function of kinetic energy and is likely indicative of additional physics missing from the model. This could include sputtering or tunneling phenomena or a change in the surface properties with the level of adsorbate coverage θ . This could be empirically addressed by either choosing a non constant adsorption efficiency function $D(E)$ or simply by

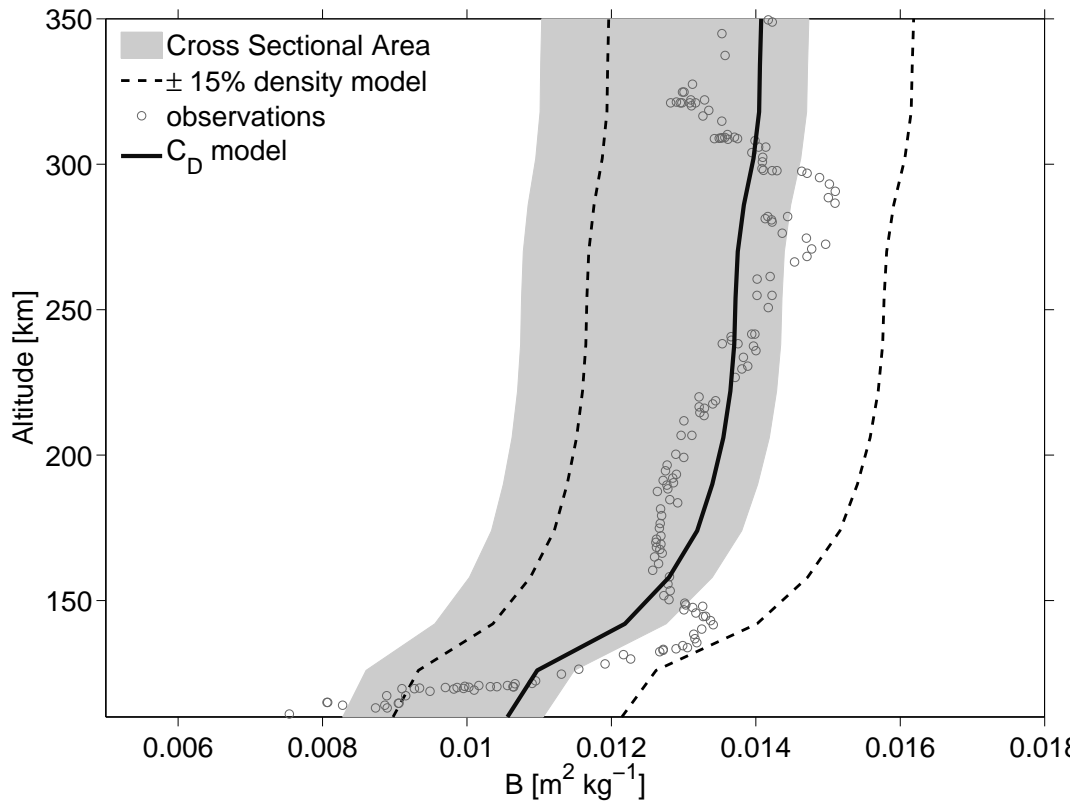


Figure 8.2: Sensitivity of the ballistic coefficient of a rocket body. The gray area indicates the range of possible values based on minimum and maximum cross sectional areas.

recognizing that T_a in equation 6.18b does not correspond to atmospheric temperature. From now on, the transition-width parameter in equation 6.18b will be referred to as T_{ad} . The tuning of model parameters as well as the determination of rocket body masses will be addressed in chapter 11.

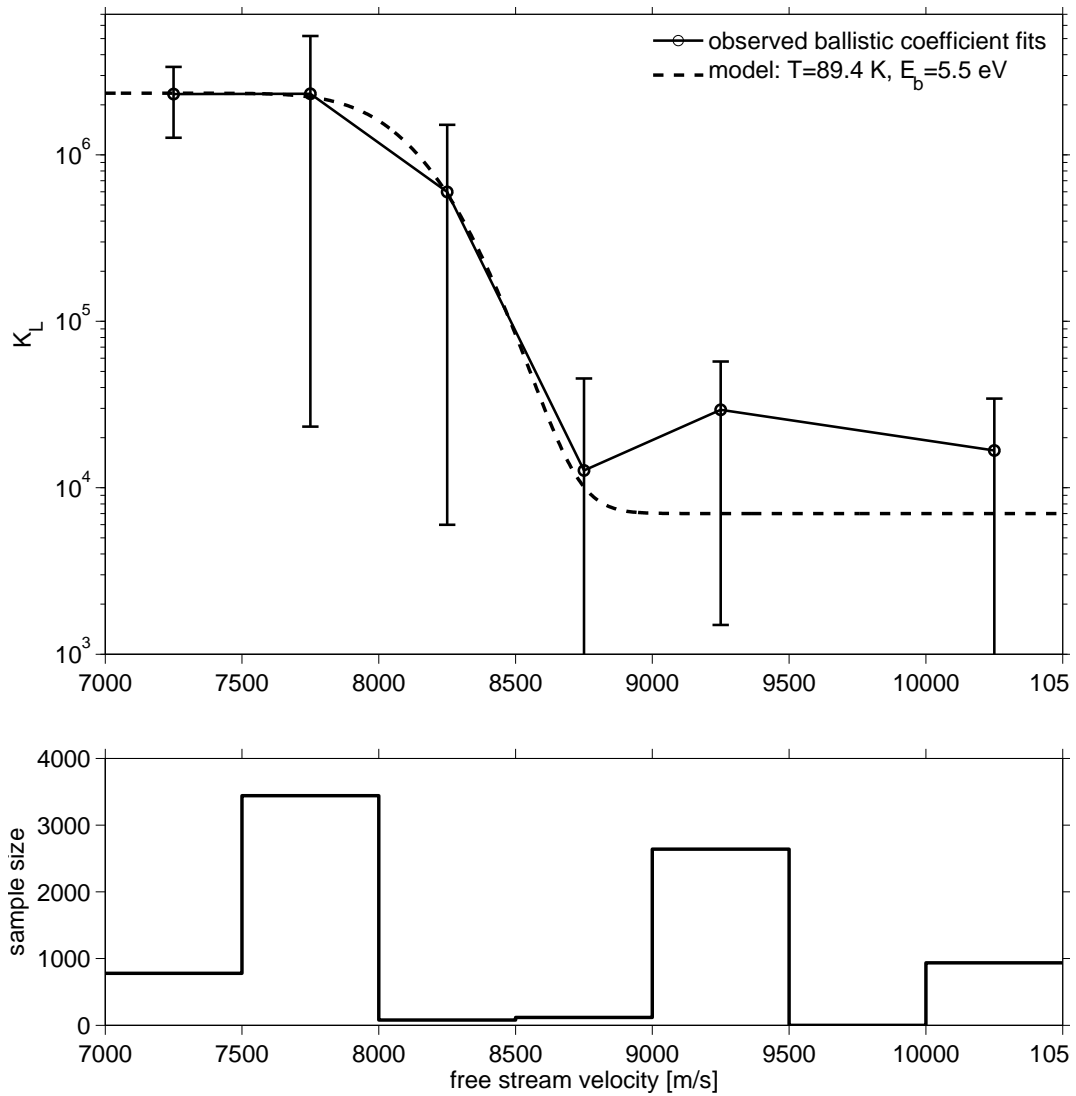


Figure 8.3: Changes in the Langmuir parameter as a function of energy with resulting fit. All rocket bodies were given a constant 2% propellant margin.

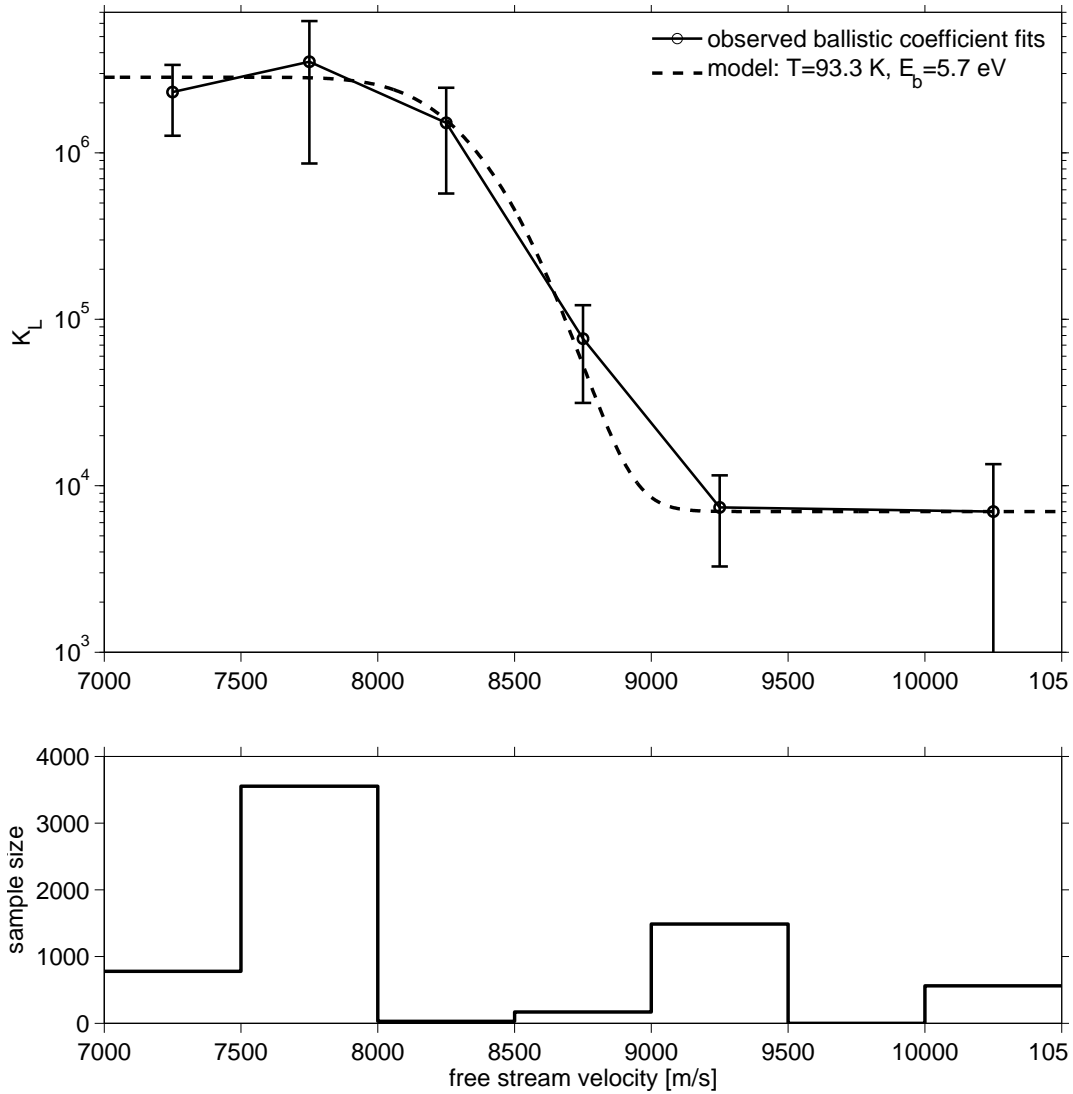


Figure 8.4: Changes in the Langmuir parameter as a function of energy with resulting fit. Propellant margin was ascertained from comparisons with spherical satellite ballistic coefficients.

Chapter 9

Evidence of Low Energy Accommodation Coefficients at Reduced Thermospheric Pressures

The availability of independent and colocated measurements of density and drag from GUVI and CHAMP observation enable a straightforward computation of drag coefficients. The underlying assumption in this analysis is that the GUVI data set has no density-dependent biases such as those associated with drag. More precisely, the GUVI limb inversion does not depend on atomic oxygen pressure which is believed to affect drag coefficients. As in Chapter 7, the product of atomic oxygen number density n_O and atmospheric temperature T_a will be referred to as atomic oxygen static pressure understanding that it is actually just a proxy thereof for any specific satellite shape. The derived drag coefficient values will be referred to as observed drag coefficients or $C_{D,GUVI}$. Equation 9.1 is the first step in computing this value by expressing the density measured by CHAMP as the ratio of a drag parameter K_D to the modeled drag coefficient used in the CHAMP analysis, $C_{D,CHAMP}$. Solving for K_D and dividing it by the GUVI-determined value, ρ_{GUVI} , yields the observed drag coefficient as shown in equation 9.2.

$$\rho_{CHAMP} = \frac{2m_{sc}a}{V_r^2 C_{D,CHAMP} A} = \frac{K_D}{C_{D,CHAMP}} \quad (9.1)$$

$$C_{D,GUVI} = \frac{K_D}{\rho_{GUVI}} \quad (9.2)$$

The primary goal of this study is to evaluate the feasibility of using joint limb-inversion and accelerometer data to study the gas-surface interactions with the aim of improving future drag and density

estimates. To do this, a simple plate model of CHAMP is used for comparisons to the observed drag coefficient, $C_{D,GUVI}$. These estimates will then be compared with $C_{D,GUVI}$ and the assumed accommodation coefficient adjusted in the model until the difference between the observed and modeled coefficients falls within a tolerance of 0.005. The selected drag coefficient model assumes that all molecules are reflected from the surface diffusely (in a cosine distribution). Equation 4.20b shows the drag coefficient equation for a flat plate at an angle of attack of θ_{in} in free-molecular flow. The assumption of free-molecular flow is valid for most satellites flying above 160-200 km and indicates that molecule-molecule conditions may be neglected. The speed ratio, s , is a ratio of free-stream velocity to the most-probable thermal speed of the gas. The reflection temperature, $T_{k,out}$, is expressed in equation 4.4 as a function of the Boltzmann constant k_b , the magnitude of free-stream velocity V_r , the surface temperature T_w , and the accommodation coefficient α . The CHAMP satellite drag is modeled using an array of 15 flat plates. Equation 4.20b is applied to each plate and a composite drag coefficient is computed as an average of all plate coefficients weighted by their planform areas. The composite drag coefficient is computed for each atmospheric constituent and the results are combined in an average weighted by the mass density of each species. Only He , O , N_2 and O_2 were used in the computation of accommodation, He being estimated by NRLMSISE while the rest were taken from GUVI measurements. GUVI limb scans of atmospheric temperature were also used as inputs to the drag coefficient model to compute the speed ratio s . Since the estimation of α depends on individual values of GUVI concentrations, and because the sensitivity of these to the GUVI-CHAMP coincidence distance cannot be determined, a conservative choice of coincident data will be made. Accordingly, the data set was reduced by excluding coincidences separated further than 150 km in space and 30 seconds in time. The CHAMP drag coefficient is very sensitive to changes in relative wind vector direction (\hat{v}_r in equation 2.3) when flying directly into the wind direction (small angle of attack). Relative atmospheric velocity is computed through the sum of the spacecraft velocity and the corotating atmosphere in the spacecraft reference frame. Because thermospheric winds are not modeled, small angles of attack can produce large errors. Flight configurations corresponding to small angles of attack will be avoided in the analysis by excluding all data above $45^\circ N$ and below $45^\circ S$ latitudes. The remaining coincidences are close to the equator where the angle of attack is relatively large and the drag coefficient much less sensitive to its variation. Figure 9.1 shows the reduction

in coincidences after refining the colocation criteria and restricting latitude values.

9.1 Multi-Instrument Results

Densities from GUVI and CHAMP were compared and the coincidence data set was checked against a previous comparison of GUVI densities with orbit-averaged drag performed by Emmert et al. [2006]. Figure 9.2 illustrates 4-month averages of GUVI and CHAMP densities from 2002 until 2007. A majority of the density values overlap within their stated $1 - \sigma$ uncertainties. Figure 9.3 shows the difference in GUVI and CHAMP densities as well as the standard deviation of those differences for the 4-month averages as a function of altitude. GUVI measurement biases are not strong functions of altitude [Meier and Picone, 1994, Emmert et al., 2006] (although the precision is) so that differences in the average densities may be due to altitude dependent biases in the CHAMP measurements. Altitude dependent biases in density measurements obtained from satellite drag have been shown to result from a variation in the drag coefficient. This variation is driven by changes in atomic oxygen static pressure which is a function of both altitude and solar activity ([Pilinski et al., 2011a, Moe and Moe, 2005]). Figure 9.4 examines the dependence of GUVI-CHAMP agreement on the static pressure of atomic oxygen as measured by GUVI. Note that many of the trends in the altitude plot are reflected in the atomic oxygen static pressure plot. This is because atomic oxygen concentration is a function of altitude while also being affected by solar activity. A histogram of the density differences is presented in Figure 9.5. The GUVI densities are biased negatively with respect to CHAMP measurements by approximately 5% and the standard deviation of the differences is 17.5%. Emmert et al. [Emmert et al., 2006] found the standard deviation to be 10-17% in the altitude range of CHAMP. The standard deviation found here falls closer to the higher value. This is not surprising considering that the present data set extends to 2007 and into an extreme solar minimum where signal to noise ratios are significantly smaller than during the 2002-2004 time range of previous analysis. The previous study also discovered a positive bias in GUVI measurements of approximately 5% however Pilinski et al. [Pilinski et al., 2011a] found a 10-11% error in the ballistic coefficient of the reference satellite used in that study (+5% relative GUVI density overestimate found by Emmert and -10% correction due to ballistic coefficient to density results in -5% density underestimate by GUVI or +5% density overestimate by CHAMP which

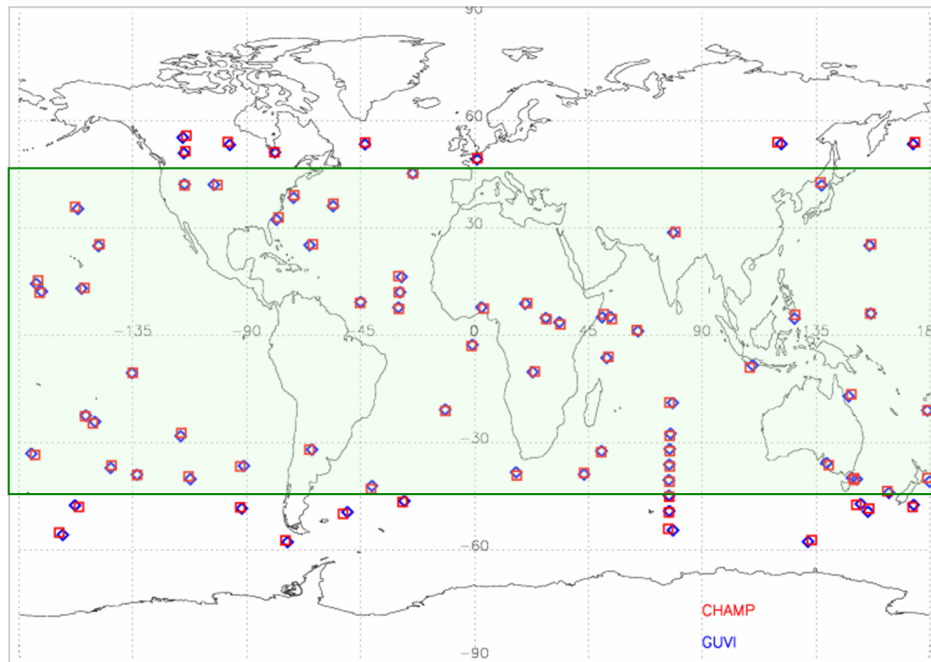


Figure 9.1: Coincidence data within 30 seconds and 150 km distance. The data was also restricted to exclude latitudes above 45°N and below 45°S latitudes.

agrees with the findings here). Taking into account a ballistic coefficient brings the previous and present bias estimates into close agreement.

Drag coefficient observations were computed using equations 9.1 and 9.2. The observed drag coefficients are plotted alongside the original values used in CHAMP density derivations [Sutton, 2007] in Figure 9.6. Accommodation values derived from observed drag coefficients are plotted as red crosses in Figure 9.7 as a function of static pressure of atomic oxygen. The blue circles are estimates of accommodation coefficient [Pilinski et al., 2011a] determined by comparing the orbital decay of seven spherical objects to an adjusted atmospheric model [Bowman and Moe, 2005]. The solid black curve is a Langmuir isotherm fitted to the blue circles. The Langmuir formula describes adsorption of atomic oxygen as a function of O static pressure. This adsorption is theorized to be the primary cause of changes in the accommodation coefficient below 500 km altitude [Moe et al., 1998]. The Langmuir isotherm fit predicts a rapid decay in accommodation below $n_O \times T_a$ values of $0.1 \times 10^{18} \text{ K m}^{-3}$. Due to the fortuitous location of the CHAMP measurements in altitude and solar activity, the GUVI-CHAMP accommodation values give coverage in this lower region. The newly derived accommodation coefficients range from 0.2 to 0.9 reinforcing the Langmuir fit prediction. Since the uncertainty in this analysis is approximately 20% in static pressure of atomic oxygen and as much as 30-40% in α , the data is best represented by a linear regression which is plotted as a solid red line. The linear regression agrees with the Langmuir fit in that it predicts a rapid decay in accommodation at low values of atomic oxygen static pressures. The overall energy accommodation result for all coincidences is 0.78 (+0.10, -0.13).

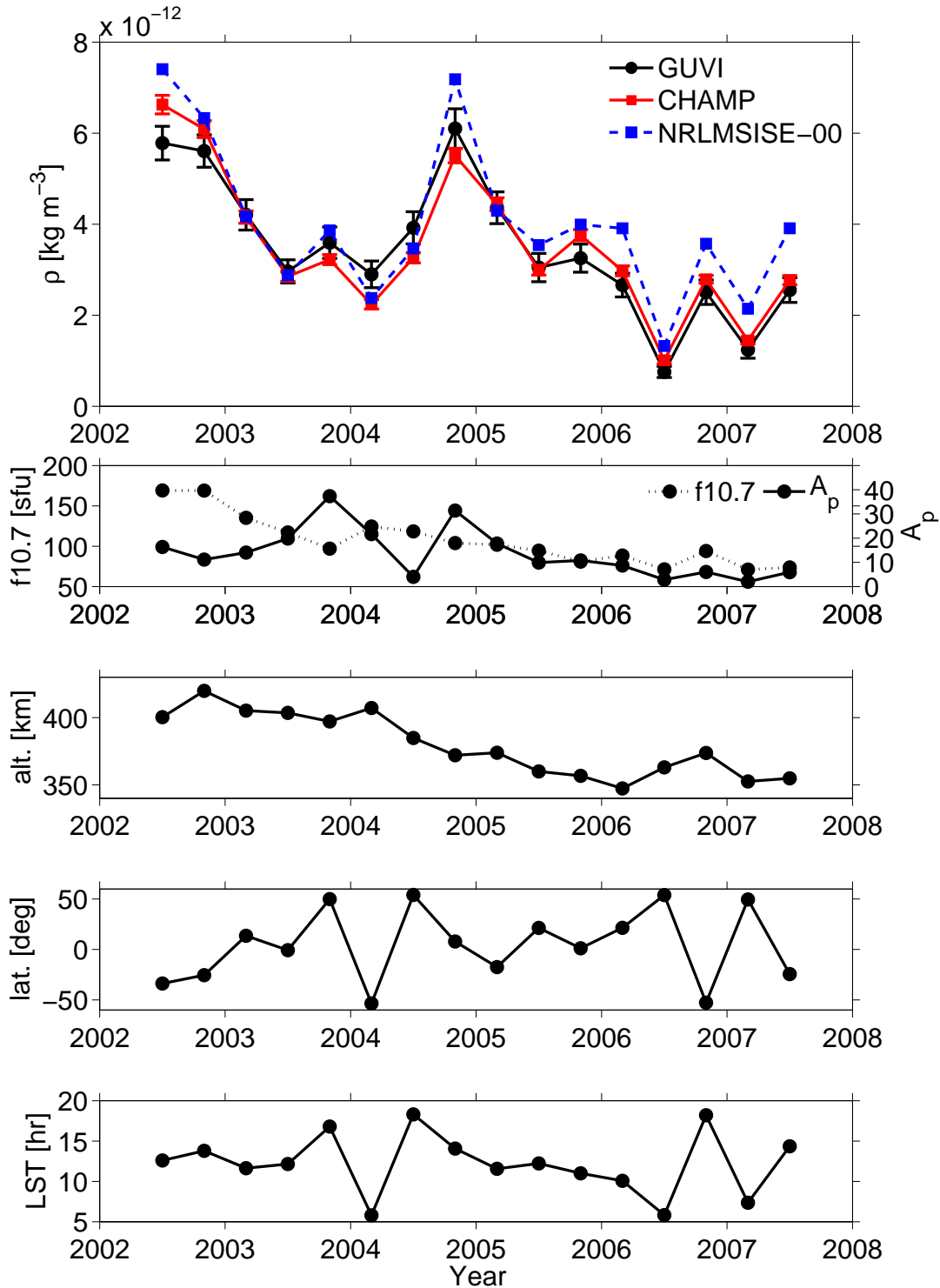


Figure 9.2: GUVI and CHAMP density measurements averaged by 4 month bins. The error bars indicate the uncertainty in each measurement as reported in the CHAMP and GUVI files. Plotted in the lower panels are the solar f10.7 and geomagnetic A_p indices, measurement altitudes, latitudes, and local-solar times.

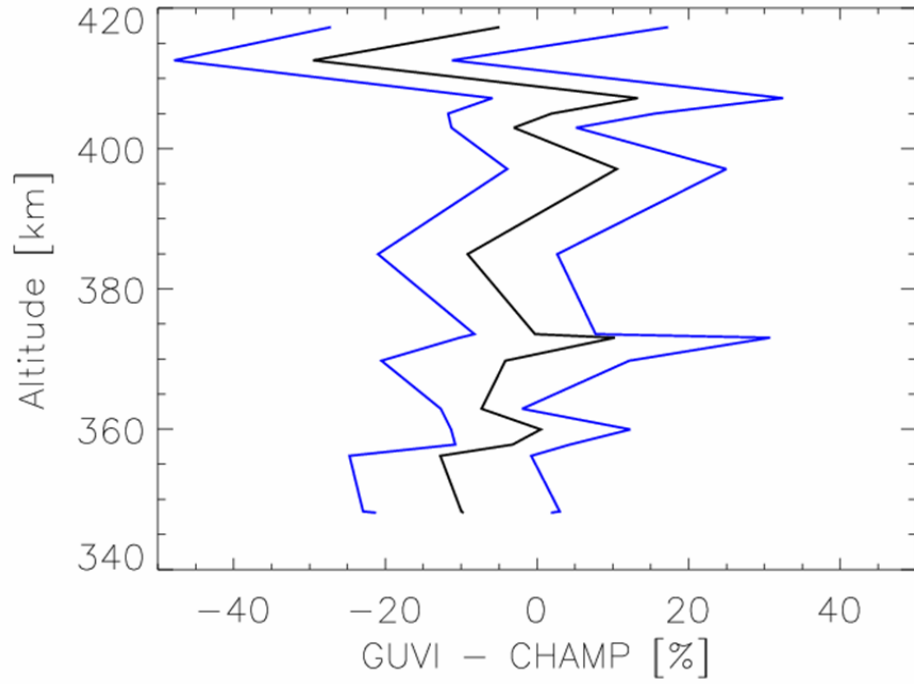


Figure 9.3: GUVI and CHAMP density differences as a function of altitude. The data was binned by altitude and the average is represented by the black line while the blue lines represent the standard deviation of each bin.

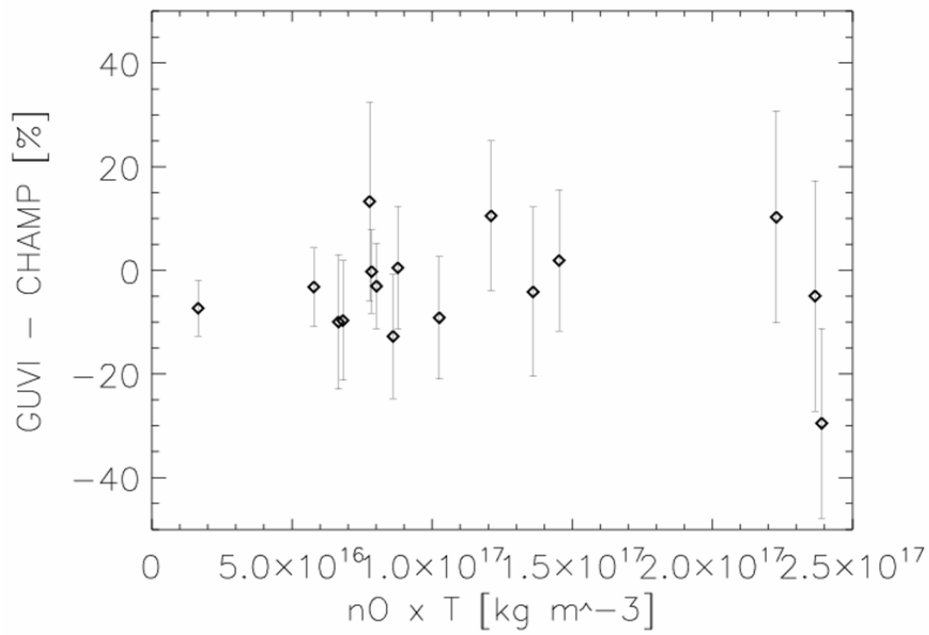


Figure 9.4: GUVI and CHAMP density differences as a function of atomic oxygen static pressure.

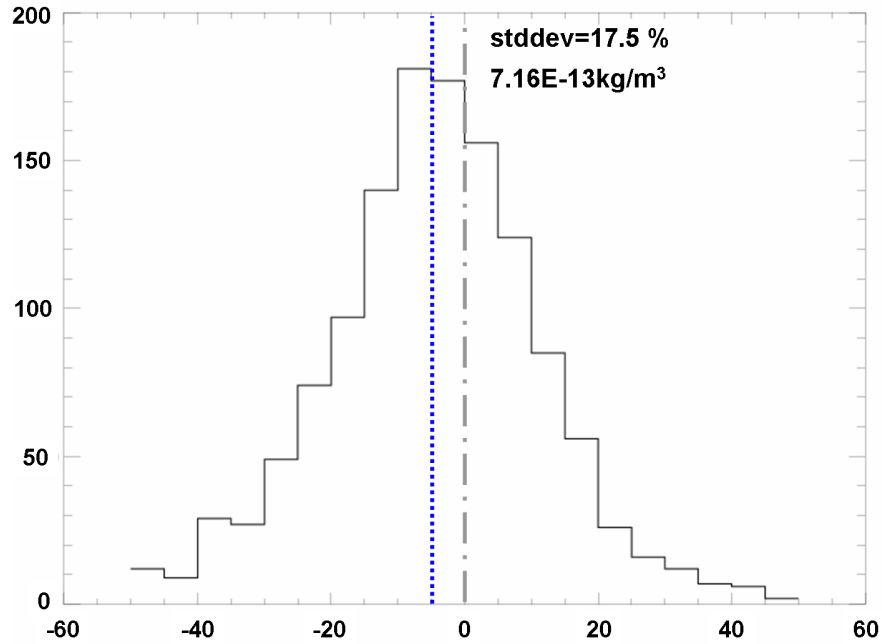


Figure 9.5: GUVI and CHAMP density difference histogram $200(\rho_{GUVI} - \rho_{CHAMP}) / (\rho_{GUVI} + \rho_{CHAMP})$. The black dashed line indicates zero-mean and the blue dotted line shows the mean of the distribution.

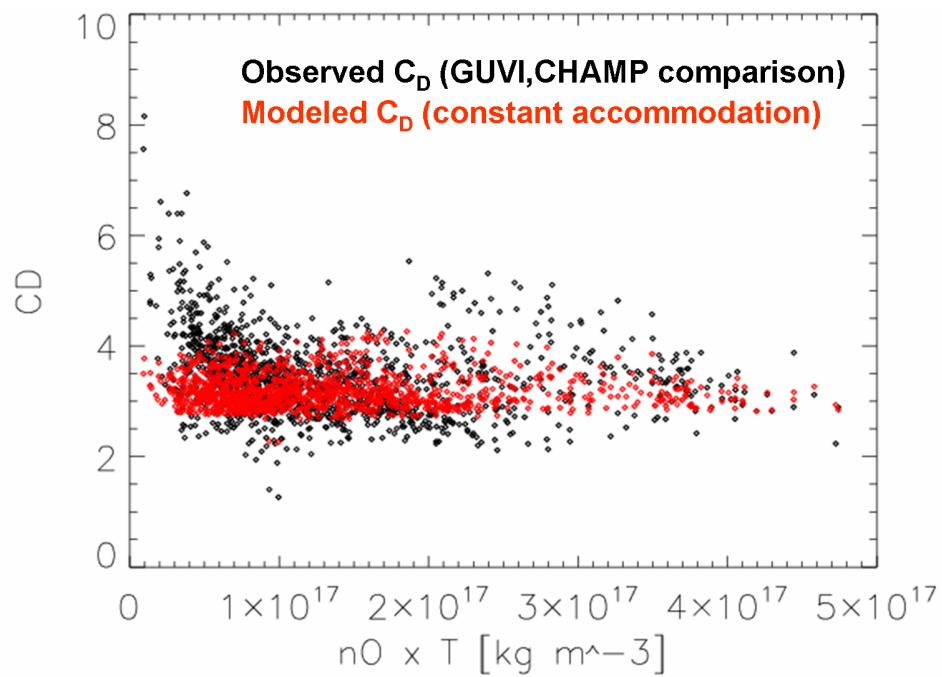


Figure 9.6: Observed and modeled drag coefficients as a function of atomic oxygen static pressure.

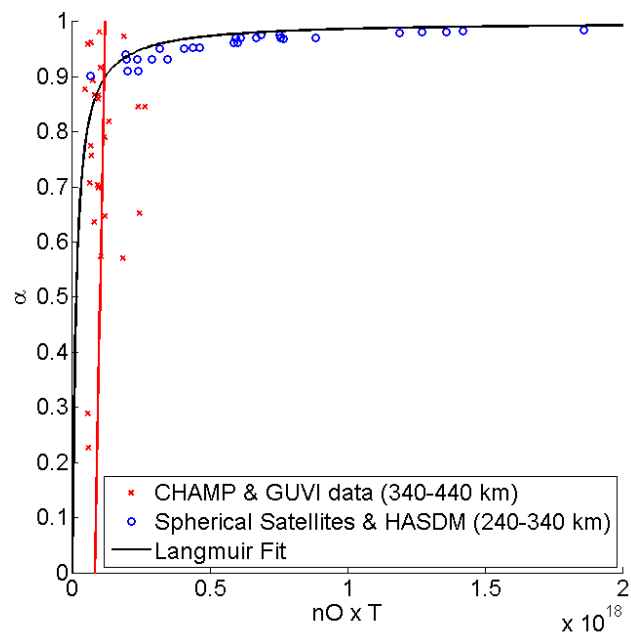


Figure 9.7: Estimated accommodation coefficients with previously determined values from lower altitudes. The red line is a linear fit to the data.

Chapter 10

Evaluating Gas-Surface Interactions Based on Orthogonal Force Coefficient Observations at Low Thermospheric Pressures

The results in this chapter have been obtained using techniques presented in section 6.3. The small-angle lift and drag data of the CHAMP and GRACE satellites will be evaluated from 2001 until 2008. In addition, gas-surface interactions will be evaluated during a yaw-maneuver performed by CHAMP on November 6th, 2002.

10.1 Small Angle Investigation

The slope of C_y/C_x was computed at the small β angles manifested in the nominal attitude mode of the CHAMP and GRACE satellites. Attitude and acceleration information was provided by Sutton [Sutton, 2008] with accelerometer scale-factors and biases derived by Bruinsma [Bruinsma et al., 2004]. The slope analysis method is explained in Chapter 6. In order to maximize signal strength, the data is restricted to geographic latitudes of $\pm 15^\circ$ and local solar times between 14h and 17h. Furthermore, the solar radio flux (F10.7) and global geomagnetic index (A_p) are limited to values under 175 sfu and 15 respectively. This sampling maximizes the ratio of corotational wind magnitudes, which can be computed exactly, to the geophysical winds, which can only be estimated. Any data collected during thruster activity was removed and the GRACE switch maneuver in December of 2005 was also omitted from the analysis. The resulting dataset consists of daily C_y/C_x slopes beginning in 2001 and ending in 2008. Only days with at least 30 C_y/C_x measurements were considered.

The CHAMP satellite flew at lower altitudes than GRACE-A or GRACE-B and experienced higher

drag accelerations. Figure 10.1 shows the distribution of small-angle C_y/C_x slopes during the analysis period. The effective pressure proxy (computed using equation 6.7) over this time was approximately 1.1×10^{-6} Torr. The figure also indicates the slopes which would be expected under the assumptions of various GSI models. Namely, the fully diffuse model with variable energy accommodation is compared to the blend of a fully accommodated diffuse model with the quasi-specular (QS) model of Schamberg having an energy accommodation based on Goodman's formula (equation 6.11). For the Schamberg model, accommodation is computed based on the surface material of each panel and the ν and ϕ_o parameters are taken to be 2.215 and 25° respectively. The data in Figure 10.1 indicates that the observations are most consistent with a fully diffuse model having an energy accommodation between 0.60 and 0.86 or a fully accommodated diffuse model with a QS fraction (f_{qs}) between 0.20 and 0.50. The 10% trimmed-mean and median of the measured distribution for CHAMP are 0.0256 and 0.0254 respectively and the standard deviation is 0.0124. This is consistent with either a fully diffuse model with an α of 0.86 (+0.04, -0.26) or a blended model with an α of 1.00 and a f_{qs} of 0.25 (+0.25, -0.05). Note that the two scattering models are not distinguishable based on this information alone. Furthermore, the two models chosen for comparison represent points along a full spectrum of models and were selected based on considerations described in Chapters 2 and 3 as well as to make the analysis tractable.

The small-angle results for GRACE-A and GRACE-B are shown in Figures 10.2 and 10.3 respectively. For GRACE-A, the 20% trimmed mean and median of the measured distribution are 0.0138 and 0.007 with a standard deviation of 0.0578. For GRACE-B, the mean and median of the slope distribution are 0.006 and 0.005 with a standard deviation of 0.108. Unfortunately the spread of the distributions for the GRACE satellites is much larger than the variation between the different models. Therefore, no conclusions about GSI may be drawn from the GRACE small-angle analysis.

10.2 Yaw Maneuver Investigation

Yaw maneuver analysis permits the evaluation of orthogonal aerodynamic forces over a wide range of β angles. The analysis is focused on the CHAMP yaw maneuver on November 6th, 2002. During this day, the average satellite altitude was 407km and the partial atomic oxygen pressure was 2.2×10^{-6} Torr. The method

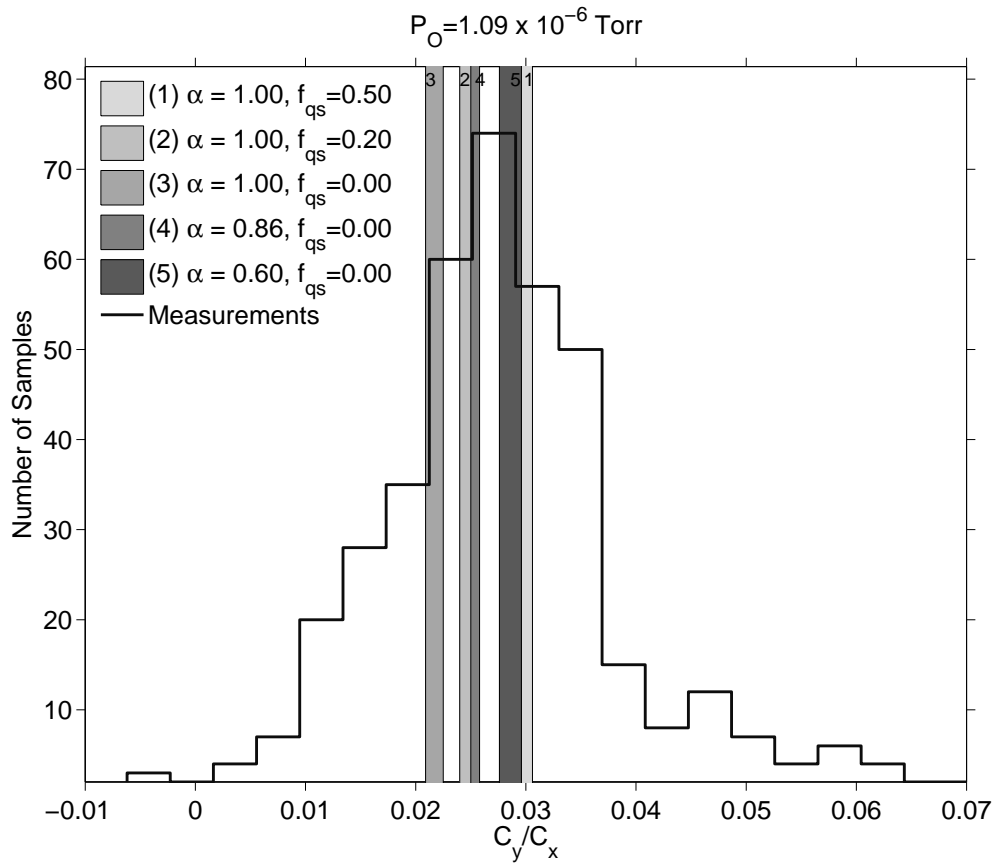


Figure 10.1: Measurements and models of C_x/C_y slopes for the CHAMP satellite from data taken between 2001 and 2008.

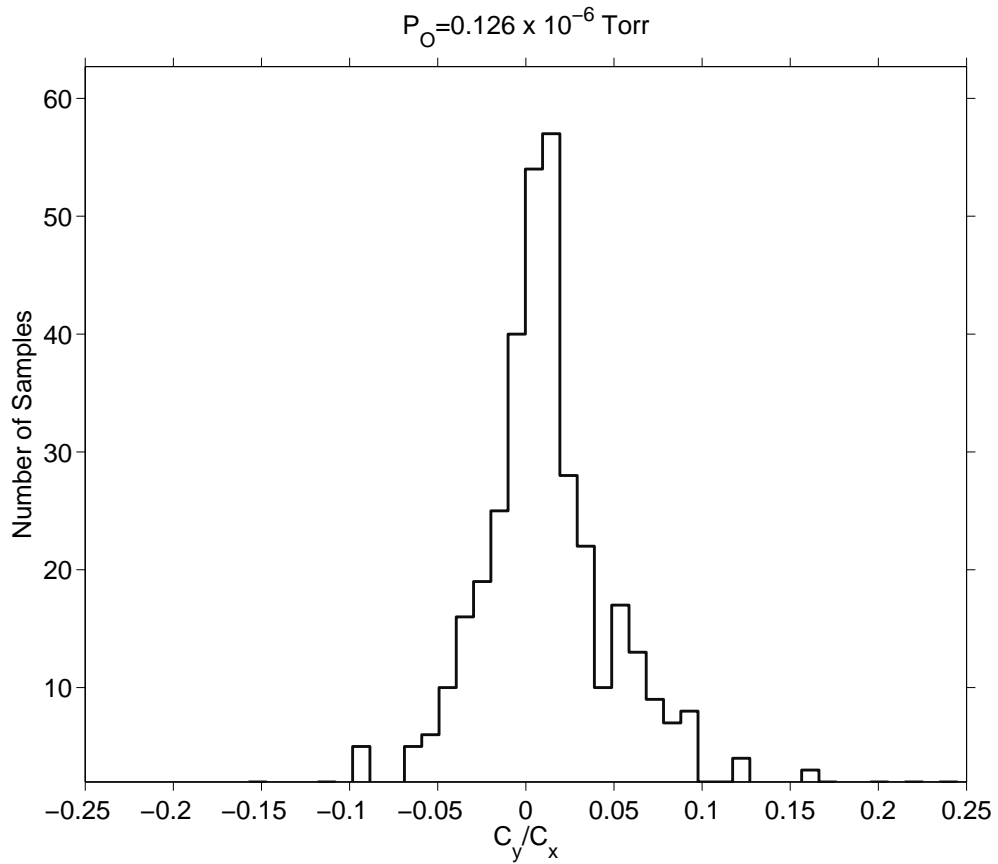


Figure 10.2: Measurements of C_x/C_y slopes for the GRACE-A satellite from data taken between 2002 and 2008.

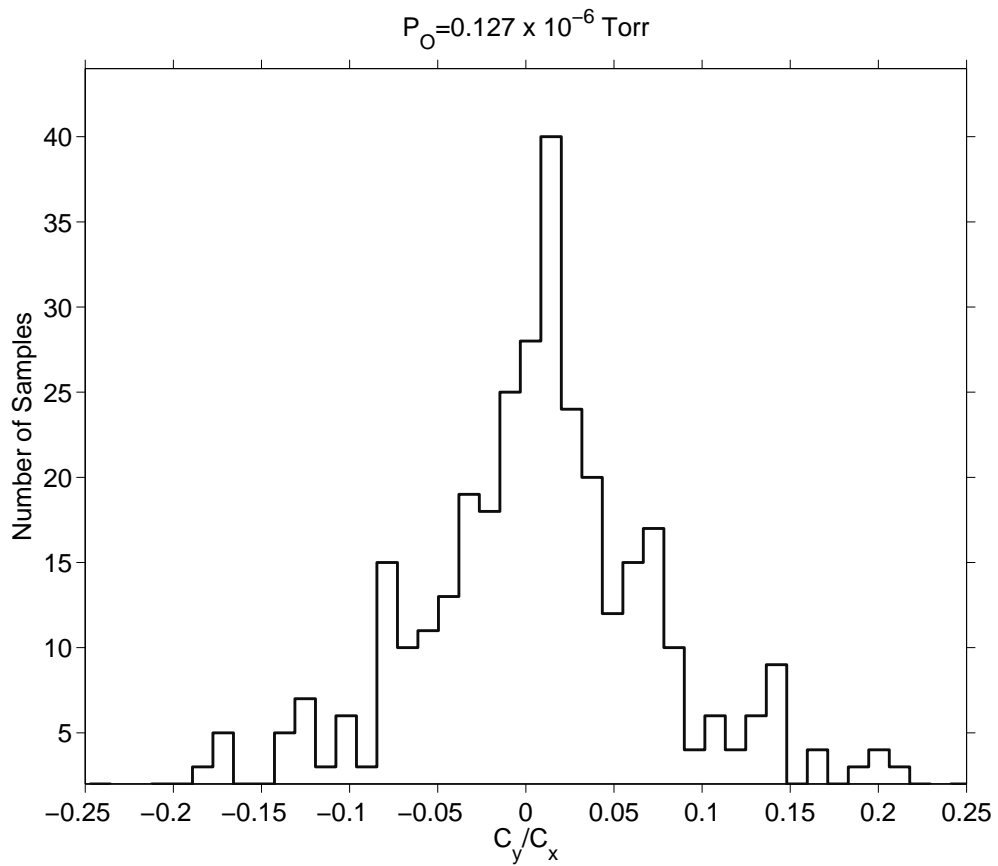


Figure 10.3: Measurements and models of C_x/C_y slopes for the GRACE-B satellite from data taken between 2002 and 2008.

of analysis is described in detail in Chapter 6. The SPARCS model is employed to map model parameters to the observed values of C_L/C_D and C_y/C_x . The CHAMP level 1 model, described in section 4.3.3, is modified such that the area orthogonal to the +Y direction matches that of the latest ESA ANGARA model (see Table 4.1). Figure 10.4 demonstrates how x and y accelerations (first panel at the top) are mapped to projected lift (second panel from top) and drag (third panel) directions, and then finally combined into the lift to drag and a_y/a_x ratios (fourth panel). Note that the a_y/a_x ratio is computed for β -angles ranging from 0° to 50° while a_x/a_y is computed from 30° to 90° . This is done to avoid the large errors associated with dividing by a small a_x near 90° and a small a_y near 0° . The last panel of Figure 10.4 also demonstrates that the value of C_L/C_D is significantly smaller than the x and y direction ratios. This results in a lower signal to noise ratio for C_L/C_D .

Next, the two models for aerodynamic force coefficients are plotted in Figures 10.5 and 10.6. For the diffuse model with incomplete accommodation of 0.93 (Figure 10.5) the drag coefficient is large at low sideslip angles and settles to a lower value at β angles near 90° . The lift coefficient is approximately zero near sideslip angles of 0° and 90° and has a maximum at around 30° . The resulting lift-to-drag ratio also has a maximum around 30° . Figure 10.5 also illustrates that while the qualitative agreement for the plate and SPARCS test-particle models is good, the absolute values of C_L/C_D are significantly different. Therefore, the SPARCS generated lookup tables will be used for model parameter inversion. For a 100% QS model, the drag coefficient behavior is qualitatively much different (Figure 10.6). Note that C_D now undergoes a minimum near a β angle of 20° and that the value near 0° is much lower than for the diffuse model. The C_L/C_D ratio is qualitatively similar to the diffuse model. In fact, a fraction of QS reflection f_{qs} can be chosen to closely match the C_L/C_D results from any α input in the fully diffuse model. To distinguish the two models, a further test will be needed and is discussed later in this section.

Note that the difference between models of various GSI parameters is greater in the lift and drag reference frame. This can be seen in Figures 10.5 and 10.8 for the diffuse model with incomplete accommodation. The measured results in these figures have been averaged by 5° β -angle bins. The comparison with diffuse models shows that neither full accommodation nor accommodation below 0.80 can reproduce the measured force ratios. Already, the impact of this method can be appreciated as a large family of GSI

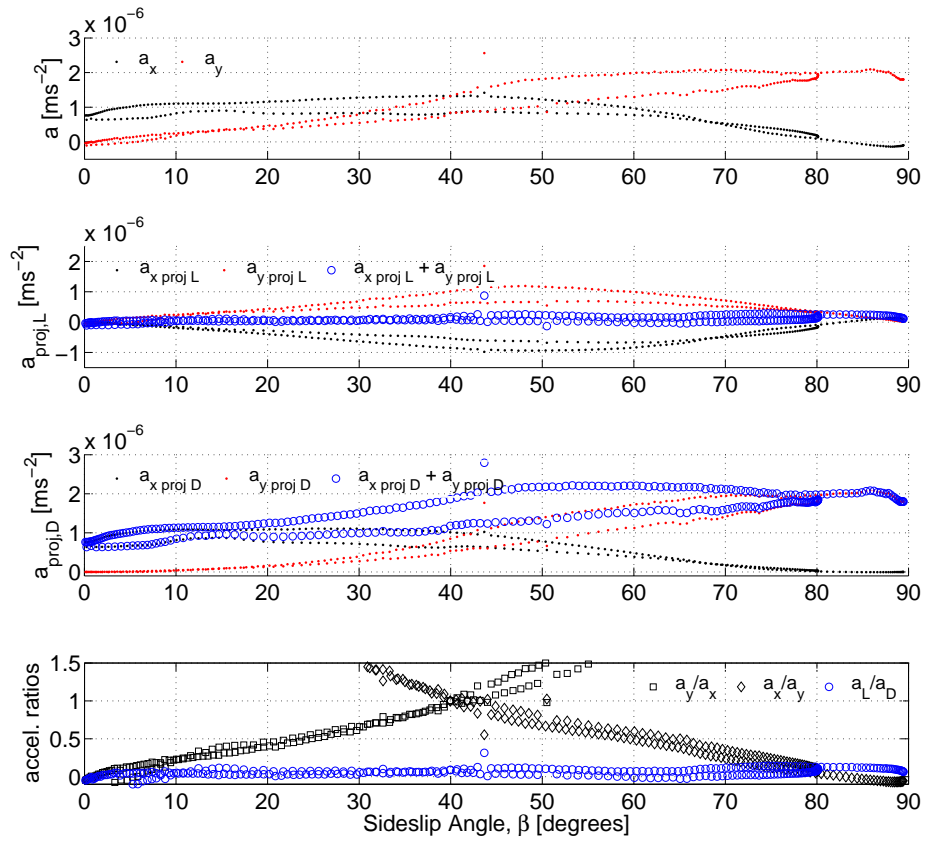


Figure 10.4: Measurements of orthogonal (x and y) accelerations and their projection onto the lift and drag directions.

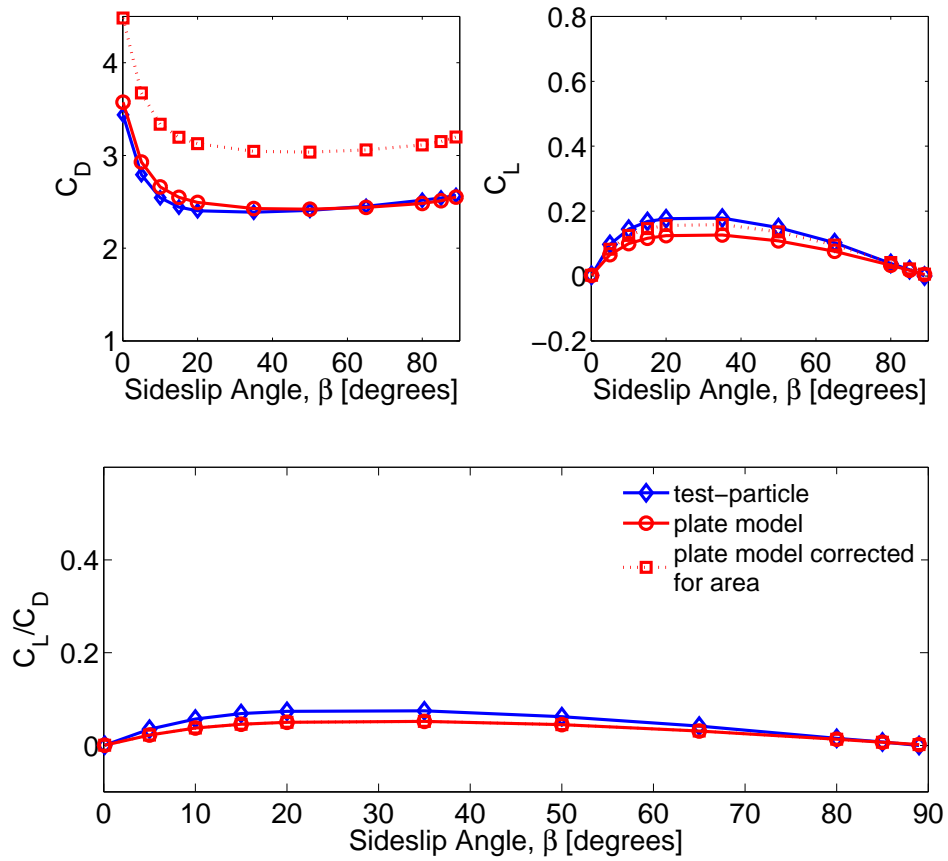


Figure 10.5: Comparison of test-particle and panel solutions for the drag and lift coefficients of CHAMP assuming fully diffuse reflection with an accommodation coefficient of 0.93.

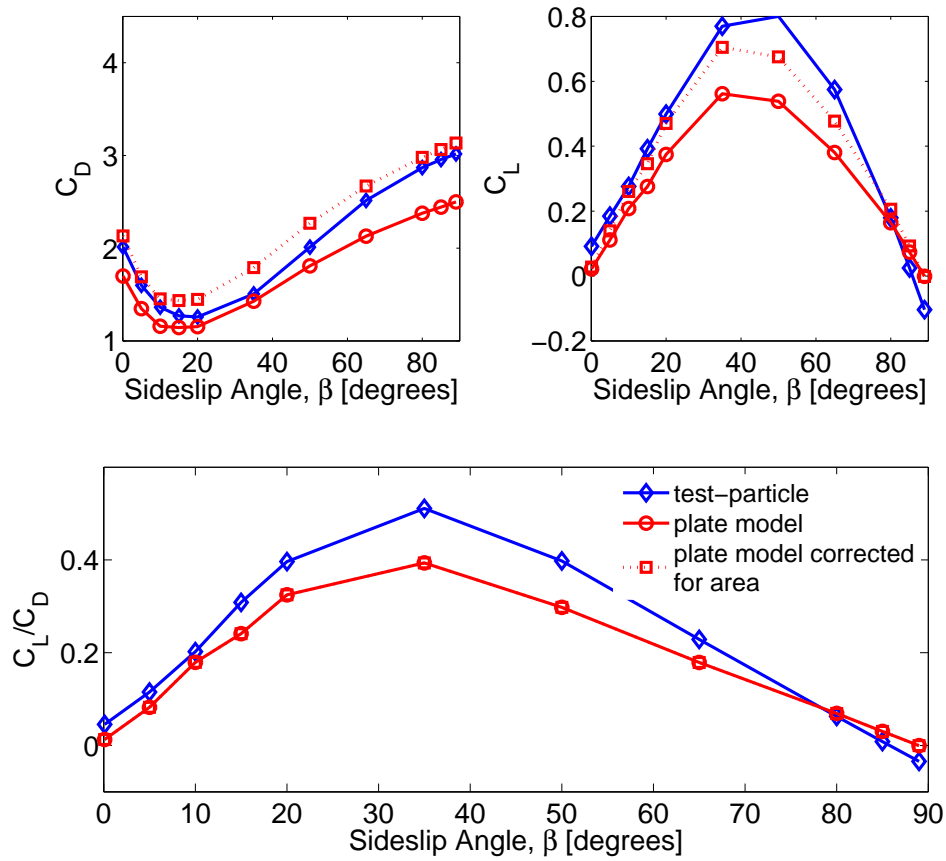


Figure 10.6: Comparison of test-particle and panel solutions for the drag and lift coefficients of CHAMP assuming Schamberg reflection only with panel dependent accommodation based on the Goodman model.

parameters can be eliminated by visual inspection alone. Figures 10.9 and 10.10 show a similar comparison for the blended QS model. It can be seen that a 50% QS overestimates the lift to drag ratio. This confirms previous assertions that specular or quasi-specular reflections do not dominate gas-surface interactions below 500 km altitudes [Imbro et al., 1975, Gregory and Peters, 1987, Moe et al., 1998, Moe and Moe, 2005, Moe and Bowman, 2005].

Figure 10.11 illustrates the RMS difference between measurements and models for C_y/C_x and C_x/C_y ratios (black circles) as well as C_L/C_D (red squares) for the fully diffuse (left panel) and quasi-specular (right panel) models. The results indicate that a diffuse model with incomplete accommodation of 0.89 (+0.02, -0.03) best fits the available data along with a blended QS model with a f_{qs} of 0.20 (+0.05 - 0.05). These results are close to the small-angle values determined in Section 10.1. Note that the value of 0.93 for the energy accommodation of the fully diffuse model commonly used to analyze CHAMP data [Sutton, 2009, Doornbos et al., 2009] seems slightly too high during November 2002.

Thus far, the blended quasi-specular model along with the fully-diffuse model are equivalent in their ability to reproduce observed aerodynamic acceleration ratios given the appropriate values of f_{qs} and α respectively. To further distinguish the two scattering models, the ratio of measured to modeled density will be evaluated. The computation of a measured to modeled density ratio, or R , is a common technique [Doornbos, 2011, Emmert et al., 2006] for removing spatial and temporal sampling differences between measurements. In this case, the value of accelerometer-measured density (ρ_{acc}) will be divided by the NRLMSISE-00 [Picone et al., 2002b] model of atmospheric density (ρ_{mod}). The variable ρ_{acc} is defined as

$$\rho_{acc} = \frac{2a_D m_{sc}}{AC_D(\alpha, f_{qs}) V_r^2} \quad (10.1)$$

where a_D is the measured value and C_D is computed for several values of α and f_{qs} . Values of $R = \rho_{acc}/\rho_{mod}$ are evaluated for November 6th, 2002 distinguishing between the forward flying mode R_f and sideways flying mode R_s . The data used to compute the transition from one mode to the other is not included. The results are displayed as $|1 - R_s/R_f|$ in Figure 10.12 wherein the candidate values from the force-ratio analysis are circled. A value of $|1 - R_s/R_f|$ near zero indicates good agreement between densities measured in forward and sideways flying modes. Note that the candidate value for blended quasi-specular reflection results in

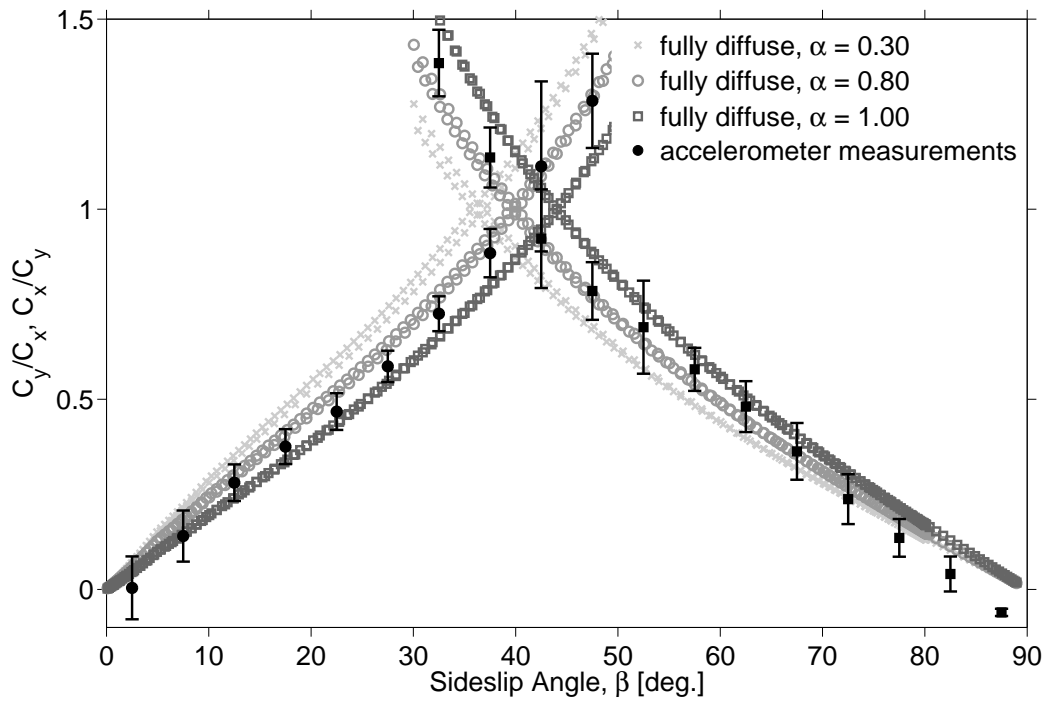


Figure 10.7: Measurements and diffuse models of C_y/C_x made by CHAMP during a yaw maneuver on November 6th, 2002.

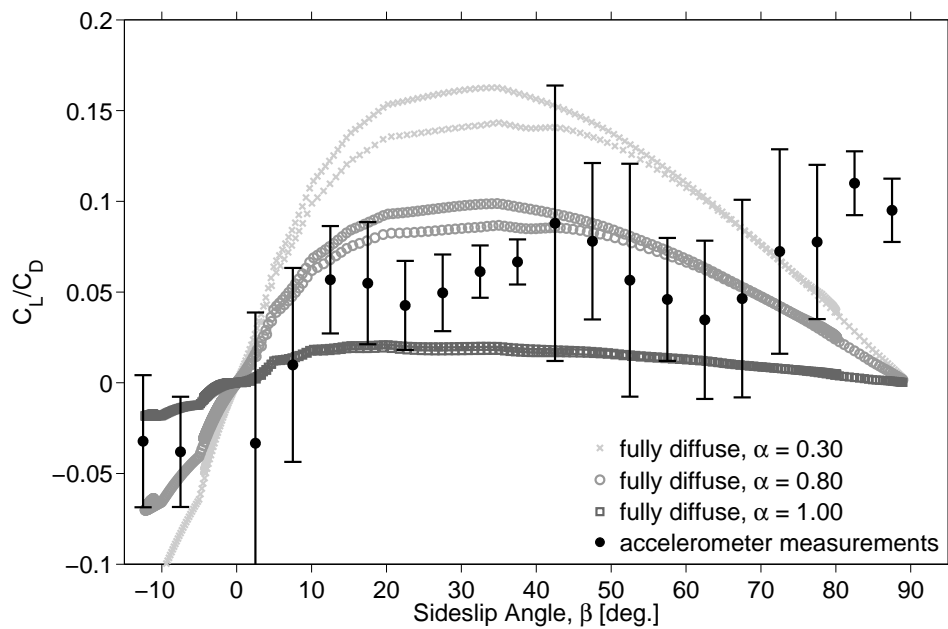


Figure 10.8: Measurements and diffuse models of C_L/C_D made by CHAMP during a yaw maneuver on November 6th, 2002.

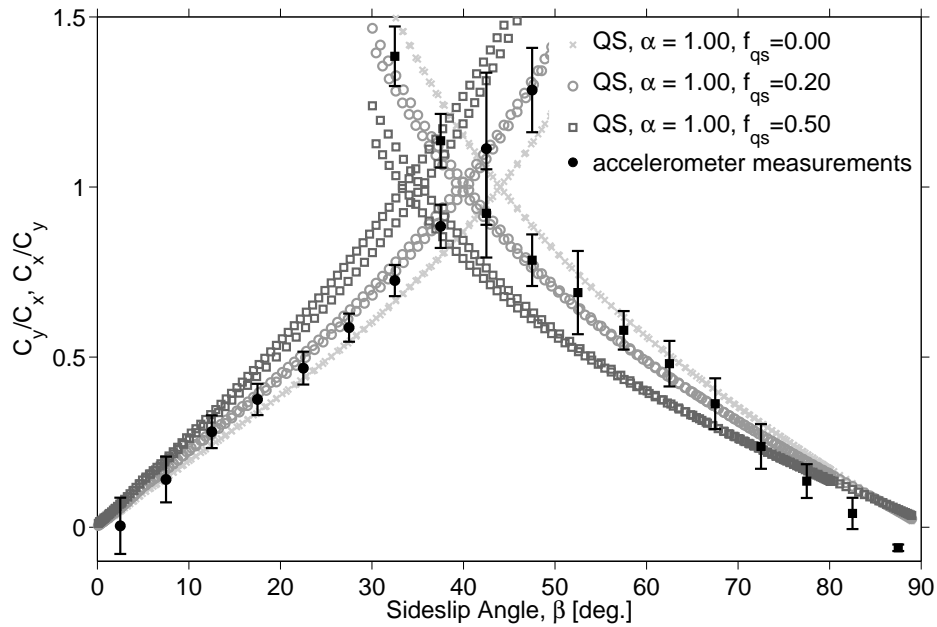


Figure 10.9: Measurements and QS models of C_y/C_x made by CHAMP during a yaw maneuver on November 6th, 2002.

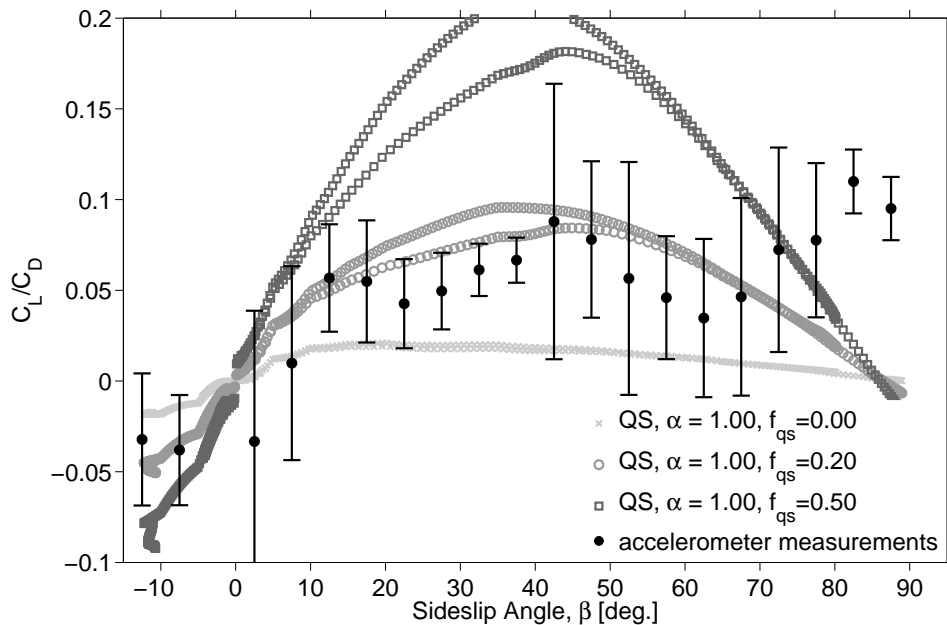


Figure 10.10: Measurements and QS models of C_L/C_D made by CHAMP during a yaw maneuver on November 6th, 2002.

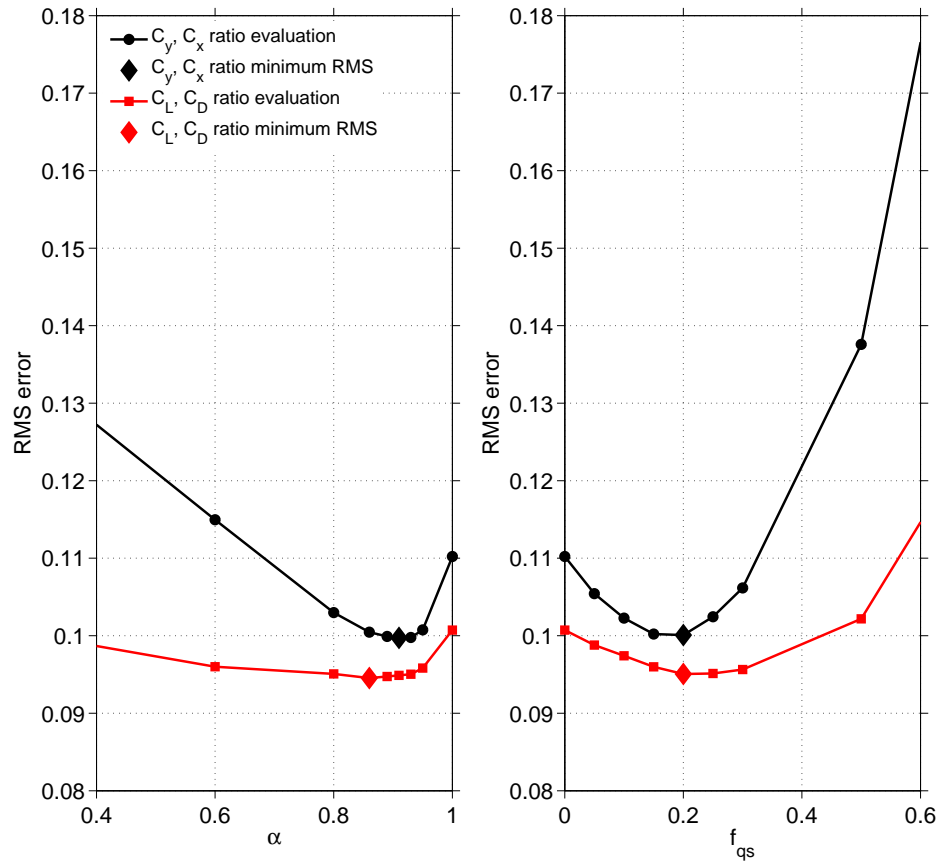


Figure 10.11: RMS error v.s. GSI model parameters for cosine reflection (left) and a cosine/Schamberg model blend (right). The RMS values are computed by comparing both lift and drag as well as x and y direction accelerations. The minima indicate the most successful GSI parameters.

a density artifact of approximately 5.6%. Meanwhile, the diffuse model results in mean densities from the forward and sideways flying modes which are within 0.5%.

A fully diffuse reflection model with partial accommodation coefficient α of 0.89 (+0.02, -0.03) best reproduces the observed accelerations in both the drag and lift directions. The small-angle measurement has resulted in an accommodation value of 0.86 (+0.04, -0.26). Note that the average atomic oxygen pressure during the November 2002 yaw maneuver is larger than for the long-term average small-angle slope measurement. The best-fit value of α at the lower atomic oxygen pressure is smaller which is in agreement with the adsorption-based theory described in chapter 8.

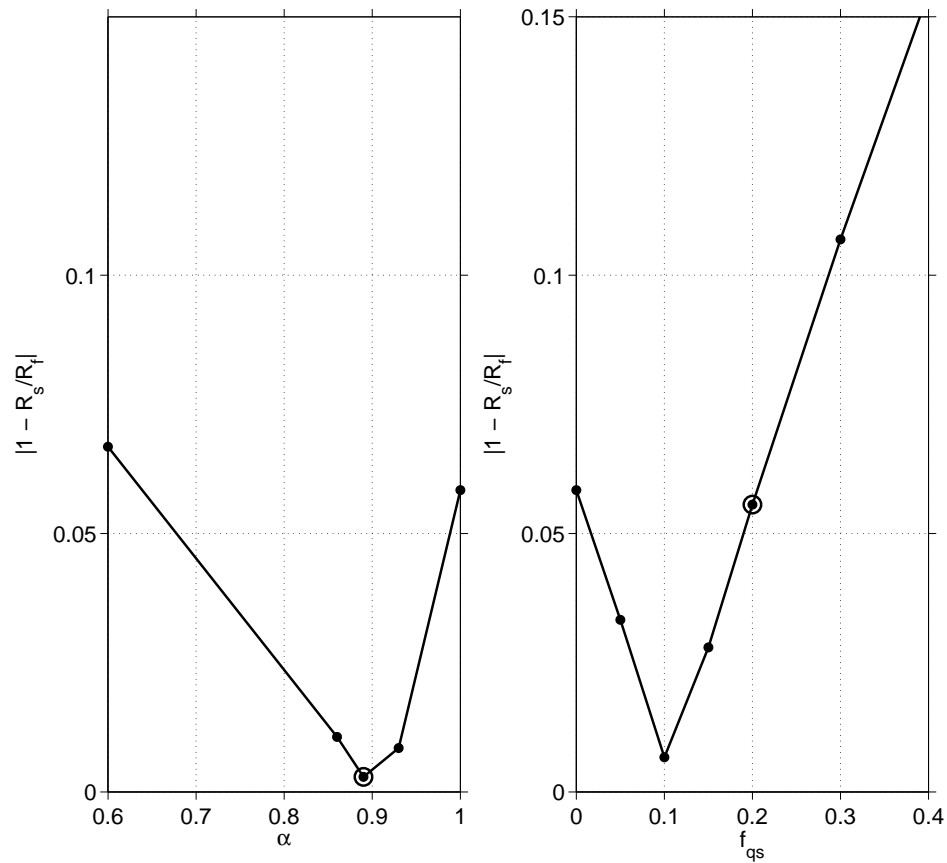


Figure 10.12: Mean ratios of measured to modeled density are computed for forward flying and sideways flying modes. The mean ratio from the sideways flying mode (R_s) is divided by that of the forward-flying mode (R_f) and the results ($|1 - R_s/R_f|$) are plotted above as a function of the GSI parameters. The two candidate values identified through lift/drag analysis are circled. Note that the cosine-reflection model with incomplete energy accommodation results in densities which are more consistent between the forward and sideways flying modes.

Chapter 11

Semi-Empirical Model for Compact Shapes

A semi-empirical model for satellite accommodation and drag coefficients can now be constructed based on the results presented in chapters 9-10. The semi-empirical satellite accommodation model (SESAM) implementation is illustrated by the block diagram in Figure 11.1. The lookup tables used in SESAM are listed in Appendix C. The model parameters are listed in Table 11.1. The specification and evaluation of recommended model parameters will be the subject of this chapter.

11.1 Model Evaluation and Tuning

The current method of determining Langmuir parameters introduces fuel margin dependence into the determination of $K_{L,o}$ as can be seen in Figures 8.3 and 8.4. However, spherical satellites whose masses are known may be used to constrain the low-velocity Langmuir parameter. Figure 11.2 shows the average observed drag coefficients of all spherical objects in Table 5.4 as a function of atomic oxygen pressure. Also shown in the figure is the SESAM model drag coefficient under three assumptions for $K_{L,o}$ as well as results of several other models. The first model is based on equation 4.20a with the energy accommodation

Table 11.1: Optimal parameters for SESAM

Parameter	Sym.	Value
adsorption energy	E_b	5.7 eV
transition temperature	T_{ad}	93 K
initial Langmuir param.	$K_{L,o}$	$5 \times 10^6 \text{ Torr}^{-1}$
final Langmuir param.	$K_{L,f}$	$3 \times 10^4 \text{ Torr}^{-1}$
average substrate mass	m_s	65 amu

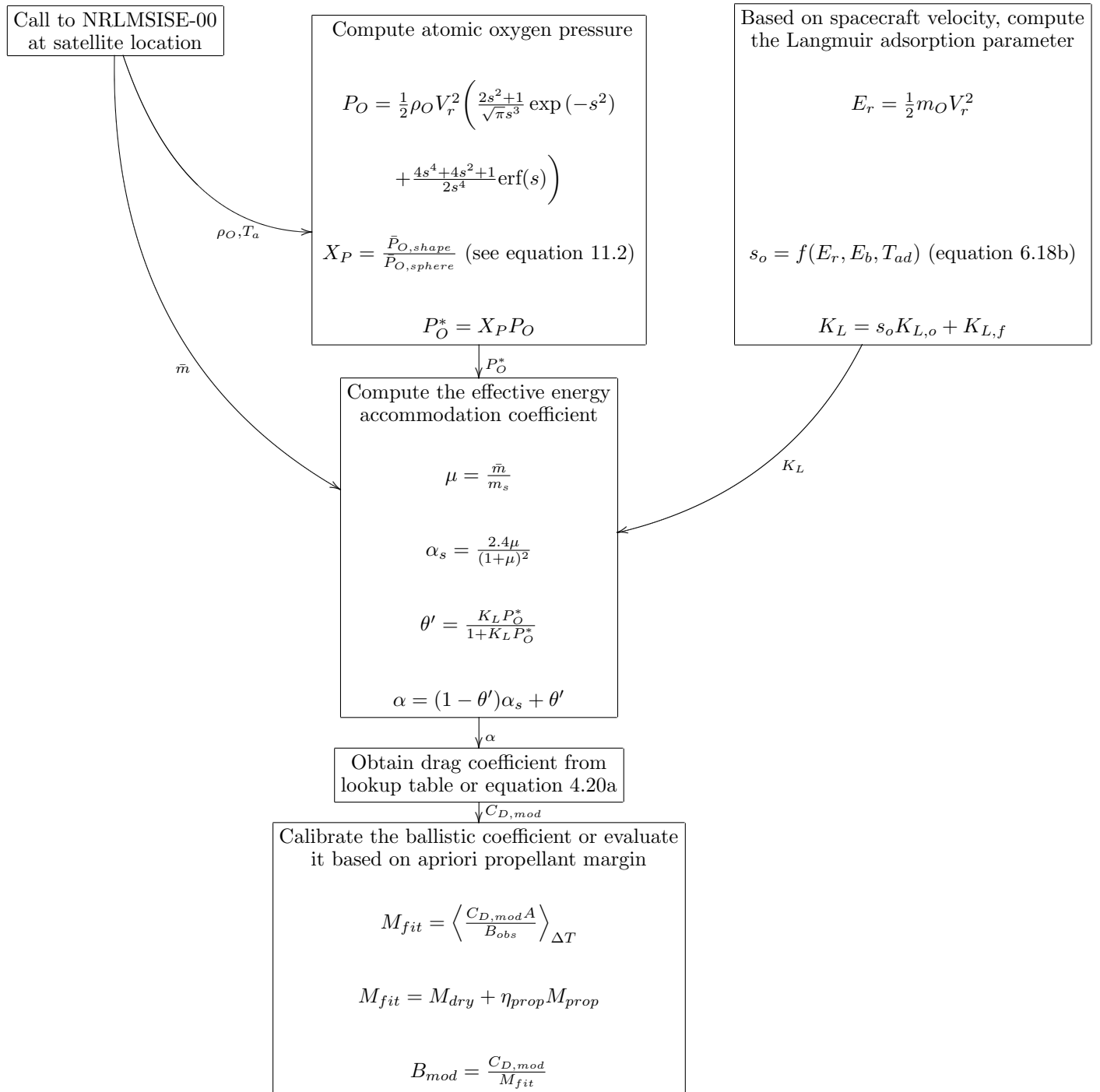


Figure 11.1: Implementation of SESAM.

coefficient fixed at several values. The second model is also based on equation 4.20a where the accommodation coefficient is based entirely on the Goodman model (equation 6.11). The C_D comparisons in Figure 11.2 indicate that the SESAM model with a $K_{L,o} = 5 \times 10^6 \text{ Torr}^{-1}$ outperforms both the Goodman and fixed accommodation models.

The sphere data can be further leveraged to examine SESAM performance as a function of surface mass (m_s) assumptions. One can compare observed drag coefficients of only those spherical satellites whose surface material is both known and homogeneous over the surface of the sphere. Figure 11.3 shows the effect of various surface masses on drag coefficient for a range of atomic oxygen pressures. There appears to be no statistically significant difference between the drag coefficients of objects having different surface masses below 500km altitude. The possible exception is gold ($m_s = 197 \text{ amu}$) which seems to cause a drag coefficient which is approximately 2% higher compared to aluminum ($m_s = 27 \text{ amu}$) at low atomic oxygen pressures. The SESAM model does reproduce this difference which can be attributed to higher fraction of Goodman accommodation model being mixed in at higher (470 km to 520 km). These findings are consistent with the results of Moe and Bowman who also concluded that the effects of surface properties on the drag coefficient of spheres is negligible [Moe and Bowman, 2005, Bowman and Moe, 2005]. Therefore, setting the SESAM model surface mass to a rather arbitrary value such as 65 amu seems to have little effect below an altitude of 500 km.

In addition to the fixed accommodation and Goodman models, it is also instructive to compare SESAM to a fixed ballistic coefficient model. This is because several derivations of atmospheric density from satellite drag such as HASDM [Bowman, 2002] or the long-term density dataset [Emmert, 2009] assume a “true” ballistic coefficient equal to the average fitted value over the beginning of the object lifetime. In the context of atmospheric density measurement the ratio of the fitted to “true” (or in our case modeled) ballistic coefficients is equal to the ratio of observed to modeled density. Therefore, the ratio of observed to modeled coefficients will be evaluated for four models (SESAM, Goodman, fixed accommodation, and fixed average ballistic coefficient). Since the observed and modeled atmospheric densities can be approximated by normally distributed random variables, the ratio of B_{obs} to B_{mod} (ΔB) should result in a Cauchy distribution. Errors in the modeled ballistic coefficient will result in a distortion of the distribution. For the three physical

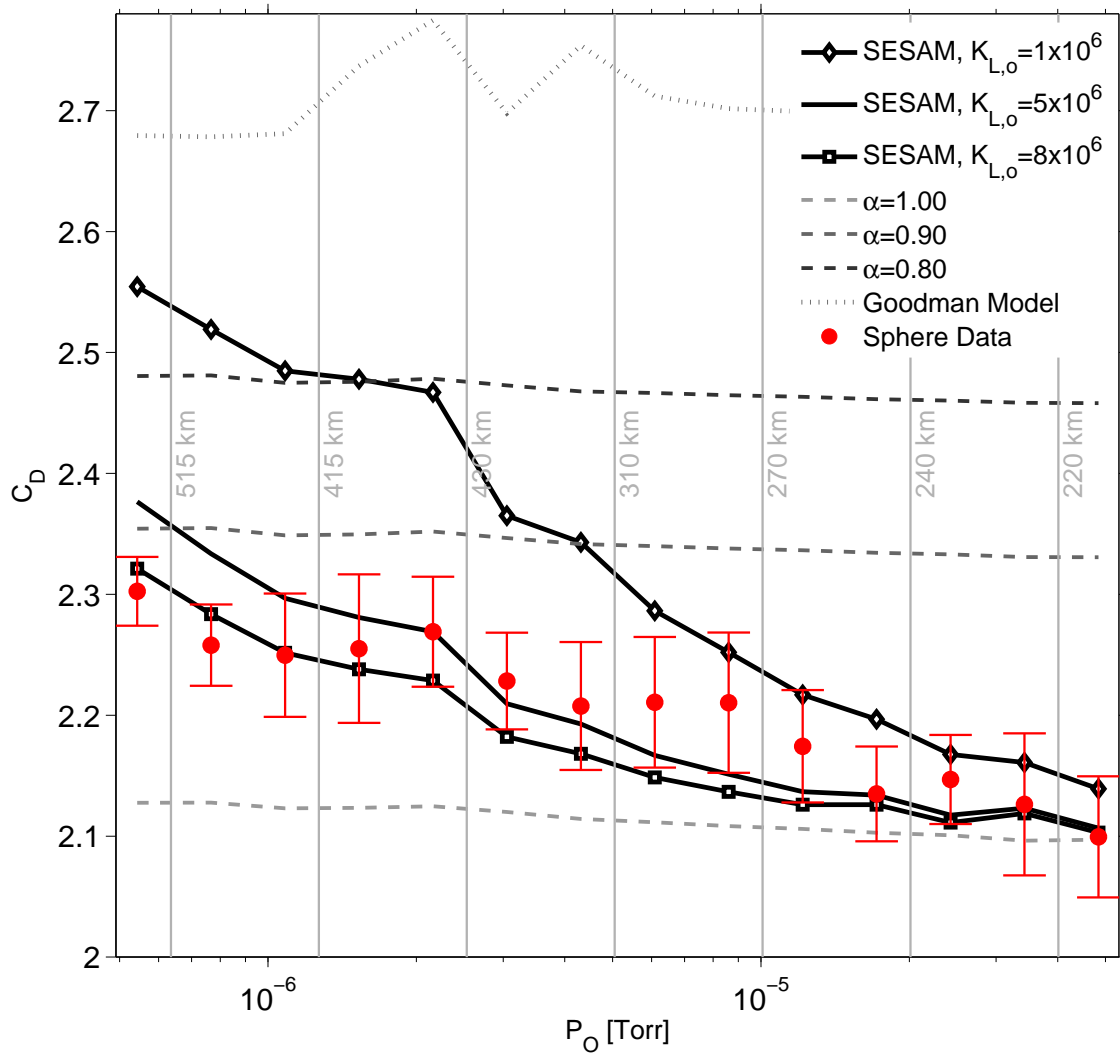


Figure 11.2: Observed drag coefficients of spherical satellites compared to fixed accommodation and Goodman models as well as SESAM with $K_{L,o} = 1 \times 10^6$ Torr $^{-1}$, $K_{L,o} = 5 \times 10^6$ Torr $^{-1}$, and $K_{L,o} = 8 \times 10^6$ Torr $^{-1}$. Average altitudes are shown in grey.

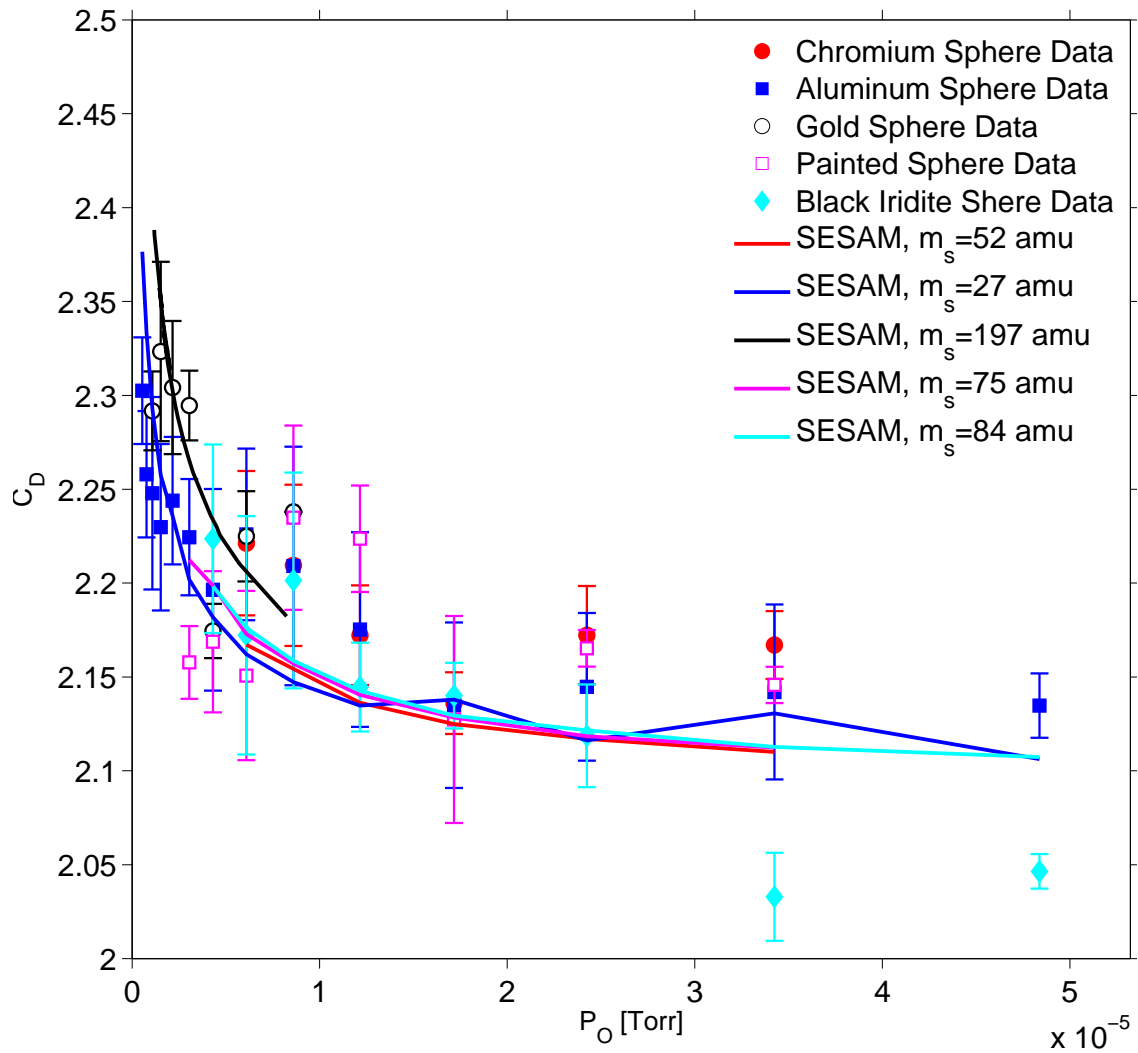


Figure 11.3: SESAM with $K_{L,o} = 5 \times 10^6 \text{ Torr}^{-1} \text{ Torr}^{-1}$ compared with sphere data of different surface compositions

models (SESAM, Goodman, and fixed accommodation) the initial (2 month) average ballistic coefficient will be compared to the modeled drag coefficient for each body to determine the mass margin appropriate for each rocket body. In the case of spheres, the published mass will be used. The B_{obs}/B_{mod} result can be seen in Figure 11.4 while the associated mass margins are shown in Figure 11.5. The values of ΔB mean ($\mu_{\Delta B}$), median ($\mu_{1/2,\Delta B}$), standard deviation ($\sigma_{\Delta B}$), and RMS difference between ΔB and the Cauchy distribution are shown in the plot. SESAM outperforms the other physical models in terms of proximity of mean and median, unity mean, and RMS difference from the reference distribution. Also, it performs at least as well or better than the average fixed ballistic coefficient model with the exception of standard deviation which is 10% higher for SESAM. Meanwhile, the Goodman model results in a bimodal distribution which is probably a result of better performance for rocket bodies with large perigee velocities (lower accommodation) and poor performance for rocket bodies and spheres with smaller values of perigee velocity (higher accommodation). The fixed accommodation model results in reasonable values of mean (2% from unity) and standard deviation (10%) though it does appear to be skew symmetric. However, examining the resulting propellant margins for the physical C_D models reveals a significant distribution of negative values associated with fitting to the fixed accommodation model (see Figure 11.5). This unphysical result eliminates the fixed-accommodation model as a viable choice for drag analysis at multiple altitudes and satellite velocities. The Goodman model fares better though resulting propellant margins can be as high as 7%. Recall however that the Goodman model results may be arbitrarily helped by adopting relatively high propellant margins (Figure 11.5) and that the model is disqualified from direct application to LEO satellites by the comparison with sphere data (Figure 11.2). Propellant margins resulting from fits to the SESAM model are near zero and primarily positive. Some slightly negative propellant margins may be due to errors in cross sectional area determination. Given the results in Figures 11.4 and 11.5, the SESAM model is thus far the only physical C_D model capable of producing reasonable propellant margins as well as B_{obs}/B_{mod} distributions which are comparable to the average fixed ballistic coefficient method.

The altitude dependence of B_{obs}/B_{mod} is shown in Figure 11.6. The outstanding feature of the altitude-based comparison is the reduction in observed versus modeled coefficients below 200 km altitude. Much of this reduction is associated with transition aerodynamics which reduce the C_D . This can be seen

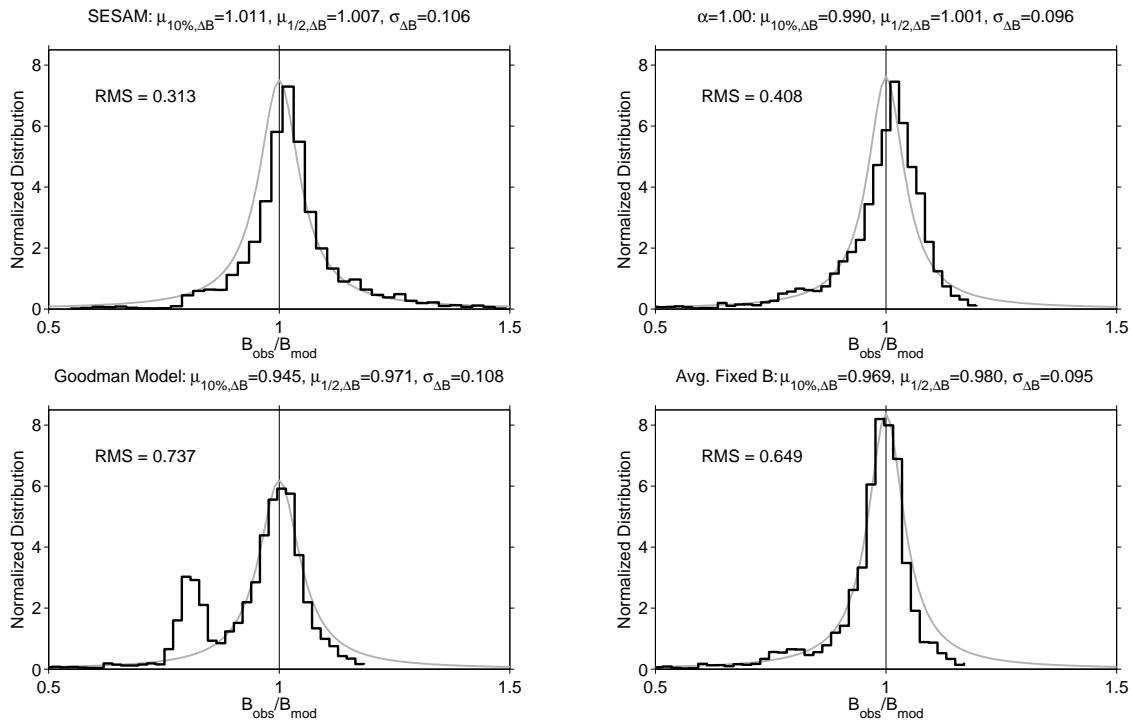


Figure 11.4: Ratios of observed and modeled ballistic coefficients for the entire dataset. The Cauchy distribution is plotted in gray for reference and the inset value is the RMS of the difference between the distribution and a zero-mean Cauchy distribution.

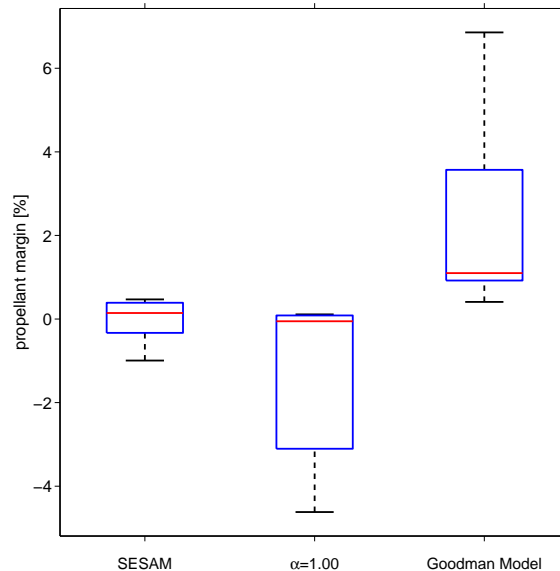


Figure 11.5: Distribution of rocket body fuel margins for three different ballistic coefficient models. Black lines indicate the maxima and minima of the distributions, the blue box extend from the bottom 25th percentile to the top 75th percentile, and the red line represents the median

most directly in the average fixed model case which begins to deviate at 170 km altitudes and results in almost 50% bias at 110 km altitudes. This bias will map directly into determination of density from these measurements and results from the fact that “true” ballistic coefficients (represented by the average-fixed model) are fixed in the free-molecular regime. Above 200 km, the SESAM model matches the average fixed model most closely while below 200 km SESAM does not result in significant altitude dependent bias until approximately 125 km altitude with the maximum bias being 20% near 110 km. As discussed previously, the measurement of B_{OBS}/B_{MOD} is indicative of atmospheric density variation from a reference model. Therefore, altitude dependent biases in Figure 11.6 can also result from errors in total atmospheric density. To evaluate this possibility, the ratio of observed and modeled ballistic coefficient is compared with the ratio of observed to modeled densities as measured by the GUVI instrument [Paxton, 2004, Emmert et al., 2006]. A technical description of the GUVI instrument and measurements is provided in Chapters 5 and 6.

Since GUVI limb-scans produce total density data only at daytime (but not near noon), the drag data is binned to restrict local time accordingly. The data is also separated into low geographic latitude (-11.5° to 11.5°) and high latitude (-65° to -55°) in both datasets to better match the sampling distribution in Figure 5.4. The time-span is restricted to include data from 2001 and 2002 but exclude 2003 and 2004 where the comparison between GUVI and TLE densities is exceptionally poor [Emmert, 2011]. Figure 11.7 shows the comparison between GUVI and drag-measured density ratios. The GUVI and drag-derived density ratios are in good agreement near the equator. Both the drag and GUVI datasets indicate an overestimation of atmospheric density by the model near 110 km by approximately 20%. The difference between average GUVI and drag densities at high latitudes seems to be maintained at approximately 10% across all altitudes. Drag-derived density ratios are reduced by 20% at 120 km while the GUVI ratios are low by approximately 18% at 110 km altitude. It is important to keep in mind that the high latitude drag data originates only from the SL-6 Molniya orbits and may therefore include idiosyncracies in modeling the ballistic coefficients of these objects. Nevertheless, the comparisons indicate that 10% to 20% of the reduction in fitted ballistic coefficients below 150 km may be due atmospheric model biases at those altitudes. The remaining 30% to 40% is due to a decrease in C_D associated with shielding effects imposed by reflected molecules in the transition regime [Koppenwallner and Legge, 1985].

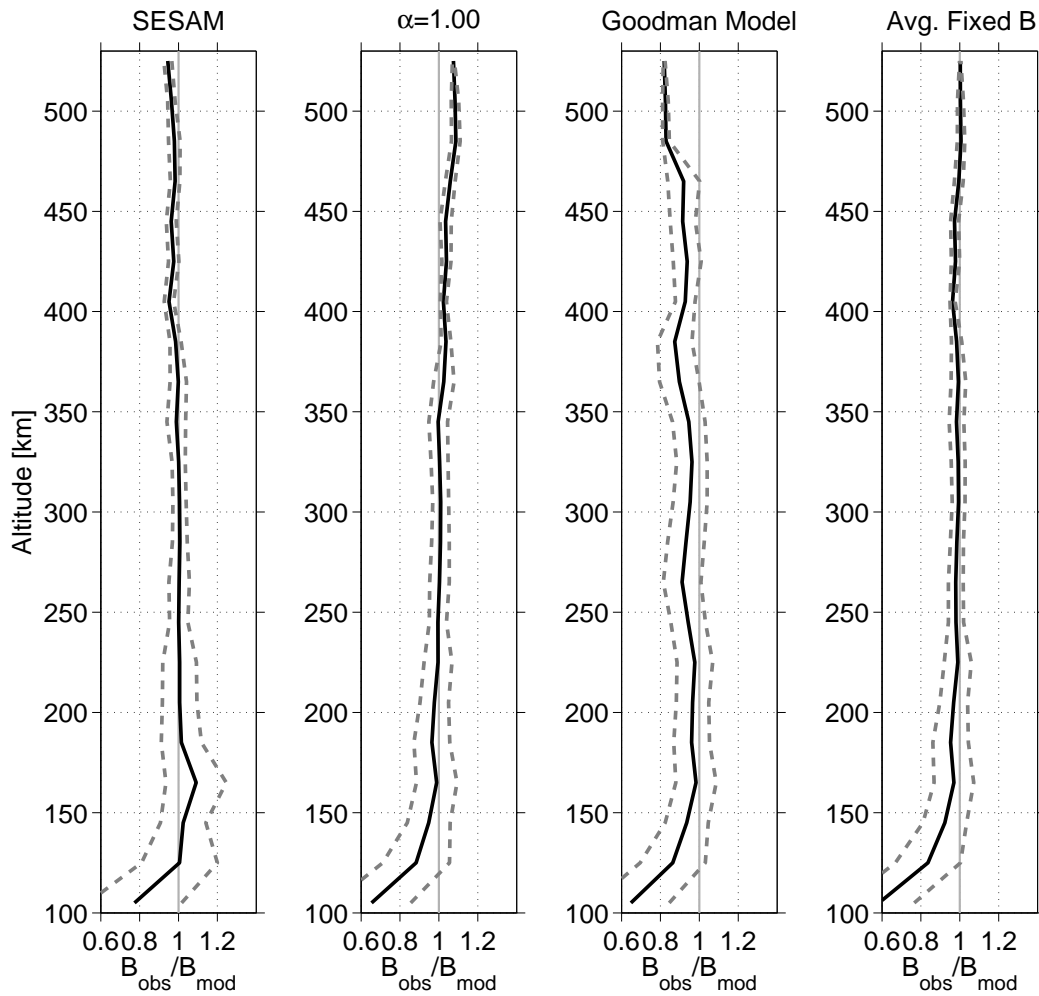


Figure 11.6: Ratios of observed and modeled BFACTORS for four models binned by altitude.

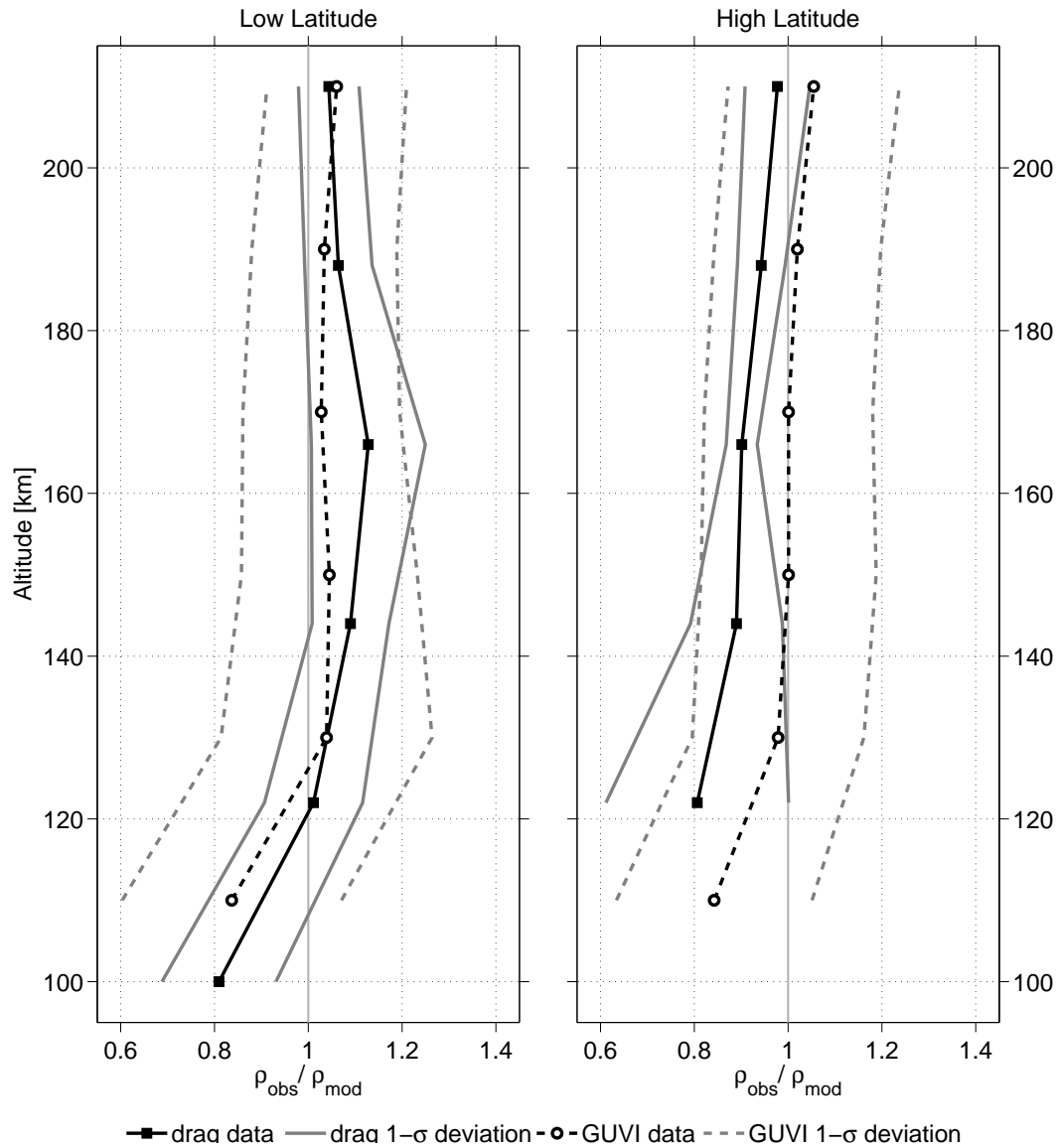


Figure 11.7: Ratios of observed and modeled densities resulting from drag analysis using SESAM as well as measurements made by the GUVI instrument.

Several measurements of satellite accommodation coefficients exist which are independent of modeled atmospheric density. The first such measurement analysis was performed in 1966 by Moe on data retrieved from the Explorer VI satellite [Moe, 1966]. Explorer VI flew in a highly eccentric orbit ($e = 0.76$) with a perigee altitude of approximately 260 km. Soon after, the orbit and spin decays of Ariel II ($e = 0.07$) at an altitude of 290 km were analyzed by Moe in 1968 and re-analyzed over longer time spans by Imbro et al. in 1975 [Moe, 1968, Imbro et al., 1975]. Following these American and British satellites, Beletsky analyzed the Russian Proton II satellite ($e = 0.03$) at a perigee altitude of 168 km [Beletsky, 1970]. Figure 11.8 shows accommodation contours produced by the SESAM model as a function of atomic oxygen pressure and perigee velocity with paddlewheel measurements indicated by black circles. The locations of the four paddlewheel α estimates in Figure 11.8 were computed by propagating the orbits of the four satellites using SGP4. Note that the Explorer VI samples a much different region of the $P_O - V_r$ space and one would thus expect the accommodation to differ significantly from the other satellites. Figure 11.9 illustrates the direct comparisons between SESAM accommodation coefficients and atmosphere-independent measurements. Note that there are two different estimates of Ariel II results. The first is the result of Moe [Moe, 1968] analyzed over several days of the orbit and the second is the value obtained by Imbro [Imbro et al., 1975] resulting from analysis of one month of data.

Figure 11.9 displays the SESAM results for several combinations of E_b and $K_{L,f}$ parameters. Recall that $K_{L,f}$ was fixed in the initial determination of model parameters (chapter 8) hence its effect on accommodation should be evaluated. A value of $3.0 \times 10^4 \text{ Torr}^{-1}$ for the $K_{L,f}$ parameter results in the best overall fit with the data, particularly Explorer VI. As for the binding energy E_b , 5.7 eV improves the agreement for the S3-1 satellite. Note that SESAM overestimates Ariel II accommodation data by 5%-10%. This discrepancy will motivate future development of the model as well as the pursuit of further atmosphere-independent measurements of gas-surface interactions. Figure 11.10 compares the model results with measurements of accommodation at different values of assumed surface mass m_s . The best agreement results from a surface mass ranging between 60 and 75 amu justifying the choice of 65 amu in the SESAM model. Figure 11.11 shows SESAM C_D compared with previously obtained accommodation coefficients based on fitted ballistic coefficients [Pardini et al., 2010, Moe and Bowman, 2005, Moe et al., 1995] as a function of altitude for

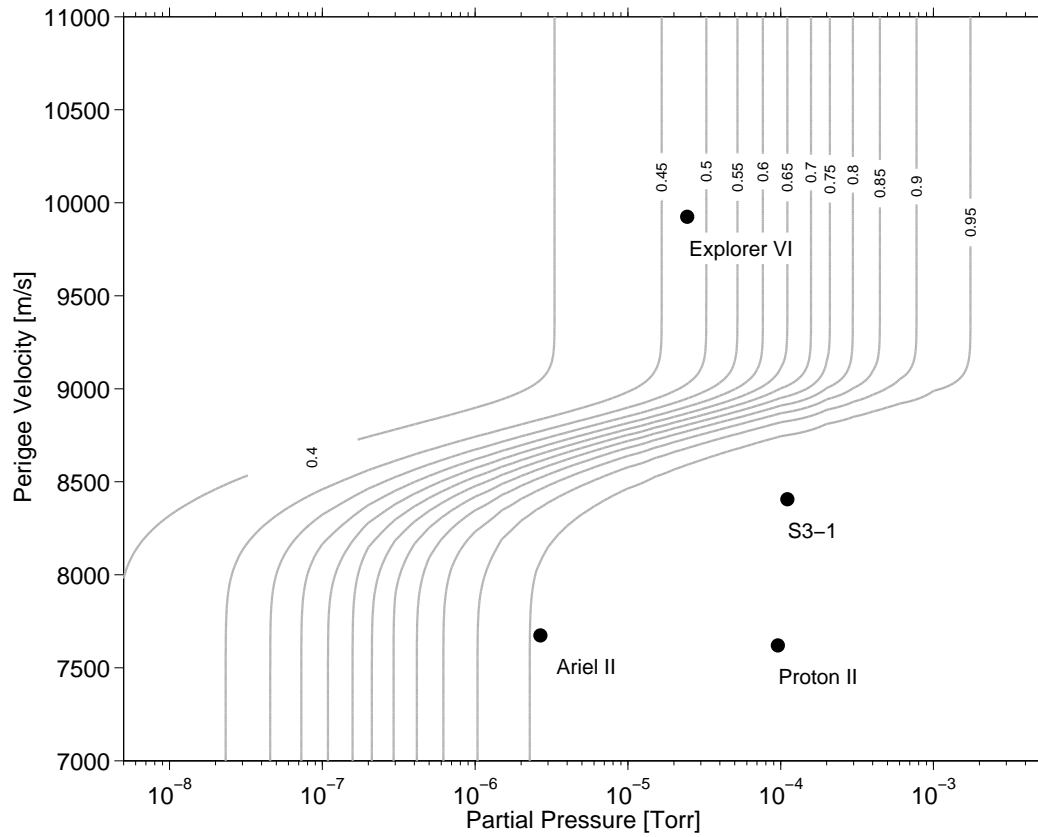


Figure 11.8: Contours of constant α from the SESAM accommodation model as a function of satellite speed and atomic oxygen pressure. The circles represent atmosphere-independent measurements of accommodation.

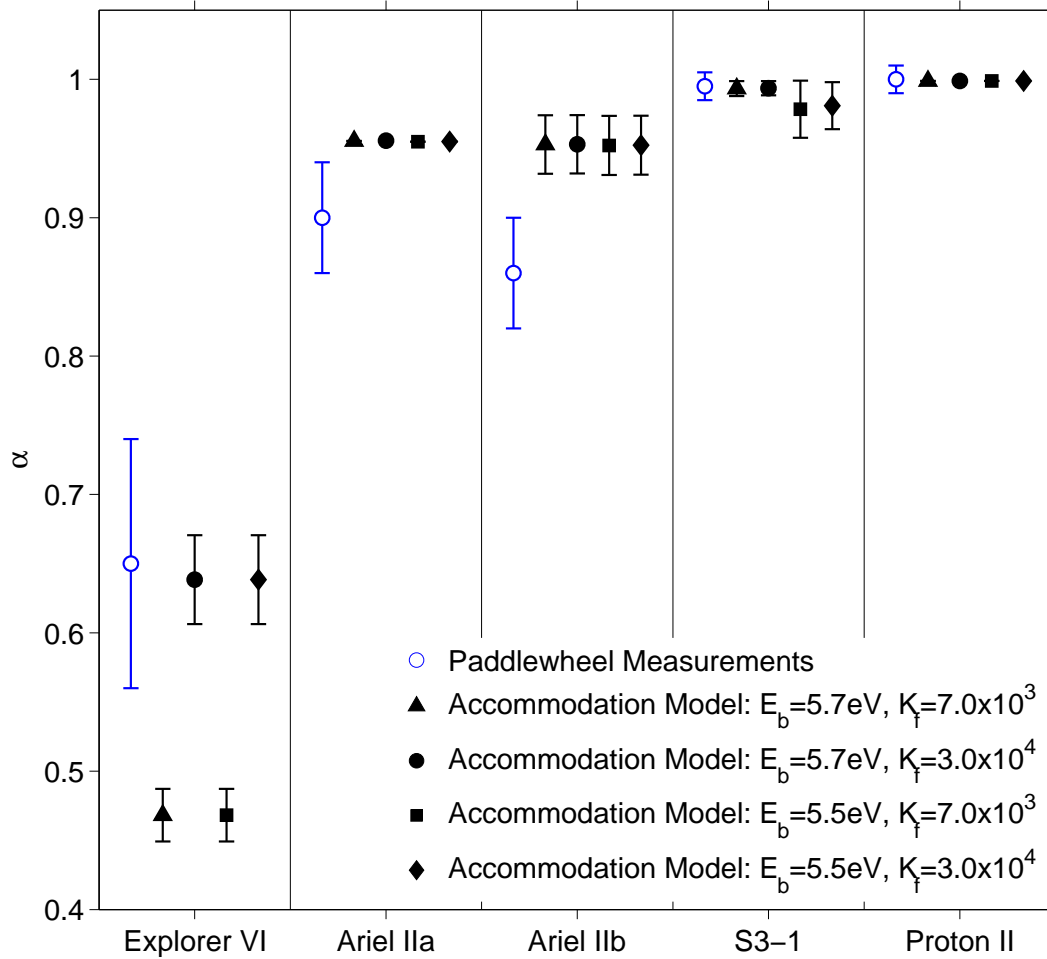


Figure 11.9: Direct comparison of the SESAM accommodation coefficients at different values of $K_{L,f}$ with independent measurements.

average atmospheric conditions. The data shown is based only on near-circular orbits of spherical satellites whose cross sectional area and mass are known precisely. Results from the preliminary implementation of an accommodation coefficient model based on adsorption of atomic oxygen (chapter 8 and [Pilinski et al., 2010]) are shown along with results of the Goodman model. The data and models are separated into solar minimum and solar maximum conditions illustrating the effect of space environment variability on the drag coefficient. Accommodation coefficients at higher altitudes are higher compared with the previous adsorption-based model and compare better with measurements like the Clementine satellite at 650 km [Pilinski et al., 2010, Pardini et al., 2010]. Note the large discrepancy (approximately 40%) between the data and the Goodman model.

While the average-fixed ballistic model is comparable to SESAM above 200 km, it is not capable of tracking changes in C_D due to changes in accommodation nor due to transition regime aerodynamics. Both of these problems are addressed by SESAM representing a first-of-a-kind capability. Furthermore, the average-fixed model cannot be used for an object unless a fitted ballistic coefficient time-series of several months to several years already exists for that object. On the other hand, SESAM provides a modeling framework for ballistic coefficient prediction provided that apriori assumptions about the cross sectional area and mass can be made.

11.2 Extension to Satellites with Large Surfaces Parallel to the Free-Stream

For the conditions of November 6th, 2002, SESAM predicts an effective energy accommodation value of 0.93 to 0.95 depending on surface mass assumptions. The model was developed using techniques described in Chapter 8 and its parameters were tuned according to measurements made by satellites of compact shape as described in the present chapter. Therefore, agreement between SESAM and the CHAMP measurements cannot be expected. However, a salient question is whether the semi-empirical model can be modified to predict CHAMP and GRACE accommodation coefficients. One fundamental difference between compact shapes and elongated shapes with large surfaces aligned with the free-stream is the effective surface pressure (average atomic oxygen pressure arriving at each surface weighted by the drag contribution of that surface). The effective or drag-weighted pressure is an important parameter in SESAM as it is the primary driver

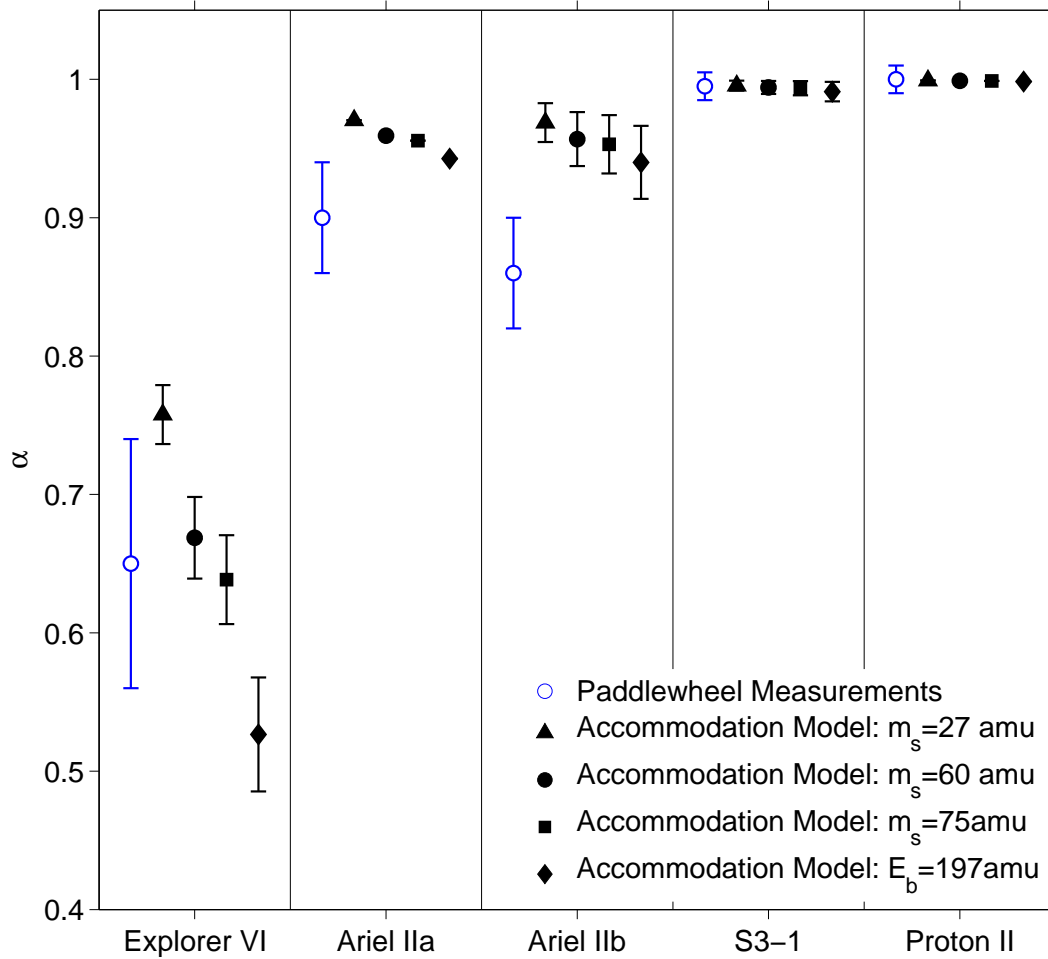


Figure 11.10: Direct comparison of the SESAM accommodation coefficients at different values of m_s with independent measurements.

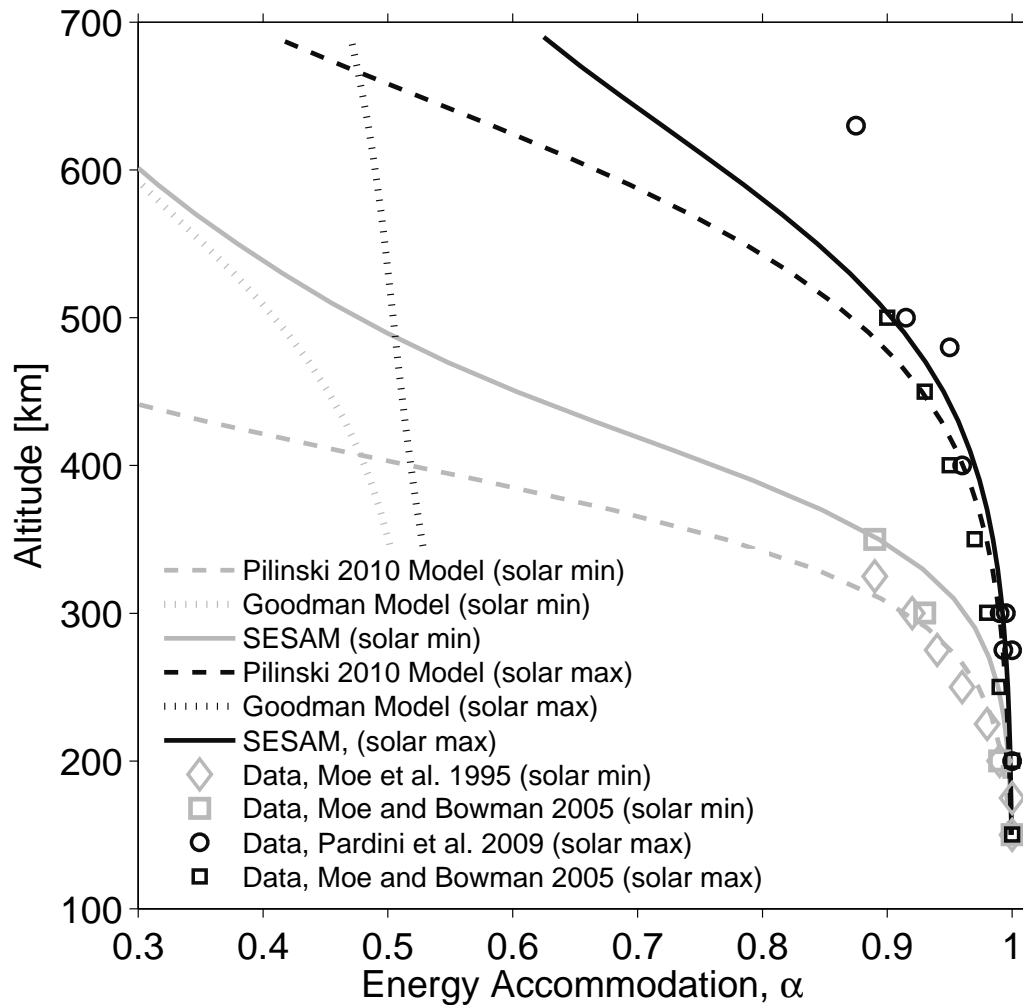


Figure 11.11: Comparison of the present accommodation model with fitted data and the preliminary model for circular orbits.

of the effective accommodation coefficient in the model. Atomic oxygen pressure on a single surface of the satellite geometry may be written as

$$P_O = \frac{1}{2} \rho_O V_r^2 C_N \quad (11.1)$$

where C_N is the normal force coefficient for a flat plate with one side exposed to the flow as defined by Sentman [Sentman, 1961]. Since only the incoming flux contribution is considered, the reflection temperature is set to 0 K. Based on this, the atomic oxygen, drag-weighted, pressure for an arbitrary object composed of N_p panels is

$$\bar{P}_{O,shape} = \frac{1}{2} \rho_O V_r^2 \frac{\sum_{k=1}^{N_p} C_{N,k} C_{D,k} A_{plan,k}}{C_D \sum_{k=1}^{N_p} A_{plan,k}} \quad (11.2)$$

where ρ_O is the mass density of atomic oxygen, V_r is the spacecraft velocity magnitude relative to the atmosphere, and $A_{plan,k}$ is the planform area of the k^{th} plate. Implementing equation 11.2 for a plate model of a sphere composed of 1088 elements where the free-stream conditions are $V_r = 7650$ m/s, $T_a = 1150$ K, $\rho_O = 5.20 \times 10^{-12}$ kg m⁻³ results in an effective pressure of 2.89×10^{-7} Torr. Similarly, for the CHAMP plate model flying in the same free-stream conditions in a nominal forward flying mode the effective pressure is 0.90×10^{-7} Torr while for the yaw-maneuver the average pressure is 1.42×10^{-7} Torr. For a simple GRACE model, the nominal atomic oxygen pressure under these conditions is 1.56×10^{-7} Torr. Now, a pressure correction factor $X_P = \bar{P}_{O,shape} / \bar{P}_{O,sphere}$ is defined to aid in the extrapolation of the SESAM model to elongated satellites. The resulting X_P for CHAMP is 0.31 in the nominal forward-flying mode and 0.41 during the slew maneuver while for the GRACE satellite it is 0.36. The coverage parameter θ' can now be computed as before adjusting the atomic oxygen pressure by the factor X_P . The results for CHAMP and GRACE are shown in Table 11.2 along with the measurements made in Chapter 9 and 10.

The SESAM results (α_{SESAM}) for effective accommodation are within experimental uncertainty of the measurements made (α_{obs}) for the CHAMP satellite. For GRACE the estimated value of energy accommodation is quite low. It is not possible to verify this result using small-angle measurements as discussed previously and further analysis based on yaw-maneuvers may be needed.

Table 11.2: Results of SESAM extended to satellites with long shapes

Satellite	Flight Mode	P_O	X_P	α_{obs}	α_{SESAM}
CHAMP	Yaw Maneuver	2.2×10^{-6} Torr	0.41	0.89 (+0.02, -0.03)	0.90
CHAMP	Nominal Small Angle	1.1×10^{-6} Torr	0.31	0.86 (+0.04, -0.26)	0.71
CHAMP	Nominal GUVI Comps.	1.3×10^{-6} Torr	0.32	0.78 (+0.10, -0.13)	0.75
GRACE	Nominal	0.1×10^{-6} Torr	0.36	-	0.51

11.3 Discussion

The fitted ballistic coefficients of 16 spheres and 46 rocket bodies were analyzed at perigee altitudes from 110 km to 500 km in order to construct a ballistic coefficient model which reconciles the drag observed by various classes of objects. In particular circular and highly elliptical orbits were included in the dataset as it has been known for over 40 years that the drag coefficient of objects in LEO may have a strong dependence on velocity. The results of this analysis indicate that there is a decrease in the energy accommodation coefficient as perigee velocities increase above 8 km/s. This transition likely corresponds to a drop in adsorption efficiency of atomic oxygen on satellite surfaces. Attributing this phenomenon to the convolution of free-stream kinetic energies with the binding energy of atomic oxygen results in an average binding energy between 5.5 eV and 5.7 eV which corresponds well with the average theoretical and laboratory-measured binding energy for spacecraft materials such as aluminum and Kapton. The observed transition in energy accommodation is fast relative to what would be predicted by modeled temperatures of the atmosphere. This finding is indicative of additional physics which, though captured empirically, are not explicitly included in the semi-empirical model of drag coefficients.

The revised semi-empirical model (SESAM) results in better agreement with observations especially for satellites in elliptical orbits. The agreement between the model and observations was first tested by evaluating the ratio of observed-to-modeled ballistic coefficients. The ballistic coefficients computed using SESAM resulted in B_{obs}/B_{mod} ratios which best approximate a unity mean distribution corresponding to the ratio of two normally distributed random variables with the median located nearest to the mean. While the improvement over the average-fixed method is marginal above 200 km, the gains are significant below 200 km altitudes with 30%-50% improvements in accuracy. This was verified by comparing drag measurements

referenced to the SESAM model with remote sensing observations made by the GUVI instrument. Furthermore the average-fixed model, which is standard in density measurement analyses based on orbit-averaged drag, has no predictive capability for objects which have not been in space long enough for an averaged “true” ballistic coefficient to be computed.

There is reasonable agreement between SESAM accommodation coefficients and paddlewheel measurements to within 1%-10% percent with the differences generally being within measurement uncertainties. Furthermore, an average surface mass adopted for all bodies in the dataset does not result in significant errors to the model owing to the significant levels of atomic oxygen adsorption. Further comparisons of SESAM results were made with accommodation coefficients estimated by Pardini and Moe [Pardini et al., 2010] and the differences were within 3% up to 500 km altitudes. There does exist an outlier at 650 km (the Clementine satellite) where there is no data on which model construction was based. The application of this model is therefore restricted to objects with perigee altitudes between 100 km and 500 km.

In addition to the average fixed model we compared SESAM with models using fixed accommodation coefficients as well as drag coefficients based on the Goodman hard-sphere model of accommodation. The fixed accommodation model has some precedent in the analysis of accelerometer data while the Goodman model can be successfully applied to reflections of molecules from clean surfaces. Both these models produced large discrepancies in terms of the reduction in altitude-based biases and comparisons with space-based measurements.

Chapter 12

Conclusions and Recommendations

12.1 Discussion

The purpose of this investigation was to evaluate gas-surface interactions in LEO and their relationship to satellite aerodynamics. Several questions were posed which probe the nature of satellite aerodynamics in Earth's thermosphere. Starting from the last question and progressing toward the first, the science objectives of this dissertation will now be addressed.

12.1.1 Scattering Kernels

Which models of molecule reflection (scattering kernels) best reproduce orbital measurements?

Multi-axis accelerometer measurements from the CHAMP satellite have been analyzed at 410 km during a yaw maneuver on November 6th, 2002. A ratio of lift to drag was computed and compared with two scattering-kernel models. The models were also used to predict changes in the ratio of measured to modeled density in forward and sideways flying modes of the CHAMP satellite. The first model was a diffuse (cosine reflection distribution) scattering law with incomplete energy accommodation. The second model was Schamberg's quasi-specular reflection blended with a cosine reflection law with a hard-sphere, surface-specific, accommodation coefficient for the former and full accommodation for the latter. The lift/drag measurements were consistent with a fully diffuse reflection having an accommodation coefficient of approximately 0.89. The quasi-specular kernel was found to be inconsistent with densities measured in the forward and sideways flying modes which led to the elimination of this model at 410 km altitudes. This result fits well with the

analysis of Gregory and Peters [1987] near 350 km, analysis performed by Imbro et al. [1975] at 290 km, as well as others [Ching et al., 1977, Moe and Moe, 2005]. Taken together with the results presented here, the data confirms that diffuse reflection is a dominant characteristic of gas-surface interactions up to at least 410 km.

The diffuse (Sentman) model of gas-surface interaction is best able to reproduce orbital measurements to within experimental uncertainty.

12.1.2 Energy Accommodation Measurements

Can independent measurements of energy accommodation be obtained with available data-sets?

Fitted ballistic coefficients were provided by Air Force Space Command (Space Analysis Office) and analyzed using free-molecular and direct-simulation techniques (Chapters 7 and 8). Since these methods depend on the assumption of atmospheric model corrections they cannot be strictly defined as independent. Nevertheless, the work performed as a part of this effort compared fitted ballistic results at various perigee velocities and confirmed that model fits based on fitted ballistic coefficients agree with paddlewheel measurements that are independent of atmospheric density assumptions. This serves as a validation of previous fitted ballistic studies.

In-track acceleration measurements made by the CHAMP satellite were analyzed to derive the drag coefficient of this satellite. However, instead of using an atmospheric model to fix the ambient free-stream density an independent measurement was used. This measurement was obtained by dayside limb observations of ultraviolet glow made by the GUVI instrument (Chapter 9). Density profile measurements were isolated at locations coincident with the CHAMP orbit measurements. The colocated density measurement was used along with the accelerometer readings to solve for the drag coefficient. The resulting data was of limited value due to the high levels of noise in the GUVI absolute density measurements. Furthermore, GUVI collects data up to around 200 km. Above 200 km, the data is extrapolated to CHAMP altitudes (approximately 350-400km) using an empirical model. The model assumes that diffusive equilibrium holds in the atmosphere which may only be a valid approximation at low values of geomagnetic and solar activity. Nevertheless, the

CHAMP-GUVI analysis indicates that drag coefficients are higher (energy accommodation lower) at low atomic oxygen pressures and this is consistent with the theory expounded throughout the dissertation.

Perhaps the most powerful technique for evaluating energy accommodation has been the measurement of calibrated in-track and cross-track accelerations on the CHAMP and GRACE satellites. During periods of large sideslip angles (yaw and switch maneuvers) the ratio of lift and drag can be measured directly using onboard accelerometers. This ratio is independent of the ambient density and has a relatively small dependence on composition and cross-track winds. However, the angular dependence of C_L/C_D is quite sensitive to GSI assumptions. Therefore, the modeled lift to drag ratio is used to invert the appropriate GSI parameters such as energy accommodation or fraction of specular reflection. The technique has been evaluated for CHAMP during one of its yaw maneuvers and the energy accommodation coefficient was recovered. The measurement has the duration of the maneuver which, in this case, was less than one day. This is an unprecedented temporal resolution as it takes several days to accumulate the fitted ballistic coefficient data necessary to recover accommodation and paddlewheel analysis time-spans are on the order of several days to several weeks. Several additional opportunities exist for analyzing accelerometer measurements of lift and drag. The first is a 2001 CHAMP maneuver. Unfortunately, the time period associated with this maneuver suffers from uncharacteristically large errors in scale factor and bias [Doornbos, 2011]. The CHAMP satellite has also changed directions, traversing 180° of orientation, in 2009 at an altitude near 300 km. Furthermore, both GRACE satellites underwent a 180° rotation during the switch of the leading and trailing satellites in December of 2005. Due to the usefulness of this technique, it is recommended that future satellites carrying precise accelerometers perform such maneuvers regularly in order to resolve changes in GSI from changes in atmospheric density.

Measurements of the lift to drag ratio made by precise accelerometers can be used to derive energy accommodation in LEO. In addition, fitted ballistic coefficients can also be used, provided that they are calibrated to previous independent measurements such as paddlewheel satellites.

12.1.3 Energy Accommodation Model

Can a predictive energy accommodation model be developed to improve satellite drag calculations?

A semi-empirical model for satellite energy accommodation has been constructed based on fitted ballistic coefficients of spheres and rocket bodies derived by Bruce Bowman at AFSPC/A9A [Bowman and Moe, 2005, Bowman and Hrncir, 2007]. This model has been verified by comparing it to independent measurements of accommodation made by paddlewheel satellites (Chapter 11). The theoretical basis of the model is that Langmuir-type adsorption drives the effective coverage of atomic oxygen contaminant on satellite surfaces. The primary model inputs are atomic oxygen pressure and the kinetic energy of incident molecules. In turn, the coverage of contaminant provides a mixing parameter between a hard-spheres, Goodman model of accommodation (clean surface) and full accommodation (adsorbate). The model is able to predict energy accommodation coefficients for satellites at altitudes up to approximately 500 km and down to 100 km. That energy accommodation coefficients are affected by adsorption was first proposed by Cook, Moe and Moe as well as others in the 1960's [Cook, 1965, Moe and Moe, 1967, Reiter and Moe, 1968]. It is a theory which has been successfully tested by the implementation and verification efforts presented in this dissertation. This work therefore, represents the first quantitative evaluation of adsorption-based accommodation modeling in LEO wherein atmospheric and satellite variables are mathematically related to a value of accommodation. The theory that higher incident kinetic energies decrease the accommodation coefficient has also been verified and implemented in a quantitative way. Furthermore, a method for extending the results to satellites having long shapes was presented. The model developed herein also provides estimates of aerodynamic coefficients and can be applied to the modeling of drag forces experienced by orbital debris. It is the hope of the author that this will aid in the prediction of the orbits of thousands of debris currently being tracked in LEO.

An improvement in LEO drag calculations can be realized by modeling the energy accommodation coefficient at the satellite surface based on the atomic oxygen pressure on that surface.

12.2 Recommendations

It is possible that uncertainties associated with computing accurate ballistic coefficients have to some extent contaminated the GSI results in this work. Although several attempts have been made to validate results against multiple sources of data, no measurement is perfect. The primary sources of uncertainty stem from inaccurate representation of satellite geometry (see work by Pilinski [Pilinski et al., 2011a] as well as section 4.3.3), difficulties in estimating satellite orientation and mass (see Chapter 8), as well as the dearth of independent measurements such as those made by paddlewheel satellites.

The first two difficulties relate to the accuracy with which the cross-sectional area and mass of a satellite can be determined. The startling variety of estimates for CHAMP cross-sectional areas underlines this point. It is impossible to accurately model the satellite ballistic coefficient and to predict its drag without prior knowledge of its mass and area. Likewise, atmospheric densities based on satellite drag will contain biases resulting from area and mass errors. Furthermore, errors associated with cross-sectional area, do not tend to average out across many satellites. This was a point made elegantly by Doornbos [2011] who noted that it is much easier for a human analyst to omit geometry details rather than to accidentally add features with cross-sectional area to the geometry. Likewise, successive attempts at analysis tend to converge to larger cross-sectional areas as the exact geometry of certain satellites is uncovered (sometimes through a process approaching detective work). This has been the case with CHAMP analysis [Doornbos et al., 2009] as well as the analysis of Starshine satellite drag [Pilinski et al., 2011a]. It is therefore of utmost importance that the as-built drawings of the external satellite geometry be available to those analyzing satellite drag. It is also recommended that photographs of the satellite taken directly before the launch be provided so that the drawings can be verified and put into context. Finally, it is helpful to know the composition of the various satellite surfaces, although as this work has confirmed, atomic oxygen tends to coat most surfaces effectively masking their individual reflection characteristics.

While fitted ballistic coefficients provide a ubiquitous measurement for the analysis of satellite drag coefficients, they are only as useful as the atmospheric model calibration associated with their derivation. This calibration has been made possible by the handful of paddlewheel satellites and lift/drag measurements

available in earth orbit. For this reason, increasing the number of absolute measurements of density and gas-surface interactions are critical to the understanding of satellite drag and decoupling the $C_D\rho$ product. As demonstrated by Pilinski et al. modern implementations of the paddlewheel concept can be made by focused cubesat missions launched as secondary payloads [Pilinski et al., 2011b]. Important additional information about gas-surface interactions and satellite drag can also be gained by slightly augmenting the operations of existing and planned satellites which fly precise accelerometers. As was demonstrated in Chapter 10, aerodynamic force calibration is possible by allowing a long satellite to yaw by at least 30 degrees from its nominal flow-aligned state. The new orientation need not be maintained for more than several orbits and nominal attitude can be restored within one day as was done for the CHAMP satellite. Performing such maneuvers a couple times every year would vastly improve the quality of thermospheric data from satellite accelerometers (densities and winds). Furthermore, over a two year mission, such operations would effectively double the number of direct measurements of satellite gas-surface interactions in LEO.

12.3 Conclusion

This work was initiated by posing the following overarching question.

What satellite gas-surface parameters result in physically realistic models of aerodynamic force behavior in LEO?

The questions discussed in the previous section were derived from this query. Since the beginning of the Space Age, it has been suspected by some that reflections characterized by strongly diffuse scattering and high values of accommodation were dominant in low-Earth orbit. However, until now, no predictive model existed for the gas-surface parameters of these reflections. By comparing physical models of aerodynamic coefficients with many measurements of drag in the LEO environment, the appropriate behavior of gas-surface interactions could be estimated. The resulting models and the theories on which they are based were tested by analyzing fitted ballistic coefficients, remote-sensing observations, previous paddlewheel satellite results, and accelerometer data. One of the primary conclusions of this work is that the level of energy accommodation on surfaces flying at and below 500 km is relatively high and is driven by the level to which the surface has been contaminated by atomic oxygen. The level of contamination can be adequately described

by specifying both the flux of atomic oxygen and its incident kinetic energy. It was found that the average bonding strength of atomic oxygen to satellite surfaces is approximately 5.7eV and that incident kinetic energies which exceed this energy cause the coverage to be reduced as indicated by a decrease in measured accommodation coefficients. The analysis throughout this dissertation has led to the description of satellite aerodynamic parameters applicable to compact and long satellite shapes at altitudes from 100 km to 500 km and in orbit eccentricities ranging from circular to Molniya and geostationary transfer orbits. Specifying the physical aerodynamic coefficients based on the ever-changing space environment leads to improved orbital drag predictions as well as to more accurate determination of atmospheric densities from satellite drag.

Bibliography

- A. W. Adamson. Physical Chemistry of Surfaces, 5th Edition. John Wiley and Sons, New York, 1990.
- B. J. Anderson and R. E. Smith. Natural Orbital Environment Guidelines for Use in Aerospace Vehicle Development. Technical Report NASA-TM-4527, NASA, 2009.
- T. A. Baker, C. M. Friend, and E. Kaxiras. Atomic Oxygen Adsorption on Au(111) Surfaces with Defects. Journal of Physical Chemistry, 113(8):3232–3238, 2009.
- M. Balat-Pichelin, J. M. Badie, R. Berjoan, and P. Boubert. Recombination coefficient of atomic oxygen on ceramic materials under earth re-entry conditions by optical emission spectroscopy. Journal of Chemical Physics, 291:181–194, 2003.
- B. A. Banks, K. K. de Groh, and S. K. Miller. Low Earth Orbital Atomic Oxygen Interactions with Spacecraft Materials. In Mater. Res. Soc. Symp. Proc., volume 851, pages NN8.1.1–NN8.1.12. Materials Research Society, 2005.
- B. A. Banks, S. K. Miller, and K. K. de Groh. Low Earth Orbital Atomic Oxygen Interactions With Materials. Technical Report NASA/TM2004-213223, Lockheed Missles and Space Co., 2004.
- V. V. Beletsky. An estimate of the character of the interaction between the airstream and a satellite. Kosmicheskie Issledovaniya, 8(10):206–217, 1970. (in Russian).
- G. A. Biggs and L. F. Phillips. BET analysis of thermal accommodation coefficients obtained via measurements of the Onsager heat of transport. Chemical Physics Letters, Chemical Physics Letters:84–88, 2008.
- G. A. Bird. A Contemporary Implementation of the Direct Simulation Monte Carlo Method. In M. Mareschal and B. L. Holian, editors, Microscopic Simulations of Complex Hydrodynamic Phenomena, pages 239–253. Plenum Press, New York, NY, 1992.
- G. A. Bird. Molecular Gas Dynamics and the Direct Simulation of Gas Flows. Oxford Science Publications, New York, 1994.
- G. A. Bird. Sophisticated DSMC. In Notes from DSMC07 meeting, Santa Fe, September 2007, 2007. Available from: <http://www.gab.com.au/Resources/DSMC07notes.pdf>.
- G. A. Bird. Recent Advances and Current Challenges for DSMC. Computers Math. Applic., 35(1):1–14, 2009.
- R. C. Blanchard and G. M. Buck. Determination of Rarefied-Flow Aerodynamics of the Shuttle Orbiter from Flight Measurements on STS-6 and STS-7. In AIAA 23rd Aerospace Sciences Meeting, January 14-17, 1985/Reno, Nevada, number 85-0347. AIAA, 1985.

- R. C. Blanchard, K. T. Larman, and M. Barrett. The High Resolution Accelerometer Package (HiRAP) Flight Experiment Summary for the First 10 Flights. Technical Report NASA RP-1267, NASA Langley Research Center, 1992.
- P. Błoński, A. Kiejna, and J. Hafner. Theoretical study of oxygen adsorption at the Fe(110) and (100) surfaces. *Surface Science*, 590:88–100, 2005.
- P. Błoński, A. Kiejna, and J. Hafner. Oxygen adsorption on the clean and O-precovered Fe (110) and (100) surfaces. *Journal of Physics: Condensed Matter*, 19:1–8, 2007.
- H. Boehnhardt, H. Koehnke, and A. Seidel. The acceleration and the deceleration of the tumbling period of rocket intercosmos 11 during the first two years after launch. *Astrophysics and Space Science*, 162: 297–313, 1989.
- B. R. Bowman. True Satellite Ballistic Coefficient Determination for HASDM. *AIAA/AAS Astrodynamics Specialist Conference and Exhibit 5-8 August 2002, Monterey, California*, (4887), 2002.
- B. R. Bowman and S. Hrcir. Drag Coefficient Variability at 100-300 km from the Orbit Decay Analyses of Rocket Bodies. In *AAS/AIAA Astrodynamics Specialist Conference*, number AAS 07-262. AAS/AIAA, 2007.
- B. R. Bowman and K. Moe. Drag Coefficient Variability at 175-500 km from the orbit decay analyses of Spheres. In *AAS/AIAA Astrodynamics Specialist Conference*, number AAS 05-257. AAS/AIAA, 2005.
- B. R. Bowman and M. F. Storz. High accuracy satellite drag model (HASDM) review. *American Astronautical Society*, (03-625), 2003.
- B. R. Bowman and W. K. Tobiska. Improvements in Modeling Thermospheric Densities Using New EUV and FUV Solar Indices. In *American Astronautical Society/AIAA Astrodynamics Specialist Conf.*, number 06-237. AAS, 2006.
- B. R. Bowman, W. K. Tobiska, and F. A. Marcos. A New Empirical Thermospheric Density Model JB2006 Using New Solar Indices. *AIAA*, (2006-6166), 2006.
- S. Bruinsma, D. Tamagnan, and R. Biancale. Atmospheric density derived from CHAMP/STAR accelerometer observations. *Planet. Space Sci*, 52:297–312, 2004.
- S. Brunauer, P. Emmet, and E. Teller. Adsorption of Gases in Multimolecular Layers. *J. Am. Chem. Soc.*, 60(2):309–319, 1938.
- C. Cercignani and M. Lampis. New Scattering Kernel for Gas-Surface Interaction. *Journal of Spacecraft and Rockets*, 35(6):1000–1011, 1997.
- A. R. Chambers, I. L. Harris, and G. T. Roberts. Reaction of spacecraft materials with fast atomic oxygen. *Material Letters*, 26:121–131, 1996.
- K. S. W. Champion. Dynamics and structure of the quiet thermosphere. *Journal of Atmospheric and Terrestrial Physics*, 37:915–926, 1975.
- K. S. W. Champion. Properties of the mesosphere and thermosphere and comparison with CIRA 72. *Advances in Space Research*, 3(1):45–53, 1983.
- L. W. Chen and C. H. Lee. Interaction Potential Between Atomic Oxygen and Polymer Surfaces in Low Earth Orbit. *Journal of Spacecraft and Rockets*, 43(3):487–496, 2006.
- B. K. Ching, D. R. Hickman, and J. M. Straus. Effects of Atmospheric Winds and Aerodynamic Lift on the Inclination of the Orbit of the S3-1 Satellite. *Journal of Geophysical Research*, 82(10):1471–1480, 1977.
- F. G. Collins and E. C. Knox. Determination of Wall Boundary Conditions for High-Speed-Ratio Direct Simulation Monte Carlo Calculations. *Journal of Spacecraft and Rockets*, 31(6):965–970, 1994.

- G. E. Cook. Satellite Drag Coefficients. Planet. Space Sci., 13:929–946, 1965.
- G. E. Cook. Variations in exospheric density during 1967-68, as revealed by ECHO 2. Planet. Space Sci., 18:387–394, 1970.
- V. K. Dogra, R. G. Wilmoth, and J. N. Moss. Aerothermodynamics of a 1.6-Meter-Diameter Sphere in Hypersonic Flow. AIAA Journal, 30(7):1789–1794, 1992.
- E. Doornbos. Thermospheric Density and Wind Determination from Satellite Dynamics. PhD thesis, Delft University of Technology, 2011.
- E. Doornbos, M. Forster, T. van Helleputte, J. van den IJssel, G. Koppenwallner, H. Luhr, D. Rees, and P. Visser. Air density models derived from multi-satellite drag observations. Technical Report 21022/07/NL/HE, European Space Agency Study Contract Report, 2009.
- E. Doornbos, J. IJssel, H. Luhr, M. Fofrster, and G. Koppenwallner. Neutral Density and Crosswind Determination from Arbitrarily Oriented Multiaxis Accelerometers on Satellites. Journal of Spacecraft and Rockets, 47(4):580–589, 2010.
- R. O. Doughty and W. J. Schaetzle. Experimental Determination of Momentum Accommodation Coefficients at Velocities up to and Exceeding Earth Escape Velocity. In Rarefied Gas Dynamics, volume 2, pages 1035–1054. Proceedings of the Sixth International Symposium, edited by L. Trilling and H. Y. Wachman (Academic, New York), Supplement 5, 1969.
- D. P. Drob. An empirical model of the Earth's horizontal wind fields: HWM07. Journal of Geophysical Research, 113, 2008.
- J. T. Emmert. A long-term data set of globally averaged thermospheric total mass density. Journal of Geophysical Research, 114(A06315), 2009.
- J. T. Emmert. personal communication, July 8th, 2011.
- J. T. Emmert, R. R. Meier, J. L. Lean, and A. B. Christensen. Thermospheric density 2002-2004: TIMED/GUVI dayside limb observations and satellite drag. Journal of Geophysical Research, 111 (A10S16), 2006.
- J. T. Emmert, J. M. Picone, and J. L. Lean. Global change in the thermosphere: Compelling evidence of a secular decrease in density. Journal of Geophysical Research, 109(A02301), 2004a.
- J. T. Emmert, J. M. Picone, J. L. Lean, and S. H. Knowles. Global change in the thermosphere: Compelling evidence of a secular decrease in density. Journal of Geophysical Research, 109(A02301), 2004b.
- J. R. Engstrom, D. J. Bonser, M. M. Nelson, and T. Engel. The reaction of atomic oxygen with Si(100) and Si(111). Surface Science, 256:317–343, 1991.
- P. J. Feibelman. The first wetting layer on a solid. Physics Today, 63(2):34–39, 2010.
- J. M. Forbes, S. Bruinsma, and F. G. Lemoine. Solar Rotation Effects on the Thermospheres of Mars and Earth. Science, 312:1366–1368, 2006.
- K. Fukutani, M-B. Song, and Y. Murata. Ultraviolet-laser-induced Desorption of CO and NO from Pt Surfaces. Royal Society of Chemistry, Faraday Discussions, 96:105–116, 1993.
- T. Fuller-Rowell, M. Codrescu, N. Maruyama, M. Fredrizzi, E. Araujo-Pradere, S. Sazykin, and G. Bust. Observed and modeled thermosphere and ionosphere response to superstorms. Radio Sci., 42(RS4S90), 2007.
- F. O. Goodman. A three-dimensional hard spheres theory of scattering of gas atoms from a solid surface. Technical Report NASA CR-933, NASA, 1967.

- F. O. Goodman. Thermal Accommodation. In Progress in Surface Science, volume 5, pages 261–375, 1974.
- J. C. Gregory and P. N. Peters. A measurement of the angular distribution of 5 eV atomic oxygen scattered off a solid surface in earth orbit. In B. G. Teubner, editor, Rarefied Gas Dynamics, volume 15, pages 644–656. Proc. Intl. Symposium, Stuttgart, Germany, 1987.
- D. Hanselman and B. R. Littlefield. Mastering MATLAB 6. Prentice Hall, Upper Saddle River, NJ, 2001.
- K. Harrison and G. G. Swinerd. A free molecule aerodynamic investigation using multiple satellite analysis. Planetary and Space Science, 44(2):171–180, 1996.
- T. V. Helleputte, E. Doornbos, and P. Visser. CHAMP and GRACE accelerometer calibration by GPS-based orbit determination. Advances in Space Research, 43(1):1890–1896, 2009.
- F. C. Hurlbut and F. S. Sherman. Application of the Nocilla Wall Reflection Model to Free-Molecule Kinetic Theory. The Physics of Fluids, 11(3):486–496, 1968.
- D. R. Imbro, M. M. Moe, and K. Moe. On fundamental problems in the deduction of atmospheric densities from satellite drag. Journal of Geophysical Research, 80:3077–3086, 1975.
- S. J. Isakowitz, J. P. Hopkins Jr., and J. B. Hopkins. International Reference Guide to Space Launch Systems. AIAA, Reston, Virginia, 1999.
- L. G. Jacchia. Static Diffusion Models of the Upper Atmosphere with Empirical Temperature Profiles. Technical Report 170, Smithsonian Astrophysical Observatory, Special Report, 1964.
- L. G. Jacchia. Empirical models of the thermosphere and requirements for improvements. Advances in Space Research, 1:81–86, 1981.
- P. Jenkins, D. Scheiman, D. Wilt, R. Raffaele, R. Button, T. Kerslake, M. Batchelder, D. Lefevre, and R. G. Moore. Results from the Advance Power Technology Experiment on the Starshine 3 Satellite. In 16th Annual AIAA/USU Conference on Small Satellites, number SSC02-X-3. AIAA/USU, 2002.
- Z. Kang, P. Nagell, and R. Pastor. Precise Orbit Determination for GRACE. Advances in Space Research, 31(8):1875–1881, 2003.
- G. R. Karr. A study of effects of the gas-surface interaction on spinning convex bodies with application to satellite experiments. PhD thesis, University of Illinois, Urbana, 1969.
- W. T. Kasprzak, A. Krankowsky, and A. O. Nier. A Study of Day-Night Variations in the Neutral Composition of the Lower Thermosphere. J. Geophys. Res., Space Physics, 73(21):6775–6782, 1968.
- B. D. Kay and M. E. Coltrin. Quantum Tunneling and the Activated Chemisorption of Methane on Tungsten. Surface Science Letters, 198(L):375–379, 1988.
- D. G. King-Hele. Improved Formulae for determining upper atmosphere density from the change in a satellites orbital period. Planetary and Space Science, 11:261–268, 1963a.
- D. G. King-Hele. Improved Formulae for Determining Upper Atmosphere Density from the Change in a Satellites Orbital Period. Planet. Space Sci., 11:261–268, 1963b.
- D. G. King-Hele. The variation of upper-atmosphere density between sunspot maximum (1957-1958) and minimum (1964). Journal of Atmospheric and Terrestrial Physics, 27:197–209, 1965.
- D. G. King-Hele. The upper atmosphere as sensed by satellite orbits. Planetary and Space Science, 40(2/3): 223–233, 1992.
- G. Koppenwallner and H. Legge. Drag of Bodies in Rarefied Hypersonic Flow. In Thermophysical Aspects of Re-Entry Flows, June 19-21, 1985/Williamsburg, Virginia, number 85-0998. Progress in Astronautics and Aeronautics, AIAA, 1985.

- R. N. Kostoff, J. B. Anderson, and J. B. Fenn. Measurements of Momentum Accommodation of Gas Molecules At Surfaces. In H. Saltsburg, J.N. Smith, and M. Rogers, editors, Fundamentals of Gas Surface Interactions, pages 512–521. Academic Press, NY and London, 1967.
- A. Krankowsky, W. T. Kasprzak, and A. O. Nier. Mass Spectrometric Studies of the Composition of the Lower Thermosphere during Summer 1957. J. Geophys. Res., Space Physics, 73(23):6775–6782, 1968.
- R. H. Krech, M. J. Gauthier, , and G. E. Caledonia. High Velocity Atomic Oxygen/Surface Accommodation Studies. Journal of Spacecraft and Rockets, 30(4):509–513, 1993.
- L. R. Lake and K. Mauersberger. Investigation of atomic oxygen in mass spectrometer ion sources. International Journal of Mass Spectrometry and Ion Physics, 13:425–436, 1974.
- L. R. Lake and A. O. Nier. Loss of Atomic Oxygen in Mass Spectrometer Ion Sources. J. Geophys. Res., Space Physics, 78(10):1645–1653, 1973.
- C. Lee and L. W. Chen. Reactive Probability of Atomic Oxygen with Material Surfaces in Low Earth Orbit. Journal of Spacecraft and Rockets, 37(2):252–256, 2000.
- F. A. Marcos. Requirements for Improved Thermospheric Neutral Density Models. In American Astronautical Society/AIAA Astrodynamics Specialist Conf., number 85-312. AAS, 1985.
- F. A. Marcos, S. T. Lai, C. Y. Huang, C. S. Lin, J. M. Retterer, S. H. Delay, and E. Sutton. Towards Next Level Satellite Drag Modeling. In Atmospheric and Space Environments Conference, number 2010-7840. AIAA, 2010.
- R. I. Masel. Principle of Adsorption and Reaction on Solid Surfaces. John Wiley and Sons, Inc., New York, NY, 1996.
- R. R. Meier and J. M. Picone. Retrieval of absolute thermospheric concentrations from the far UV dayglow: An application of discrete inverse theory. Journal of Geophysics Research, 99:6307–6320., 1994.
- M. J. Meshishnek, C. H. Jagers, and C. S. Hemminger. Exposure of LDEF materials to Atomic Oxygen: Results of EOIM-III. Technical Report SMC-TR-94-32, Prepared by the Aerospace Corporation for the Space and Missile Systems Center, 1995.
- T. K. Minton, M. Tagawa, and G. M. Nathanson. Energy Accommodation in Hyperthermal Gas-Surface Collisions: Aerobraking in PLanetary Atmospheres. Journal of Spacecraft and Rockets, 41(3):389–396, 2004.
- R. A. Minzner. The 1976 Standard Atmosphere and Its Relationship to Earlier Standards. Review of Geophysics and Space Physics, 15(3):375–384, 1977.
- K. Moe. Absolute atmospheric densities determined from the spin and orbit decays of Explorer VI. Planetary and Space Science, 14:1065–1075, 1966.
- K. Moe. Recent experimental evidence bearing on satellite drag coefficients. AIAA Journal, 6(7):1375–1377, 1968.
- K. Moe. Density and Composition of the Lower Thermosphere. J. Geophys. Res., 78(10):1633–1644, 1973.
- K. Moe and B. R. Bowman. The effects of surface composition and treatment on drag coefficients of spherical satellites. In AAS/AIAA Astrodynamics Specialist Conference, number AAS 05-258. AAS/AIAA, 2005.
- K. Moe and M. Moe. The effect of adsorption on densities measured by orbiting pressure gauges. Planetary and Space Science, 15:1329–1332, 1967.
- K. Moe and M. Moe. Gas-surface interactions and the satellite drag coefficients. Planetary and Space Science, 53:793–801, 2005.

- K. Moe and M. Moe. CIRA Section 5: Outstanding Issues. Technical report, Committee for Space Research (COSPAR) International Reference Atmosphere, 2008.
- K. Moe, M. Moe, and E. Doornbos. Outstanding Issues Related to Thermospheric Measurements and Modeling. presented at the COSPAR meeting, Bremen, July, 2010, 2010.
- K. Moe, M. Moe, and N. W. Yelaca. Effect of Surface heterogeneity on the Adsorptive Behavior of Orbiting Pressure Gages. Journal of Geophysical Research, 77(22):4242–4247, 1972.
- K. Moe, M. M. Moe, and S. D. Wallace. Drag Coefficients of Spheres in Free-Molecular Flow. American Astronautical Society, 126:391–401, 1996.
- K. Moe, M. M. Moe, and S. D. Wallace. Improved satellite drag coefficient calculations from orbital measurements of energy accommodation. Journal of Spacecraft and Rockets, 35:266–272, 1998.
- M. Moe and K. Moe. The roles of kinetic theory and gas-surface interactions in measurements of upper atmospheric density. Planetary and Space Science, 17:917–922, 1969.
- M. M. Moe and S. D. Wallace. Refinements in Determining Satellite Drag Coefficients: Method for Resolving Density Discrepancies. Journal of Guidance, Control, and Dynamics, 16:441–445, 1993.
- M. M. Moe, S. D. Wallace, and K. Moe. Recommended Drag Coefficients for Aeronomic Satellites. Geophysical Monograph, 87:349–445, 1995.
- P. Moore. The Effect of Aerodynamic Lift on Near Circular Satellite Orbits. Planetary and Space Science, 33(5):479–491, 1985.
- P. Moore and A. Sowter. Application of a satellite aerodynamics model based on normal and tangential momentum accommodation coefficients. Planetary and Space Science, 39(10):1405–1419, 1991.
- W. D. Niven. The Scientific Papers of James Clerk Maxwell. Dover Publications, New York, 1965.
- S. Nocilla. The Surface Re-emission Law in Free Molecule Flow. In Rarefied Gas Dynamics, pages 327–346, 1963.
- D. Offermann. On the Atomic Oxygen Measurements by Rocket-Borne Mass Spectrometers. J. Geophys. Res., 77(31):6284–6286, 1972.
- D. Offermann and H. Trinks. A Rocket Borne Mass Spectrometer with Helium Cooled Ion Source. Review of Scientific Instruments, 42(12):1836–1843, 1971.
- K. Oura, V. G. Liftshits, A. A. Saranin, A. V. Zotov, and M. Katayama. Surface Science. Springer-Verlag, Berlin, 2003.
- C. Pardini, L. Anselmo, K. Moe, and M. Moe. Drag and Energy Accommodation Coefficients During Sunspot Maximum. Advances in Space Research, 45(5):638–650, 2010.
- C. Paxson, H. Snell, J. Griffin, K. Kraemer, S. Price, M. Kendra, and D. Mizuno. Space Object Temperature Determination from Multi-Band Infrared Measurements. In Proceedings of the Advanced Maui Optical and Space Surveillance Technologies Conference, held in Wailea, Maui, Hawaii, September 17-19, 2008, Ed.: S. Ryan. The Maui Economic Development Board, 2008.
- L. J. Paxton. Validation of Remote Sensing Products Produced by the Special Sensor Ultraviolet Scanning Imager (SSUSI) - a Far-UV Imaging Spectrograph on DMSP F16. Proc. of SPIE, 4485:338–348., 2002.
- L. J. Paxton. GUVI: A Hyperspectral Imager for Geospace. Proc. of SPIE, 5660:228–240., 2004.
- J. M. Picone, J. T. Emmert, and J. L. Lean. Thermospheric densities derived from spacecraft orbits: Accurate processing of two-line element sets. Journal of Geophysical Research, 110(A03301), 2002a.

- J. M. Picone, A. E. Hedin, and D. P. Drob. NRLMSISE-00 empirical model of the atmosphere: Statistical comparisons and scientific issues. Journal of Geophysical Research, 107, 2002b.
- M. D. Pilinski. An Innovative Method for Measuring Drag on Small Satellites. In Proceedings of the 23rd Annual AIAA/USU Conference on Small Satellites, Logan, UT, August 2009, 2009.
- M. D. Pilinski, B. M. Argrow, and S. E. Palo. Semi-Empirical Model for Satellite Energy-Accommodation Coefficients. Journal of Spacecraft and Rockets, 47(6):951–956, 2010.
- M. D. Pilinski, B. M. Argrow, and S. E. Palo. Drag Coefficients of Satellites with Concave Geometries: Comparing Models and Observations. Journal of Spacecraft and Rockets, 48(2):312–325, 2011a.
- M. D. Pilinski, K. Moe, S. E. Palo, and B. M. Argrow. Measuring Absolute Thermospheric Densities and Accommodation Coefficients Using Paddlewheel Satellites: Past Findings, Present Uses, and Future Mission Concepts. In IN PUBLICATION: American Astronautical Society/AIAA Astrodynamics Specialist Conf., number 11—. AAS, 2011b.
- B. De Pontieu. Database of photometric periods of artificial satellites. Advances in Space Research, 19(2): 229–232, 1997.
- L. Qian, S. C. Solomon, and T. J. Kane. Seasonal variation of thermospheric density and composition. JOURNAL OF GEOPHYSICAL RESEARCH, 114(A01312), 2009.
- V. Ramesh and D. J. Marsden. Rotational and translational accommodation coefficients of nitrogen on nickel, silver and gold. Vacuum Science, 24(7):291–294, 1974.
- M. R. Reddy. Effect of low earth orbit atomic oxygen on spacecraft materials. Journal of Material Science, 31:281–307, 1995.
- C. Reigber, H. Luehr, and P. Schwintzer. CHAMP Mission Status. Advances in Space Research, 30(2): 129–134, 2002.
- G. S. Reiter and K. Moe. Surface-Particle-Interaction Measurements Using Paddlewheel Satellites. In H. Y. Wachman, editor, Rarefied Gas Dynamics, volume 6, pages 6–20. Proc. Intl. Symposium, Boston, MA, 1968.
- R. Reynolds, J. Jost, G. Rubin, and J. Vila. Radar measurements of the reentry of the ariane 504 EPC. Advances in Space Research, 28(9):1269–1275, 2001.
- J. A. Riley and C. F. Giese. Interaction of Atomic Oxygen with Various Surfaces. The Journal of Chemical Physics, 53(1):146–150, 1970.
- W. Rudzinski and D. H. Everett. Adsorption of Gases on Heterogeneous Surfaces. Academic Press, London, UK, 1992.
- S. Bruinsma, Jeffrey M. Forbes, Steven Nerem, and Xiaoli Zhang. Thermosphere density response to the 20–21 November 2003 solar and geomagnetic storm from CHAMP and GRACE accelerometer data. Journal of Geophysical Research, 111, 2006.
- S. A. Schaaf and P. L. Chambre. Flow of Rarefied Gases. Princeton University Press, New Jersey, 1961.
- R. Schamberg. Analytic Representation of Surface Interaction For Free Molecule Flow with Application to Drag of Various Bodies. Technical Report R-339, The RAND Corporation, 1959. Available in PROJECT RAND, Aerodynamics of the Upper Atmosphere, Compiled by David J. Masson.
- R. Schamberg. On concave bodies in free molecule flow. Technical Report P-3164-1, The RAND Corporation, 1967.
- L. Sehnal. Determination of Basic Constants of Satellite-Atmosphere Interaction from the Analysis of Motion of 1974-70A. Advances in Space Research, 3(1):91–94, 1983.

- L. H. Sentman. Free Molecule Flow Theory and its Application to the Determination of Aerodynamic Forces. Technical Report LMSC-448514, Lockheed Missiles and Space Co., 1961.
- S. C. Solomon, T. N. Woods, L. V. Didkovsky, J. T. Emmert, and L. Qian. Anomalously low solar extreme-ultraviolet irradiance and thermospheric density during solar minimum. Geophysical Research Letters, 37 (L16103), 2010.
- J. A. Storch. Aerodynamic Disturbances on Spacecraft in Free-Molecular Flow. Technical Report SMC-TR-03-06, Aerospace Corp., 2002.
- M. F. Storz. Satellite Drag Accuracy Improvements Estimated from Orbital Energy Dissipation Rates. Advances in the Astronautical Sciences, (99-385), 1999.
- M. F. Storz, B. R. Bowman, J. I. Branson, and S. J. Casali. High accuracy satellite drag model (HASDM). Advances in Space Research, 36:2497–2505, 2005.
- E. Sutton. Density and Winds in the Thermosphere Deduced from Accelerometer Data. Journal of Spacecraft and Rockets, 44(6):1210–1219, 2007.
- E. Sutton. Effects of Solar Disturbances on the Thermosphere Densities and Winds from CHAMP and GRACE Accelerometer Data. PhD thesis, University of Colorado at Boulder, 2008.
- E. Sutton. Normalized Force Coefficients for Satellites with Elongated Shapes. Journal of Spacecraft and Rockets, 46(1):112–116, 2009.
- M. Tagawa, M. Umeno, and N. Ohmae. Influence of 5eV Atomic Oxygen on Surface Properties of Ag Films and Graphite. In 28th Aerospace Sciences Meeting, January 8-11, 1990/Reno, Nevada, number 90-6728. AIAA, 1990.
- Byron D. Tapley, Bob E. Schutz, and George H. Born. Statistical Orbit Determination. Elsevier Academic Press, MA, 2004.
- L. Thomas. Thermal Accommodation of Gases on Solids. In H. Saltsburg, J.N. Smith, and M. Rogers, editors, Fundamentals of Gas Surface Interactions, pages 346–369. Academic Press, NY and London, 1967.
- L. Trilling. Theory of gas-surface collisions. In H. Saltsburg, J.N. Smith, and M. Rogers, editors, Fundamentals of Gas Surface Interactions, pages 392–421. Academic Press, NY and London, 1967.
- J. Trost, H. Brune, J. Wintterlin, R. J. Behm, and G. Ertl. Interaction of oxygen with Al(111) at elevated temperatures. The Journal of Chemical Physics, 108(4):146–150, 1998.
- D. A. Vallado, P. Crawford, R. Hujsak, and T. S. Kelso. Revisiting Spacetrack Report 3: Rev 1. AIAA, (2006-6753-Rev1), 2006.
- D. A. Vallado and D. Finkleman. A Critical Assessment of Satellite Drag and Atmospheric Density Modeling. AIAA, (2008-6442), 2008.
- J. Vieceli, M. Roeselova, and D. J. Tobias. Accommodation coefficients for water vapor at the air/water interface. Chemical Physics Letters, 393:249–255, 2004.
- A. F. Whitaker, R. R. Kamenetzky, M. M. Finckenor, and J. K. Norwood. Atomic Oxygen Effects on LDEF Experiment AO171. LDEF: 69 Months in Space. Part 3: Second Post-Retrieval Symposium, NASA, Langley Research Center, (N93-28254 10-99):1125–1135, 1993.
- C. B. White, G. T. Roberts, and A. R. Chambers. Measurement of 5-eV Atomic Oxygen Using Carbon Based Films: Preliminary Results. IEEE SENSORS JOURNAL, 5(6):249–255, 2005.
- H. F. Winters and P. Sigmund. Sputtering of chemisorbed gas (nitrogen on tungsten) by low energy ions. Journal of Applied Physics, 45(11):4760–4766, 1974.

- B. J. Wood. The Rate and Mechanism of Interaction of Oxygen Atoms and Hydrogen Atoms with Silver and Gold. Journal of Physical Chemistry, 75(14):2186–2195, 1971.
- K. Yokota, N. Ohmae, and M. Tagawa. Effect of Relative Intensity of 5 eV Atomic Oxygen and 172 nm Vacuum Ultraviolet in the Synergism of Polyimide Erosion. High Performance Polymers, 16:221–234, 2004.

Appendix A

Drag Coefficient of a Cylinder

The formulas presented here were derived by Sentman under the assumptions of free-molecular flow and cosine reflection [Sentman, 1961]. The equation for the drag coefficient of a cylinder, $C_{D,cyl}$, can be decomposed into the drag coefficient of the cylindrical section $C_{D,side}$ and that of two end caps $C_{D,cap-n}$ (see Figure A.1).

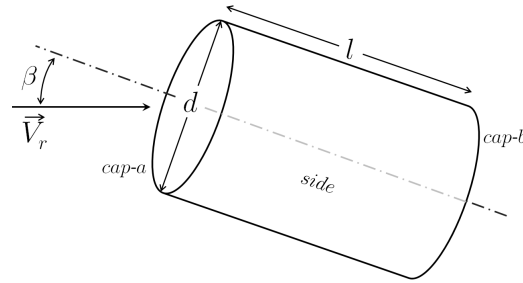


Figure A.1: Cylinder of diameter d and length l flying at angle of attack β .

$$C_{D,cyl} = \frac{((C_{D,cap-a} + C_{D,cap-b})\pi d^2 / 4 + C_{D,side} l d / 2)}{A_{cyl}} \quad (\text{A.1})$$

In equation A.1, l and d refer to the length and diameter of the cylinder respectively. For the cylindrical section, the equation is

$$C_{D,cap-n} = C_{N,cap-n} \sin x + C_{A,cap-n} \cos x \quad (\text{A.2a})$$

$$\begin{aligned}
C_{N,cap-n} = & \\
& \left(s \sin x / \sqrt{\pi} + 0.5 \sqrt{T_{k,out}/T_a} \right) \exp(-s^2 \sin^2 x) / s^2 + \\
& \left((0.5 + s^2 \sin^2 x) + (0.5 \sqrt{T_{k,out}/T_a} \sqrt{\pi} s \sin x) \right) \cdot \\
& (1 + \operatorname{erf}(s \sin x)) / s^2
\end{aligned} \tag{A.2b}$$

$$\begin{aligned}
C_{A,cap-n} = & \\
& \left((s \cos(x) / \sqrt{\pi}) [\exp(-s^2 \sin^2(x)) + \right. \\
& \left. \sqrt{\pi} s \sin(x) (1 + \operatorname{erf}(s \sin(x)))] \right) / s^2
\end{aligned} \tag{A.2c}$$

$$x = \begin{cases} \beta & \text{if } n = a, \text{ plate a} \\ \beta + \pi & \text{if } n = b, \text{ plate b} \end{cases} \tag{A.2d}$$

where s is the speed ratio and β is the angle of attack (angle between the free-stream velocity vector and the axis of the cylinder). The drag coefficient of the cylindrical side is taken to be

$$C_{D,side} = C_{N,side} \sin \beta + C_{A,side} \cos \beta \tag{A.3a}$$

$$\begin{aligned}
C_{N,side} = & s \sqrt{\pi} \sin(\beta) (2 \sin^2(\beta) + 1/s^2) \\
& \exp\left(-\frac{s^2 \sin^2(\beta)}{2}\right) \left[I_0\left(\frac{s^2 \sin^2(\beta)}{2}\right) + I_1\left(\frac{s^2 \sin^2(\beta)}{2}\right) \right] + \\
& (2\sqrt{\pi}/s) \sin(\beta) \exp\left(-\frac{s^2 \sin^2(\beta)}{2}\right) I_0\left(\frac{s^2 \sin^2(\beta)}{2}\right) + \\
& \sqrt{T_{k,out}/T_a} ((\pi^3/2)/(2s)) \sin(\beta)
\end{aligned} \tag{A.3b}$$

$$\begin{aligned}
C_{A,side} = & \\
& 2s \sqrt{\pi} \sin^2(\beta) \cos(\beta) \exp\left(-\frac{s^2 \sin^2(\beta)}{2}\right) \\
& \left[I_0\left(\frac{s^2 \sin^2(\beta)}{2}\right) + I_1\left(\frac{s^2 \sin^2(\beta)}{2}\right) \right] + \\
& (2\sqrt{\pi}/s) \cos(\beta) \exp\left(-\frac{s^2 \sin^2(\beta)}{2}\right) I_0\left(\frac{s^2 \sin^2(\beta)}{2}\right)
\end{aligned} \tag{A.3c}$$

where I_0 and I_1 are the modified Bessel functions of first kind with degree 0 and 1 respectively. Equations A.4a through A.4h describe the total cross sectional area of the cylinder.

$$A_{cyl} = A_{cap-a} + A_{cap-b} + A_{side} \quad (A.4a)$$

$$A_{cap-a} = \frac{\pi d^2 \cos|\beta|}{4} \quad (A.4b)$$

$$A_{cap-b} = A_{cap-a} \quad \text{if } \frac{l \sin|\beta|}{2} \geq \frac{d \cos|\beta|}{2} \quad (A.4c)$$

$$A_{cap-b} = A_{cap-a} - 2(A_{sec} - A_{tri}) \quad \text{if } \frac{l \sin|\beta|}{2} < \frac{d \cos|\beta|}{2} \quad (A.4d)$$

$$A_{sec} = \frac{d^2 \cos|\beta|}{4} \left[\text{atan}(\cos|\beta| \tan(\pi/2)) - \text{atan}(\cos|\beta| \tan(\text{asin}(l \sin|\beta| / (d \cos|\beta|))) \right] \quad (A.4e)$$

$$A_{tri} = \left((l \sin(|\beta|)/2) / \tan(\text{asin}(l \sin|\beta| / (d \cos|\beta|))) \right) L \sin|\beta| / 2 \quad (A.4f)$$

$$A_{side} = l d \sin|\beta| - A_{cap-a} \quad \text{if } \frac{l \sin|\beta|}{2} \geq \frac{d \cos|\beta|}{2} \quad (A.4g)$$

$$A_{side} = l d \sin|\beta| - (A_{cap-a} - 2(A_{sec} - A_{tri})) \quad \text{if } \frac{l \sin|\beta|}{2} < \frac{d \cos|\beta|}{2} \quad (A.4h)$$

Appendix B

Numerical Program Validation

Several cases were run to compare the output of the test particle code with that of Bird's Direct Simulation Monte Carlo (DSMC) [Bird, 1994]. For these runs, the flow was composed entirely of atomic oxygen. We show here only the drag coefficient comparisons. First, a simple "wedge" geometry was modeled in rarefied flow. For such convex geometry, an equivalent analytical solution may also be obtained using a "plate model" technique [Sutton, 2009]. The results are shown in Table B for various flow conditions. The test particle drag coefficient agrees with DSMC and plate model results within 0.3%.

Validation using a cube was performed to test both the validity of the SPARCS embedded plate model and test particle codes against the plate model equations already in use for orbital drag analysis of the CHAMP and GRACE satellites [Sutton, 2007] (Sutton 2007). Results are shown in Figures B.2 (a) and (b). The plate model and test particle results from the cube geometry also agree within 0.3%.

A concave geometry was also tested. The CHAMP satellite was modeled (boom facing aft). The results show agreement between Bird's DSMC and test particle within 0.25%. However, the plate model underestimates drag coefficient of CHAMP by approximately 7.5%. This is because the plate model cannot account for flow shadowing. Each CHAMP run took approximately 8 minutes for SPARCS and 20 minutes for Bird's DSMC on a 2.7 GHz dual core Athlon processor.

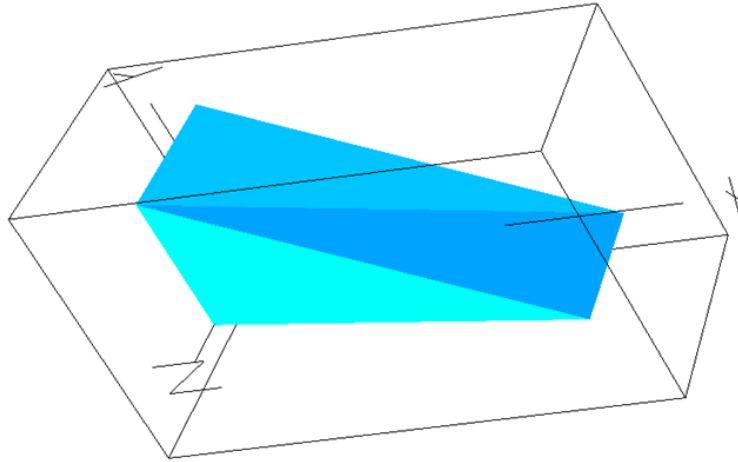
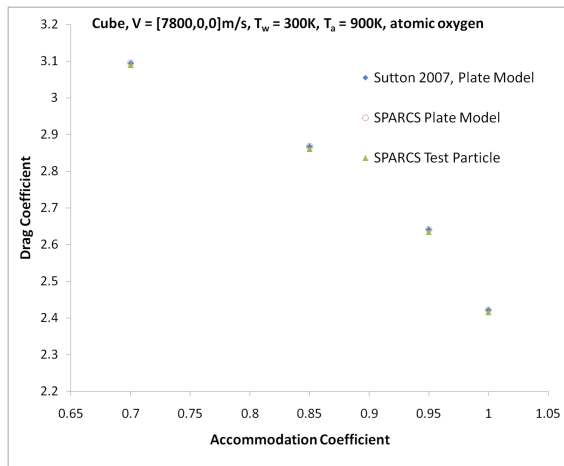
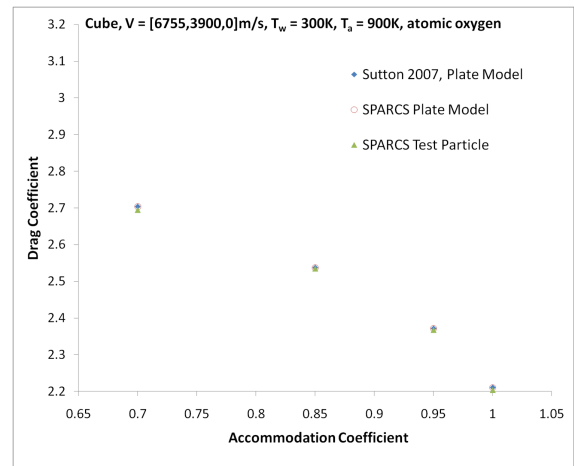


Figure B.1: The wedge used to validate against convex (integral) equations.



(a)



(b)

Figure B.2: Test particle validation for a cube geometry (a) free stream normal to face, (b) free-stream at oblique angle

Table B.1: Convex geometry validation.

[Vx, Vy, Vz]= [7800 0 0] m/s			
	Tatm = 100 K Tsurf = 300 K $\alpha = 1.00$	Tatm = 1500 K Tsurf = 300 K $\alpha = 1.00$	Tatm = 1500 K Tsurf = 300 K $\alpha = 0.60$
Test Particle Code	2.122 ± 0.001	2.200 ± 0.002	2.843 ± 0.004
Direct Simulation Monte Carlo	2.123 ± 0.001	2.198 ± 0.001	2.838 ± 0.001
Analytic Solution	2.121	2.197	2.840
[Vx, Vy, Vz]= [4503 -4503 4503] m/s			
	Tatm = 100 K Tsurf = 300 K $\alpha = 1.00$	Tatm = 1500 K Tsurf = 300 K $\alpha = 1.00$	Tatm = 1500 K Tsurf = 300 K $\alpha = 0.60$
Test Particle Code	2.076 ± 0.004	2.191 ± 0.005	2.603 ± 0.006
Direct Simulation Monte Carlo	2.074 ± 0.001	2.188 ± 0.001	2.601 ± 0.001
Analytic Solution	2.069	2.185	2.597
[Vx, Vy, Vz]= [0 -7800 0] m/s			
	Tatm = 100 K Tsurf = 300 K $\alpha = 1.00$	Tatm = 1500 K Tsurf = 300 K $\alpha = 1.00$	Tatm = 1500 K Tsurf = 300 K $\alpha = 0.60$
Test Particle Code	2.127 ± 0.001	2.236 ± 0.003	2.836 ± 0.004
Direct Simulation Monte Carlo	2.126 ± 0.001	2.237 ± 0.001	2.835 ± 0.001
Analytic Solution	2.127	2.238	2.836

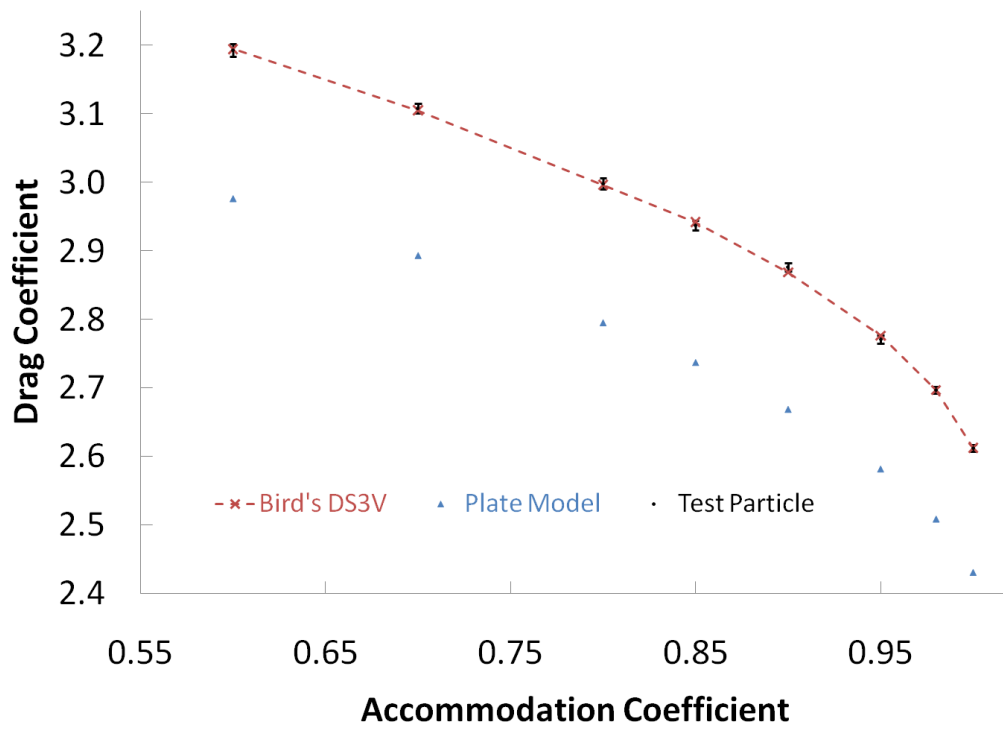


Figure B.3: Concave (CHAMP) geometry validation.

Appendix C

SESAM Drag Coefficient Lookup Tables

The results of Direct Simulation Monte Carlo runs for a 1.6 diameter sphere flying in the Earth's thermosphere are shown here in tables C.1 and C.2. These results form the basis of SESAM lookup tables.

Table C.1: DSMC drag coefficient results for velocities of 7,500 m/s.

accommodation	120 km	130 km	140 km	160 km	200 km	225 km	300 km
1.00	1.886	1.963	2.006	2.046	2.087	2.096	2.111
0.86	2.187	2.282	2.316	2.352	2.377	2.381	2.391
0.65	2.407	2.516	2.546	2.559	2.577	2.583	2.590
0.00	2.828	2.909	2.935	2.947	2.961	2.963	2.970

Table C.2: DSMC drag coefficient results for velocities of 10,300 m/s.

accommodation	120 km	130 km	140 km	160 km	200 km	225 km	300 km
1.00	1.871	1.929	1.969	2.006	2.043	2.055	2.070
0.86	2.237	2.308	2.331	2.346	2.358	2.361	2.365
0.65	2.449	2.519	2.541	2.551	2.564	2.563	2.568
0.00	2.848	2.914	2.923	2.935	2.946	2.949	2.957